Curso 2009/10
CIENCIAS Y TECNOLOGÍAS/26
I.S.B.N.: 978-84-7756-972-5

SÉBASTIEN COMERÓN LIMBOURG

Morfología y propiedades físicas de la formación estelar en galaxias

Directores
JOHAN H. KNAPEN
JOHN E. BECKMAN

SERVICIO DE PUBLICACIONES
UNIVERSIDAD DE LA LAGUNA

SOPORTES AUDIOVISUALES E INFORMÁTICOS
Serie Tesis Doctorales

Fecha de examen: 25 Junio de 2010
Directores de Tesis: Dr. Johan H. Knapen y Dr. John E. Beckman

Algunas de las figuras incluidas en este documento ya han sido publicadas en *Astronomy & Astrophysics*, *The Astrophysical Journal Letters* y *Monthly Notices of the Royal Astronomical Society.* Parte del material incluido en este documento ya ha sido publicado en *Astronomy & Astrophysics*, *The Astrophysical Journal Letters* y *Monthly Notices of the Royal Astronomical Society.*

Adolfo Comerón Martín

In Memoriam,
químico, maestro y abuelo
1921 — 2010

Resumen

El principal objetivo de esta tesis ha sido encontrar relaciones entre la formación estelar en los bulbos de las galaxias (principalmente por parte de anillos nucleares de formación estelar) y otras propiedades de la galaxia huésped, como pueden ser la fuerza de la barra o la presencia de sigma-drops. Para ello, hemos estudiado las no-axisimetrías de las galaxias y sus efectos, como por ejemplo las calles de polvo en barras. Adicionalmente, al final de ester trabajo, incluimos un Capítulo sobre una galaxia espiral muy inclinada, NGC 4244, y un Capítulo con un estudio preliminar sobre descomposiciones de galaxias con anillos externos usando GALFIT en imágenes tomadas en infrarrojo.

El primer Capítulo trata sobre un estudio en el que investigamos caídas de la dispersión estelar de velocidades en las regiones centrales de las galaxias. Dichas caídas son conocidas con el nombre de sigma-drops (σ-drops). En este Capítulo, presentamos una muestra de 20 galaxias con σ-drop emparejada con una muestra de galaxias de control sin σ-drop con la intención de buscar correlaciones entre la presencia de σ-drops y las propiedades, principalmente morfológicas, de las zonas nucleares y de los discos de las galaxias huésped. Para las dos muestras, hemos estudiado las distribuciones de polvo y de luz emitida en Hα a escalas de 0.1 segundos de arco usando imágenes del *Hubble Space Telescope* (*HST*) de las zonas circumnucleares, buscando diferencias entre las dos muestras e intentando encontrar relaciones entre la cinemática del bulbo y su morfología. Hemos tomado en cuenta la emisión en CO y H I de las galaxias y sus perfiles de luminosidad. Hemos clasificado las dos muestras teniendo en cuenta criterios morfológicos y los perfiles de luminosidad estelar y hemos descubierto una mayor proporción de espirales nucleares de polvo y de anillos de formación estelar en la muestra de galaxias con σ-drop. Hemos descubierto que la proporción de galaxias Seyfert en la muestra de galaxias con σ-drop es mayor que la de LINERs y que lo opuesto es cierto para la muestra de control. Las conclusiones del Capítulo 1 son que los σ-drop son probablemente debidos a la formación estelar en un disco o un anillo de gas (debido a resonancias internas de Lindblad) dinámicamente fríos alimentados por un flujo de gas proveniente de partes más externas de la galaxia. El mismo mecanismo que alimenta el anillo o el disco nuclear es probablemente el causante de que haya una mayor tasa de galaxias con un núcleo Seyfert en las galaxias con σ-drop. Algunos de los resultados de este Capítulo han sido publicados en Comerón et al. (2008a).

En el Capítulo 2 estudiamos cuatro Anillos Nucleares Ultra-Compactos (UCNRs por sus siglas en inglés) descubiertos en imágenes del *HST* cuando preparábamos las muestras para el Capítulo 1. Los UCNRs son definidos como anillos nucleares con un radio inferior a los 200 pc. La meta de este Capítulo es descubrir si, al igual que en el caso de sus contrapartidas de mayor tamaño, son debidos a un aporte de gas proveniente de zonas más externas de la galaxia después de que éste haya perdido momento angular debido a una componente no-axisimétrica (como por ejemplo una barra) y haya sido atrapado en órbitas x_2 relacionadas con Resonancias Internas de Lindblad (ILRs por sus silgas en inglés) o si, por lo contrario, han sido creados por otro proceso físico. A partir de imágenes en UV y Hα del archivo del *HST* y a partir de mapas de estructura de las regiones circumnucleares, analizamos la morfología de la formación estelar y del polvo de los UCNRs, con radios entre 30 y 130 pc, que hemos descubierto en NGC 2985, NGC 4579 y NGC 4800. Excepto por su tamaño, no hemos descubierto ninguna diferencia entre los UCNRs y los anillos nucleares

'clásicos'. Algunos de los resultados de este Capítulo han sido publicados en Comerón et al. (2008b).

En el tercer Capítulo presentamos el atlas de anillos nucleares más completo que se ha hecho hasta la fecha. Lo hemos llamado Atlas of Images of NUclear Rings (AINUR). Hemos incluido en él 113 anillos descubiertos en 107 galaxias, seis de las cuáles son galaxias elípticas, cinco son galaxias con disco muy inclinadas, 18 son galaxias con disco no barradas y 78 son galaxias con disco barradas. Nuestro objetivo ha sido buscar relaciones entre el tamaño y la morfología de los anillos nucleares de formación estelar y varios parámetros de las galaxias como el tamaño de las mismas y las propiedades de sus barras. También hemos querido confirmar si los UCNRs son una población separada de anillos nucleares con un origen distinto o si, por lo contrario, son la cola de bajo tamaño de la distribución de anillos nucleares 'canónicos'. A partir de imágenes de archivo del *HST* hemos preparado mapas de color y de estructura, así como imágenes en Hα y Paα con el continuo substraído. Hemos producido perfiles de elipticidad a partir de imágenes en banda H del Two-Micron All-Sky Survey (2MASS) para detectar barras y medir sus propiedades. Para nuestras galaxias, hemos medido el parámetro de torsión de las estructuras no-axisimétricas, $Q_{\rm g}$. Hemos descubierto que los anillos nucleares tienen tamaños que van de pocas decenas de párseces a pocos kilopársecs en radio. Hemos descubierto que los anillos nucleares de polvo se encuentran en galaxias elípticas y en galaxias de tipo S0 y que los anillos nucleares de formación estelar se encuentran en un $20 \pm 2\%$ de las galaxias con disco con tipos entre $T = -3$ y $T = 7$, con un pico en la distribución que se encuentra entre los tipos $T = 2$ y $T = 3$. Hemos descubierto que los anillos nucleares de formación estelar no tienen una fuerte preferencia por galaxias barradas. Las elipticidades de los anillos descubiertos en galaxias con disco van de $\epsilon_{\rm r} = 0$ a $\epsilon_{\rm r} = 0.4$, siempre y cuando consideremos que los anillos son coplanares con el disco de la galaxia. Para las galaxias barradas, hemos descubierto que el radio máximo que un anillo nuclear puede alcanzar es una cuarta parte del semi-eje mayor de la barra. Hemos descubierto que existe una distribución aleatoria de diferencias entre el ángulo de posición de las barras y el ángulo de posición de los anillos nucleares. Hemos descubierto ciertos indicios que podrían indicar que la elipticidad máxima de los anillos se ve limitada por la elipticidad máxima de la barra. Confirmamos que el máximo tamaño relativo al tamaño de la galaxia posible para un anillo nuclear de formación estelar es inversamente proporcional a $Q_{\rm g}$ ("las barras más fuertes hospedan anillos más pequeños") y que el origen de los anillos nucleares, incluso los que se encuentran en galaxias no barradas, está muy relacionado con resonancias dinámicas. Los UCNR no son más que la cola a bajo tamaño de la distribución de anillos nucleares. En este Capítulo también discutimos lo que estos descubrimientos implican sobre la duración de vida de los anillos y sobre su origen y evolución. Algunos de los resultados de este Capítulo han sido publicados en Comerón et al. (2010).

En el Capítulo 4 hemos intentado comprobar la predicción teórica de que, de las calles de polvo en barras, las menos curvadas son las que se encuentran en las barras más fuertes, o, más específicamente, que el grado de curvatura de las calles de polvo es inversamente proporcional a la fuerza de la barra. Para esta comprobación hemos usado imágenes de archivo de galaxias barradas para las cuáles hubiera disponibles en la literatura buenas medidas del parámetro de torsión de la barra ($Q_{\rm b}$; también llamado fuerza de la barra) y del radio en el cuál $Q_{\rm b}$ ha sido medido ($r(Q_{\rm b})$). Nuestros resultados confirman la predicción

teórica pero muestran una gran dispersión que no puede ser explicada por los errores en la medida. Hemos simulado 238 galaxias con diferentes parámetros de barra y de bulbo para investigar el origen de dicha dispersión. A partir de las simulaciones, hemos llegado a la conclusión de que la dispersión se ve muy reducida cuando se describe la fuerza de la barra como una combinación lineal de $Q_{\rm b}$ y el cociente entre el eje mayor y el eje menor de la barra, a/b. Por lo tanto, llegamos a la conclusión de que la curvatura de las calles de polvo viene determinada, en su mayo parte, por parámetros que dependen de la barra. Algunos de los resultados de este Capítulo han sido publicados en Comerón et al. (2009).

En el Capítulo 5 presentamos un estudio en profundidad de NGC 4244. NGC 4244 es una galaxia de tipo tardío que se nos presenta casi de canto y que se encuentra a 4.4 Mpc. Es conocida como la única galaxia cercana de canto en la que no se ha podido confirmar la existencia de un disco grueso. Si los discos gruesos son, como se ha propuesto, el resultado de la evolución interna de la galaxia, todas la galaxias con disco lo suficientemente antiguas y que no hayan sufrido interacciones fuertes deberían tener uno. Encontrar una galaxia sin un disco grueso supondría un reto para algunos modelos de formación de galaxias. Hemos usado datos del *Spitzer Survey of Stellar Structure in Galaxies* (S^4G) y hemos descubierto que la galaxia tiene un disco grueso muy débil. También encontramos que las diferencias en el perfil de luminosidad entre un lado y otro del plano central de la galaxia pueden ser explicadas por una combinación del hecho de que la galaxia no está perfectamente de canto y por cierto grado de opacidad del disco delgado. Inferimos que la baja densidad del disco grueso es causada por una falta de evolución secular en NGC 4244.

En el Capítulo 6 hemos estudiado galaxias con anillos externos usando imágenes de S^4G. Hemos emparejado una muestra de once galaxias con anillo externo con una muestra de control con once galaxias sin anillo externo. Hemos utilizado Galfit para descomponer las galaxias en sus componentes principales con el objetivo de encontrar diferencias entre los parámetros estructurales de las galaxias con anillos y los de las galaxias sin anillos. Hemos descubierto que los anillos externos tienden a encontrarse en galaxias con las barras más largas, más masivas y más anchas (pero no en las más fuertes).

Hemos resumido las principales conclusiones de esta tesis en el Capítulo 7 (en inglés) y en el Capítulo 8 (en español).

Códigos UNESCO: 210104 y 210106

Abstract

The main goal of this thesis work is to find the links between star formation in galaxy bulges (mainly in the form of star-forming nuclear rings) and other properties of the host galaxy, such as the bar strength or the presence of sigma-drops. To do so we study galaxy non-axisymmetries and their side effects, such as dust lanes in bars. At the end of this work we also include a Chapter on a highly inclined spiral galaxy, namely NGC 4244, and a Chapter on a preliminary study on GALFIT decomposition of infrared images of disc galaxies with outer rings.

In the first Chapter we describe a study of localized minima of the stellar velocity dispersion in the central regions of galaxies, which are known as sigma-drops (σ-drops). In this Chapter we present a sample of 20 σ-drop galaxies matched with a control sample of galaxies without σ-drops in order to search for correlations between σ-drops and the properties, primarily morphological, of the nuclear zones and the discs of their host galaxies. For these two samples we study the dust and Hα distribution on 0.1 arcsec scales, using *Hubble Space Telescope* (*HST*) imaging, in the circumnuclear zones, searching for differences and trying to establish a link between the bulge kinematics and its morphology. We have also considered the CO and H I emission distribution of the galaxies, and their luminosity profiles. We classify the two samples following both morphological parameters and the stellar luminosity profiles and we find a larger fraction of nuclear dust spirals and star-forming nuclear rings in the σ-drop sample. We also find that the fraction of Seyfert galaxies in the σ-drop sample is bigger than that of LINERs and that the reverse is true for the control sample. The conclusions of Chapter 1 are that σ-drops are very probably due to inflow-induced star formation in a dynamically cool disc, or in a gas ring (shock focused by an inner Lindblad resonance), above a certain critical density level. The same mechanism that feeds the nuclear ring or the nuclear disc is probably responsible for the higher rate of Seyfert galaxies among the σ-drop hosts. Some of the results of this Chapter have been published in Comerón et al. (2008a).

In Chapter 2 we study four Ultra-Compact Nuclear Rings (UCNRs) found in the *HST* images used to prepare the samples for Chapter 1. UCNRs are nuclear rings which we define to be less than 200 pc in radius. The point of this Chapter is to find evidence to know whether they have been formed (like their larger counterparts) by an inflow of gaseous material that has been driven to central regions of the galaxy after the loss of angular momentum due to a non-axisymmetric structure (e.g. a bar) and has been trapped in x_2 orbits related to Inner Lindblad Resonances (ILRs), or whether they have been created by another physical process. From archival *HST* UV and Hα images and from dust structure maps of the circumnuclear regions, we analyse the morphology of the star formation and dust of the UCNRs, which are 30 − 130 pc in radius, that are found in NGC 2985, NGC 4579, and NGC 4800. We find no difference, except for the size, between UCNRs and 'classical' nuclear rings. Some of the results of this Chapter have been published in Comerón et al. (2008b).

In the third Chapter we present the most complete atlas of nuclear rings to date, which has been named Atlas of Images of NUclear Rings (AINUR). We include 113 rings found in 107 galaxies, six of which are elliptical galaxies, five are highly inclined disc galaxies, 18 are unbarred disc galaxies, and 78 are barred disc galaxies. Our aim is to explore possible

relationships between the size and morphology of the star-forming nuclear rings and various galactic parameters such as the galaxy size and the galaxy bar properties. We also aim to establish whether UCNRs are a distinct population of nuclear rings, with a distinct origin, or if they are merely the low-end tail of the nuclear ring size distribution. We produce colour index and structure maps, as well as Hα and Paα continuum-subtracted images from *HST* archival data. We derive ellipticity profiles from H-band Two-Micron All-Sky Survey (2MASS) images in order to detect bars and find their metric parameters. We measure the non-axisymmetric torque parameter, $Q_{\rm g}$, and search for correlations between bar and ring metric parameters, and $Q_{\rm g}$. We find that nuclear rings span a range from a few tens of parsecs to a few kiloparsecs in radius. We find that dust nuclear rings are found in elliptical and S0 galaxies. We find that star-forming nuclear rings occur in $20 \pm 2\%$ of disc galaxies with types between $T = -3$ and $T = 7$, with a peak in the distribution between $T = 2$ and $T = 3$ and without strong preference for barred galaxies. The ellipticities of rings found in disc galaxies range from $\epsilon_{\rm r} = 0$ to $\epsilon_{\rm r} = 0.4$, assuming that nuclear rings lie in the galactic plane. For barred galaxies, the maximum radius that a nuclear ring can reach is a quarter of the bar semi-major axis. We found a nearly random distribution of position angle offsets between nuclear rings and bars. There is some evidence that nuclear ring ellipticity is limited by bar ellipticity. We confirm that the maximum relative size of a star-forming nuclear ring is inversely proportional to the non-axisymmetric torque parameter, $Q_{\rm g}$ ("stronger bars host smaller rings") and that the origin of nuclear rings, even the ones in non-barred hosts, is closely linked to the existence of dynamical resonances. Ultra-compact nuclear rings constitute the low-radius portion of the nuclear ring size distribution. We discuss implications for the lifetimes of nuclear rings and for their origin and evolution. Some of the results of this Chapter have been published in Comerón et al. (2010).

In Chapter 4 we test the theoretical prediction that the straightest dust lanes in bars are found in strongly barred galaxies, or more specifically, that the degree of curvature of the dust lanes is inversely proportional to the strength of the bar. The test used archival images of barred galaxies for which a reliable bar non-axisymmetric torque parameter ($Q_{\rm b}$; also called bar strength) and the radius at which $Q_{\rm b}$ has been measured ($r(Q_{\rm b})$) have been published in the literature. Our results confirm the theoretical prediction but show a large spread that cannot be accounted for by measurement errors. We simulate 238 galaxies with different bar and bulge parameters in order to investigate the origin of the spread in the dust lane curvature versus $Q_{\rm b}$ relation. From these simulations, we conclude that the spread is greatly reduced when describing the bar strength as a linear combination of the bar parameter $Q_{\rm b}$ and the ratio of the major and minor axis of the bar, a/b. Thus, we conclude that the dust lane curvature is predominantly determined by the parameters of the bar. Some of the results of this Chapter have been published in Comerón et al. (2009).

In Chapter 5 we present an in-depth study of NGC 4244. NGC 4244 is a late-type nearly edge-on galaxy 4.4 Mpc away. It has been reported as the only nearby edge-on galaxy without a confirmed thick disk. If thick disks are indeed, as has been proposed, products of internal evolution, all old enough undisturbed disc galaxies should have a thick disk. Finding such a galaxy without a thick disc would be a serious challenge to a range of galaxy formation models. Using data from the *Spitzer Survey of Stellar Structure in Galaxies* (S^4G) we have found that this galaxy has a tenuous thick disk. We have also found that the asymmetries between the light profiles on either side of the mid-plane of

NGC 4244 can be explained by a combination of the galaxy not being perfectly edge-on and a certain degree of opacity of the thin disk. We argue that the low density of the thick disk is a consequence of the lack of secular evolution in NGC 4244.

In Chapter 6 we study galaxies with outer rings using S^4G images. We have matched a sample of eleven galaxies with outer rings with another sample of eleven galaxies without an outer ring. We used GALFIT to decompose the galaxies into their main components in order to find differences between the structural parameters of ringed and non-ringed galaxies. We find that outer rings tend to be hosted in galaxies with more massive, wider, and longer, but not stronger, bars.

We list the main conclusions of this thesis in Chapter 7 (in English) and in Chapter 8 (in Spanish).

UNESCO CODES: 210104 and 210106

Index

List of Tables

List of Figures

1

On the morphology of sigma-drop galaxies

1.1 Introduction

It is normally considered physically reasonable that the stars closest to the centre of a galaxy, close to the bottom of the potential well, should have the highest velocity dispersions. In other words, a radial plot of velocity dispersion across a galaxy should peak on the nucleus. This prediction, however, would only be true if the stellar orbits were isotropic in a spheroid in equilibrium under gravity with its mass centrally concentrated. As the angular resolution of spectroscopic data has improved, detailed measurements on nearby galaxies have shown in some galaxies an unexpected drop in the stellar velocity dispersion as the nucleus is approached, a phenomenon referred to as a dispersion drop or σ-drop (Emsellem et al. 2001; Emsellem 2004). One of the first known examples of this phenomenon can be found in Jarvis et al. (1988), later results include those reported by Jarvis & Peletier (1991), Bottema (1993), Van der Marel (1994), Bertola et al. (1996), Bottema & Gerritsen (1997), Fisher (1997), Simien & Prugniel (1997a, b, and c), Héraudeau & Simien (1998), Simien & Prugniel (1998), Héraudeau et al. (1999), Simien & Prugniel (2000), Emsellem et al. (2001), Simien & Prugniel (2002), de Zeeuw et al. (2002), Aguerri et al. (2003), Márquez et al.(2003), Shapiro et al. (2003), Chung & Bureau (2004), Falcón-Barroso et al. (2006), Ganda et al. (2006), Emsellem et al. (2006), and Dumas et al. (2007).

The frequency of σ-drops in galaxy populations has still not been determined with precision, but estimates currently go as high as 50% of disc galaxies (from the previously cited articles). They have been found in a wide variety of galaxy types in both active and non-active galaxies. A few cases have been observed in lenticular and elliptical galaxies (Emsellem 2006).

Explanations have been proposed for this phenomenon with theoretical arguments and also using numerical simulations. For disc galaxies a scenario has been proposed in which the stellar population in a σ-drop galaxy was formed from a circumnuclear rapidly rotating dynamically cool gaseous component. The stars inherit the velocity pattern of the gas from which they form, so their velocity dispersion is lower than that of the older, 'underlying' stars. A young stellar population dominates an older population in luminosity, so the resulting spectrum is dominated by the lower velocity dispersion of the younger stars (see,

e.g., Wozniak et al. 2003, also Allard et al. 2005, 2006). This effect can be enhanced by a falling velocity dispersion of the gas towards the centre of a galaxy, due to a strong accumulation of gas in a dissipative disc that would cool the gas in a cold component (i.e., a cold disc as shown in Falcón-Barroso et al. 2006). Hydro/N-body simulations (Wozniak & Champavert 2006) have shown that a σ-drop can form in less than 500 Myr, but that its lifetime can exceed 1 Gyr if the nuclear zone is continually fed with gas to sustain star formation. This continued formation of stars is required to maintain a long term σ-drop, which in turn is required for the observed large σ-drop fraction among the galaxy population. When star formation ceases, dynamical relaxation will cause the σ-drop to dissipate in a time-scale that goes from few hundred Myr for short-lived σ-drops (circumnuclear volume feeding during less than 500 Myr) to the order of 1 Gyr or even more for long-lived σ-drops (see Fig. 2 in Wozniak & Champavert 2006). It is worth keeping in mind that the phenomenon of σ-drops and that of gas inflow are both considered to be indications of the type of phenomena which occur in secular evolution (as reviewed by Kormendy & Kennicutt 2004).

Although this model is considered not only plausible but probable, there are a number of alternatives. A massive, concentrated dark matter halo could remove kinetic energy from the stellar component. Numerical simulations of this effect can be found in Athanassoula & Misiriotis (2002), their Fig. 13. In this model the massive halo gives rise to a strong bar, and the σ-peak is suppressed compared with galaxies having smaller halos. However, these numerical simulations are only done with particles (stars) and do not take into account the effects of gas concentration in the galactic centre. It has also been argued (Dressler & Richstone 1990) that a σ-drop might be a symptom of the absence of a central supermassive black hole, but van der Marel (1994) argues against this that a cause might even be the widening of spectral line wings in the presence of a black hole, giving rise to an apparent reduction in σ due to the fact that 'standard' Gaussian spectral line fits are insensitive to widened wings.

In this Chapter we present a statistical study of 20 of these σ-drop galaxies, and match the sample with a control sample to see if we can identify characteristics which distinguish the overall morphologies of the σ-drop hosts.

In Section 1.2 we explain the sample selection criteria, and give a brief description of the resulting samples. In Section 1.3 we show how we processed the data, in Section 1.4 we study the σ-drop properties such as the radius, in Section 1.5 we describe the morphological classification adopted, in Section 1.6 we study the presence of activity in nuclei, and in Section 1.7 we show a test based on the use of luminosity profiles of the sample galaxies. In Section 1.8 we add H I+CO radio observations to the previous optical and near IR data sets, applying these to the task of differentiating σ-drop galaxies from the control sample, and in Section 1.9 we discuss the material presented in this Chapter, and present our conclusions.

1.2 Sample selection

Our σ-drop galaxy sample is a sub-sample of the selection of galaxies listed by Emsellem et al. (2006) as having spectroscopic evidence for the presence of a drop in the central stellar velocity dispersion. We selected those galaxies that had been imaged with the *Hubble Space Telescope* (*HST*) and which were not classified as edge-on in the RC3 catalogue (de

Table 1.1: Source of the velocity dispersion profiles or 2D dispersion maps that we used to construct the samples.

σ-drop sample		Control sample	
Galaxy	Source	Galaxy	Source
NGC 1068	Dumas et al. (2007)	NGC 488	Ganda et al. (2006)
NGC 1097	Emsellem et al. (2001)	NGC 864	Ganda et al. (2006)
NGC 1808	Emsellem et al. (2001)	NGC 1566	Bottema (1993)
NGC 2460	Shapiro et al. (2003)	NGC 2964	Ganda et al. (2006)
NGC 2639	Márquez et al. (2003)	NGC 2985	Dumas et al. (2007)
NGC 2775	Shapiro et al. (2003)	NGC 3031	Héraudeau & Simien (1998)
NGC 3021	Héraudeau et al. (1999)	NGC 3169	Héraudeau & Simien (1998)
NGC 3412	Aguerri et al. (2003)	NGC 3198	Bottema (1993)
NGC 3593	Bertola et al. (1996)	NGC 3227	Dumas et al. (2007)
NGC 3623	Falcón-Barroso et al. (2006)	NGC 3368	Héraudeau et al. (1999)
NGC 3627	Dumas et al. (2007)	NGC 3675	Héraudeau & Simien (1998)
NGC 4030	Ganda et al. (2006)	NGC 3718	Héraudeau & Simien (1998)
NGC 4303	Héraudeau & Simien (1998)	NGC 4102	Ganda et al. (2006)
NGC 4477	Jarvis et al. (1988)	NGC 4151	Dumas et al. (2007)
NGC 4579	Dumas et al. (2007)	NGC 4459	Dumas et al. (2007)
NGC 4725	Héraudeau et al. (1999)	NGC 5055	Dumas et al. (2007)
NGC 4826	Héraudeau & Simien (1998)	NGC 6340	Bottema (1993)
NGC 6503	Bottema & Gerritsen (1997)	NGC 6501	Falcón-Barroso et al. (2006)
NGC 6814	Márquez et al. (2003)	NGC 7331	Héraudeau et al. (1999)
NGC 6951	Dumas et al. (2007)	NGC 7742	Falcón-Barroso et al. (2006)

Vaucouleurs et al. 1991). We added one galaxy, NGC 4826 (Héraudeau & Simien 1998) bringing the number up to 20 galaxies. For all of these galaxies we retrieved Wide Field and Planetary Camera 2 (WFPC2) or Advanced Camera for Surveys (ACS) green or red images from the *HST* archive, and whenever available also Hα images taken with the WFPC2 or ACS cameras.

We then constructed a control sample that matches almost exactly the σ-drop sample in the statistical distribution across four key parameters of the host galaxies. The four parameters are:

- Distance (from radial velocity corrected for Virgo infall with a Hubble constant $H_0 = 70\,\mathrm{km\,s^{-1}\,Mpc^{-1}}$ for galaxies with radial velocities greater than $1400\,\mathrm{km\,s^{-1}}$, and from distance determinations from the literature, where possible, in other cases),

- Absolute magnitude (from the HyperLEDA database), corrected for galactic extinction and internal extinction of the target galaxies,

- Ratio of minor and major axis diameter, d/D, of the galaxy, which is directly related to the inclination (from HyperLEDA, except for NGC 1097 and NGC 6814 where the axis ratio measurement given there is obviously biased by the strong bar. In the first

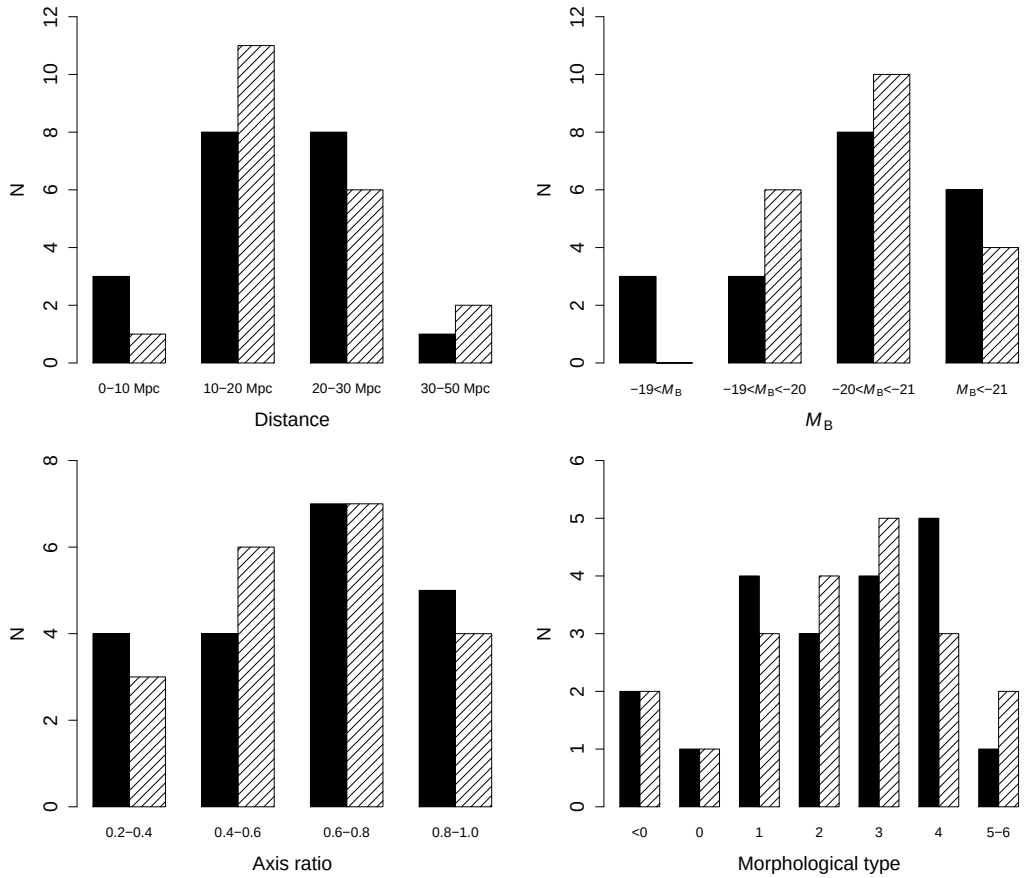

Figure 1.1: Matching of the σ-drop and the control sample with respect to four parameters of the host galaxy: distance (top left), absolute M_B magnitude (top right), axis ratio d/D (bottom left), and morphological type (bottom right). The filled bars correspond to the σ-drop sample and the dashed bars denote the control sample.

case we determined the axis ratio by measuring the kpc-scale ring of star formation and assuming that it is intrinsically round. This assumption is not necessarily true; in Chapter 3 we will show that the nuclear ring in NGC 1097 has an ellipticity $\epsilon = 0.32$ when deprojecting the galaxy using the ellipticity as derived from outer H I morphology. In the case of NGC 6814 the inner morphology suggests that this is an almost face-on galaxy),

- Morphological type of the galaxy in the Hubble sequence (from de Vaucouleurs et al. 1991).

We started the sample matching process by classifying the σ-drop host galaxies into several bins for each parameter. To create the control sample, we then selected from the *HST* archive all galaxies that have at least visible, red or near-IR imaging obtained with the WFPC2 and/or the ACS. Our control sample is made up of galaxies with evidence for the absence of a σ-drop in the literature. The stellar velocity dispersion profiles and 2D

maps we used for this can be found in Jarvis et al. (1988), Bottema (1993), Fisher (1997), Héraudeau & Simien (1998), Héraudeau et al. (1999), Falcón-Barroso et al. (2006), Ganda et al. (2006), and Dumas et al. (2007), as detailed in Table 1.1. A possible caveat in our control sample is that several dispersion profiles are measured only along the major axis of the galaxies (Bottema 1993; Héraudeau & Simien 1998; Héraudeau et al. 1999; seven of our control galaxies in total) while σ-drops sometimes only are detectable when measuring the velocity dispersion along the minor axis (Fisher 1997, in four of the seven galaxies with a σ-drop in his paper), which could generate some contamination in our control sample. This contamination is probably below 20%, especially considering that in the kinematic studies the proportion of σ-drop hosts is around 50% and that only six galaxies in the control sample have only single-slit spectra.

It is easy to match a σ-drop sample with a control sample for early-type galaxies but it is much more difficult to do so for late-type galaxies. This is due to the lack of late-type galaxies without a σ-drop in the literature; probably a selection effect because Fisher (1997), Simien & Prugniel (2002), de Zeeuw et al. (2002), Aguerri et al. (2003), and Falcón-Barroso et al. (2006) include only early-type galaxies, and the work of Ganda et al. (2006) is the only relevant study devoted to late-type galaxies. 19 of 20 of our σ-drops come from the list of Emsellem (2006), in which the selection is independent of morphological type, contrary to the works we used to make the control sample.

From the list produced by this first stage in the selection, we proceeded to take random galaxies and populate the bins until achieving the best possible match between the two samples. In some cases, several combinations of galaxies yielded similarly good overall matching. In those cases we favoured the distribution in morphological type over the other three parameters because we are primarily interested in investigating possible links between morphology and dynamics, and thus prefer to minimise any biases in that area. The limits of the bins we selected are (see also Fig. 1.1):

- For distance, we split the samples at distances R <10 Mpc, $10-20$ Mpc, $20-30$ Mpc, and $30-50$ Mpc.
- For luminosity, we split the samples at magnitudes $M_{\rm B} < -21.00$, $-21.00 < M_{\rm B} < -20.00$, $-20.00 < M_{\rm B} < -19.00$, and $M_{\rm B} > -19.00$.
- For the axis ratio d/D we split the samples at $d/D = 0.2-0.4, 0.4-0.6, 0.6-0.8$, and $0.8-1.0$.
- For morphological type, we created a bin for the lenticular galaxies and further bins for galaxy types $0, 1, 2, 3, 4$ and $5-6$.

The final σ-drop and control samples are listed in Tables 1.2 and 1.3. Figure 1.1 and Table 1.4, which shows the mean and the median for each parameter and for each sub-sample, indicate that the two samples are very similar. The only noticeable differences are that the median luminosity and axis ratio for the control galaxies are smaller, and that the lower magnitude distribution end is sub-populated in the control sample. This is because there is only one galaxy without a σ-drop with $B > -19$ in the papers with velocity dispersion studies in the literature, and this galaxy has not been included because it is almost edge-on.

Table 1.2: Results of the morphological classification of dust structure and Hα nuclear and circumnuclear structure of the 20 galaxies from the σ-drop sample.

Galaxy	Type (RC3)	Activity (NED)	Distance (Mpc)	M_B	d/D	Dust structure	Nucl Hα structure	Circ. nucl Hα structure
(1)	(2)	(3)	(4)	(5)	(6)	(7)	(8)	(9)
NGC 1068	RSAT3	Sy1 Sy2	15.3	−21.47	0.87	TW	Amorphous	Filaments
NGC 1097	.SBS3	Sy1	15.2	−20.89	1.00	LW	Peak	Diffuse+Ring
NGC 1808	RSXS1	Sy2	10.9	−19.91	0.34	LW	Peak	Ring+Patchy
NGC 2460	.SAS1	–	23.8	−19.75	0.74	C	–	–
NGC 2639	RSAR1	Sy1.9	48.7	−21.10	0.76	LW	–	–
NGC 2775	.SAR2	–	19.2	−20.60	0.79	N	–	–
NGC 3021	.SAT4	–	23.9	−19.79	0.59	TW	–	–
NGC 3412	.LBS0	–	11.3	−18.97	0.55	N	–	–
NGC 3593	.SAS0	H II Sy2	9.9	−18.28	0.39	C	Peak	Ring
NGC 3623	.SXT1	LINER	12.6	−20.94	0.26	C	Peak	None
NGC 3627	.SXS3	LINER Sy2	12.8	−21.46	0.45	C	Amorphous	None
NGC 4030	.SAS4	–	21.1	−20.76	0.71	TW	–	–
NGC 4303	.SXT4	H II Sy2	23.1	−21.84	0.89	LW	–	–
NGC 4477	.LBS.	Sy2	21.0	−20.43	0.87	TW	–	–
NGC 4579	.SXT3	LINER Sy1.9	23.0	−21.69	0.78	CS	Peak+Bipolar Structure+UCNR	Filaments
NGC 4725	.SXR2	Sy2	13.2	−21.69	0.69	C	–	–
NGC 4826	RSAT2	Sy2	7.5	−20.64	0.49	TW	Peak	Patchy
NGC 6503	.SAS6	H II/LINER	5.2	−18.70	0.33	C	Peak	Ring+Patchy
NGC 6814	.SXT4	Sy1.5	22.6	−20.48	1.00	GD	–	–
NGC 6951	.SXT4	LINER Sy2	24.4	−21.86	0.71	LW	Peak	Ring

Notes: galaxy ID (col. 1); morphological type (RC3, col. 2); nuclear activity (from NED, col. 3); distance in Mpc, (col. 4); B magnitude (NED, col. 5); axis ratio d/D (NED, except in NGC 1097 where we measured d/D from the Hα ring and NGC 6814 that looks face-on), (col. 6); dust structure within the radius r_c (col. 7); nuclear Hα structure (col. 8); circumnuclear Hα structure (col. 9). Statements such as 'Ring+Patchy' describe in which order we find each Hα structure, starting at the nucleus.

Table 1.3: As Table 1.2, now for the 20 control sample galaxies.

Galaxy	Type (RC3)	Activity (NED)	Distance (Mpc)	M_B Magnitude	d/D	Dust structure	Nucl Hα structure	Circ. nucl Hα structure
(1)	(2)	(3)	(4)	(5)	(6)	(7)	(8)	(9)
NGC 488	.SAR3	–	32.1	−21.76	0.72	LW	–	–
NGC 864	.SXT5	–	21.8	−20.57	0.69	CS	–	–
NGC 1566	.SXS4	Sy1	17.4	−21.43	0.51	CS	–	–
NGC 2964	.SXR4	H II	20.6	−19.81	0.74	C	–	–
NGC 2985	PSAT2	LINER	22.6	−20.82	0.81	TW	Peak+UCNR	Diffuse
NGC 3031	.SAS2	LINER Sy1.8	3.6	−20.76	0.48	CS	Peak+Nuclear Spiral	None
NGC 3169	.SAS1	H II LINER	17.7	−20.32	0.62	C	Peak	Diffuse+Patchy
NGC 3198	.SBT5	–	14.5	−19.54	0.28	C	–	–
NGC 3227	.SXS1	Sy1.5	23.6	−20.74	0.47	CS	Peak	Filaments
NGC 3368	.SXT2	Sy LINER	10.4	−20.31	0.66	CS	Peak	Diffuse
NGC 3675	.SAS3	H II LINER	13.8	−20.21	0.55	TW	Peak	Patchy+Diffuse
NGC 3718	.SBS1	Sy1 LINER	18.6	−20.21	0.49	C	Peak	None
NGC 4102	.SXS3	H II LINER	18.6	−19.71	0.56	C	–	–
NGC 4151	PSXT2	Sy1.5	17.1	−20.17	0.78	CS	Peak	Filaments
NGC 4459	.LAR+	H II LINER	16.1	−19.79	0.76	TW	–	–
NGC 5055	.SAT4	H II/LINER	16.5	−21.32	0.36	C	Peak	Diffuse+Patchy
NGC 6340	PSAS0	LINER	21.6	−19.92	0.95	N	Peak	None
NGC 6501	.LA.+	–	43.5	−20.51	0.85	LW	–	–
NGC 7331	.SAS3	LINER	15.1	−21.73	0.39	C	–	–
NGC 7742	.SAR3	LINER H II	24.2	−19.92	0.95	N	–	–

Table 1.4: Statistical properties of the σ-drop and control samples, showing mean and median values of the four parameters used for matching the samples.

	σ-drop sample		control sample	
Property	mean	median	mean	median
Distance (Mpc)	18.24	17.25	19.47	18.15
$M_{\rm B}$	-20.53	-20.70	-20.48	-20.32
d/D	0.66	0.71	0.63	0.64
Type	2.2	2.5	2.3	2.5

1.3 Data processing

In some images cosmic rays have been removed with the QZAP algorithm.

1.3.1 Structure maps

The structure map technique (Pogge & Martini 2002) allows one to observe the distribution of structure, and in particular that of dust, in a galaxy on the scale of the PSF using only one image in one filter. The structure map is mathematically defined as

$$S = \left(\frac{I}{I \otimes P} \right) \otimes P^{\rm t} \tag{1.1}$$

where S is the structure map, I is the image, P is the point-spread function (PSF), $P^{\rm t}$ is the transform of the PSF, and $\otimes$ is the convolution operator (Pogge & Martini 2002). We used synthetic PSFs which were created with the Tiny Tim software (Krist & Hook 1999).

We used images taken through green or red optical filters to apply the structure map operator, namely $F547M, F606W, F791W$, and $F814W$ for WFPC2 images, and $F625W$ and $F814W$ for ACS images. The resulting images are shown in Appendix A.

1.3.2 Hα images

For 10 of the 20 galaxies in our σ-drop sample and for ten more in our control sample we could retrieve Hα narrow-band imaging from the *HST* archive. We used Hα images taken through the narrow filters $F656N$ or $F658N$, and a continuum image taken through a red broad-band filter. In the few cases where images taken through both Hα filters were available in the archive, we chose the $F658N$ image, because the Hα line of our sample galaxies was better centred in its passband. The images used for the continuum subtraction were those from which we derived the structure maps.

After selecting the images from the archive, the continuum and narrow-band images were aligned using standard IRAF software. We then plotted for each pixel in the whole image the number of counts in the narrow-band filter versus that in the continuum filter. In the absence of Hα line emission, the number of counts in the narrow-band filter will be proportional to the number of counts in the continuum, and the constant of proportionality

Table 1.5: Sizes of the σ-drop and r_c.

Galaxy	σ-drop radius		r_c size		σ-drop radius/r_c
	($''$)	(pc)	($''$)	(pc)	
NGC 1068	3	220	4.06	300	0.74
NGC 1097	4	290	6.43	470	0.62
NGC 1808	1.5	80	3.30	170	0.46
NGC 2460	3.5	400	1.09	130	3.21
NGC 2639	1.5	350	0.97	230	1.55
NGC 2775	5	470	2.56	240	1.95
NGC 3021	5	580	0.81	90	6.17
NGC 3412	3	160	2.50	140	1.20
NGC 3593	20	960	2.94	140	6.80
NGC 3623	5	310	4.55	280	1.10
NGC 3627	4	250	5.35	330	0.75
NGC 4030	3	310	2.28	230	1.32
NGC 4303	5	560	3.79	420	1.32
NGC 4477	4	410	2.23	230	1.79
NGC 4579	4	450	3.37	380	1.19
NGC 4725	5	320	5.73	370	0.87
NGC 4826	7.5	270	6.00	220	1.25
NGC 6503	10	250	3.70	90	2.70
NGC 6814	4	440	1.85	200	2.16
NGC 6951	7.5	890	1.99	240	3.77

is the factor by which the continuum has to be scaled before subtracting from the narrow-band image. Since even for a star-forming galaxy most pixels trace only continuum emission, those pixels without Hα emission can easily be recognised in the graph, and a fit to them yields the continuum scaling factor (see Knapen et al. 2005, 2006 for details and a graphic illustration). In most cases, there is a contribution from the [N II] line in the Hα images but this is not a problem because we do not use the Hα images for photometry, and [N II] emission is unlikely to affect the morphology on the scales we are interested in here. The resulting continuum-subtracted Hα images are shown in Appendix A.

1.4 Size of the σ-drop region

We have searched for correlations between size of the σ-drop region and other properties of their host galaxies, such as differences in morphology or in radio emission from gas (see further sections for details on how we study those properties). We have found no correlation between any of these properties and the size of the σ-drops.

We have also made a comparison between the radius of the σ-drop (r_σ) and r_c, a measure of radius which is directly related to the visible size of the galaxy and which we define as 2 % of the radius of the galaxy (where the radius is half of D_{25} as taken from the RC3). We use the definition for r_c because it is similar to the effective radius of the bulge of a spiral

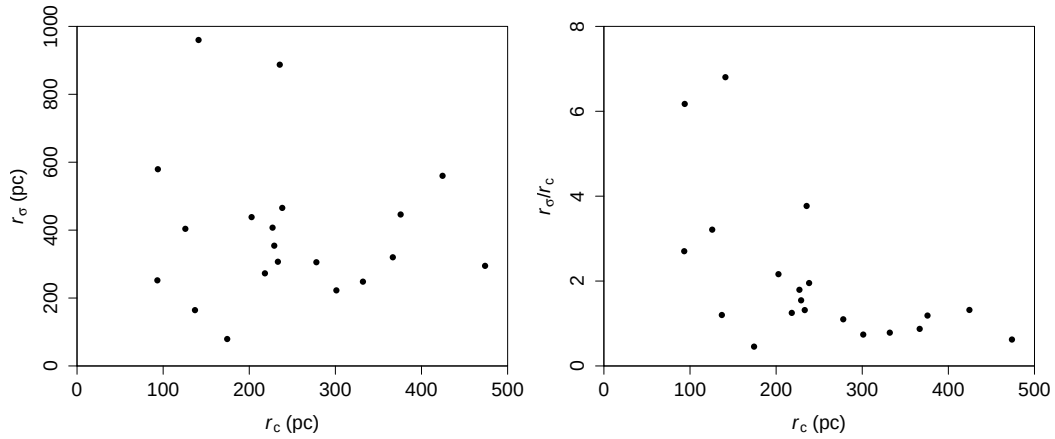

Figure 1.2: In the left panel, radius of the σ-drop (r_σ) versus the photometric radius of the host galaxy r_c, and in the right panel, the ratio of r_σ and r_c versus r_c.

galaxy (Laurikainen et al. 2004a)–it thus provides an objective but simple and effective working definition of the central region.

The data used appear in Table 1.5 and the plots are in Fig. 1.2. The radii of the σ-drops were taken from the velocity dispersion plots in the papers cited in Section 1.2. These dispersions are not always very well defined because in several papers the spectra are taken only along one axis of the galaxy (usually the major axis) and this does not provide as good a measure of the σ-drop radius as *IFU* spectroscopy. We note that the galaxy with the highest value of the ratio r_σ/r_c, NGC 3593, is a 'strange' galaxy with two counter-rotating discs (Bertola et al. 1996). We find some hint that higher r_σ/r_c ratios are found in smaller galaxies and vice versa. That would indicate that r_σ *is not directly related to the size of the galaxy*, which is confirmed by the plot in the right panel of Fig. 1.2.

1.5 Morphological classification

1.5.1 Bars

Because we ignored bars in our sample selection procedure (Section 1.2), we can as a first step investigate the presence and properties of the bars in our σ-drop and control sample galaxies. The interest in this lies primarily in the fact that bars can facilitate the inflow of cool gas into the inner regions of galaxies by removing angular momentum from the gas in the outer parts. If σ-drops are related to star formation from dynamically cold gaseous material close to the nucleus, it is reasonable to conjecture that bars may play an important role in the process. In Table 1.2 and Table 1.3 we therefore summarise the bar classification of the galaxies. This is based primarily on the RC3 catalogue (de Vaucouleurs et al. 1991), where, as is conventional, SA galaxies are those without a bar, SAB (also known as SX) are weakly or moderately barred, and SB galaxies have a prominent bar in the optical.

Although the RC3 is based on optical imaging and is therefore not optimal in recognising all bars, it is generally reliable in reporting well-defined bars. We did check the literature and

Table 1.6: Bars in the sample galaxies. The data come from the RC3 except in the cases that are explained in the text.

Sample	SA	SAB	SB
σ-drop	7 ($35\% \pm 11\%$)	10 ($50\% \pm 11\%$)	3 ($15\% \pm 8\%$)
control	8 ($40\% \pm 11\%$)	9 ($45\% \pm 11\%$)	3 ($15\% \pm 8\%$)

archive images of individual galaxies though, and refined the classification in the following cases. Some galaxies are catalogued as non-barred in the RC3 but do in fact have weak and/or small bars. The first case is NGC 1068, part of our σ-drop sample, where a bar has been discovered from near-IR imaging (e.g., Scoville et al. 1988). Other galaxies with a bar discovered on the basis of modern imaging are the control sample galaxies NGC 3169 (Laurikainen & Salo 2002), NGC 3593 and NGC 3675 (Laurikainen et al. 2004a), and NGC 2460, NGC 7331, and NGC 7742 (Laine et al. 2002). Fitting ellipses to a $2MASS$ image we also found strong evidence for a weak bar in NGC 2985.

The bar fractions in our σ-drop and control samples can thus be seen in Table 1.6, where we use Poisson statistics to give an estimate of the error in the numbers ($\epsilon = \sqrt{f(1 - f/N)}$, where f is the quantity that is measured and N is the sample size in which the quantity is searched). For the statistics of this table we use the RC3 bar data (presented in Table 1.2 and Table 1.3) which have been modified according to the references in the precedent paragraph. The conclusion from the numbers presented in Table 1.6 is that there are no statistically significant differences between the two samples. What is evident from this test, however, is that a bar is not needed to cause a σ-drop, and that, conversely, the presence of a bar does not automatically, or even preferentially, lead to a dip in the central stellar velocity dispersion. As for inner bars, we have found six of them in σ-drop galaxies (NGC 1068, NGC 1097, NGC 1808, NGC 2460, NGC 4303, and NGC 4725) and three in galaxies of the control sample (namely NGC 3169, NGC 3368, and NGC 7742). All of these inner bars have been reported independently by Laine et al. (2002) and/or Erwin (2004).

The difference between inner bar fraction in the σ-drop and control samples is not very significant ($30\% \pm 10\%$ and $15\% \pm 8\%$ respectively), but points in the direction of a link between inner bars and σ-drops. It is worthy to note here that, except in the case of NGC 3593, σ-drops have a much smaller scale than outer bars. On the other hand, σ-drops occur on a size scale similar to that of inner bars (our nine inner bars have a mean size of 350 pc, compared to the mean radius of the σ-drops in the sample, which is 400 pc).

1.5.2 Dust classification

Dust is well traced by structure maps, and we thus used the structure maps we constructed for our sample galaxies to characterise the central dust morphology across our samples. The structure maps we made are shown in Appendix A. We draw two ellipses that indicate the scale of each image, an inner ellipse that indicates r_c, as defined above, in Section 1.4, and an outer one which indicates the inner kiloparsec in radius.

We applied the classification criteria developed by Peeples & Martini (2006) to the central area (r_c) of each galaxy. Examples of each classification class are given in Fig. 2 of

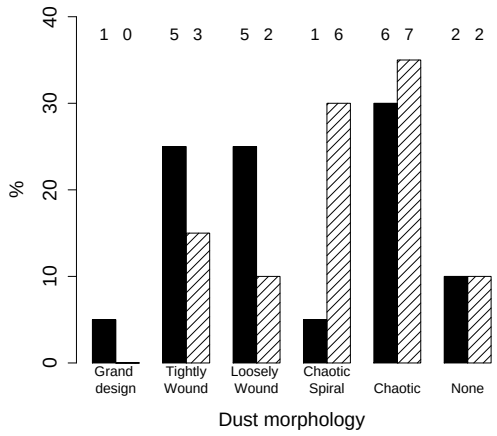

Figure 1.3: Comparison between the dust distribution in the two samples. Filled bars correspond to the σ-drop sample and dashed bars denote the control sample. The numbers at the top of each bin refer to the number of galaxies in each bin.

Peeples & Martini (2006). The classes are:

- *Grand design (GD)*: Two spiral arms with a 180° rotational offset between them. At least one arm must reach the unresolved centre of the galaxy and must be a dominant feature.
- *Tightly wound (TW)*: A coherent spiral over a wide range of radius, with a pitch angle smaller than 10°.
- *Loosely wound (LW)*: A coherent spiral over a wide range of radius, with a pitch angle greater than 10°.
- *Chaotic spiral (CS)*: Evidence of spiral arms with a unique sense of chirality, but not coherent over a wide radial range.
- *Chaotic (C)*: No evidence of spiral structure.
- *No structure (N)*: No dust seen.

The results of the classification for the σ-drop and the control sample are in Tables 1.2 and 1.3, respectively. One result that is obvious from the Tables is that there is a correlation between the dust distribution and the axis ratio. Galaxies with 'chaotic' dust distribution tend to have lower axis ratios (they are more highly inclined), which we interpret as being due to the dust in the disc obscuring the nucleus and the small-scale dusty features that are in the same plane as the external discs of dust. To quantify this we can compute the mean d/D for the 13 chaotic galaxies ($\overline{d/D} = 0.48$) and for the 40 studied galaxies ($\overline{d/D} = 0.65$)

Figure 1.3 summarises the dust morphology for the σ-drop and control samples. There is some correlation between the presence of a σ-drops and the morphology of the dust structure. Whereas galaxies with dust spirals (grand design, tightly wound, and loosely wound)

are preferentially σ-drop hosts, control sample galaxies are significantly more prevalent among the chaotic morphological classes (chaotic and chaotic spiral; see below).

When using broader bins, i.e., separating galaxies with clear spiral dust structure (classes LW, TW, and GD) from those without it (N, C, and CS), and thus to some extent overcoming the low-number statistics, the result is amplified. Eleven of the 20 σ-drop galaxies show clear dust spiral structure ($55\% \pm 11\%$), versus only five ($25\% \pm 10\%$) in the control sample .

Does this mean that galaxies without a σ-drop are preferentially chaotic? To test this idea we first have to remember how the sample was composed. The key matching parameter is morphological type, so axis ratio is not so well matched. This causes the mean and median axis ratios of the control sample to be slightly smaller than those of the σ sample. This might explain part of the fraction of control galaxies in the C category whose inner structure is hidden by a dust disc seen edge-on. But CS galaxies clearly show the bulge dust structure and therefore are barely affected by disc dust so the size of the CS class is not overestimated. In summary, chaotic morphologies are indeed favoured by the control sample galaxies.

1.5.3 Hα classification

The classification of the Hα emission (images shown in Appendix A) is based on the scheme developed by Knapen (2005). We classify the images separately for two radial regions, $r_{\rm c}$, as defined above, and the inner kpc. In the very central region ($r_{\rm c}$) the Hα emission can be dominated by the following features:

- *Peak*: A peaked emission region centred on the nucleus of the galaxy.
- *Amorphous*: Clear Hα emission, but without any significant peak.
- *Peak+UCNR*: A peaked emission region centred on the nucleus of the galaxy surrounded by an Hα-emitting Ultra-Compact Nuclear Ring (UCNR; Chapter 2 and Comerón et al. 2008b) of a few tens of parsec in radius. This nuclear morphology appears in NGC 2985.
- *Peak+Bipolar Structure+UCNR*: A peak in the centre accompanied by both a bipolar structure and an UCNR. This appears only in NGC 4579 where the inner peak and the bipolar structure are surrounded by an extremely fuzzy UCNR ring of 130 pc in radius. Its existence has been confirmed from UV images (Maoz et al. 2005; Comerón et al. 2008b; see also Chapter. 2).
- *Peak+Nuclear spiral*: A peak in the centre surrounded by a short Hα spiral that does not reach $r_{\rm c}$. NGC 3031 is the only example of this kind of galaxy in our samples.

In the zone between $r_{\rm c}$ and the inner kpc radius, we used the following classification criteria:

- *Patchy*: Individual regions of Hα emission, not centrally peaked, looking like the H II regions that can be found in the discs of galaxies.

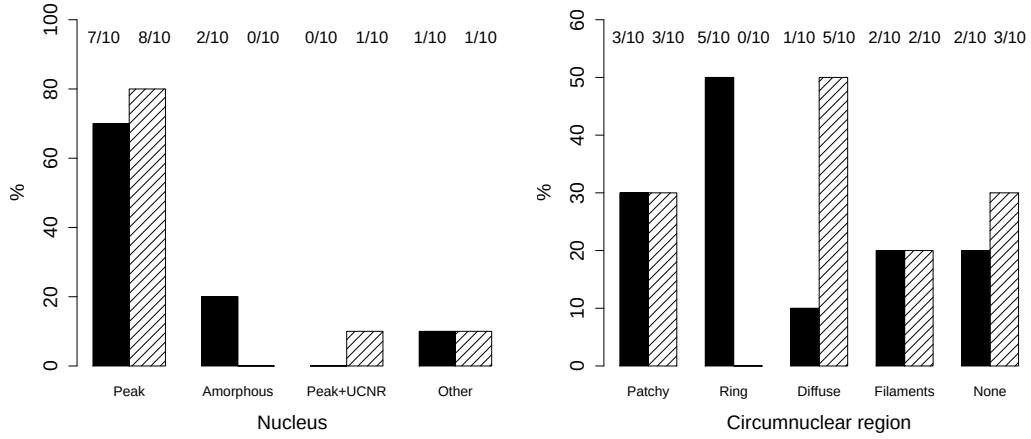

Figure 1.4: Comparison between the Hα distribution in the two samples. Filled bars correspond to the σ-drop sample and dashed bars denote the control sample. In the histogram that shows the nuclei classification the 'other' bars refer to the 'Peak+Bipolar Structure', and 'Peak + Bipolar Structure + UCNR'. The numbers at the top of each bin refer to the number of galaxies in the bin and the number of galaxies in the subsample.

- *Ring*: Hα emission organised in a well-defined ring of star formation bigger than a UCNR, which means that it measures, at least, two hundred parsecs in radius. We are classifying only the inner kpc in radius, so rings with bigger radii are not taken into account.
- *Diffuse*: Hα emission is present but cannot be ascribed to individual and well-defined H II regions.
- *Filaments*: Hα emission distributed in long filaments of H II regions.
- *None*: Less than 1% of the area of the inner kiloparsec region has any Hα emission.

This classification has been applied to the 10 σ-drop galaxies and the 10 control sample galaxies for which we have Hα images. Results for the σ-drop sample are listed in Table 1.2, and for the control sample in Table 1.3, and are summarised as histograms in Fig. 1.4.

There are no significant differences at all in the very central Hα emission morphology. For the inner 1 kpc region, however, we notice that star-forming activity is much higher in σ-drop galaxies than in control-sample galaxies. Patches and filaments in σ-drop host galaxies are more extended (covering a larger surface area) and more obvious in the images than in the control sample galaxies (even if there is the same number of galaxies with patchy and filamentary emission in the two samples). Most of the control galaxies are devoid of Hα formation or have a weak diffuse emission. Galaxies in the σ-drop sample often show strong starbursts with bright Hα rings and patches.

The differences between these two subsamples could be due to the fact that they are not as well matched as the two samples of 20 galaxies. The mean axis ratio for the σ-drop galaxies is 0.56 while it is 0.62 for the control galaxies. Four σ-drop galaxies have axis ratios smaller than 0.4. Two of these galaxies (NGC 1808 and NGC 3593) show clear evidence of nuclear star-burst rings, which means that we are seeing the inner region

without strong extinction. In the other two cases (NGC 3623 and NGC 3627) there is no Hα emission, possibly due to dust obscuration. In the control sample dust seems to hide the inner regions in NGC 3169 ($d/D = 0.62$ and diffuse circumnuclear emission) and in NGC 3718 ($d/D = 0.49$ with no circumnuclear emission). It is difficult to explain using only obscuration the virtual absence of circumnuclear emission in the two other galaxies, NGC 3031 which shows a tiny nuclear spiral and the nearly face-on galaxy NGC 6340.

The other difference between the two subsamples is that the mean morphological type of the control sample is earlier than that of the σ-drop sample (mean Hubble morphological type 1.8 and 2.6, respectively). Both subsamples have galaxies with types ranging between zero and six. In Knapen et al. (2006) galaxies with no circumnuclear emission tend to be early type and patchy emission tends to be in later-type galaxies which is coherent with what we have found in the two subsamples. Diffuse emission is also more prevalent in the control sample. As the diffuse emission is an intermediate case between no emission and patchy emission, the overabundance of this type in the control sample is probably due to the fact that it contains earlier-type galaxies. But in Knapen et al. (2006) the nuclear starburst ring distribution peaks around $T = 1$, *so the control sample should have a higher number of nuclear rings, which is not the case.* According to the statistics of Knapen et al. (2006), corrected for the nuclear ring fractions reported there for each morphological type of the host galaxy, four of our σ-drop galaxies and six control galaxies should have a circumnuclear ring—the actually observed numbers are five and zero. Therefore it is reasonable to think that the higher proportion of circumnuclear star-forming rings in σ-drop galaxies is a true effect correlated with the σ-drop.

1.6 Nuclear activity

From Tables 1.2 and 1.3 we can see that the proportion of galaxies in the σ-drop sample that have a Seyfert nucleus is $65\% \pm 11\%$ while in the control sample it is $30\% \pm 10\%$. On the other hand, LINERs make up $25\% \pm 10\%$ of the σ-drop sample but $60\% \pm 11\%$ of the control sample. This points to a link between σ-drops and Seyferts, and links the other galaxies with a more reduced level of activity.

If this is indeed the case, assuming that Seyfert nuclei are more active than LINERs, we might intuitively think that more energetic phenomena are related to a bigger inflow of gas. This gas could have been partly spent in a generation of stars in the inner volume of the galaxies. The signature of this recent star formation would be a σ-drop. This result has to be handled with care because in both samples we have a proportion of AGN of around 80%, which is far higher than the proportion of active galaxies that is found in a randomly taken sample. A direct explanation might be that *HST* is usually employed to observe 'interesting' objects, which implies an enhanced fraction of AGN in the galaxies that have been observed with the space telescope.

One possibility is that the inflow of gas giving rise to a σ-drop feeds the energetic phenomena detected as nuclear activity. When the inflow stops the activity fades, and the σ-drop gradually relaxes. As the timescale for the former is shorter than that for the latter, any correlation will be only partial.

A way to test if this correlation is indeed true is to study a bigger sample, for example all the galaxies from the papers from which we selected the the samples. That yields 85

σ-drop galaxies and 95 control galaxies. There are around 40 galaxies that are difficult to classify and therefore are not included in this test. We found that of the σ-drop galaxies $32\% \pm 5\%$ are Seyfert hosts and $19\% \pm 4\%$ are LINER hosts. For the control sample we find that $16\% \pm 4\%$ are Seyfert hosts and $24\% \pm 4\%$ are LINER hosts. These data must be taken with caution because they do not come from matched samples, so the differences in galaxy properties that we see may be due to other effects such as differences in morphological type. More than a half of the galaxies used for this test (as made on the total sample of $85 + 95$ galaxies, defined above) come from the papers from Héraudeau & Simien (1998), Héraudeau et al. (1999), and Simien & Prugniel (1997abc, 1998, 2000, and 2002), which have dispersion profiles from galaxies that are so distant that in many cases they have not been studied in any survey of nuclear activity.

From this discussion we may tentatively conclude that σ-drop are preferably accompanied by Seyfert nuclei, and that both phenomena can be traced to increased gas inflow. Given the different spatial and time scales involved, exactly why and how this is so is slightly puzzling. We note that a similar, and similarly puzzling, relation has been reported in the literature between the presence of nuclear activity and that of nuclear rings (see Knapen 2005, in particular the discussion in Section 6 of that paper); however, we will see in Chapter 3 that this link between nuclear rings and nuclear activity does not appear in the largest and most complete nuclear ring survey up to now (AINUR).

1.7 Luminosity profiles

As a way to check another possible connection between σ-drops and their host galaxies, we searched for a correlation between the presence of a σ-drop and the shape of the luminosity profiles of their host galaxies. Our *modus operandi* here was to derive luminosity profiles from the nucleus to the outer parts of the galaxies or to use profiles obtained by other authors. We obtained Sloan Digital Sky Survey Data Release 5 (SDSS DR5) (Adelman-McCarthy et al. 2007) r-band images to make the profiles. In several cases we had to join two or three SDSS frames to get a complete image of a galaxy. Each pixel in the SDSS images subtends 0.396 arcsec, obviously not nearly small enough to do an analysis at the same scale as we did for dust and Hα, so we concentrate on the host disc here.

We obtained, either from the literature, or from SDDS DR5 images, 13 profiles for the σ-drop sample and 13 more for the control subsample. These subsamples are very well matched in morphological type. There are not so well matched in axis ratio but this is only marginally important because ellipse fitting and posterior deprojection allow good photometry. The biggest difference between the samples is in the galaxies' magnitudes. The σ-drop subsample is on average 0.23 magnitudes brighter than the control one.

To produce the luminosity profile, we start by subtracting the sky background contribution from the images. That was done using the average of sky measurements over outer parts of an image where the disc of the galaxy is well below the noise level. The sky measures were done by averaging circles of 10 pixels in radius. Once the sky had been subtracted, we fitted ellipses for increasing radius, which yielded, first of all, the position angle (PA) and the ellipticity of the outer regions of the galaxy. The radial profiles were usually featureless across the outer regions. We used this PA and ellipticity to measure surface photometry at increasing radii from the centre of the galaxy until the disc 'fades

out'. More details about the method can be found in Erwin et al. (2008). The results are shown as radial surface brightness profiles for all the galaxies for which we made a luminosity profile fit in Appendix A. The fitted exponentials are overplotted. The vertical dashed-dotted lines correspond to the position of the end of the bar. When there are two vertical lines, they indicate a lower and an upper limit estimate of the end of the bar.

We classified each profile following Erwin et al. (2008), and thus divide the galaxies in three groups:

- *Type I*: The radial variation in disc surface brightness is described by a single exponential, allowing some irregularities due to structure (e.g., arms, big star-forming regions). This type of profile was established by Freeman (1970).
- *Type II*: Galaxies with a break in the surface brightness characterised by a convex, steeper, outer slope (*truncation*). This type of profile was also established by Freeman (1970). In barred galaxies the Type II class can be subdivided into two subclasses, namely *Type II.i*, where the break is inside the bar radius, and *Type II.o*, where it is outside, as explained by Erwin et al. (2008). All the *Type II* galaxies in this paper have the break outside the bar radius, so we ignored this subdivision.
- *Type III*: Galaxies with a concave break followed by a less steep slope (*antitruncation*; Erwin et al. 2005).

In some cases, antitruncations and truncations appear in the same galaxy at different radii. That is the reason that we can have, for example, II+III and II+III+II galaxies. We fitted exponentials to every section of the surface brightness profile that was roughly straight in the plots, except in the case of features directly related to bars or dust rings, as judged from a visible comparison with the images.

Table 1.7 summarises the classified shapes of the surface brightness profiles for all the galaxies of our samples that are either in the SDSS survey, or in Pohlen & Trujillo (2006; NGC 1068 and NGC 5806), in Erwin et al. (2008; NGC 3368 and NGC 4102), or in L. Gutiérrez et al. (2010, in preparation; NGC 2460, NGC 2775, and NGC 2985). NGC 4151 also appears in Erwin et al. (2008) but we have made deeper photometry and have shifted the classification of this galaxy from Type I to Type II. In the latter two papers, the procedure for constructing the luminosity profiles is the same as that used in the current paper.

The data in Table 1.7 show that there is no apparent correlation between the presence of a σ-drop and the shape of the disc surface brightness profile.

We have also fitted a Sérsic+exponential profile to the 2MASS H-band profiles in order to find excess or lack of light in the circumnuclear zone. This excess or lack could be either related to a recent star-burst or to a high dust extinction. We find no differences between the two samples.

1.8 Analysis of radio data

The spatial resolution of radio observations is not generally good enough to allow us to see details in the centres of galaxies. It seems, nevertheless, reasonable to think that there may

Table 1.7: Luminosity profiles of the studied galaxies.

σ-drop sample		Control sample	
Galaxy	Type	Galaxy	Type
NGC 1068	II	NGC 2964	I
NGC 2460	II	NGC 2985	II+III+II
NGC 2639	I	NGC 3031	II
NGC 2775	III	NGC 3169	III+II
NGC 3021	II+III	NGC 3198	II+III
NGC 3593	III	NGC 3227	I
NGC 3623	I	NGC 3368	II
NGC 3627	II+III	NGC 3675	III+II
NGC 4030	III	NGC 3718	III
NGC 4477	II+III	NGC 4102	I
NGC 4579	II+III	NGC 4151	II
NGC 4725	I	NGC 4459	I
NGC 4826	III	NGC 5055	III

be a link between the total quantity of gas in a galaxy, as measured through their 21 cm in H I, or the millimetre emission in CO, and the quantity of gas available in the central region. We thus investigate whether there are any statistical differences between the gas content of the σ-drop and the control galaxies.

1.8.1 Analysis of CO data

We have used data from two CO surveys (Young et al. 1995 and Helfer et al. 2003) to search for a correlation between CO emission and the presence of σ-drops. Not all the galaxies in our samples were included in the surveys; the CO fluxes and the uncertainties of those that do appear are listed in Table 1.8. Using the distance to each galaxy, we converted the observed flux values into the total emission of the galaxy in the CO line. We obtained CO emission data for 13 galaxies for the σ-drop sample and 12 more for the control sample. These two subsamples are well matched in axis ratio, morphological type, and brightness. They are not so well matched in distance which is not really important because we are interested in an integrated CO luminosity.

The statistical results for the CO are summarised in Table 1.9, which shows that there are no significant differences between the two samples. This is relevant because CO is a good tracer of molecular gas and σ-drops are thought to be related to accumulations of gas in the nuclear region. The absence of observed differences between the amount of gas in galaxies with and without σ-drops could thus be seen as evidence against this assumption, although our current data do not allow us to say anything about the level of concentration of the CO, and thus of the amount of gas in their nuclear regions.

Table 1.8: Emission in CO and H I by the sample galaxies. Fluxes are in units of 10^{54} W km (Hz s)$^{-1}$ for CO, and of 10^{52} W km (Hz s)$^{-1}$ for H I. The error corresponds to the photometric error and does not take into account the uncertainty in the distance. A hyphen (–) means that no data are available.

Galaxy	CO flux	H I flux	Galaxy	CO flux	H I flux
σ-drop sample			Control sample		
NGC 1068	114.9 ± 6.1	71.0 ± 4.0	NGC 488	66.6 ± 16.0	190.1 ± 10.7
NGC 1097	–	256.9 ± 10.3	NGC 864	29.0 ± 7.4	358.9 ± 11.5
NGC 1808	–	80.3 ± 4.8	NGC 1566	–	312.7 ± 17.5
NGC 2460	–	235.0 ± 9.4	NGC 2964	17.3 ± 3.1	86.6 ± 3.1
NGC 2639	–	Very little	NGC 2985	39.0 ± 13.2	361.6 ± 28.9
NGC 2775	24.3 ± 4.4	20.4 ± 1.8	NGC 3031	–	133.8 ± 8.6
NGC 3021	–	79.2 ± 3.2	NGC 3169	48.7 ± 9.8	127.6 ± 13.3
NGC 3412	–	–	NGC 3198	–	123.8 ± 5.9
NGC 3593	10.7 ± 1.9	8.7 ± 0.7	NGC 3227	–	81.6 ± 4.9
NGC 3623	$< 16.7 \pm 8.4$	26.5 ± 1.4	NGC 3368	–	73.8 ± 3.8
NGC 3627	83.5 ± 8.4	78.8 ± 3.5	NGC 3675	32.8 ± 6.4	89.1 ± 3.2
NGC 4030	55.9 ± 11.2	202.6 ± 8.1	NGC 3718	$< 8.3 \pm 4.4$	381.1 ± 15.2
NGC 4303	155.0 ± 9.6	433.7 ± 15.6	NGC 4102	27.3 ± 6.2	38.1 ± 2.3
NGC 4477	–	–	NGC 4151	13.6 ± 3.2	122.5 ± 5.4
NGC 4579	57.6 ± 12.7	58.3 ± 4.7	NGC 4459	$< 5.0 \pm 2.5$	–
NGC 4725	40.7 ± 14.6	139.0 ± 6.7	NGC 5055	124.2 ± 9.0	693.4 ± 36.1
NGC 4826	12.4 ± 1.5	26.6 ± 1.3	NGC 6340	–	55.3 ± 4.4
NGC 6503	3.3 ± 1.1	23.9 ± 1.1	NGC 6501	–	103.5 ± 17.4
NGC 6814	16.5 ± 3.1	162.3 ± 6.5	NGC 7331	75.4 ± 9.7	366.4 ± 10.3
NGC 6951	102.6 ± 21.4	172.5 ± 5.5	NGC 7742	–	59.4 ± 2.1

Table 1.9: Statistics of CO emission in the σ-drop and control samples. All data are in units of 10^{54} W km (Hz s)$^{-1}$.

sample	mean	median	std. deviation
σ-drop	52.1	40.7	48.88
control	39.5	30.9	35.5

Table 1.10: Statistics of H I emission in σ-drop and control samples. All data are in units of 10^{52} W km (Hz s)$^{-1}$.

sample	mean	median	std. deviation
σ-drop	115.3	79.0	112.8
control	197.8	123.8	170.1

1.8.2 Analysis of H I data

We obtained integrated H I emission for our sample galaxies from HyperLEDA, except for NGC 2639 where the data come from Springob et al. (2005). As in the case of the CO emission, we used the distance to each galaxy to derive the total emission. The results are listed in Table 1.8. We found data for 18 galaxies from the σ-drop sample and 19 for the control sample. The two subsamples of galaxies for which we have H I data are well matched.

The statistical results for the integral H I emission are summarised in Table 1.10. Although the H I emission of the σ-drop sample is almost two times lower than that of the control sample, this difference is not statistically significant. The conclusion from our analysis of both CO and H I emission must be that there is no compelling evidence for either more or less gas in the σ-drop galaxies as compared to those without σ-drops.

1.9 Discussion and conclusions

In this Chapter we have presented an analysis of the morphology of dust and Hα emission on scales smaller than 0.1 arcsec and within the central 1 kpc radius, of the disc surface brightness profiles, and of the CO and H I emission of a sample of σ-drop host galaxies, and compared the results to those obtained for a matched control sample.

Our control sample is not guaranteed to be completely free of σ-drop galaxies, but we estimate (Section 1.2) that less than 20% of our control sample galaxies can be expected to host a σ-drop. This possible contamination somewhat weakens the significance of our results. Another factor that can weaken our results is that, even though this is the biggest σ-drop galaxy sample studied in such a consistent way, it is not big enough to avoid problems with small number statistics. In addition, to study correlations for several parameters we had to work with subsamples that were not as well matched.

Our overall conclusion is that σ-drops are related to nuclear dust spirals and nuclear star-forming rings. We find that the σ-drop radius is independent of the other tested parameters of the host galaxy. We note the possibility that Seyfert galaxies are related to σ-drops and find that LINERs are found more often in galaxies without this feature. We also find that bars, at least strong bars, are not likely to be a necessary feature to cause a σ-drop in a galaxy.

One of the theories for the creation of σ-drops is based on a massive and concentrated dark matter halo which can remove kinetic energy from the stellar component of galactic nuclei (Athanassoula 1992). Such a dark matter halo would, however, have other effects on a galaxy's morphology and kinematics, such as the stimulation of a strong bar (Athanassoula 1992). But in our σ-drop sample there are only three strongly barred and ten weakly barred galaxies, and these numbers are not significantly different for the control sample. This indicates that massive and compact dark matter halos are not likely to be the only σ-drop formation mechanism, and may well not affect this phenomenon at all.

There are other theories for σ-drops. Dressler & Richstone (1990) propose that σ-drops may be due to the lack of a central super-massive black hole and van der Marel (1994) suggests that a σ-drop may be due to the presence of a super-massive black hole that broadens the wings of emission lines and makes 'traditional' Gaussian spectral line fitting

underestimate the true velocity dispersion (this is due to a Gaussian fit being insensitive to extended wings). These hypotheses can now be completely discarded, mainly because the presence of a σ-drop has been found to be a widespread phenomenon (in the literature cited in the introduction they are found in 30%-50% of the disc galaxies) and because σ-drops are not found only in galaxies whose velocity profiles indicate the presence of an anomalous super-massive black hole.

Another theory for σ-drop formation points to cold gas accumulation and a posterior starburst in the inner parts of the galaxy (e.g., simulations by Wozniak et al. 2003). Such a concentration of gas would start to create stars at a given density threshold. This critical density would probably only be related to local gas properties so the σ-drop size is independent of macroscopic galactic parameters. This is confirmed by our results. The huge dispersion in σ-drop sizes can be related to a reduction of their size when they become old or to the different extents of the cool gas volume at the moment it reached the critical density.

As we have shown in Section 1.5.2, σ-drop hosts have in more than 50% of the cases a clear inner dust system of spiral arms that probably trace the path of the inflowing material. In contrast, less than 20% of the control sample galaxies show such a clear spiral pattern. As there are no significant differences in bar characteristics between the two samples, it is safe to say that there is some correlation between σ-drops and inner dust spiral arms. This dust could trace the inflowing gas fuelling the σ-drop, or it could be the product of relatively recent star-formation.

We have also found that σ-drop galaxies often (in 50% of the cases) have a nuclear star-forming ring visible in Hα with a size between 400 pc and 1 kpc and that there are no star-forming rings at those scales in the control sample. It thus seems reasonable to say that the rings are a manifestation of the same phenomena causing the σ-drops. The stars that compose the σ-drops can be formed in such nuclear starburst rings, usually due to shock focusing of gas near the location of one or more inner Lindblad resonances (ILRs; Schwarz 1984a; Athanassoula 1992; Knapen et al. 1995, Heller & Shlosman 1996; see also Shlosman 1999, Knapen 2005 for reviews). The ILRs are thought to be related to bars or interactions between close galaxies. Four of our five galaxies with star-forming kpc-scale nuclear rings are barred. The fifth, NGC 6503 is so edge-on that a bar may be difficult to detect. This five nuclear rings will be described with more detail in Chapter 3 and in Comerón et al. (2010).

We have found that σ-drop galaxies are more often Seyfert than LINER hosts. On the other hand, control galaxies more often have LINER emission than Seyfert emission. Seyfert galaxies are more energetic phenomena, which probably implies a more continuous or more recent inflow of material to maintain the central activity. The dust spiral arms that are frequent in σ-drop galaxies are a plausible method to feed the central black hole. It is therefore possible to postulate that both σ-drops and Seyferts are due to a more efficient feeding of the inner parts of galaxies. As Seyferts are shorter lived than σ-drops (few 10^8 yrs versus 1 Gyr) the correlation can only hold partially.

We thus suggest the following model for the creation of a σ-drop. Gas is driven inwards by spiral arms and maybe by bars. The gas is focused by an ILR into a dynamically cold ring where the density increases until it reaches a critical value when star formation starts. These stars are dynamically cold and start to create a σ-drop. Alternatively, if there is

no ILR, gas can be focused in a cold nuclear disc that also starts to create stars when it reaches the critical density. In both cases friction causes some gas to lose enough angular momentum to drift inwards to feed the super-massive black hole. This gas can be traced with the dust related to the relatively recent star formation. It is entirely possible that σ-drops are exclusively created in rings that disappear due to the transient nature of the bars and/or the inflow. As a σ-drop is a long-lived feature (as shown by modelling by Wozniak & Champavert 2006, and as indicated by the high fraction of galaxies that host them) it would survive long after the ring has disappeared. These conclusions should be strengthened in future work by improving the statistics and by further numerical modelling.

2

Detailed study of four UCNRs in three spiral galaxies

2.1 Introduction

Star-forming nuclear rings are caused by shock-focusing of gas near the location of one or more inner Lindblad resonances (ILRs; Schwarz 1984a; Athanassoula 1992; Heller & Shlosman 1996; Comerón et al. 2010; see also Shlosman 1999; Knapen 2005 for reviews). The typical size of well-known nuclear rings, typically $\sim 1\,\mathrm{kpc}$, allows them to be easily resolved in local galaxies in ground- and space-based observations. Studies using high resolution imaging with the *Hubble Space Telescope (HST)* have led to the detection of some unusually compact nuclear star-forming regions, where unambiguous signatures of recent episodes of star formation (SF) coexist with the active galactic nucleus (AGN)—so-called *composite* Sy 2 nuclei (González Delgado et al. 1998). These star-forming regions exhibit morphologies which are not incompatible with those of 'standard' nuclear rings—an issue that had never been addressed before in the literature. The prevalence of such 'Ultra-Compact Nuclear Rings' (UCNRs) and their origin have been unknown for long time. We have conducted the first comprehensive survey of nuclear rings (AINUR, described in Chapter 3 and in Comerón et al. 2010) which shows that UCNRs are simply the small-end tail of the nuclear ring distribution, but prior to doing this, we made a detailed study of four UCNRs found in *HST* archival imaging when preparing the sample for the study presented in Chapter 1. These UCNRs were found in NGC 2985, NGC 4579 and NGC 4800.

Before producing AINUR, star-forming nuclear rings of less than 200 pc in radius (besides the composite Sy 2 nuclei mentioned above) were known in a few galaxies such as the two found in the Sy 2 Circinus galaxy (Wilson et al. 2000; not considered as nuclear rings in AINUR) and in galaxies without AGN: NGC 5248 (Laine et al. 2001; Maoz et al. 2001; Jogee et al. 2002) and possibly in NGC 3245 (Barth et al. 2001a), and IC 342 (Böker, Förster-Schreiber, & Genzel 1997). The smallest of the UCNRs we found in the literature were around $\sim 40\,\mathrm{pc}$ in radius. Even more tantalising was the detection of molecular rings or discs of $\sim 1 - 100\,\mathrm{pc}$ in low-luminosity AGN, such as M51 (Kohno et al. 1996) or in NGC 1068 (Galliano et al. 2003). We also knew that the Milky Way, a 'normal' galaxy,

hosts a massive molecular ring within $\sim 1.6 - 7$ pc from the Galactic Centre. At that moment it was not clear that all these rings had a similar origin. A major open question was whether the UCNR population was the small-radius tail of the general population of nuclear rings (e.g., shown in Laine et al. 2002) or whether it characterised a different physical phenomenon.

Nuclear rings in general are taken to be by-products of gas inflow in response to gravitational torques induced by bars, galaxy interactions or any other deviation of the potential from axis-symmetry (more details in Chapter 3), so it is significant that rings are found so close to the region dominated by the supermassive black hole (SMBH). UCNR hosts are nuclear starburst galaxies (by definition) and potentially related to the triggering and fuelling of AGN.

There are some scenarios which could account for the tiny UCNRs compared to their 'classical' counterparts, namely:

- a shallower radial mass distribution in the central kpc of the host galaxy, implying a smaller bulge,
- ring formation in response to a non-axisymmetric mass distribution in the inner few hundred pc that tumbles exceedingly fast,
- a nuclear ring could potentially form everywhere between two ILRs,
- nuclear rings may shrink with time,
- an unknown mechanism acting in the vicinity of SMBHs.

In the first two cases this would imply that the ILR region is located close to the centre. The first scenario would indicate that one might expect a deficiency of UCNRs in early-type spirals. The second scenario would favour the presence of nuclear gaseous or stellar bars (Shlosman 1999). The third and fourth possibilities would imply no differences between the hosts of UCNRs and the hosts of 'classical' nuclear rings. The fifth possibility, would imply an UCNR origin completely different to that of the resonance scenario for 'classical' nuclear rings, which would cause a morphology quite different from that found in ILR-induced nuclear rings. These alternatives could be distinguished using a number of observational tests as we did with AINUR (Chapter 3).

2.2 Observations and data reduction

We inspected *HST* archival images of ~ 50 nearby spiral galaxies, all at a distance of less than 50 Mpc, for which images in Hα and/or in UV bands (filters F218W, F250W, F300W, or F330W) were available. These galaxies were studied to prepare the samples used in Chapter 1. We used images from both ACS, with 0.05 arcsec resolution, and WFPC2, with 0.0455 arcsec resolution. Cosmic rays were removed with the QZAP algorithm.

We focus here on the three galaxies in which we discovered UCNRs. For NGC 2985, we combined two UV 1400 s WFPC2 F218W exposures of a field centred on the nucleus of the galaxy. An Hα image was obtained through the F658N filter with ACS, while we used an ACS F814W image for continuum subtraction. We used the ACS F814W image and

a WFPC2 F606W image to construct a colour index image. For NGC 4579 we combined two WFPC2 F791W 300 s exposures to subtract the continuum from an ACS set of three combined F658N images. We also used two sets of two UV ACS 300 s exposures, taken through the F250W and F330W filters. For the colour index image we used the WFPC2 F791W images and a set of two F547M WFPC2 images that we combined. For NGC 4800, we used a 1000 s F300W WFPC2 exposure, a pair of ACS F658N and F814W images for Hα, and F606W and F814W WFPC2 images in order to build a colour index image. We used standard image reduction software, and followed the recipe described by Knapen et al. (2006) for the Hα continuum subtraction. The resulting UV and Hα images of the three galaxies are shown in Fig. 2.1 (top and centre-top panels, respectively). Colour-index images are in the bottom panel.

We produced 'structure maps' (Pogge & Martini 2002; description in Chapter 1) from the broad-band red images to bring out the distribution of dust in the central regions of the sample galaxies, which are enhanced on the scale of the point spread function (PSF). We used synthetic PSFs, created with the 'Tiny Tim' software (Krist & Hook 1999) The structure maps are shown in the centre-bottom panels of Fig. 2.1.

2.3 Results

2.3.1 NGC 2985

NGC 2985 is an SAab galaxy at $D = 22.4$ Mpc (Tully 1988). In the UV and Hα images (Fig. 2.1) we can readily see a ring of emission, caused by the presence of massive SF. The ring is well defined: the intensity falls off sharply both within and outside the ring. There is no equivalent in the F814W band which is a further indication that the ring is due to a young stellar component. In both UV and Hα the radius of the ring is approximately 0.5 arcsec or 50 pc. The intense peak of emission at the nucleus is due to a LINER (Wilner et al. 1985). It is more extended in Hα, with a half intensity radius of close to 25 pc, than in the UV band. The UCNR is not uniform azimuthally, but quite patchy, being clearly composed of a number of individual massive star clusters. Each cluster emits in UV and Hα, though the structure in UV is finer, as would be expected since the Hα comes from the more extended ionised gas around the clusters. The structure map shows dust lanes spiralling in towards the central region of the galaxy, but fading out as they approach the radius of the UCNR. These dust lanes are not necessarily related to material flowing towards the centre and can be formed from a mild compression not accompanied by SF (Laine et al. 1999; Englmaier & Shlosman 2000). Some dust structure inside the ring may hint at the presence of a residual flow towards the nucleus, which is compatible with the nuclear SF peak.

This galaxy shows indications of a possible very weak oval that was discovered when preparing AINUR (Chapter 3). Gravitational torques triggered by a minor merger are an alternative way to induce inflow (see Knapen et al. 2004; 2006 for examples) as well as ILRs and UCNRs. Indeed NGC 2985 ($B = 11.2$ mag) has two close neighbours. NGC 3027 is a 12.2 mag SB(rs)d galaxy at projected distance 160 kpc, with a systemic velocity difference of only 300 km s^{-1}. The 17.2 mag irregular galaxy KDG 59 (Karatchentseva et al. 1987) is closer at 90 kpc and $\Delta v = 140$ km s^{-1}, but its faintness implies that its gravitational

influence on NGC 2985 is ~ 10 times less than that of NGC 3027. HI observations clearly show a morphological and kinematical disturbance of NGC 2985, possibly due to KDG 59, but there is no evidence for a tidal tail which connects to NGC 3027 (Noordermeer et al. 2005; T. A. Oosterloo, private communication). We conclude that one or both of these companions can cause a deviation from axisymmetry in the centre of NGC 2985, which in turn can trigger the observed UCNRs.

2.3.2 NGC 4579

NGC 4579 has been studied extensively. It has been classified as SABb in the RC3, and as SBab and SBa in the B and H-bands by Eskridge et al. (2002). García-Burillo et al. (2005) reported a 1.5 arcsec diameter ring-like structure in $V-I$ images of NGC 4579, which corresponds to a radius of 80 pc at $D = 16.8$ Mpc (Tully 1988). On the basis of our UV image (Fig. 2.1), we can say that it is not a true ring. Our UCNR is not centred on the AGN nucleus (Seyfert 1.9: Maiolino et al. 1997, or LINER: Barth et al. 2001b). Upon close inspection, the Hα image reveals a very diffuse ring shape following the UCNR which is defined more clearly in the UV (ring also seen in Maoz et al. 2005). A set of much more brightly emitting arc-shaped regions is seen, well within the UCNR, partly traced by dust as outlined in the structure map in Fig. 2.1, and possibly related to the outflow from the AGN (see below). The inner arcs have a semi-major axis of about 80 pc and a position angle (PA) of 69°, the ring's radius is 135 pc and PA=89°. The latter is approximately the same as that of the galaxy (PA=95°). The southern sections of the ring and the arcs are almost coincident (Fig. 2.1). Part of the inner arcs coincides with the structure that was suggested by García-Burillo et al. (2005), but they gave a very different PA.

The UCNR so clearly visible in the UV image of NGC 4579 is clearly off-centred, which can be readily explained in terms of a resonance ring in a mass distribution that is induced by a superposition of $m = 1$ and $m = 2$ perturbations.

The inner arcs seen in the UV can originate in the AGN activity detected in this low-luminosity LINER (or Sy) galaxy. The line emission in the central 100 pc can be reconciled with the presence of a jet and emitted by $\sim 100\,\mathrm{km\,s^{-1}}$ shocks triggered by the interaction of the compact radio jet with the cloudy ambient gas (Contini 2004). SF can be induced in dense clumps embedded in the jet backflow (cocoon). Radio surveys of low-luminosity AGN find that low radiative efficiency accretion flows in these objects can coexist with the collimated outflows (e.g., Doi et al. 2005). In particular, the PA of the jet in NGC 4579 (Sofue et al. 2004; Doi et al. 2005), $\sim 57^{\mathrm{o}} - 65^{\mathrm{o}}$, is well aligned with the PA of the inner arcs, $\sim 69^{\mathrm{o}} \pm 20^{\mathrm{o}}$, shown in Fig. 2.1, which probably is the orientation of the ionisation cone in this AGN. García-Burillo et al. (2005) find signatures of outflow velocities in this region, thus indirectly supporting this picture. While such low-luminosity AGN can lack fully developed molecular tori, their radio loudness is known to increase with a decreasing accretion rate (Ho 2002; Greene, Ho, & Ulvestad 2006). This effect is apparently related to AGN switching their outflows from molecular tori at high luminosities to jets at lower ones (Elitzur & Shlosman 2006).

2.3.3 NGC 4800

NGC 4800 is an SAb galaxy at $D = 15.2\,\mathrm{Mpc}$ (Tully 1988). A double-ring structure in the circumnuclear zone is seen in the UV and Hα images (Fig. 2.1). The inner of these two rings, with a radius of only about 30 pc, is very close to the bright nucleus (classified as H II) and is rather faint and patchy. The outer ring, with a radius of $\sim 130\,\mathrm{pc}$, is much brighter and wider. A dust trail covers a part of its perimeter. The structure map shows dust spiralling inwards until the outer edge of the bigger ring. The lack of structure between the rings implies a lack of ordered dust.

Profile analysis of a 2MASS near-IR image of NGC 4800 indicates the presence of a weak bar (with a deprojected ellipticity some 0.2 higher than the disc) with a semi-major axis of some 35 arcsec, although it is classified as a non-barred galaxy. The fact that NGC 4800 has an exponential 'bulge' (Andredakis & Sanders 1994) argues in favour of bar-induced dynamics in the central region of this galaxy. NGC 4800 does not have a close companion, and the H I morphology, which could yield information on a possible interacting past (e.g., Knapen et al. 2004) is unknown.

Photometric analysis of the UCNRs indicate that they are likely to be highly obscured by dust. This obscuration is probably greater than two magnitudes in Hα and may be specially important in the case of the UCNRs of NGC 4800.

2.4 Star formation rates

We have estimated star formation rates (SFRs) for the UCNRs from the Hα and UV, using the empirical formulae given by Kennicutt (1998). We could not apply these in the case of the UV image of NGC 4800 because its wavelength is outside of the range of the Kennicutt formula, which is 1500−2800 Å. We assumed a conservative dust extinction value of $A_{\mathrm{H}\alpha} = A_{\mathrm{UV}} = 2\,\mathrm{mag}$, and find values for the SFRs which are around $0.04\,M_{\odot}\,\mathrm{year}^{-1}$ (Table 2.1). We find that the SFRs as derived from the Hα and UV images are of the same order of magnitude for those galaxies where we could derive the UV SFR. This is surprising given that we used the same extinction correction in both cases, but can be explained by one or, most plausibly, a combination of the following arguments.

Firstly, and as a most plausible explanation, at the rather modest SFRs we find in the UCNRs, it is likely that the upper end of the Salpeter IMF assumed by Kennicutt (1998) is not fully populated. Purely due to low-number statistics, there are too few O stars to produce Hα emission commensurate with the SFR. In contrast, the low-mass (e.g., B-type) stars which produce UV emission are much more common and will be present in sufficient numbers. This means that the Hα SFR may be underestimated by an unknown amount. Secondly, the UCNRs may be coeval and rather old, so that the Hα emission due to the most massive stars is fading, but the UV not yet.

This leads to the conclusion that the true SFR is underestimated by the numbers in Table 2.1. For instance, in the first option, we would use only the UV SFR, and in that case an A_V of 2 mag seems very conservative indeed, given that the UCNRs are so close to the nucleus. Assuming an A_V of 3 mag already yields a SFR close to $0.1\,M_{\odot}\,\mathrm{year}^{-1}$. It is, unfortunately, not feasible to reach reliable determinations of A_V from, e.g., the colour index images in Fig. 2.1, because of the combined reddening effect of extra dust and a

Table 2.1: SFRs (columns 2 and 3) and SFR densities (columns 4 and 5) of the discovered UCNRs, as determined from the Hα and UV images. Foreground dust extinction of $A_{\mathrm{H}\alpha} = A_{\mathrm{UV}} = 2\,\mathrm{mag}$ was assumed in all cases.

Galaxy	Hα ($M_\odot$ yr^{-1})	UV ($M_\odot$ yr^{-1})	Hα ($M_\odot$ yr^{-1}pc^{-2})	UV ($M_\odot$ yr^{-1}pc^{-2})
NGC 2985	0.026	0.050	1.8×10^{-6}	3.4×10^{-6}
NGC 4579	0.042	0.064	1.5×10^{-6}	2.3×10^{-6}
NGC 4800 (inner UCNR)	0.00063	–	2.7×10^{-7}	–
NGC 4800 (outer UCNR)	0.030	–	6.0×10^{-7}	–

relatively older stellar population. We thus conclude that a reasonable estimate of the SFR of a typical UCNR is $0.1\,M_\odot\,\mathrm{year}^{-1}$. Given the small size of the UCNRs, the SFR densities, or SFR per unit area (see Table 2.1) are, at a value of order $10^{-6}\,M_\odot\,\mathrm{yr}^{-1}\,\mathrm{pc}^{-2}$, comparable to that in the starburst region in M83 (Harris et al. 2001). If UCNRs are even moderately long-lived and stable, this is a significant SFR, which may transform important quantities of gas into stars, very close to the nuclei of their host galaxies. For instance, this SFR during $10^8\,\mathrm{yr}$ would yield a mass transformed from gas into stars of $10^7\,M_\odot$, which would add to the inner bulge mass and thus assist in secular evolution.

2.5 Discussion

In this Chapter we describe four UCNRs in a non-AGN (NGC 4800) and in two AGN hosts (NGC 2985 and NGC 4579). The number of known UCNRs and their appearance among early and late Hubble types, as well as in AGN and non-AGN hosts, points to a common phenomenon in galaxy evolution (this topic will be developed in Chapter 3). Finding UCNRs with similar morphology in both AGN non-AGN galaxy confirms that they are originated by dynamical processes and not by radiative processes related to the AGN activity (NGC 2787, described in Chapter 3, may be an exception).

In addition to the three ringed galaxies described in this Chapter, the set of ~ 50 galaxies that we were preparing at that moment for the σ-drop study contained NGC 5248. NGC 5248 is known to have an UCNR with 95 pc in radius (Laine et al. 2001; Maoz et al. 2001; Jogee et al. 2002). We thus find UCNRs in four of the ~ 50 galaxies that we were studying at the moment, which, if extrapolated, implies that 8% of spiral galaxies may contain one or more UCNRs— this value, of course, has to be taken with caution as the ~ 50 galaxy sample is neither complete nor unbiased. Actually, the sample was biased in favour of disc galaxies which showed a spatially large (1 kpc in diameter) central drop in the stellar velocity dispersion— hence they may have a dynamically young stellar population inside the central kpc. Afterwards, when preparing AINUR (Chapter 3), we found that the UCNR fraction was lower than 5% in spiral galaxies.

The UCNRs presented here resemble closely their larger counterparts (e.g., Knapen 2005). Their morphology: round, with knots of massive SF spread around the ring, and with structured dust lanes reaching from the outside, but with little dust structure inside

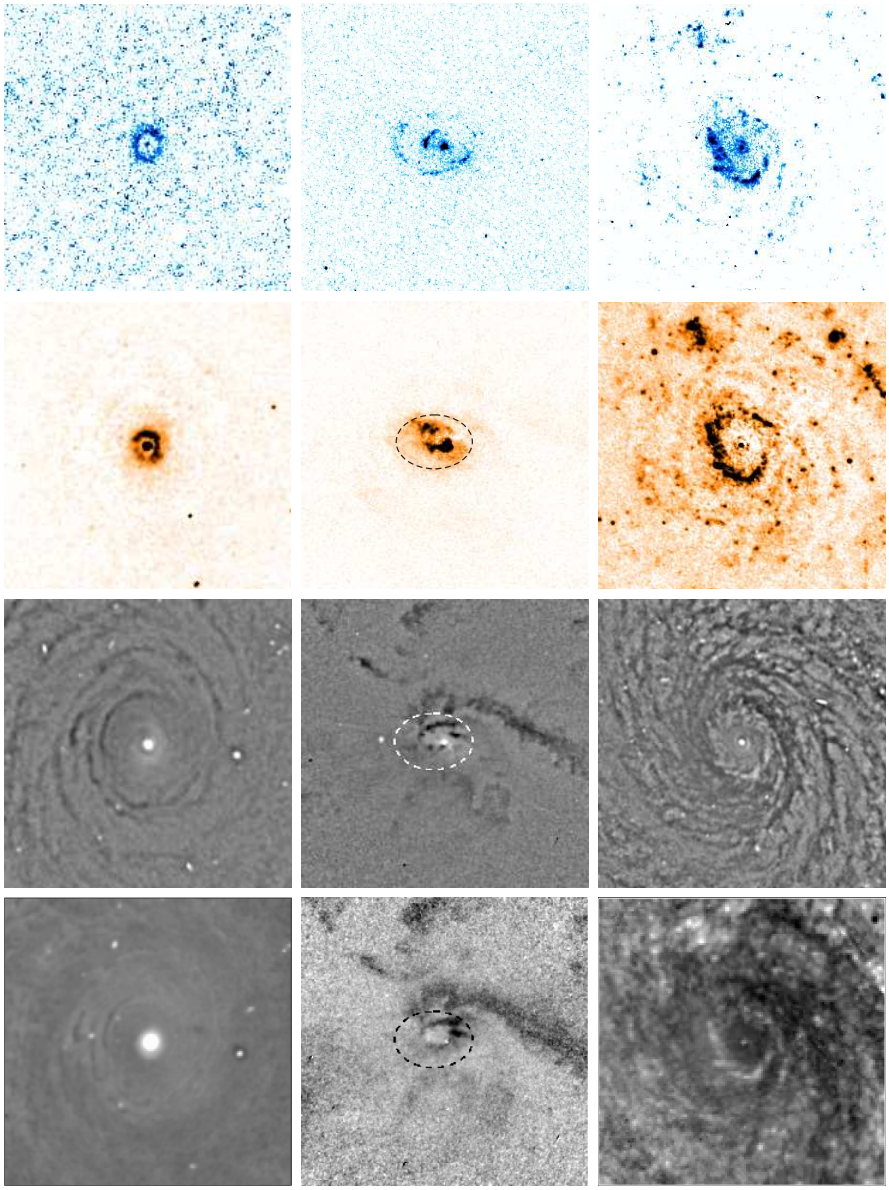

Figure 2.1: Images of the central regions of the three galaxies of studied in this Chapter (NGC 2985, left; NGC 4579, centre; and NGC 4800, right). Images in the top row are in the UV (filters F218W, F250W and F300W, from left to right), the central-top row is Hα, the central-bottom row shows the structure maps and the bottom row show colour index images (F606W-F814W, F547M-F791W and F606W-F791W, from left to right). All images span 1 kpc on the side and the scales are such that this corresponds to 9 arcsec for NGC 2985, 12 arcsec for NGC 4579, and 13.5 arcsec for NGC 4800. The shape of the UCNR in NGC 4579, as derived from the UV image, is outlined with ellipses. North is up and East to the left.

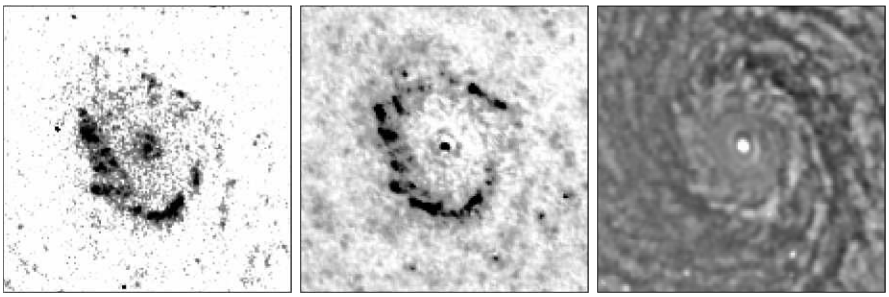

Figure 2.2: Close-up of the images of NGC 4800 (Fig. 2.1). From left to right UV, Hα, and the structure map. The colour index image has much poorer spatial resolution and is thus not included here. All images span 0.5 kpc on the side, which corresponds to 6.7 arcsec. North is up and East to the left.

the ring, fits the generic picture of nuclear rings in which the gas, driven inward under the influence of a bar (or other non-axisymmetric) potential, slows down near one or more ILRs. The UCNRs look very much like 'classical' nuclear rings, albeit much smaller than usual.

There are several ways to explain the presence of such as small nuclear rings, namely that (1) the mass distribution in the host galaxy is shallower, which places the ILRs further in, that (2) there is a small-scale non-axisymmetry in the mass distribution that tumbles with a fast pattern speed, that (3) a nuclear ring could potentially form everywhere between the ILRs, that (4) nuclear rings shrink with time, or that (5) there is another, presently unknown mechanism, which operates in the vicinity of the SMBHs, e.g., of a purely hydrodynamical or radiatively-hydrodynamical nature. The first option implies that UCNRs would prefer galaxies with small bulges, which is apparently not borne out by the classifications of NGC 2985 and NGC 4800: Sab and Sb. The second possibility would correlate UCNRs with nuclear bars, which have not been found in the three galaxies described in this Chapter. The last possibility would mean that there is a physical difference in the origin of, at least, some of the UCNRs and the 'classical' nuclear rings; this is unlikely, because UCNRs morphologically very similar to 'classical' rings. The statistical study made in Chapter 3 indicates that in most of the cases the existence of UCNRs is caused by a combination of the third and the fourth options.

3

AINUR: Atlas of Images of NUclear Rings

3.1 Introduction

Most nuclear rings (also known as circumnuclear rings in the literature) are thought to be produced as a result of an inflow of gaseous material that has been driven to the central parts of a galaxy after the loss of angular momentum (Combes & Gerin 1985), which may be driven by non-axisymmetric features such as bars, ovals or strong spiral arms (see e.g. Shlosman et al. 1990; Athanassoula 1994; Combes 2001). They are generally assumed to be related to the Inner Lindblad Resonances (ILRs) in a barred potential (Simkin et al. 1980; Combes & Gerin 1985). Nuclear rings are thus tracers of recent gas inflow to the circumnuclear region (Knapen et al. 1995). Since they have star formation rates of up to 5% of the total star formation in the galaxy (Kennicutt et al. 2005), they are part of a secular process that may help to build up pseudo-bulges (Kormendy & Kennicutt 2004). Star-forming nuclear rings are statistically related to σ-drops (circumnuclear drops in the stellar velocity dispersion with a typical scalelength of one kpc) which are tracers of young circumnuclear populations and thus are another key piece in the study of secular evolution (Chapter 1 and Comerón et al. 2008a). As nuclear rings are relatively small they are one of the galactic morphological features that is most likely to be related to nuclear activity. In fact, evidence for such a link has been presented by Knapen (2005) and Knapen et al. (2006). Nuclear rings have been related to nuclear bars because for both features, in many cases, their size is limited by the outer ILR (Laine et al. 2002; Englmaier & Shlosman 2004).

Early photographical surveys of spiral galaxies made by de Vaucouleurs (1963) found that 35% are strongly barred (SB galaxies) and that 29% are weakly barred (SAB galaxies). Some new bars have been discovered recently, thanks to observations in new spectral ranges, notably the near-infrared (see e.g. Scoville et al. 1988; Thronson et al. 1989; Eskridge et al. 2000; Knapen et al. 2000; Zurita et al. 2004) and the millimetre domain (e.g. in the study of NGC 6946 performed by Ball et al. 1985), but the bar fraction estimate has not significantly increased. The canonical estimate of the fraction of bars is around two-thirds (Mulchaey & Regan 1997; Menéndez-Delmestre et al. 2007; Marinova & Jogee 2007) among luminous, normal galaxies. Fourier analysis techniques applied to bar detection have

confirmed these results (Laurikainen et al. 2004a). Whether the bar distribution shows some variation with Hubble morphological type is still an uncertain issue; some authors show that the bar distribution is nearly constant with the morphological type (Eskridge et al. 2000; Marinova & Jogee 2007), other authors have shown that lenticular galaxies are less likely to be barred than spiral galaxies (Aguerri et al. 2009; Laurikainen et al. 2009). As the studies stating that lenticular galaxies are less likely to have bars use samples with a much larger number of S0 galaxies than those which found a bar fraction constant with morphological type, we think that the fact of S0 galaxies having a lower fraction of bars seems to have been confirmed. What is certain is that bars, even if they are common, are not found in every spiral galaxy. Unbarred galaxies can host oval distortions which are deviations of the disc from a perfect axisymmetric shape. Ovals have lower ellipticities than bars and generally do not have Fourier terms with order higher than $m = 2$ (Laurikainen et al. 2009). Their dynamical effects are very similar to those produced by bars (Kormendy & Kennicutt 2004).

Detailed knowledge of whether a galaxy hosts a bar or not is necessary to explore the links between non-axisymmetric features and circumnuclear star-forming activity. The central regions of galaxies can maintain strong star-forming nuclear rings or Ultra-Compact Nuclear Rings (UCNRs), the latter defined by Comerón et al. (2008b) (see also Chapter 2) as circumnuclear rings with a radius smaller than 200 pc. Most nuclear rings have enhanced star formation rates, making them plausible tracers of recent inflow of material (Knapen et al. 2006).

In barred galaxies the gas is driven inward along shocks that may be delineated by dust lanes (Roberts et al. 1979; Athanassoula 1992; Shlosman 1999; Shlosman 2001). When the shocked gas crosses an ILR, the trajectory is gradually shifted from (nearly) radial to (nearly) circular (Knapen et al. 1995; Shlosman 2001). This shock-focused azimuthal flow creates a molecular nuclear ring between the two ILRs (when two ILRs are found) or just inside a single ILR (Shlosman 1999; Pérez-Ramírez et al. 2000). The molecular gas may at some point become dense enough to initiate star formation. However, at exactly which radius (relative to the ILRs) a nuclear ring may appear is a subject that is still under discussion (see e.g. the introduction of van de Ven & Chang 2009). Some small nuclear rings could also be related to resonances that are even closer to the nucleus such as nuclear Lindblad Resonances (see e.g. Fukuda et al. 1998; Shlosman 1999; Maciejewski 2003).

Even though nuclear rings have often been related to non-axisymmetric features and ILRs, a few have been found in galaxies with no known non-axisymmetric features. This is the case for NGC 473 (Heckman 1978), NGC 2985 (Chapter 2 and Comerón et al. 2008b), NGC 3011 (Gil de Paz et al. 2003), NGC 4826 (Pogge 1989), NGC 7217 (Pease 1917), and NGC 7742 (Morgan 1958).

Another phenomenon that may be called a nuclear ring is the presence of hundred pc-scale dust rings in elliptical and early lenticular galaxies (see e.g. Lauer et al. 2005). These features have the size of nuclear rings but they show little or no star formation. Rings in elliptical galaxies may be caused by the depletion from inside out of dust nuclear discs (Lauer et al. 2005).

The aim of this Chapter is to present the most complete atlas of nuclear rings up to now and to study their links with other galactic features, notably bars. Samples of nuclear rings have already been published (Sérsic & Pastoriza 1965; Pogge 1989; Buta & Crocker

1993; Knapen et al. 2002; Knapen 2005) but *Hubble Space Telescope* (*HST*) has provided much better resolution imaging that allows us to study the intermediate and small-sized nuclear rings. Since the launch of *HST*, tens of nuclear rings have been discovered but they have been studied individually or in small groups and no attempt has yet been made to make a uniform study of all of them. We also aim to explore possible relationships between the size and morphology of the rings and various galactic parameters such as the non-axisymmetries.

This Chapter is structured in the following fashion. In Section 3.2 we define nuclear rings and in Section 3.3 we describe our selection criteria. We then describe in Section 3.4 the reduction procedures of the data and data processing. In Section 3.5 we describe the bars that are found in the sample. Section 3.6 is devoted to the description of how the ring parameters of the Atlas of Images of NUclear Rings (AINUR) were measured and we describe the ring size distribution. In Section 3.7 we search for links between the bar parameters and the nuclear rings. In sections 3.8−3.9 we explore the links between nuclear rings and Hubble morphological type and nuclear activity. Section 3.10 contains comments about nuclear rings in unbarred galaxies. Section 3.11 has an individual discussion of all the rings included in AINUR. We discuss our results in Section 3.12 and present a summary of our conclusions in Section 3.13.

3.2 Identification of nuclear rings

3.2.1 Definition of nuclear rings

We define a star-forming nuclear ring as a ring of intense star formation in the proximity of the nucleus of a galaxy (see, e. g., Buta et al. 2007). We will assume in first instance that nuclear rings lie in the galaxy plane. An inside-out surface brightness profile of them shows a rise and a fall in surface brightness with a maximum that we use to define the ring radius. We set the criterion that the width of a ring has to be at most half the ring radius; if not the nuclear ring is called a nuclear disc. These rings are usually located between the two ILRs where they exist and, if not, they are found just inside a single ILR (Knapen et al. 1995; Shlosman 1999). Nuclear rings are usually found inside the bar of a galaxy, but several nuclear rings are found in unbarred galaxies and may be related to ILRs due to strong spiral patterns, weak ovals or disturbances due to a companion galaxy. We will also include into this category purely stellar rings that once contained star formation and which have since faded.

In this Chapter we also include nuclear rings that are made of dust but have the size of star-forming nuclear rings. These dust nuclear rings are found in elliptical and early S0 galaxies. These features must not be confused with heavily dust-obscured star-forming rings which may need infrared imaging to directly see the star formation. The distinction between dust and star-forming nuclear rings is thus in their origin, not in their aspect.

NGC 2787 (Sil'chenko & Afanasiev 2004) is a galaxy with a polar disc whose two nuclear rings do not lie in the main plane of the galaxy. As in the case of dust nuclear rings, the rings of this galaxy have been included in AINUR for completness (they have the size of UCNRs) but are not plotted nor used for statistics in which 'normal' star-forming nuclear rings are involved.

Nuclear rings are in most cases easily distinguished from inner rings. In barred galaxies, inner rings are related to the inner 4:1 ultraharmonic resonance, found slightly inside the corotation radius of the bar (Schwarz 1984b). Thus inner rings usually encircle main galactic bars (this is why they were called ϕ-type spirals by Curtis in 1918) and nuclear rings are found well inside the bar (they may be encircling nuclear bars). When there is no obvious bar, distinguishing between nuclear and inner rings may be impossible if a galaxy does not have both a nuclear and inner ring.

The difference between pseudo-rings and rings is much fuzzier. According to Buta & Crocker (1993) a pseudo-ring is a ring which is not well defined and probably represents a variation of the same phenomenon. A pseudo-ring may be seen as an intermediate state between a nuclear spiral and a well-defined nuclear ring. For practical purposes and due to the difficulty of quantifying how 'ringy' a feature is, we are going to consider as a limiting case the nuclear ring in NGC 4321. We do not include pseudo-rings in this Chapter, but the distinction between the two types of features is not watertight and some of our nuclear rings may still be considered by some to have pseudo-ring characteristics. Previous catalogues of rings (not only nuclear, but also inner and outer) such as those by Buta & Crocker (1993) and Buta (1995) include pseudo-rings. Thus, direct comparative statistics between these catalogues and AINUR may not be valid.

The nuclear rings in AINUR were detected by visual inspection of digital images (continuous R-band, B-band and UV images, continuum-subtracted Hα and Paα line emission images, colour index maps and structure maps).

3.2.2 Huge rings and tiny rings

Prior to *HST*, the typical nuclear ring identified on ground-based images had an average radius of about 750 pc (Buta & Crocker 1993; adjusted for current distance scale). Extensive *HST* imaging has revealed a significant population of much smaller rings, 200pc or less in radius, called ultra-compact by Comerón et al. (2008b) (see also Chaper 2). At the time of starting to write this Chapter it was not yet known whether UCNRs were the lower diameter tail of the nuclear ring size distribution or if they had a distinct origin. As one of the aims of the work in this Chapter is to solve this problem we do not set a lower limit to the size of our rings.

The maximum radius of nuclear rings is not well defined. Laine et al. (2002) relate the size distribution of nuclear rings to that of nuclear bars whose maximum radius is claimed by the authors to be around 1.6 kpc. There are, nevertheless, some exceptionally big rings that have been defined as nuclear, as in ESO 565-11 (for a complete analysis of this galaxy see Buta et al. 1999). The innermost ring of this galaxy, whose radius is around 3.5 kpc, is a *bona fide* nuclear ring because the galaxy has two more ring features that can be unambiguously identified as an inner ring and an outer pseudo-ring. In addition, the nuclear ring is inside the bar of the galaxy and cannot be an x_1 ring (a ring of gas at the largest non-looping orbit whose major axis is parallel to the major axis of the bar as defined by Regan & Teuben 2004) because it is not aligned with the bar.

We decided to include in AINUR those nuclear rings with radii above 2.0 kpc that were found inside a bar (ESO 565-11) or in unbarred galaxies that had outer, inner, and nuclear rings (ESO 198-13). If these criteria were not satisfied, we concluded that any ring feature

with a radius above 2.0 kpc could not be classified unambiguously and we thus did not include it in our sample. We have found three rings in the latter category, with radii between 2 and 3 kpc in the unbarred galaxies NGC 4750 and NGC 7213. These rings were not included in AINUR.

3.3 Sample selection

AINUR includes 113 nuclear rings distributed in 107 galaxies. The parameters of the host galaxies are found in Table B.1 (Appendix B) and the parameters of the nuclear rings and the host galaxy bar (if present) are found in Table B.2 (Appendix B). Images of all the nuclear rings are presented in Appendix B.

3.3.1 Unbiased sample of nuclear rings

Our galaxy sample was based on the survey by Ho et al. (1995) aimed at 'dwarf' Seyfert nuclei in nearby galaxies. They selected all those galaxies from the Revised Shapley-Ames Catalogue of Bright galaxies (RSA; Sandage & Tammann 1981) and the Second Reference Catalogue of Bright Galaxies (RC2; de Vaucouleurs et al. 1976) with $B_{\rm T} \leq 12.5$ mag and $\delta \geq 0^{\circ}$. $B_{\rm T}$ is the apparent total B magnitude reduced to the RC3 system (de Vaucouleurs et al. 1991). Twelve additional objects of special or historical interest were added to the sample by Ho et al. (1995), reaching a total of 503 galaxies. To the 503 galaxies in this sample we added a similar selection from the southern celestial hemisphere: we selected all those galaxies with $\delta < 0^{\circ}$ and $B_{\rm T} \leq 12.5$ mag in the Third Reference Catalogue of Bright Galaxies (RC3; de Vaucouleurs et al. 1991). We took into account the fact that some of the galaxies in RC3 have just a $V_{\rm T}$ measurement, and we corrected this effect by calculating the $B_{\rm T}$ magnitude as $B_{\rm T} = V_{\rm T} + (B-V)_{\rm T}$ in the cases where $(B-V)_{\rm T}$ is provided by RC3. The RC3 contains galaxies brighter that 15.5 mag which implies that we have no problems with completeness in the Southern hemisphere. Our combined sample consists of 888 galaxies with $B_{\rm T} \leq 12.5$ mag in both Northern and Southern hemispheres.

As we were looking for nuclear rings that are assumed to lie in the galactic plane, we excluded from the list of 888 galaxies all those that were classified as edge-on in the RC3 catalogue (galaxies with a slash, '/',in the morphological type as reported by the RC3 catalogue). We also removed from our selection all the galaxies with an axis ratio smaller than 0.35 ($i > 70^{\circ}$) in HyperLEDA (Paturel et al. 2003) because we considered that they are too highly inclined to give reliable results. We removed a total of 157 very inclined galaxies from the sample.

Next we retrieved those Advanced Camera for Surveys (ACS), Faint Object Camera (FOC), Near-Infrared Camera and Multi-Object Spectrometer (NICMOS), and Wide Field Planetary Camera 2 (WFPC2) images from the *HST* archive which included the nuclear zones of our non edge-on galaxy sample. All the 248 galaxies that have not been observed by *HST* were removed from the sample at this stage because the resolution reached by ground-based telescopes would not allow us to detect UCNRs at the distances of most of the galaxies. We also removed all the satellite galaxies of the Milky Way because these dwarf irregular galaxies, though very well studied, are known not to have rings. The final sample has 483 galaxies, with morphological types ranging from giant ellipticals to irregular

dwarfs.

To summarize, our sample satisfies all of the following criteria:

- $B_{\rm T} \leq 12.5$ in the RC3 and/or they appear in the survey of galaxies by Ho et al. (1995),
- not catalogued as edge-on in the RC3,
- axis ratio $d/D > 0.35$ in the HyperLEDA database,
- not a Milky Way satellite,
- imaged by *HST* with one or more of the following cameras: ACS, FOC, NICMOS, WFPC2.

The 483 selected galaxies include 107 elliptical galaxies ($T < -3.0$), 363 disc galaxies ($-3.0 \leq T \leq 9.0$) and 13 irregular galaxies ($T > 9.0$).

Among these 483 selected galaxies we have found 76 galaxies with at least one nuclear ring, which form the majority of the atlas of nuclear rings discussed in the present Chapter. However, for one of the galaxies, NGC 3414, the *HST* image is not deep enough to detect the ring, which was in ground-based images by Buta et al. (2007).

3.3.2 Extended sample of nuclear rings in AINUR

The survey of 483 galaxies searching for nuclear rings is used in Section 3.8, where an unbiased sample is necessary to investigate the nuclear ring proportion as a function of morphological type. In Section 3.9, where we study the nuclear activity, we have used the subset of galaxies which appears in the survey made by Ho et al. (1995). For other purposes high statistics are preferred over an unbiased sample and that is why, except for Sections 3.8 and 3.9, we have used an extended sample, in which we include nuclear rings found in the literature.

Twenty-nine galaxies with a nuclear ring were added on the basis of the literature search. All these nuclear rings were confirmed by us using digital images. Section 3.3.4 discusses literature cases that we could not confirm. There are three reasons why these 29 nuclear ring host galaxies were not included in our 483-galaxy sample (galaxies can fall in more than one category), as follows.

- Twenty-one galaxies are dimmer than $B_{\rm T} = 12.5$ in the RC3. These galaxies are ESO 198-13, ESO 437-33, ESO 437-67, ESO 565-11, IC 1438, IC 4933, NGC 473, NGC 718, NGC 1241, NGC 1415, NGC 1819, NGC 2595, NGC 3011, NGC 3081, NGC 5135, NGC 5905, NGC 5135, NGC 5945, NGC 7469, NGC 7716, NGC 7570, and NGC 7771.
- Three galaxies have $d/D < 0.35$ in HyperLEDA. Even though these galaxies are highly inclined, in a few cases it is possible to distinguish a nuclear ring. These galaxies are NGC 1808 ($d/D = 0.34$), NGC 4100 ($d/D = 0.28$), and NGC 6503 ($d/D = 0.33$). In the case of NGC 1808 the value of the axis ratio given in HyperLEDA is too low and we have used $d/D = 0.74$ (Laurikainen et al. 2004a).

- Nineteen galaxies have not been imaged by *HST*: ESO 198-13, ESO 437-33, ESO 437-67, IC 1438, IC 4214, IC 4933, NGC 473, NGC 521, NGC 718, NGC 1343, NGC 1415, NGC 1819, NGC 2595, NGC 2935, NGC 3011, NGC 3313, NGC 5905, NGC 5945, and NGC 7570. Five of these galaxies (IC 4214, NGC 718, NGC 2935, NGC 3313, and NGC 5905) were bright enough to be in the 888 galaxy original sample.

The literature sources of these 29 galaxies are: ESO 198-13, ESO 437-33, ESO 437-67, ESO 565-11, IC 1438, IC 4214, NGC 1343, NGC 1808, NGC 1819, NGC 2595, NGC 2935, NGC 3081, NGC 3313, NGC 4100, NGC 5945, and NGC 7469 from Buta & Crocker (1993), IC 4933 from Ryder et al. (2010), NGC 521 from Buta et al. (2009), NGC 718 from Erwin & Sparke (2003), NGC 1415 and NGC 5135 from García-Barreto et al. (1996), NGC 3011 from Gil de Paz et al. (2003), NGC 473, NGC 1241, NGC 5905, NGC 6503, NGC 7570, and NGC 7716 from Knapen et al. (2006), and NGC 7771 from Smith et al. (1999). Nine of these galaxies have been imaged by *HST* and therefore they can be studied with the same detail as the other 76. These galaxies are ESO 565-11, NGC 1241, NGC 1808, NGC 3081, NGC 4100, NGC 5135, NGC 6503, NGC 7469, and NGC 7771. Seven galaxies, namely IC 1438, NGC 473, NGC 1343, NGC 5905, NGC 5945, NGC 7716, and NGC 7570 have been studied by us with the Hα images from Knapen et al. (2006) and one more, NGC 1415, with an Hα image from García-Barreto et al. (1996). NGC 2595 has been studied with Sloan Digital Sky Survey Data Release 7 (SDSS DR7; Abazajian et al. 2009) images. The images of the remaining galaxies have been provided by Ronald J. Buta.

Two more nuclear rings have been discovered by us in galaxies which do not meet the criteria to enter into the 483-galaxy sample and which do not appear in the literature. They are as follows. The first is a UCNR in an *HST* Hα image of UGC 10445 in an unpublished study searching for nuclear clusters in late-type galaxies. The galaxy was too faint to be in our 483-galaxy sample. We also included the nuclear ring in NGC 5020, a galaxy not imaged by *HST* and dimmer than $B_{\rm T} = 12.5$, that was brought to our attention by a discussion on the forum pages of the galaxy zoo project (Lintott et al. 2008). This galaxy has been studied with SDSS DR7 (Abazajian et al. 2009) images.

3.3.3 Incompleteness and biases

A source of incompleteness in our catalogue is that we have not been able to access good quality images for all the galaxies that have nuclear rings in the literature, so we have not been able to confirm them. This is the case for ESO 219-37, NGC 3147, and NGC 4984 (Buta & Crocker 1993). None of these galaxies has been included in our study.

We can estimate the completeness of the Atlas from Fig. 3.1, where we plot the nuclear ring radius (Section 3.6) versus distance to the host galaxy. We can deduce empirically that we are able to detect UCNRs (defined as nuclear rings with a radius smaller than 200 pc) using *HST* at a distance of 40 Mpc. This is confirmed when we consider that the largest UCNRs would span $2''$ at $D = 40$ Mpc. Farther away, UCNRs are not detectable due to the lack of resolution.

AINUR is restricted to galaxies that have been imaged by *HST* or that have been well-studied in the literature. It is possible that many close non-studied galaxies host nuclear rings. An SDSS-type survey in the whole sky would be very useful to detect these unknown nuclear rings.

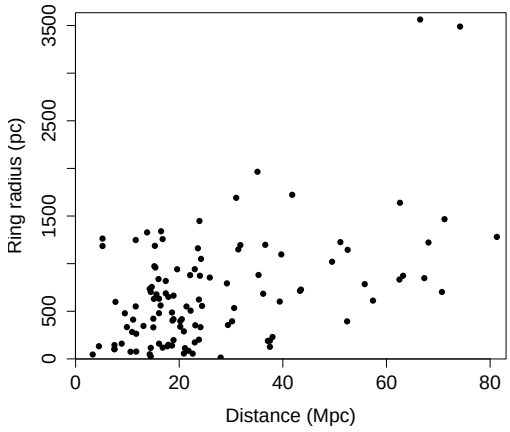

Figure 3.1: Distribution of nuclear ring radius with distance to the host galaxy for the 113 nuclear rings of our sample. How the nuclear ring radius is measured is described in Section 3.6.

Finally, it is possible that we are missing several nuclear rings, especially the smallest ones, due to dust obscuration in the inner parts of galaxies.

3.3.4 Features called nuclear rings in the literature but not included in AINUR

The Atlas of nuclear rings that we have produced does not include all galaxies that have been called 'nuclear ring galaxies' in the literature.

Nuclear rings found in the literature for which we do not have access to digital images have not been included (see preceding subsection).

In three cases, what had been termed nuclear rings are most probably inner rings. NGC 3344 was considered to have a nuclear ring by Knapen (2005). We established that the bar of this galaxy is inside the ring and that there is no outer bar. Furthermore, this ring would be, compared to the extinction-corrected D_{25} radius of the galaxy ($D_{\rm o}$, defined by Bottinelli et al. 1995), by far the biggest nuclear ring of the sample. NGC 3184 has a 2.2 kpc ring that was considered a nuclear ring by Knapen (2005) but has a bar within it. Another case similar to NGC 3184 and NGC 3344 is NGC 253 (Engelbracht et al. 1998). Another ring that has been called a nuclear ring in the literature and that we now think is really an inner ring is the outermost ring-like feature in NGC 278. This galaxy has been studied in detail by Knapen et al. (2004), who argue that this galaxy has two nuclear rings, one 450 pc in diameter and another with a diameter of 2.2 kpc. Knapen et al. (2004) found no bar in this galaxy, but we found a small bar with a length of 0.8 kpc using ellipticity profiles. This bar is evidence for the larger of the two rings being an inner ring. The relative radius (ring diameter divided by $D_{\rm o}$) of the larger ring is again much bigger than in any other nuclear ring in the sample. Even if this ring-like feature were nuclear, a close examination of *HST* images leads to classify it as a pseudo-ring than a ring.

In various cases, features are called nuclear rings based on images that barely resolve the possible ring. As examples, we mention ESO 153-20, NGC 4254, and UGC 12646 (Buta & Crocker 1993), NGC 5347 (García-Barreto et al. 1996), and NGC 1530 and NGC 5953

(Knapen et al. 2006), which nuclear rings have been reported, but which actually have nuclear spirals or pseudo-rings when observed with high resolution *HST* images. We included nuclear ring galaxies without *HST* images *only* when the images from literature were unambiguous.

There are some difficult cases that are in discussion in the community. NGC 1068 is reported to have a nuclear pseudo-ring by Buta & Crocker (1993), but this feature is considered a nuclear ring by Knapen et al. (2006). We included this feature as a nuclear ring because we consider it to be a complete ring which is partially covered by a dust lane. Another case under discussion, NGC 4321, has been included in the sample, albeit as the borderline case separating rings and pseudo-rings, as discussed in Section 3.2.1. We have not included the nuclear ring in NGC 2681 (Buta & Crocker 1993) because it has been recognized as a pseudo-ring afterwards (Buta et al. 2007).

We have not included the possible nuclear ring in NGC 3489 (Erwin & Sparke 2002) because it is too inclined for us to be completely sure about its nature.

We have not included features that are considered edge-on rings such as the one at 150 pc radius in NGC 4570 (van den Bosch & Emsellem 1998) because we cannot accurately deproject the galaxies to confirm their ringed nature or to study the exact ring shape.

Finally, we have not included the nuclear ring-like features in the Circinus galaxy reported by Wilson et al. (2000) because we consider that they are in fact pseudo-rings.

3.3.5 AINUR

The sample selection process has led us to create AINUR, an atlas with 113 nuclear rings in 107 galaxies. We found 82 nuclear rings in 76 galaxies in the 483 galaxy unbiased sample. Four galaxies (NGC 2787, NGC 4371, NGC 4459, and NGC 5248) are double-ringed and one (NGC 4800) is triple-ringed.

Most of the spiral and lenticular galaxies in AINUR are known to be barred. Eighteen galaxies (NGC 2985, NGC 2997, NGC 3011, NGC 3245, NGC 3593, NGC 4100, NGC 4138, NGC 4459, NGC 4571, NGC 4736, NGC 4826, NGC 5033, NGC 5247, NGC 6503, NGC 6753, NGC 6861, NGC 7217, and NGC 7742) are not known to be barred.

AINUR contains dust nuclear rings in six elliptical galaxies (NGC 3258, NGC 3268, NGC 3379, NGC 4494, NGC 5812, and NGC 6958). Two nuclear rings in lenticular galaxies (the inner one in NGC 4371 and the one in NGC 7049) may be either dust or star-forming rings. They have been considered as star-forming nuclear rings for the statistics in this Chapter.

The parameters of the galaxies in AINUR are found in Table B.1 . In this table we use, if possible, the morphology given by Buta et al. (2007). In other cases we used the morphology from NASA/IPAC Extragalactic Database (NED) which, in most cases, is the same as in the RC3. Some galaxies that are not listed as barred in Table B.1 are barred following some literature sources. These galaxies are NGC 1068 (Scoville et al. 1988), NGC 4800 (Chapter 2 and Comerón et al. 2008b), NGC 5194 (Laurikainen & Salo 2002), and NGC 5427 (Marinova & Jogee 2007).

3.4 Data processing

We have used images from the *HST* archive to identify nuclear rings and images from other archives only to confirm a nuclear ring in galaxies for which *HST* images were not available. Two Micron All-Sky Survey H-band images have been used to determine bar parameters. Images of all the nuclear rings are presented in Appendix B (Fig. B.1).

3.4.1 Image processing of *HST* images

Structure maps

We used structure maps as defined in Section 1.3.1. To prepare thm we used images taken through green or red optical filters to apply the structure map operator, namely $F547M$, $F606W$, $F791W$, or $F814W$ for WFPC2, and $F625W$, $F606W$, or $F814W$ for ACS images.

For NGC 936 we produced a structure map from an R-band image taken with the William Herschel Telescope (WHT). The PSF was generated from field stars in the image.

Hα images

We used Hα ACS and WFPC2 images taken through the narrow-band filters $F656N$ or $F658N$, and a continuum image taken through a red broad-band filter. In the few cases where images taken through both Hα filters were available in the archive, we chose the $F658N$ image, because the Hα line of our sample galaxies is better centred in its passband. The images used for the continuum subtraction were in most cases the same ones from which we derived the structure maps.

The continuum subtraction procedure we used has been described in Knapen et al. (2004), Knapen et al. (2006), and Comerón et al. (2008a).

Paα images

We downloaded relevant NICMOS Paα narrow-band images from the archive. We used one of two techniques to remove the continuum component from the Paα images, depending on which images are available in the archive. If there is a broad-band near-IR image at a wavelength close to that of Paα, the procedure is the same as for Hα. The wide band filter images used for continuum subtraction are taken through the $F110W$ ($\sim J$) or the $F160W$ ($\sim K$) filter. In some cases, the set of images in the archive is an $F187N$ and an $F190N$ image. At zero redshift, Paα, at a wavelength of 1874.5 nm, is centred on $F187N$, and for galaxies with $v > 3000\,\mathrm{km\,s^{-1}}$, on $F190N$. For galaxies with velocities lower than this threshold, we directly subtracted the $F190N$ image from the $F187N$ image after multiplying the $F190N$ image by a number ranging from 0.9 to 1.0 due to its slightly greater efficiency. This value was calculated in each case by plotting the counts from continuum emission areas in one filter against those in the other one, fitting a line and using its slope to find a correction factor. For galaxies with greater velocities we performed the inverse operation ($F190N$-$F187N$). No cases where the line is in the overlap region of filter transmission curves have been found.

Colour-index images

Most of the colour index images have been obtained using filters close to V and I with ACS and WFPC2. We first aligned the images and then we performed the operation $V - I = -2.5 \log V/I$ to get the colour index image. In some cases where we had no V or I image, we produced $I - J$ images.

UV images

We also downloaded ACS, FOC, and WFPC2 UV images because it is possible to detect star-forming nuclear rings in the UV. No processing was needed for these images.

3.4.2 Ground-based images

Images that were obtained from authors of previous studies (see Section 3.3.2 for details) had already been processed by them. These images are mostly Hα and colour index images. For IC 4933 we used a Paβ image and for NGC 1819 we used a V-band image.

3.4.3 2MASS image processing

Measuring bar length and ellipticity

Bars have previously been detected in most of the galaxies in our sample. Unfortunately, the bar measurement procedures vary greatly from one study to another (discussed by Athanassoula & Misiriotis 2002). For example, bar length can be measured visually in B-band images (Martin 1995), as the radius at which is located a sharp rise in the amplitudes of the even Fourier components (e.g., Aguerri et al. 1998), as the location of the peak in ellipticity (e.g., Knapen et al. 2000) or as the length of the region with a constant $m = 2$ phase in near-IR images (Laurikainen & Salo 2002). Other authors, such as Erwin (2005), assign as a lower limit to the bar length the location of the maximum in ellipticity and as an upper limit the minimum of two ellipse fit measures: the first minimum in ellipticity outside the peak ellipticity of the bar, or the point at which the position angles (PAs) of the fitted ellipses differ by $\geq 10^\circ$ from the PA of the bar. Gadotti (2008) prefers to fit a Sérsic profile to the bar with a truncation radius that corresponds to the bar length. This variety of criteria can cause the measured length of the bar to vary by a factor of up to two. Even though the length of a bar is a loosely defined concept, for practical purposes a consistency in the criteria would be useful. That is why we have performed our own measurements of bar lengths, as well as of bar maximum ellipticities, using H-band images from the 2MASS for all the galaxies hosting a nuclear ring.

First, we deprojected the 2MASS images, where possible using orientation parameters from deep optical and NIR images as reported by Laurikainen et al. (2004a), Laurikainen et al. (2005), Buta et al. (2006), and Laurikainen et al. (2006). For other galaxies we used the axis ratio and PA values from the HyperLEDA database, which were calculated using the 25 mag arcsec^{-1} isophote in B-band plates. We used the deprojection parameters from these literature sources in all cases, except those ones listed below, where we could improve them using the data sources identified. In particular, we used data from Ondrechen et al. (1989) for NGC 1097, Lindblad et al. (1997) for NGC 1300, Ryder et al. (1996) for

NGC 1433, Hawarden et al. (1979) for NGC 1512, Becker et al. (1988) for NGC 1566, Mulder et al. (1995) for NGC 3310, and Erwin (2005) for NGC 3945. For NGC 4448 we used our own determination of the orientation parameters from a 2MASS H-band image. For NGC 7570 we did the same as for NGC 4448 but using an r-band SDSS image. In the case of ESO 437-67 the orientation data from HyperLEDA clearly correspond to the bar. Deeper images from the DSS show a roughly face-on outer pseudo-ring feature, which led us to consider this galaxy to be face-on. Finally, we preferred the HyperLEDA orientation parameters for NGC 5248 to the one given by Laurikainen et al. (2004a) because it leads to a more realistic deprojection. The HyperLEDA values we used for NGC 5248 are very close to the ones derived by Jogee et al. (2002).

In the deprojected images, we masked all the stars and background or close-companion galaxies and then ran the ELLIPSE task from IRAF to fit the ellipticities and the PAs of the galaxies as a function of radius. We first fixed the centre of the galaxy to the position found using the centroid search option from the IMEXAM task. We plotted the data to visualize the variations of ellipticity and PA with radius. Then we followed the most restrictive criterion from Knapen et al. (2000) to identify bars, namely that a bar is characterized by a significant rise in the radial ellipticity profile followed by a significant fall over a range in radius where the position angle of the major axis is roughly constant. The amplitude of the ellipticity variation must be at least 0.1. The highest values of bar ellipticity, $\epsilon_{\rm b} = 0.8$, correspond to the more elliptical class of bars (the upper limit in bar ellipticity is set by the appearence of chaotic orbits in very elliptical bars; see Martínez-Valpuesta & Shlosman 2004).

We define the end of the bar as the radius where the ellipticity reaches its local maximum value in a region of roughly constant PA, following the approach of, among others, Knapen et al. (2002). This length estimation is known to be a lower limit to the true bar length (Erwin 2005). The uncertainty in the measurement of the maximum in ellipticity and thus in the measurement of the bar length is of the order of 5-10 per cent. The bulge component usually has a radius of only one kpc or so and is not expected to affect the measured bar lengths to a significant degree. We used the galaxy distances as given in Table B.1, obtained from the references given bellow the table, to calculate absolute bar lengths. The basic bar parameters (length and maximum ellipticity) are tabulated in Table B.2.

Bar parameters such as bar length and bar maximum ellipticity are highly dependent on the orientation parameters which are the main error source. In particular, the characteristics of the weakest bars are highly dependent on the fine-tuning of the deprojection. For example, the bar that appears in the nearly face-on galaxy NGC 2985 (whose bar does not appear in any catalogue) is invisible in the non-deprojected image even though the ellipticity of the disc of the galaxy is only $\epsilon_{\rm d} = 0.19$. Some weak bars can be hidden or fictiously created by an incorrect deprojection.

In two galaxies, NGC 473 and NGC 1386, we have not found any trace of a bar after the deprojection of the galaxy even though NED and HyperLEDA state that they are barred. NGC 1386 is one of the most inclined galaxies in the sample, which makes bar identification difficult. NGC 5427, which is listed as barred only in HyperLEDA, does not seem to be barred.

We also used the deprojected H-band 2MASS images to calculate the scalelength of the stellar discs of the galaxies. We performed a radial Sérsic+exponential fit to the deprojected

image of the galaxy which yields the disc scalelength, as tabulated in Table B.1. This disc scalelength will be used in the next subsection as a key element for the the measurement of $Q_{\rm g}$.

Non-axisymmetric torque parameter ($Q_{\rm g}$)

The non-axisymmetric torque parameter, $Q_{\rm g}$, quantifies the impact of non-axisymmetries in a galaxy (Combes & Sanders 1981). It is defined as the highest value of tangential forces normalized by the axisymmetric force field. The mathematical expression is

$$Q_{\rm g} = \max(F_{\rm T}^{\rm max}(r)/\langle F_{\rm R}(r)\rangle), \tag{3.1}$$

where $F_{\rm T}^{\rm max}(r)$ is the maximum tangential force at a given radius and $\langle F_{\rm R}(r)\rangle$ is the average radial force at the same radius (Combes & Sanders 1981). This maximum is located in the region of the bar or a strong arm perturbation. Spurious absolute $Q_{\rm g}$ maxima can appear in the outer parts of galaxies due to low signal-to-noise ratio. Higher values of $Q_{\rm g}$ are in a statistical sense related to strong bars and lower values to arm perturbations and oval distortions. However, exceptionally strong arms can cause high $Q_{\rm g}$ values in unbarred galaxies (e.g., in NGC 5427). For around half of the galaxies, we found non-axisymmetric torque parameter values in at least one of the following papers: Block et al. (2001), Buta & Block (2001), Laurikainen & Salo (2002), Block et al. (2004), Laurikainen et al. (2004a), Buta et al. (2006), and Laurikainen et al. (2006). Not all the previous papers report $Q_{\rm g}$; some list $Q_{\rm b}$, the perturbation related just to the bar (bar strength) which is very close to $Q_{\rm g}$ in most cases (see Durbala et al. 2009). We decided to determine our own set of $Q_{\rm g}$ values from H-band 2MASS images so that all galaxies have a $Q_{\rm g}$ value measured from an image of similar quality and in a consistent manner.

The method we followed is that of Laurikainen et al. (2004a), Buta et al. (2006), and Laurikainen et al. (2006). The basics of the method are described in Laurikainen & Salo (2002) and the bulge subtraction procedure has been described in Laurikainen et al. (2004a). To properly perform a $Q_{\rm g}$ measurement following the steps explained in the literature, we need to know the orientation parameters of the galaxy and the scaleheight of the disc. We also need to model the bulge.

For deprojecting a galaxy, we used the same orientation parameters as when we performed the ellipticty profiles and the maximum bar ellipticity measurement. The deprojection of the whole galaxy causes the deformation of the bulge within it, and will cause the stretching of an intrinsically spherical component, and possibly a wrong $Q_{\rm g}$ value. To avoid this problem, we subtract a bulge model from the image before the deprojection and add it again once the deprojection has been performed. In that way, even though the disc has been deprojected prior to the measurement of $Q_{\rm g}$, the bulge remains unchanged. This procedure assumes that the bulge is intrinsically spherical. To subtract and then add a bulge model we performed 2D decompositions of the 2MASS H-band images of the sample galaxies. The software we used for the 2D decomposition is described in Laurikainen et al. (2005). We fixed the disc PA and axis ratio as obtained from the literature and the disc scalelength from the 1D Sérsic+exponential fit described in the previous subsection. Sometimes the nuclear ring was so intense that it strongly perturbed the bulge fit. In these cases, the nuclear rings were (crudely) modelled with a Ferrers function (Ferrers 1877) with an index

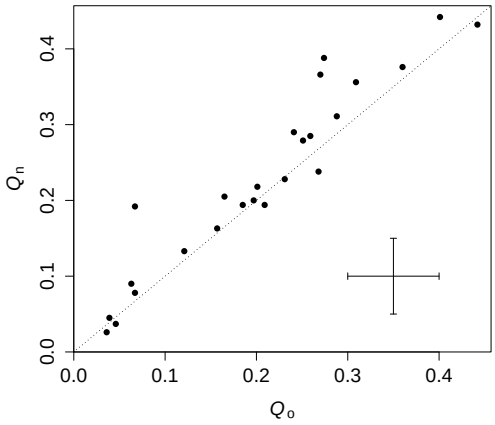

Figure 3.2: Comparison of Q_g values obtained by us (Q_n) and in the literature (Q_o) in those galaxies for which we have used the same orientation parameters as in the literature. Data used for this plot come from Laurikainen & Salo (2002), Laurikainen et al. (2004a; 2006) and Buta et al. (2006). The dashed line has a slope equal to one.

$n = 0$. This added component is not ring-like (actually it is lens-like), but the excess light it adds inside the nuclear ring is significantly fainter than the bulge contribution.

The disc scaleheight is an important parameter and one of the main sources of uncertainty in the Q_g measurement (see discussion in Laurikainen & Salo 2002). De Grijs (1998) showed that the scaleheight of the disc (h_z or exponential scaleheight) is proportional to the scalelength and that the proportionality factor varies with morphological type. From his results we deduce that this factor is 1/4 for galaxies with $T < 1.5$, 1/5 for galaxies with $1.5 < T < 4.5$, and 1/9 for galaxies with $T > 4.5$. It has to be noted than in de Grijs (1998), the vertical scaleheight is defined to be $z_0 = 2h_z$. The disc scalelength was taken from the 1D luminosity profiles as derived from the H-band 2MASS images.

The same non-axisymmetric feature (e.g. a bar) in two different galaxies may cause different Q_g values. On average, Q_g will be smaller in an earlier type galaxy. There are two reasons for this as follows. First, a higher central mass concentration affects the Q_g by increasing the $F_R(r)$ factor in eq. 2 (by higher central mass concentration we are meaning a higher total mass of the bulge, not a higher Sérsic index). Secondly, a bigger disc scaleheight makes the Q_g go down. This second effect is well seen in Fig. 6 from Laurikainen et al. (2004a) where it is shown that, on average, S0s have smaller Q_g than later-type galaxies.

We have been able to obtain a Q_g value for all the disc galaxies except for NGC 1386, NGC 3593, NGC 4100, NGC 4526, and NGC 6503 which are too inclined and to detect a bar or to produce Q_g profiles. The 2MASS images of ESO 198-13 and UGC 10445 are too shallow to measure Q_g reliably.

We check our results by comparing our Q_g values with those reported in the literature for 25 galaxies (Fig. 3.2). The correlation factor between Q_{new} and Q_{old} is $\rho = 0.95$ which corresponds to a scatter value lower than 0.03 in Q_g. We found that only NGC 4571 has a significantly different Q_g value (Laurikainen et al. 2004a), caused by these authors using a

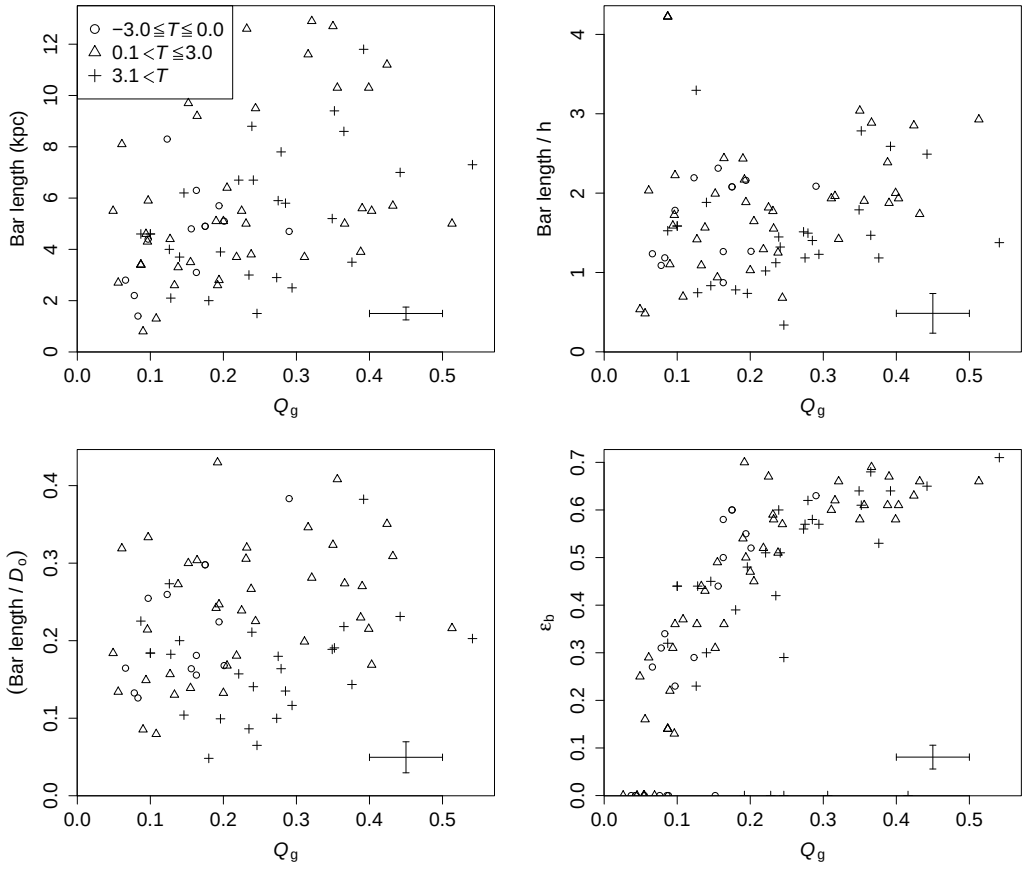

Figure 3.3: Bar length and strength parameters. In the top left-hand panel, the bar length as function of the non-axisymmetric torque parameter $Q_{\rm g}$ is given. In the top right-hand panel, the relative bar length, i.e. the ratio of bar length and exponential disc scalelength, as a function of $Q_{\rm g}$ is given. In the bottom left-hand panel, the ratio of bar length to $D_{\rm o}$ as a function of $Q_{\rm g}$ is given. In the bottom right-hand panel, the ellipticity of the bar, $\epsilon_{\rm b}$, as a function of $Q_{\rm g}$ is given. In the bottom-right panel, $Q_{\rm g}$ value of galaxies with no bar are plotted at $\epsilon_{\rm b} = 0$.

much lower Sérsic index in their bulge model than we did. In general we found that even though the near-IR images we used are shallower, the results are very similar, and can thus conclude that 2MASS images are indeed good enough to measure $Q_{\rm g}$.

The $Q_{\rm g}$ values as well as the radii, $r_{\rm Q_g}$, at which they are measured are found in Table B.2.

3.5 Comments on bar parameters

With the information in Table B.2 we can check the correlation between the bar strength and length reported by Martinet & Friedli (1997), Knapen et al. (2002), and also discussed by Elmegreen et al. (2007). In the top-left panel of Fig. 3.3 we show how the length of the bar is correlated with $Q_{\rm g}$ (also found by Laurikainen et al. 2002). We find that weak bars

can be both short and long; on the other hand, there are no short strong bars. The edge between the populated and non-populated area of the graph is sharp. If we plot (Fig. 3.3 top-right) the length of the bar relative to the scalelength of the disc, the trend previously noted remains. This trend is especially obvious for galaxies with $T \leq 3.0$ and is coincident with that found by Laurikainen et al. (2002; circles in their Fig. 4) and by Laurikainen et al. (2004b; crosses in their Fig. 16). In their papers, they use as a bar length indicator the radius at which they measured $Q_{\rm g}$, which scales well with the bar length measured as the maximum in the bar ellipticity (Fig. 6 in Laurikainen et al. 2002). In the sample of AINUR there are no examples of the population of late-type galaxies with a small bar length and a high $Q_{\rm g}$ which is described in Laurikainen et al. (2004b). This makes sense because in Laurikainen et al. (2004b) this population is described as rarely having nuclear star formation. A similar trend to the one we find between the bar length relative to disc scalelength and $Q_{\rm g}$, but with a much larger scatter, is found for the ratio between the bar length and the extinction-corrected galaxy diameter, $D_{\rm o}$ (Fig. 3.3, bottom-left). It thus appears that in our sample the parameters galaxy size, disc scalelength and minimum allowed bar length for a given $Q_{\rm g}$ are closely related and that there is a roughly linear relationship between $Q_{\rm g}$ and the minimum allowed bar length.

Our results are compatible with Fig. 2 in Elmegreen et al. (2007) if we consider that $Q_{\rm g}$ roughly scales with A_2 (as shown in Fig. 8 of Laurikainen et al. 2004b; however, they state that this correlation has a slope which changes with morphological type). In their Letter, Elmegreen et al. (2007) state that corotation should move outwards with time as the bar evolves, causing an increase in the semi-major axis of the orbits of the stars in the bar that is related to bar length (theoretically described by Martínez-Valpuesta et al. 2006). This would explain why only the upper-left parts of the top-row plots in Fig. 3.3 are filled and would set the minimum allowed bar size as an initial bar length for a given $Q_{\rm g}$.

The top left-hand panel in Fig. 3.3 shows that spiral galaxies with early morphological types, between $0.1 < T \leq 3.0$, have longer bars, confirming results by Laurikainen et al. (2002) and Erwin (2005). Bars in galaxies with types between $0.1 < T \leq 3.0$ are longer when scaled with $D_{\rm o}$ (as reported by Elmegreen & Elmegreen 1985; Martin 1995; Regan & Elmegreen 1997; Erwin 2005) although the effect is not as spectacular as when the absolute bar size is used. This effect is not seen when bar size is scaled with h (but it is seen in Erwin 2005), probably because a lack of statistics for high bar size relative to the disc length values.

The bottom right-hand panel of Fig. 3.3 shows how the maximum bar ellipticity, $\epsilon_{\rm b}$, is an indicator of $Q_{\rm g}$. The correlation factor between these two parameters is $\rho = 0.81$. For a given $\epsilon_{\rm b}$ early-type galaxies are found to have a slightly lower $Q_{\rm g}$, as found by Laurikainen et al. (2002). Thus early-types galaxies are on the upper envelope of the distribution. This is at least partly because for early-type galaxies, we are using a lower value of $h_{\rm r}/h_{\rm z}$ (the ratio between the disc scalelength and the disc scaleheight). A larger disc scaleheight reduces the impact of high ellipticity bars in the galaxy.

3.6 Comments on nuclear ring parameters

From our images we have measured the sizes of the nuclear rings, the deprojected differences between the PAs of the major axes of the rings and those of the bar of their host galaxy,

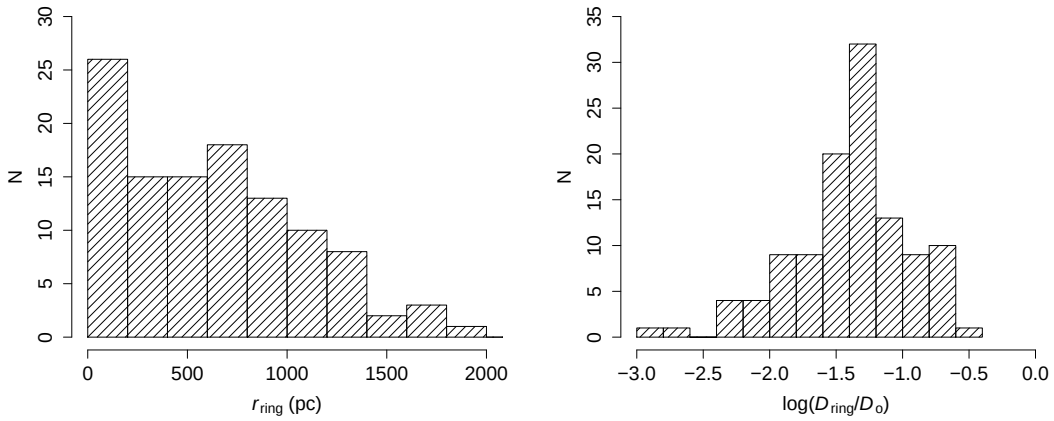

Figure 3.4: Left panel: size distribution of the nuclear rings. ESO 198-13 and ESO 565-11 are too large to be in this plot. The bin size is 200 pc. Right panel: distribution of nuclear ring sizes relative to the size of the galaxy (D_o).

and the deprojected, or intrinsic, ellipticities of the rings.

The dimensions and the orientation of the nuclear rings were measured directly from the deprojected images (mostly from *HST*, but some from literature sources as explained in Section 3.3) and their semi-major axis measurements are in Table B.2. The size of the rings was measured by fitting an ellipse to the ridge line in Hα images, Paα images, colour index images, UV images, or in structure maps. This fitted ellipse allowed us to make an estimate of the ellipticity and the orientation of the rings. The uncertainties in these measurements are highly dependent on the errors in the orientation parameters that we used. These orientation parameters are less likely to be accurate in strongly-barred galaxies. Another factor that adds some uncertainty is the assumption that the nuclear rings lie in the galactic plane of disc galaxies, but we have no evidence to the contrary (except for NGC 2787. See Sil'chenko & Afanasiev 2004).

3.6.1 Ring size distribution

Fig. 3.4 shows the size distribution of the nuclear rings. It is evident that smaller rings are much more frequent than bigger rings, especially when considering resolution limitations and dust obscuration close to the centre. As an example, in our sample rings with sizes smaller than 200 pc are four times more frequent than rings with size between 1000 pc and 1200 pc. The bottom panel of Fig. 3.4 is very similar to the one presented by Laine et al. (2002) who use D_{25} instead of D_o for scaling the nuclear rings; the two values are almost identical for most of the galaxies and thus the plots can be safely compared. The only qualitative difference between the two plots is that our histogram shows a longer small-size tail. The reason is that Laine et al. (2002) used mostly data from Buta & Crocker (1993) which were collected before high-resolution images from *HST* were available. Our plot peaks around $D_r/D_o = 0.05$ (where D_r denotes the nuclear ring diameter), which is similar to the result from Laine et al. (2002).

3.7 Non-axisymmetries and nuclear rings

3.7.1 Ring sizes and $Q_{\rm g}$

Fig. 3.5(a) shows the relative size of the nuclear ring, defined as the ring diameter divided by the host galaxy diameter, $D_{\rm o}$, as a function of the non-axisymmetric torque, $Q_{\rm g}$, of the host. We see that, as a general trend, small $Q_{\rm g}$ values allow a wider range of relative sizes of nuclear rings and that for high $Q_{\rm g}$ values only small rings are allowed. Knapen (2005) found this from a sample of 16 nuclear rings: "large nuclear rings occur in weak bars". This effect has also been seen previously in simulations (Salo et al. 1999). The outlier in the $D_{\rm r}/D_{\rm o}$ plot is ESO 565-11, by far the biggest and most elliptical nuclear ring in the Atlas, which may be in an early stage of development (Buta et al. 1999). This ring, however, is not an outlier in the $D_{\rm r}/h$ plot (Fig. 3.5*b*). Fig. 3.5(c) shows that for absolute ring size, the trend is still marginally visible. The edge between the populated and unpopulated area in the third plot (Fig. 3.5*c*) is quite sharp, and almost linear with maximum ring radii of 2000 pc at $Q_{\rm g} = 0.1$ and around 500 pc for $Q_{\rm g} = 0.5$. The morphological type does not affect the relation between either absolute or relative ring size and $Q_{\rm g}$.

We explored possible relations between nuclear ring parameters and the local non-axisymmetric torque value. We define this local non-axisymetric torque as

$$Q_{\rm nr} = (F_{\rm T}^{\rm max}(r_{\rm nr})/\langle F_{\rm R}(r_{\rm nr})\rangle) \tag{3.2}$$

where $F_{\rm T}^{\rm max}(r_{\rm nr})$ is the maximum tangential force at the deprojected major axis radius of the nuclear ring, $r_{\rm nr}$, and $\langle F_{\rm R}(r_{\rm nr})\rangle$ is the average radial force at the same radius. For small nuclear rings, the determination of $Q_{\rm nr}$ is harder because of a lack of resolution (PSF of $2''$ in 2MASS images) and because its behaviour becomes much more dependent on the model of the bulge that we subtract. We have found no trend when repeating the plots shown in Fig. 3.5 using $Q_{\rm nr}$ in the horizontal axis. This may indicate that nuclear ring sizes do not depend on local conditions; higher resolution images and better 2D bulge modelling are necessary to confirm this.

3.7.2 Ring and bar sizes

A relation between the bar length as derived from 2MASS images and the maximum nuclear ring radius can be seen in Fig. 3.6, where only one galaxy is significantly above a sharp edge that is located at approximately $r_{\rm r} = r_{\rm b}/4$. The outlier galaxy is ESO 565-11. ESO 565-11 has a nuclear ring that is probably in a very quick initial phase of its evolution, and is, as we have already seen, an outlier in some of our plots. Fig. 3.6 also shows that the longest bars are found in galaxies of morphological type $0.1 < T \leq 3.0$, as already shown in Fig. 3.3.

3.7.3 PA offset between nuclear rings and bars

The PA offset between the bar major axes and the nuclear ring is the measure with the highest uncertainty in this Chapter. Many rings are intrinsically round which makes it difficult to measure the PA and makes the measurement very sensitive to small deprojection errors. Thus if any trend existed between PA offset and $Q_{\rm g}$, it would be much more evident for more elliptical rings. Knapen et al. (2002) found no correlation between the PA offset

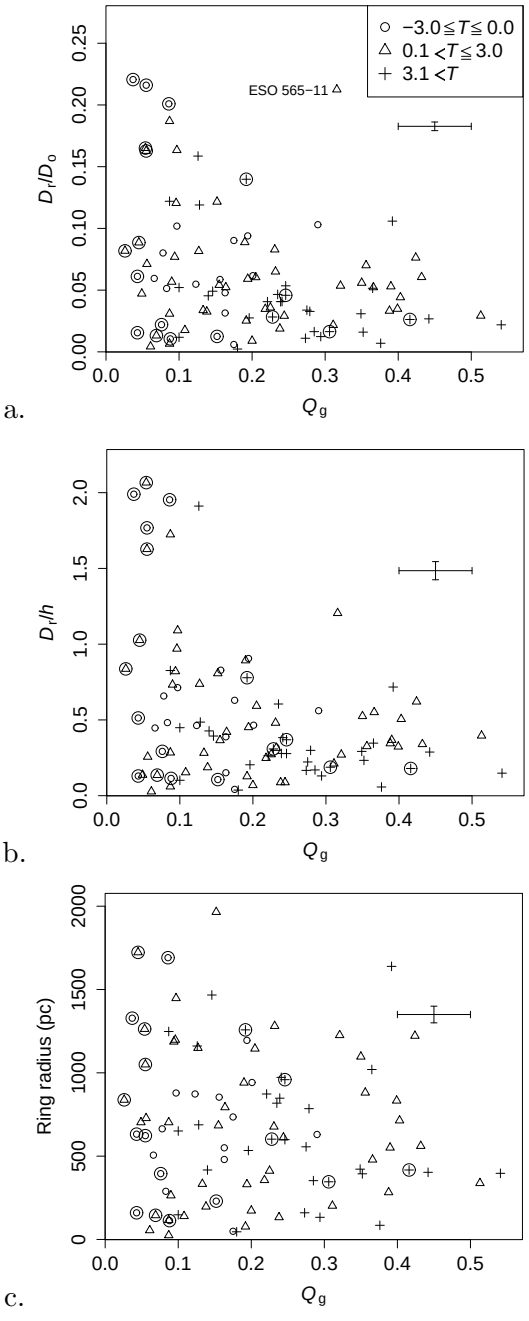

Figure 3.5: Top panel: Nuclear ring size relative to D_o as a function of the non-axisymmetric torque parameter of the host galaxy Q_g. Middle panel: same but using the disc scalelength to scale the ring size. Bottom panel: same but using absolute ring size. Two outlying points corresponding to ESO 198-13 and ESO 565-11 do not appear in the bottom panel. Encircled symbols denote unbarred galaxies.

and the Q_b of the galaxy. Our results are shown in Fig. 3.7 and they confirm the previously cited work. The morphological type of the host galaxy does not cause any segregation in

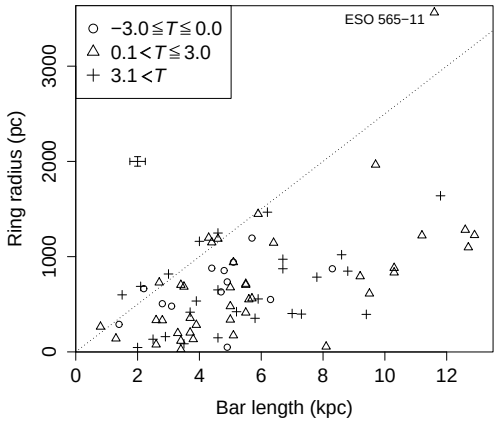

Figure 3.6: Nuclear ring radius versus bar length as determined from fits to 2MASS data. The dashed line indicates $r_{\rm r} = r_{\rm b}/4$.

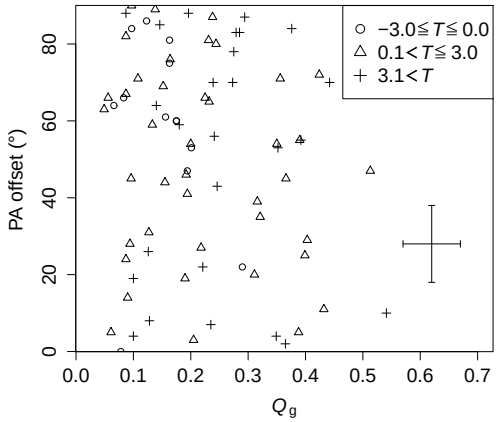

Figure 3.7: Difference between the major axis PA of the nuclear ring and that of the bar which hosts it, as a function of gravitational torque parameter $Q_{\rm g}$.

the scatter plot. If instead of using $Q_{\rm g}$ in the horizontal axis we use the maximum bar ellipticity, ϵ_b, the results are very similar.

When we compare the individual PA offset values from our survey with those from Knapen et al. (2002), we find that the differences between the two surveys range between 3° and 32° (there is a bigger difference in NGC 2903 but the nuclear ring is defined differently), with an average difference of 18°. Uncertainties in the orientation parameters could explain these differences, since the differences in the inclination angle used for the deprojection are as large as 20°.

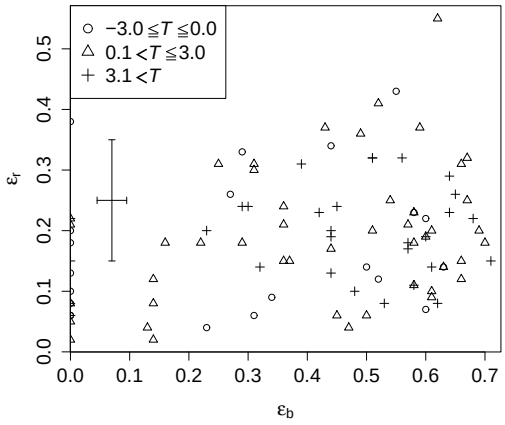

Figure 3.8: Deprojected ellipticity of star-forming nuclear rings as a function of bar ellipticity. Spiral galaxies with no noticeable bar are plotted at $\epsilon_b = 0$. We do not include galaxies too edge-on to detect any bar and galaxies too faint to have a bar ellipticity reliably measured in 2MASS H-band images.

3.7.4 Ring ellipticities and bar ellipticities

Figure 3.8 shows the ellipticities of the nuclear rings versus those of their host bars, and demonstrates how the most elliptical rings can only be found in the most elliptical bars. There is a maximum ring ellipticity for a given bar ellipticity and this limit is roughly linear as a first approximation. Galaxies with no bar have rings with ellipticities up to $\epsilon_{\rm r} \sim 0.4$. This maximum value corresponds to NGC 6861 which is a very early-type galaxy with a dusty nuclear ring. The scatter plot does not show any hint of different behaviour for different morphological type bins. Plotting $Q_{\rm g}$ instead of the bar ellipticity causes a much more subtle effect.

We found no correlation between the ring ellipticity and the PA offset between bar and ring. There is a theoretical explanation for this. Knapen et al. (1995) and Shlosman (1999) state that these parameters are regulated primarily by the gas inflow into the circumnuclear regions. Since gas inflow does not depend exclusively on the parameters of the bar but more generally on the available fuel, correlations of ring ellipticity and PA offset are not expected, and in fact not observed. The dynamical time scale in the circumnuclear region is around 10^7 years, and thus the availability of the fuel can be expected to be variable, reducing any possible correlation with the bar strength.

The two rings of NGC 2787 (not plotted in Fig. 3.8) have ellipticities of $\epsilon_{\rm r} \sim 0.7$ when projected into the main plane of the galaxy. This is because the rings are lying in a disc that is polar to the bar orientation of the galaxy (Sil'chenko & Afanasiev 2004). The rings probably have a much smaller intrinsic elongation.

3.8 Nuclear rings and morphological type

Star-forming nuclear rings have been found to occur preferably in galaxies with morphological types between S0 and Sbc (Knapen et al. 2006).

To study the dependence of the fraction of nuclear rings on the morphological type of the host galaxy type we consider only the 76 nuclear-ringed galaxies that are found in our statistically meaningful sample of 483 galaxies. The other nuclear rings were found in a literature search and not in a survey and are thus less suitable for a reliable statistical analysis.

In Fig. 3.9 we show the absolute number of nuclear rings in each type bin (top panel, double-hatched) and the fraction of nuclear rings in each bin (bottom panel). Nuclear rings are mainly found in galaxies with $-2 < T < 5$ (S0 − Sc). In $T < -3$ galaxies, rings usually are dusty and have probably little if anything to do with a resonance framework. For types Sdm or later no nuclear rings have been found (see Knapen et al. 2006). Late-type spirals (of types Sd to Sm) usually have slowly rising, low-amplitude rotation curves which prevent ILRs from forming (see the review by Sofue & Rubin 2001 and a case study by Elmegreen et al. 1998). A galaxy without ILRs would be very unlikely to host a star-forming nuclear ring.

A possible alternative explanation for the lack of nuclear rings in late-type galaxies can be deduced from the work of Dalcanton et al. (2004). They found from a study of edge-on late-type galaxies that dust lanes are found only in galaxies rotating faster than $V_c \sim 120\mathrm{kms}^{-1}$ because above this threshold the dust scaleheight drops drastically. As cold molecular gas is linked to dust, Dalcanton et al. (2004) speculate that the ISM scaleheight should drop similarly at this threshold value of $V_c \sim 120\mathrm{kms}^{-1}$, which would be the velocity at which the disc becomes gravitationally unstable. In a stable disc, turbulent velocities are much higher and the star formation rate drops considerably (by a factor of roughly 3; Dalcanton et al. 2004). In a more rapidly rotating, earlier-type, gravitationally unstable disc the ISM would be concentrated closer to the plane and would form molecular clouds that would interact with resonances and thus may form nuclear rings.

Knapen (2005) found that the maximum of the nuclear rings distribution occurs at $T = 4$ (Sbc) but we find that it occurs in earlier-type galaxies ($T = 2-3$ Sab − Sb). There is another maximum around $T = -1$ (S0) but low statistics cause a big uncertainty in this particular measurement.

We find that $6 \pm 2\%$ of the elliptical galaxies ($-5 \leq T < -3$) have dust rings. $24 \pm 5\%$ of lenticular galaxies ($-3 \leq T \leq 0$), and $19 \pm 2\%$ of non late-type spiral galaxies ($0 < T \leq 7$) have star-forming nuclear rings. We find that $20 \pm 2\%$ of the galaxies with types $-3 \leq T \leq 7$ (the range of disc galaxies where nuclear rings are found) host star-forming nuclear rings. Irregular galaxies never have a nuclear ring. These results confirm those of Knapen (2005) who concluded that a fifth of disc galaxies have star-forming nuclear rings.

3.9 Nuclear activity

In discussing nuclear activity we are excluding those galaxies classified as nuclear starbursts, which are naturally correlated with nuclear rings, as small nuclear rings may be confused with genuine nuclear star formation. As a consequence, many galaxies with a nuclear ring are listed in catalogues as starbursting galaxies because they have a nuclear ring.

The most extensive survey to date of nuclear activity in local galaxies has been published by Ho et al. (1997a; 1997b). Forty-nine of our nuclear ring galaxies appear in their survey. We compared the proportion of each kind of nuclear activity (LINER, Seyfert,

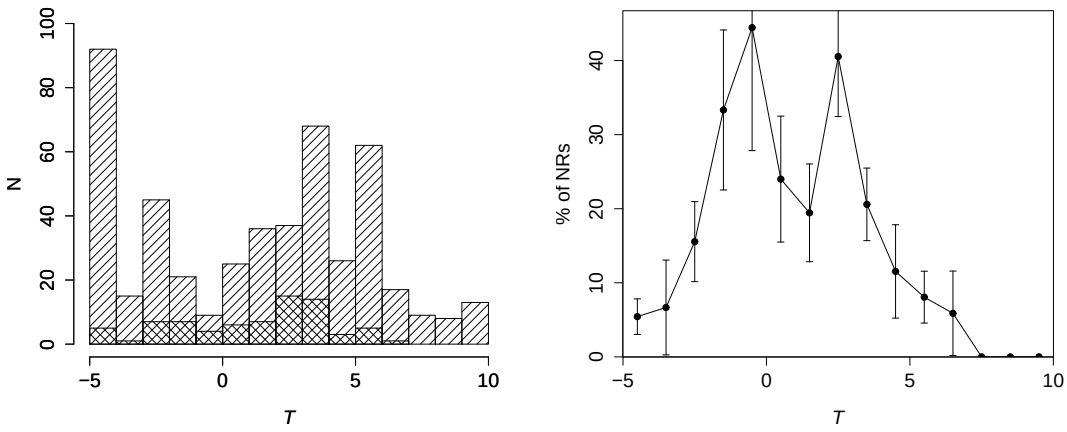

Figure 3.9: Left panel: histogram showing the distribution in the morphological type of the 483-galaxy sample. Overplotted (double-hatched areas) we show the galaxies with nuclear rings. Right panel: fraction of nuclear rings in each morphological type. Bin size $T = 1$. Error bars calculated using Poisson binomial statistics.

and Transition) in Ho et al. (1997a; 1997b) with that in the 49 AINUR galaxies which matched with their catalogue, taking into account the morphological type of AINUR galaxies. We find no significant differences (larger than one sigma) between the proportion of active galaxies in AINUR and Ho et al. (1997a; 1997b). This is in contradiction both with Knapen et al. (2006), who found a significantly higher proportion of active galaxies among galaxies with nuclear rings, and with Comerón et al. (2008a), who found that nuclear rings are related to σ-drops (see also Chapter 1), which are in turn related to nuclear activity. This may be because in Knapen et al. (2006) and Comerón et al. (2008a) the sample selection criteria favour 'famous' galaxies, which tend to be active (Comerón et al. 2008a and Chapter 1).

3.10 Nuclear rings in unbarred disc galaxies

Several of the nuclear rings we studied are found in unbarred galaxies. If we do not consider NGC 1386, NGC 3593, NGC 4100, NGC 4526, and NGC 6503 which are too highly inclined to tell whether they are barred or not, we have 18 *bona fide* unbarred spiral galaxies with nuclear rings. We explore the properties of these galaxies in some detail to find evidence that their nuclear rings are of resonance origin.

NGC 2997, NGC 5033, and NGC 5247 have very prominent arms that cause $Q_{\rm g} > 0.2$ and are likely to generate resonance effects similar to those of a bar (see e.g. Lindblad (1961); Shlosman (1999); Shlosman (2001); Rautiainen & Salo 2000).

Several galaxies have ovals: NGC 4571 (Eskridge et al. 2002), NGC 4736 (Bosma et al. 1977; Trujillo et al. 2009), NGC 6753 (Laurikainen et al. 2004a), and possibly NGC 7049 (Corwin et al. 1985). Ovals have dynamical effects very similar to those produced by bars (Kormendy & Kennicutt 2004).

Other galaxies can have dynamical resonances due to a tidal interaction with a close

companion (see e.g. Buta et al. 1992). A good case is the ring in NGC 5427, a galaxy which may be interacting with NGC 5426 (even if according to Fuentes-Carrera et al. 2004, NGC 5427 has a bar of 32″ in length that we have not detected). Other nuclear rings which may be caused by the same mechanism are the ones in NGC 3245 (this galaxy is close to NGC 3245A), NGC 6861 (near IC 4943), and NGC 4459 (which could be weakly interacting with NGC 4468 and NGC 4474). Simulations also show that an inflow of material to nuclear regions due to tidal interactions (Hernquist 1989; Hernquist & Mihos 1995) may cause starbursts in the central areas of the galaxy.

Counterrotating components have been reported in NGC 4138 (Jore et al. 1996), NGC 4826 (Braun et al. 1992), NGC 7217 (Merrifield & Kuijken 1994) and NGC 7742 (de Zeeuw et al. 2002; Mazzuca et al. 2006). In both these unbarred galaxies the presence of a nuclear ring and a counter-rotating component would be explained by a past minor merger with a gas-rich dwarf galaxy in a retrograde orbit (see Jore et al. 1996 for NGC 4138, Braun et al. 1994 for NGC 4826, Sil'chenko & Moiseev 2006 for NGC 7217, and Mazzuca et al. 2006 for NGC 7742). Such a merger could have led to the counter-rotating component and to an oval distortion strong enough to create a nuclear ring.

We then still have three galaxies (ESO 198-13, NGC 473, and NGC 3011) that have nuclear rings for which we have no observational indications for an explanation in terms of a resonance framework.

We have found that nuclear rings are mostly found in barred galaxies. Most of the unbarred hosts have features that may be driving resonances. For the three remaining galaxies, the existence of an undetected weak oval distortion cannot be ruled out.

3.11 Notes on individual galaxies

For each galaxy we first list the original citation to the nuclear ring if this exists. We also describe the particularities of the ellipticity and the 2D bulge/disc/fit when necessary. Other interesting particularities have been described when necessary. The reference after the galaxy name indicates the first mention we have found in the literature for the nuclear ring in the galaxy.

ESO 198-13: Buta (1986). This galaxy is visually unbarred. We have not been able to perform an ellipticity profile to check it because the 2MASS H-band image is too shallow. This galaxy has three ring features which makes the identification of the innermost ring as a nuclear ring secure, although it is more than 3 kpc in radius.

ESO 437-33: Buta & Crocker (1991). The non-axisymmetry profile is very flat which causes a large uncertainty in the radius at which $Q_{\rm g}$ is found.

ESO 437-67: Buta & Crocker (1991). We decided to adopt a face-on orientation for this galaxy because the HyperLEDA values are clearly for the bar rather than the disc of the galaxy. Also, the galaxy has an R'_1 ring that looks nearly face-on. During the 2D decomposition we have not been able to fit a disc due to its shallowness in the 2MASS H-band image.

ESO 565-11: Buta & Crocker (1991), see Buta et al. (1995; 1999) for detailed studies. This galaxy has the biggest and most intrinsically elliptical ring in our sample. It is unambiguously a nuclear ring because the galaxy has also inner and outer resonance features.

The nuclear ring cannot be an x_1 ring because its major axis is not aligned with the bar. The ring may be at an early and fast stage of its formation (Buta et al. 1999).

IC 342: Ishizuki et al. (1990) in CO line emission. Böker et al. (1997) in NIR. This nearby galaxy is very close to the Milky Way plane so it is highly extinguished. The 2MASS images we used for the ellipticity profile and the 2D decomposition had to be cleaned of many foreground stars (of the order of 1000). Apart from fitting the disc, the bulge, and the bar, the 2D decomposition also needs two circular Ferrers components to produce a reasonable fit. The smaller one has the size of the nuclear ring, while the other corresponds to a circular lens of $10''$ in radius. The nuclear ring is small and irregular.

IC 1438: Buta & Crocker (1993).

IC 4214: Buta & Crocker (1991).

IC 4933: Ryder et al. (2009).

NGC 278: Pogge (1989). This galaxy has an unambiguous ring $9''$ in diameter with a somewhat octagonal shape. It has an other ring-like structure that we think is an inner pseudo-ring. Knapen et al. (2004) called it a nuclear ring on the basis that this galaxy has no bar and that the feature is 2.2 kpc in radius. We found, however, a bar inside this feature. This bar is doubtful and very weak, but it has also been found by P. Erwin and L. Gutiérrez (private comunication). Another argument against the 2.2 kpc ring being a nuclear ring is that its size relative to the galaxy or to the disc scalelength is much larger than that of all the other nuclear rings in the sample.

NGC 473: Heckman (1978). It is considered an inner ring in de Vaucouleurs et al. (1980). The galaxy appears as barred in NED and RC3, but there is no sign of a bar or an interacting companion that could explain a nuclear ring. The nuclear ring has an ellipticity that is different from that of the disc of the galaxy, so a bar can be fitted to it, which may explain the false detection in the catalogues. The nuclear ring is one of the biggest in the sample.

NGC 521: Buta et al. (2009). This ring is made of dust and is visible as a dark annulus in B images. Its morphology is coincident with that of nuclear star-forming rings; thus it is likely to be a star-forming nuclear ring deeply embedded in dust. The nucleus of the galaxy is off-centred. (Note: The ring radius of $7.7''$ given by Buta et al. (2009) was based on an incorrect image scale. The radius given in Table. B.2 uses the correct image scale.)

NGC 613: Hummel et al. (1987). The nuclear ring has also been considered a nuclear spiral (Buta & Crocker 1993). The presence of the ring makes it difficult to fit the inner $10''$ in the 2D decomposition, but adding a round lens component with the size of the ring yielded a reasonable fit. Most of the ring surface is made up of dust which at some places has been torn away by intense star formation.

NGC 718: Erwin & Sparke (2002).

NGC 864: Martini et al. (2003). This is one of the smallest rings in the sample. It is composed of bright knots of star formation arranged in a c shape, with the 'open' part of the ring located to the south-west.

NGC 936: Erwin & Sparke (2002). This ring is purely stellar with no traces of recent star formation. It encircles an inner bar. It appears as a brighter area in a structure map. The archive *HST* images from this galaxy are too shallow to detect the nuclear ring; thus we used a WHT r-band image.

NGC 1068: Scoville et al. (1988). This ring is controversial and, sometimes interpreted as a nuclear pseudo-ring (de Vaucouleurs & Buta 1980; Knapen et al. 2006). We consider that it is a complete ring, partially obscured by a dust lane that comes from the bar to the centre of the galaxy. This galaxy needed two bars to be properly fitted (with lengths of $8''$ and $80''$). It also needed a central point-like component to take into account the bright Seyfert nucleus.

NGC 1079: Maoz et al. (1996). The ring looks smooth; there are few detectable clumps.

NGC 1097: Burbidge & Burbidge (1962). Sérsic (1958) found a feature that he described as a 'single spiral arm' with the same size as the nuclear ring. This galaxy appears strongly barred but $Q_{\rm g}$ is only 0.241. The bar may look stronger than it really is due to the interaction with the dwarf elliptical galaxy NGC 1097A. The ring can be fitted approximately with a lens component. Buta & Crocker (1993) state that the ring is a pseudo-ring. At high resolution, we see that the ring is made up of small spiral sections with a high pitch angle.

NGC 1241: Böker et al. (1999).

NGC 1300: Pogge (1989). Suspected by Peterson & Huntley (1980). This galaxy has the strongest bar in the sample ($Q_{\rm g} = 0.541$). The north-west section of the ring is double.

NGC 1317: Schweizer (1980). The bar is not very evident in the ellipticity profile and in the 2D decomposition, and the $Q_{\rm g}$ profile is not very peaked. The 2D fit of the galaxy is dominated by the disc component. The galaxy is double-barred and has a nuclear bar inside the nuclear ring that is clearly seen in the images and in the $Q_{\rm g}$ profile.

NGC 1326: García-Barreto et al. (1991a). The ring causes a poor fit in the inner parts of the 2D decomposition.

NGC 1343: Zwicky & Zwicky (1971). The ring again causes a poor fit in the inner parts of the 2D decomposition. The 2MASS image is so shallow that it has not been possible to fit the bar.

NGC 1386: Tsvetanov & Petrosian (1995). This galaxy is too highly inclined to measure the bar parameters. We have not detected a bar in the ellipticity profile but the NED reports it as barred. The ring is bright enough in Hα to be clearly traced even at the high inclination of the galaxy.

NGC 1387: Laurikainen et al. (2006) by subtracting a modelled galaxy from a 2.2 micron image. The ring is seen in a colour index image as blue patches distributed in a ring embedded in a dusty red disc.

NGC 1415: García-Barreto et al. (1996). The nuclear ring is well fitted with a lens component.

NGC 1433: Buta (1983). The 2D decomposition yields a nuclear bar with the same length as the ring radius. This inner bar was discovered by Buta (1986). The ring looks a bit like a pseudo-ring but there are clear dust lanes crossing the ring, and covering part of it. The detection of the ring was performed using a colour index image with exposures taken by *HST* in 2001. The galaxy was previously imaged by *HST* in the UV using the FOC camera (Maoz et al. 1996), leading to the identification of a feature defined as a nuclear ring by the authors. Their ring partly corresponds to the one presented here, but of half its diameter and off-centred. We think that this ring-like feature is an artefact and that it can be ruled out on the basis of more recent imaging in other bands.

NGC 1512: Buta et al. (1988). Hawarden et al. (1979) described the nuclear ring as an 'exquisite central spiral pattern' and showed a picture where the ring is clearly identifiable. The ellipticity of the nuclear ring is very different from that of the inner ring. This is probably due to the distortions caused by the bar ($Q_{\rm g} = 0.366$).

NGC 1566: Indirectly detected by Agüero et al. (2004), who added the radial fluxes along six spectrograph slits and discovered three radii where the Hα is enhanced, at the approximate locations where ILR, corotation and outer Lindblad resonance should be. To our knowledge the present Chapter shows the first direct detection of the ring, which is seen as a dusty feature in the colour index map. The paper of Agüero et al. (2004) suggests that it should have strong star-forming areas. Unfortunately, we do not have Hα imaging for this galaxy and the *HST* UV image we used is too shallow to show any ring. The dusty feature we have found is distorted in the south-east.

NGC 1672: Díaz et al. (1999). The eastern part of the ring is fainter than the western part which may indicate that it is more heavily obscured by dust.

NGC 1808: Sérsic & Pastoriza (1965) as a 'hot spot' nucleus. The ring is nearly round after deprojection, except for its south-east part. The orientation parameters we used for this galaxy are the ones of the outer ring. The inner parts of the galaxy make it appear as a highly-inclined Sb in shallow images.

NGC 1819: Buta & Crocker (1993). The ring is so bright that a lens component has to be introduced in the 2D fit to take it into account. The nuclear ring is incomplete in the east. The western part is made up of two arcs of intense star formation.

NGC 2273: Ferruit et al. (2000). This nuclear ring is composed of two tightly wound star-forming arms.

NGC 2595: Buta & Crocker (1993).

NGC 2787: Sarzi et al. (2001) for the dust ring. The two rings are found in a polar disc perpendicular to the main disc of the galaxy and to the outer H I ring of the galaxy (Sil'chenko & Afanasiev 2004). The dust ring is the innermost part of a tightly wound dust spiral. Just inside the dust ring and with a slightly higher ellipticity is an Hα ring, which may be caused by the ionization of the inner part of the dust disc by the Seyfert nucleus. The two rings are probably polar and their deprojected ellipticity and PA values are thus not reliable. Because we round some of the values in Table B.2, they appear identical for the two rings, even though the ionization ring is slightly smaller than the other.

NGC 2859: Erwin & Sparke (2002). This star-forming nuclear ring is a dusty feature that is not visible in an Hα image and has an inner bar inside it (Erwin & Sparke 2002).

NGC 2903: Sakamoto et al. (1999). The ring size is a matter of discussion. Alonso-Herrero et al. (2001) consider the ring to be twice as large as we do, but their ring is extremely elliptical after deprojection while what we consider to be the ring is intrinsically much rounder. The 2D decomposition yields an almost bulgeless galaxy where the central regions are dominated by a lens that has the size of the intense star-forming area. This area of star formation causes an artificial peak in the $Q_{\rm g}$ profile.

NGC 2935: Buta & Crocker (1991).

NGC 2950: Erwin & Sparke (2002). This ring is purely stellar with no traces of recent star formation. It encircles an inner bar. It appears as a brighter area in a structure map. It has been sugested to be either a faded star-forming ring or a side-effect of the double-barred nature of NGC 2950 (Erwin & Sparke 2002).

NGC 2985: Comerón et al. (2008b) and Chapter 2. This nuclear ring is one of the smallest in the sample. This galaxy is unbarred in the literature; however, we found that in the deprojected image a slight oval distortion is detectable even though its strength and even its existence are very dependent on the orientation parameters. We could not fit a bar in the 2D decomposition. A possible cause of a resonance ring may be the dwarf irregular satellite KDG 59 that is probably causing the disturbances seen in H I maps (Comerón et al. 2008b). NGC 3027 may also cause these disturbances but there is no evidence for a tidal tail connecting the two galaxies (Noordermeer et al. 2005; Oosterloo, private communication).

NGC 2997: Sérsic & Pastoriza (1965) as a 'hot spot' nucleus. The northern part of the ring is obscured by dust. It consists of several spiral fragments made of H II regions.

NGC 3011: Gil de Paz et al. (2003). The galaxy is a dwarf spiral with a $5''$ (~ 600 pc) nuclear ring and it also contains an outer ring of $19''$ (~ 2 kpc) in radius (Gil de Paz et al. 2003). These rings are the first rings discovered in a dwarf galaxy. As the galaxy has no obvious bar, Gil de Paz et al. (2003) suggests that the nuclear ring may have been caused by the sweeping out of the interstellar medium by a nuclear episode of star formation. This gas may reach densities high enough to become molecular and to form H II regions. The relative size of the nuclear ring is not incompatible with the 'classical' rings in the sample, although it is found on the upper boundary.

NGC 3081: Heckman (1978). There is an inner bar inside the ring (Erwin 2004) and no bright source at the centre of the ring. Several compact knots of emission could be candidates for the nucleus, but they are off-centred. A lens with the radius of the nuclear ring was needed for the 2D decomposition. Buta et al. (2007) show a colour index image of this galaxy with the outer, inner, and nuclear rings perfectly seen; in this image, the three rings are particularly sharp and are elongated with different PAs and ellipticities which is evidence for the rings not being circular.

NGC 3185: Comerón et al. (2008c).

NGC 3245: Barth et al. (2001a). They suggest that the ring may be the outer edge of a nuclear disc. The western part of the ring is probably covered by dust. The galaxy has no bar and the ring may be caused by the gravitational perturbations of NGC 3245A.

NGC 3258: first reference as a ring in Comerón et al. (2008c) but has been called disc by Capetti & Balmaverde (2005).

NGC 3268: first reference as a ring in Comerón et al. (2008c) but has been referred to as a small disc of dust and ionized gas by Ferrari et al. (1999) and as dust filaments by Capetti & Balmaverde (2005).

NGC 3310: Telesco & Gatley (1984). Called an inner arm system by Walker & Chincarini (1967). The nucleus is off-centred. This galaxy is the one least well fitted in the 2D decomposition, due to the intense star-formation at a radius of $15''$. We fitted this activity with a lens but this did not yield a particularly good approximation to the morphology of the central region of the galaxy.

NGC 3313: Buta & Crocker (1993).

NGC 3351: Sérsic & Pastoriza (1965) as a 'hot spot' nucleus. A lens was needed to fit the nuclear ring in the 2D decomposition.

NGC 3379: van Dokkum & Franx (1995). This ring is clearly visible as a dust feature in structure maps and in colour index images but also emits in Hα. Inside the ring, there

is some Hα that could correspond to small arms of star formation spiralling from the ring to the AGN. Statler (2001) states that the ring is a decoupled nuclear component whose orientation is not linked to the main body of the galaxy.

NGC 3414: Buta et al. (2007). This galaxy has a nearly round component with an exponential profile and a thin bar-like component. Many explanations have been given for this peculiar morphology. The bar-like component could be either a real bar (Sil'chenko & Afanasiev 2004) or a polar ring (Whitmore et al. 1990). The possible bar, although it is extremely thin in the 2D models of the galaxy, is very weak ($Q_{\rm g} = 0.097$) and has no dust lanes.

NGC 3486: Buta & Crocker (1993). Appears as an inner ring in de Vaucouleurs & Buta (1980). The ring appears to be a collection of spiral arms with high pitch angle. This galaxy is known to have only a nuclear bar (Martin 1995), but we have also found a very weak bar by looking the ellipticity profile.

NGC 3504: Buta & Crocker (1993). The northern part of the ring is probably hidden by dust. It is surprising that the size we measured for this ring is a half of the values that appear in literature (Buta & Crocker 1993, Elmegreen et al. 1997).

NGC 3593: Pogge (1989). The inner parts of the galaxy are too hidden by the disc to allow a proper 2D decomposition and thus to make a bulge model to measure $Q_{\rm g}$ with precision. The galaxy type could be either S0/a pec or I0 pec according to Buta et al. (2007).

NGC 3945: Erwin & Sparke (2002). This ring is purely stellar with no traces of recent star formation. It encircles an inner bar. It appears as a brighter area in a structure map. The disc scalelength we have measured is the one from the outer disc, which is heavily affected by a strong outer ring. It has been sugested to be either a faded star-forming ring or a side-effect of the double-barred nature of NGC 3945 (Erwin & Sparke 2002).

NGC 3982: de Vaucouleurs & Buta (1980) as an inner ring. The ring needed a lens in the 2D decomposition to be fitted. The nuclear ring consists of flocculent Hα areas and is not very well defined.

NGC 4100: Buta & Crocker (1993). The galaxy is too inclined to measure $Q_{\rm g}$. Eskridge et al. (2002) state that this galaxy is barred.

NGC 4102: Comerón et al. (2008c).

NGC 4138: de Vaucouleurs & Buta (1980) as an inner ring. This large nuclear ring is in an unbarred galaxy, so it may be an inner ring. We do not have Hα or Paα *HST* imaging for this galaxy and the UV exposures are too short to detect the ring. In the structure map, subtle dust structures tracing the ring can be seen. The $Q_{\rm g}$ profile is flat and close to zero which indicates a very symmetric structure. This galaxy contains a counter-rotating component (Jore et al. 1996).

NGC 4245: Erwin & Sparke (2002).

NGC 4262: first reference to this dusty star-forming nuclear ring, which appears as featureless and wide in structure maps.

NGC 4274: Falcón-Barroso et al. (2006). The nucleus of the galaxy is off-centred.

NGC 4303: Möllenhoff & Heidt (2001), referred to as a nuclear spiral by Colina et al. (1997) and Colina & Wada (2000). The ring is wide and made up of small spiral bits. This galaxy has a nuclear bar with 175 pc in radius (Colina & Wada 2000, adjusted for distance).

NGC 4314: Benedict et al. (1977).

NGC 4321: Sérsic & Pastoriza (1965) as a 'hot spot' nucleus. This nuclear ring could be considered a pseudo-ring, but we find in the structure maps that the dust is distributed in arms that cross the areas where parts of the ring are missing. We used a round lens to fit the ring area in the 2D decomposition.

NGC 4340: Erwin (2004). The nuclear ring appears sharp and thin, and it contains an inner bar (Erwin 2004).

NGC 4371: Erwin & Sparke (1999) for the outer nuclear ring. They consider the inner nuclear ring as a possible dust nuclear disc. The outer nuclear ring appears much bluer than the inner one in the colour index maps. Thus, the outer nuclear ring is probably a resonance star-forming ring related with the bar and the inner one may have its origin in the depletion of inner parts of a dusty disc.

NGC 4448: Comerón et al. (2008c). The ring is made of several aligned knots of star formation which leave an empty space to the north-east.

NGC 4459: de Vaucouleurs (1957) for the outer nuclear ring. AINUR contains the first known reference for the inner nuclear ring. The inner nuclear ring, unlike that in NGC 4371, looks thin and sharp; thus it is less likely to be an inner disc whose inner parts have been depleted. In the UV *HST* image the innermost ring is clearly seen as emitting. The outer nuclear ring cannot be seen. The UV image shows that inside the innermost ring, there is a lens of diffuse star formation. NGC 4459 has no bar (the $Q_{\rm g}$ profile is completely flat) and the rings could be due to a weak interaction with NGC 4468 and/or NGC 4474.

NGC 4494: Lauer et al. (2005). Similar to NGC 3258.

NGC 4526: Sandage (1961). Dust ring in a nearly edge-on galaxy where we have not been able to measure $Q_{\rm g}$.

NGC 4571: de Vaucouleurs & Buta (1980) as an inner pseudo-ring. This galaxy is not barred but it has a lens with the size of the nuclear ring (Eskridge et al. 2002).

NGC 4579: Terashima & Wilson (2003). The nuclear ring is off-centred which can be explained in terms of a resonance ring in a mass distribution that is induced by a superposition of $m = 1$ and $m = 2$ perturbations (Comerón et al. 2008b and Chapter 2). The inner arcs could be related to shocks caused by the interaction of a compact radio jet with the cloudy ambient gas (Contini 2004).

NGC 4593: González Delgado et al. (1997).

NGC 4736: Pease (1917) as the 'periphery of an ellipse'. This SA galaxy has an oval disc too subtle to be detected in the 2MASS images (Erwin 2004; Trujillo et al. 2009). If we consider this oval as causing the nuclear ring, it has often been misclassified as an inner ring. This galaxy has also a nuclear bar, $20''$ in length (Erwin 2004).

NGC 4800: de Vaucouleurs & Buta (1980) for the outer nuclear ring, Comerón et al. (2008b) and Chapter 2 for the two other nuclear rings. The innermost nuclear ring may be doubtful but structure maps make it appear clearly (Comerón et al. 2008b). The galaxy appears unbarred, but ellipse fitting in the H band reveals a weak bar.

NGC 4826: Pogge (1989). This galaxy is unbarred and has counter-rotating components (Braun et al. 1992).

NGC 5020: first reference to this nuclear ring. The southern part of the nuclear ring is hidden by a dust lane.

NGC 5033: Considered as a 'spiral or ring-like pattern of H II regions' in Mediavilla et al. (2005). The galaxy is unbarred, but it has a strong arm pattern that could cause a

nuclear ring.

NGC 5135: García-Barreto et al. (1996). What we see in the image is actually half of a nuclear ring. The other half is probably hidden in the dust patches that are seen in visible *HST* images.

NGC 5194: Worden (1974). The orientation parameters of this galaxy are very difficult to derive because of its interaction with NGC 5195. The galaxy has a weak bar but the peak in $Q_{\rm g}$ is located in the prominent arms caused or enhanced by the interaction. The ring is wide and not very well defined and it is made of small patches of star formation distributed in spiral arms.

NGC 5236: Buta & Crocker (1993). The nuclear region has such a huge star formation rate that the 2D decomposition yields uncertain bulge parameters. We used an inner lens to model this star formation region; this lens has a radius similar to the nuclear ring.

NGC 5247: first reference to this nuclear ring. The UV *HST* image we have is shallow, but it seems that the ring is not complete and some parts are missing in the south-west. This galaxy is non-barred but the prominent non-axisymmetric arms yield one of the highest $Q_{\rm g}$ values in the sample. The strong arms probably affect the determination of the orientation parameters.

NGC 5248: Sérsic & Pastoriza (1965) as a 'hot spot' nucleus for the outer nuclear ring and Laine et al. (1999) for the inner nuclear ring. Both rings are patchy. The inner one appears as a double ring of H II regions. The intense circumnuclear star formation makes a reliable determination of the bulge parameters in the 2D decomposition difficult.

NGC 5377: Carollo et al. (1998). This star-forming ring is dusty and wide, made up of tightly wound dust spirals.

NGC 5427: Buta & Crocker (1993). This circumnuclear feature is an ambiguous case between nuclear rings and nuclear pseudo-rings. Parts of it are missing in both north and south. This galaxy is unbarred, but its possible interaction with NGC 5426 may be the cause of the ring. Fuentes-Carrera et al. 2004, however, visually detected a bar in this galaxy. This bar is not detected by us because the peak in ellipticity is found in a radius of fast-changing PA, which is in contradiction with the bar detection criteria we have used.

NGC 5728: Buta & Crocker (1993). The ring is highly off-centred.

NGC 5806: first reference to this nuclear ring.

NGC 5812: called dusty disc by Tran et al. (2001) and nuclear ring by Comerón et al. (2008c). This is a dust ring in an elliptical galaxy, probably the same kind of structure as in NGC 3258 and NGC 4494, but here the ring is much smaller. The ring is so perfectly round that it can lead to the false conclusion that it results from the saturation of the camera. We tested this and confirmed that even the brightest pixel of the nucleus has a count value well below the saturation level.

NGC 5905: Friedli et al. (1996). They say that the ring is just outside a secondary bar. The ring is brighter in its north-east sector.

NGC 5945: Buta & Crocker (1993). The ring is on the edge of an Hα-emitting lens.

NGC 6503: Knapen et al. (2006). This galaxy has been classified as unbarred, but its high inclination makes it difficult to detect a bar. The ring is 1.2 kpc in radius, which is not exceptional, but the galaxy is quite small, making this one of biggest nuclear rings relative to $D_{\rm o}$.

NGC 6753: de Vaucoulers & Buta (1980) as an inner ring. This galaxy has no bar and a completely flat $Q_{\rm g}$ profile. The large size of the ring and the lack of a bar could give the impression it is an inner ring, but Laurikainen et al. (2004a) have found an oval with a size bigger than the ring.

NGC 6782: Buta & Crocker (1993).

NGC 6861: First reference to this dust nuclear ring located in a very early-type unbarred S0 galaxy. This galaxy has a companion, IC 4943, which may cause ILRs. The other possibility in such an early-type galaxy is to have a ring formation mechanism similar to that found in elliptical galaxies.

NGC 6951: Burbidge & Burbidge (1962) as a 'spiral ring'.

NGC 6958: Comerón et al. (2008c). A dust ring in an elliptical galaxy.

NGC 7049: Véron-Cetty & Véron (1988). A dust ring in a lenticular unbarred galaxy. The ring may be caused by x_2 orbits related to a possible oval distortion (Corwin et al. 1985). It also may have an origin similar to that of dust rings in elliptical galaxies (see e. g. NGC 3258).

NGC 7217: Pease (1917). This ring is in an unbarred galaxy with a completely flat non-axissymmetry profile. The ring could have been caused by the oval due to a minor merger with a dwarf gas-rich galaxy in a retrograde orbit that could also have caused the counter-rotating component of the galaxy (Sil'chenko & Moiseev 2006).

NGC 7469: Wilson et al. (1991). As NGC 4321 and NGC 5427, this is an intermediate case between rings and pseudo-rings.

NGC 7552: Forbes et al. (1994) in radio. We see the ring as a dust feature in optical images, but radio observations show that it is actually a star-forming ring.

NGC 7570: Knapen et al. (2006). Although NED and HyperLEDA state that it is a highly inclined SBa galaxy, an inspection of SDSS images shows that this galaxy has a nearly face-on outer ring.

NGC 7716: de Vaucouleurs & Buta (1980) as an inner ring. It probably is a nuclear ring because we found a bar that is bigger than the ring radius. The $Q_{\rm g}$ profile is rather flat and the peak caused by the bar is barely noticeable.

NGC 7742: Morgan (1958) as a 'brilliant ring'. This nuclear ring is double and is located in an unbarred galaxy with a completely flat $Q_{\rm g}$ profile. As in NGC 7217, the ring could have been caused by the oval due to a minor merger with a dwarf gas-rich galaxy in a retrograde orbit that could also have caused the counter-rotating component of the galaxy (Mazzuca et al. 2006).

NGC 7771: Smith et al. (1999). The eastern hole in the ring as seen in the Paα emission image is due to a dust lane. This galaxy is probably interacting with NGC 7770.

UGC 10445: First reference to this nuclear ring. This Sd galaxy is rather exceptional because very few late-type galaxies host nuclear rings. It is a barred galaxy in the NED and HyperLEDA catalogues but we have not been able to make ellipticity profiles or $Q_{\rm g}$ measurements because the galaxy is so faint that it is barely visible in 2MASS images.

3.12 Discussion

3.12.1 Nuclear ring lifetimes

In Section 3.8 we reported our result that $20 \pm 2\%$ of disc galaxies in the range of morphological types $-3 \leq T \leq 7$ host a star-forming nuclear ring. This confirms, using a much larger and more robustly selected sample, the result of Knapen (2005) who found $21\% \pm 5\%$ from a sample of 57 galaxies, with 12 nuclear rings. Two effects may have influenced the result by Knapen (2005): namely ground-based images were used so small nuclear rings were not included, and the definition of a nuclear ring was slightly different, so the former study included some rings (those in NGC 3184 and NGC 3344) that we consider to be inner rather than nuclear rings in the present study. These two effects go in opposite directions, which leads to the almost identical ring fractions in the two studies.

Two models for star-forming nuclear rings can be envisaged, each having different implications for the nuclear ring life-time. In the first, star-forming nuclear rings are short-lived starburst-like events, with a lifetime of a few Myr, while in the second, the rings would be long-lived, but undergoing several distinct episodes of enhanced massive star formation. The evidence is overwhelmingly in favour of the second of these two options, on the basis of observations (e.g., García-Barreto et al. 1991b; Knapen et al. 1995), simulations (Knapen et al. 1995; Heller & Shlosman 1996; Salo et al. 1999; Regan & Teuben 2003), and stellar population synthesis (Allard et al. 2006; Sarzi et al. 2007). In the case of the nuclear ring in NGC 4321, numerical modelling shows that the dynamical structure upholding the ring is stable (Knapen et al. 1995), the amount of molecular gas estimated to be present in the central region could be sustaining episodes of star formation for $\sim 6 \times 10^8$ years, even without inflow (e.g., Knapen et al. 1995), and stellar population modelling shows that short bursts of star formation have been going on periodically in this nuclear ring for about 500 Myr (Allard et al. 2006). The total lifetime for the nuclear ring in NGC 4321 is estimated to be at least a Gyr and quite plausibly more if we consider that there is a bar-driven inflow of gas into the circumnuclear region.

Making the safe assumption that nuclear rings are in general long-lived phenomena, we can use the derived fraction of occurrence of nuclear rings to place back-of-the-envelope limits on how long-lived they may be. To do this, we first assume that at a given moment in their existence all disc galaxies are able to create a stable star-forming nuclear ring, and that they have been able to do so for a Hubble time. Thus, the observed present fraction of around 20% of disc galaxies with nuclear rings would yield a lifetime of order $2-3$ Gyr. If we then consider that only galaxies from $z = 1$ have been able to create star-forming nuclear rings like those studied here, because the physical conditions may well have been different at earlier times, we arrive at an estimate for a typical nuclear ring lifetime of around 1.5 Gyr. This value increases if not all disc galaxies are able to create a nuclear ring, but the typical lifetimes deduced are compatible with observational and numerical results in the literature.

3.12.2 Are we missing small nuclear rings?

One of the main results of this Chapter is the relative size distribution of nuclear rings, which, among other things, seems to show that there is no separate population of very

small rings. The existence of such a population of UCNRs was speculated on by Comerón et al. (2008b) (see also Chapter 2), but our current systematic study using the highest spatial resolution imaging available for a large sample of galaxies shows that the size distribution of nuclear rings shows one peak, at $\log(D_{\rm r}/D_{\rm o}) = -1.3$, accompanied by a gradual rise at smaller sizes and a gradual fall at larger ones. The latter is not affected by observational biases, because even if large rings fell outside the field of view of our *HST* images such large rings would have been noticed in ground-based imaging and reported in the literature. Definition problems confusing inner with nuclear rings can in principle occur for large nuclear rings, but only in very few cases, as discussed in previous sections.

There are, however, two observational bias issues which could lead us to miss small nuclear rings. First, the presence of significant quantities of dust in the central regions of galaxies could hide nuclear rings of small absolute size, and, second, insufficient spatial resolution can make us miss angularly small nuclear rings. The first effect, that of dust extinction, is difficult to quantify and model. But it seems extremely unlikely that a significant population of galaxies exists in which large and uniformly distributed quantities of dust would completely hide a star-forming nuclear ring from view, even in the red Hα band (if the dust were distributed preferentially in a ring shape we would see it as such in our structure maps, and the galaxy might well be classified as having a dust ring). Even if this were the case, the quantities of dust needed (we estimate typical A_V of some 5 mag to hide a typical star-forming nuclear ring), over the scales, of a few tens of parsec, needed to cover up a hypothetical population of ultra-small rings would certainly show up in broad-band, colour index, and structure images of galaxies. There is no evidence for this effect to be present, and we conclude that dust is extremely unlikely to hide a population of very small nuclear rings.

We can, on the other hand, make estimates on the second effect identified, namely how many nuclear rings may be missing in our Atlas due to insufficient spatial resolution. The maximum of $\log(D_{\rm r}/D_{\rm o}) = -1.3$ (bottom panel in Fig. 3.4) in the relative ring size distribution is unaffected by resolution issues because even in the most distant galaxies in our sample this size corresponds to an angular resolution of 5 arcsec—such nuclear rings can easily be distinguished in our *HST* data. In fact, Laine et al. (2002) found the same maximum using ground-based data. However, the small-size tail in Laine et al. (2002) is shorter than the one found here (Fig. 3.4), which implies that they were indeed missing rings due to a lack of resolution.

For galaxies imaged by *HST* we estimate that the threshold above which we can find a nuclear ring is 2 arcsec in diameter (see Fig. 3.1 and Section 3.3.3), although this may be slightly smaller (about 1.5 arcsec) for galaxies imaged with an *HST* camera with small pixels and with a high signal-to-noise ratio. To check what the likelihood is that we have missed a significant population of very small nuclear rings, we started by considering each of the 347 disc galaxies with types $-3 \leq T \leq 7$ (the range of types in which star-forming nuclear rings are found) of the sample that we studied with *HST* images. For each galaxy we determine the relative size, $D_{\rm r}/D_{\rm o}$, of a nuclear ring that corresponds to a diameter of 2 arcsec, which is the detection threshold for *HST* images. We then count in how many galaxies a star-forming nuclear ring of a given relative size $D_{\rm r}/D_{\rm o}$ would be detectable, and in how many such a ring would be smaller than the detection limit. We then estimate the uncertainty in the number of star-forming nuclear rings counted in a given $D_{\rm r}/D_{\rm o}$ bin by assuming

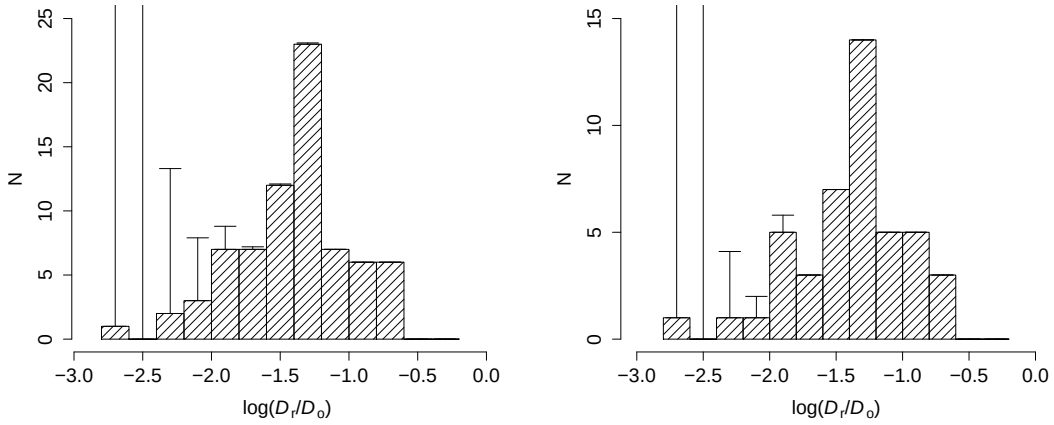

Figure 3.10: Experiment on the size distribution of star-forming nuclear rings found in the sample of 347 disk galaxies with types $-3 \leq T \leq 7$ for which we have *HST* imaging (leftpanel), and of the subset of those which are at a distance of less than 20 Mpc (right panel). The error bars show an estimate of the nuclear rings that may be missing from our Atlas due to a lack of spatial resolution in the imaging (see text for details).

a constant nuclear ring occurrence frequency, in other words, that the proportion of star-forming nuclear rings in galaxies where the ring is, in principle, detectable is the same as that in galaxies where they are not detectable. The result of this test has been represented in the top panel of Fig. 3.10, where the error bars indicate our calculated estimates of the numbers of undetected rings. This figure shows that the observed peak in relative nuclear ring size is true and that a possible second peak indicating a separate population of smaller nuclear rings can in principle be located at relative sizes $\log(D_{\rm ring}/D_{\rm o}) < -1.9$, corresponding to a radius of just under 200 pc for a galaxy of average size at 30 Mpc.

If we repeat the experiment described above but reducing our sample to the nearby galaxies, those at $D < 20$ Mpc, we find similar results (bottom panel of Fig. 3.10). In this test, we have a sample of 45 galaxies, and considering a sample of even closer galaxies is not feasible (selecting only those at $D < 15$ Mpc, for instance, would reduce the sample size to 21 which is insufficient to draw statistically valid conclusions). The maximum relative size of a possible second peak in the distribution, which would correspond to a population of nuclear rings small enough to be unresolved in our *HST* imaging, is now located at $\log(D_{\rm ring}/D_{\rm o}) < -2.1$. This corresponds to a maximum radius of 80 pc for a galaxy of average size at 20 Mpc. The conclusion from this series of tests are that the peak in the size distribution is real, although we cannot formally rule out the possibility of a second population of smaller nuclear rings, with a peak in radius smaller than 80 pc. The implications of this will be further discussed in the next section.

3.12.3 Are star-forming UCNRs normal nuclear rings?

The occurrence and properties of the smallest nuclear rings, with radii smaller than a few hundred parsec, have so far not been explored systematically. Such small nuclear rings were termed UCNRs by Comerón et al. (2008b) (see also Chapter 2), and defined as those

with a radius smaller than 200 pc. Although this 200 pc size limit is arbitrary, it is useful in allowing us to define small rings as a class, and subsequently study their properties. A handful of UCNRs were known from the literature, and the study by Comerón et al. (2008b) increased the known sample, to 16 UCNRs. In the present Atlas, the total number of nuclear rings smaller than 200 pc in radius has been increased to 28, which allows us to make more definite statements on their properties. In particular, it allows it to ascertain that UCNRs do not, in fact, form a separate class of nuclear rings, but instead merely constitute the small-size part of the overall nuclear ring size distribution.

The justification for defining UCNRs as such (in Comerón et al. 2008b and Chapter 2) was based in part on the theoretical possibility of the existence of a bimodal distribution of nuclear ring sizes. This would be related to the smaller class of rings (UCNRs, presumably) forming near nuclear Lindblad resonances (as described by e.g. Fukuda et al. 1998; Shlosman 1999; Maciejewski 2003). The size distribution of the nuclear rings in our Atlas, of which 28 (out of 113 rings in total) can be classed UCNR, however, is not bimodal (Fig. 3.4, and discussion on possible biases in Section 3.12.2) when the peak of a nuclear ring distribution related to nuclear Lindblad resonances is expected to peak around $\log(D_{\rm r}/D_{\rm o}) = -1.7$ (from ring expected size in Fukuda et al. 1998).

Considering their much smaller sample of three new and 13 literature UCNRs, Comerón et al. (2008b) suggested that UCNRs may be related to ILRs. The existence of an ILR at the small radius implied by the UCNRs would imply a shallow radial mass distribution in the central kpc of the host galaxy, which in turn would imply that UCNR host galaxies should have a small bulge. As a consequence, a deficiency of UCNRs in early-type galaxies would be observed. In contrast, we find here that star-forming UCNRs are, without preference, found in host galaxies ranging from morphological types S0 to Sd. which makes this possibility unlikely.

UCNRs may also be related to nuclear bars (Comerón et al. 2008b and Chapter 2), implying they would be found near the corotation radius of the nuclear bar. To dismiss this possibility for each individual UCNR we would need near-IR images at significantly higher resolution than the 2MASS images to perform detailed ellipticity fits of the inner parts of the galaxies. A literature search, however, indicates that of the 27 UCNR host galaxies in the Atlas, only NGC 4371 and NGC 5236 have been reported as having nuclear bars (by Wozniak et al. 1995; Elmegreen et al. 1998, respectively). For NGC 4371, Erwin & Sparke 1999 argued that the nuclear bar from Wozniak et al. (1995) was actually the outer nuclear ring reported in the present Chapter. We conclude that a direct and ubiquitous link between UCNRs and nuclear bars is unlikely.

The conclusion from the current work is that UCNRs merely constitute the low-radius tail of the nuclear ring size distribution and that there is no evidence that they are a manifestation of a different physical phenomenon. The AINUR images show that the morphology of the UCNRs is very similar to that of larger nuclear rings. In addition, the UCNRs do not populate preferential regions in any of the diagrams presented in this Chapter, which implies that the properties of these rings and of their host bars and galaxies are not systematically different from those of larger nuclear rings. We thus conclude that UCNRs are not a separate class of nuclear ring phenomenon.

3.12.4 What determines nuclear ring size?

Our analysis of nuclear ring sizes confirms that stronger bars host smaller nuclear rings, and that weaker bars can host larger nuclear rings, but also smaller ones. The maximum allowed nuclear ring radius is thus inversely proportional to the torque parameter $Q_{\rm g}$ (Fig. 3.5), while for a given $Q_{\rm g}$, the allowed range in nuclear ring radius spans from this maximum down to the smallest measured radius of a few tens of parsecs. This is seen particularly clearly when plotting relative nuclear ring size ($D_{\rm r}/D_{\rm o}$; Fig. 3.5a), but is also recognisable in absolute nuclear ring size (Fig. 3.5c). These results confirm those published by Knapen et al. (2002) and Knapen (2005), but with more nuclear rings due to the comprehensive nature of our new Atlas, and extending to much smaller nuclear ring sizes due to the use of archival *HST* imaging. Knapen (2005) noted that the findings are in agreement with predictions from numerical and theoretical work on the evolution of nuclear rings in a framework of resonances and orbit families in bars (Knapen et al. 1995; Heller & Shlosman 1996), something that we will expand on below.

Two scenarios can help explain why the complete parameter space below the limiting maximum ring radius at a given $Q_{\rm g}$ is populated by nuclear rings. The first of these is that nuclear rings do not necessarily form very close to the maximum radius, most probably related to the outer ILR as explained above. In terms of resonances and using a linear approximation, thus considering that the gravitational potential of the bar is axi-symmetric, it is quite intuitive that the nuclear ring will form close to the outer ILR. But although the linear approximation may be useful for weak bars, it is not correct in the presence of a strong bar (Sellwood & Wilkinson 1993). Avoiding the linear approximation, Shlosman (2001) finds that no nuclear ring is found close to an outer ILR; rather, rings are formed halfway between the two ILRs when both of these resonances are present. Some simulations show that in the case of a weak bar, the nuclear ring is created close to the outer ILR (Salo et al. 1999).

When considering a formation scenario related to the x_2 orbits in a barred potential, it is unclear where a nuclear ring will form. Although is it known that x_2 orbits are all resonant (Regan & Teuben 2003), and that they are located between a pair of ILRs (Contopoulos & Papayannopoulos 1980), there is no quantitative study of which of the orbits are populated with gas or stars (or even particles in theoretical studies). It is thus impossible to know whether the stars will at a given time be at the right position and velocity to be trapped by an x_2 orbit, and as a consequence, where exactly an x_2-orbit-induced nuclear ring may form. This could thus, presumably, happen anywhere between the ILRs, and it is unclear what physical parameters influence the exact radius of the nuclear ring.

In addition, the maximum possible radius is not a strictly defined quantity and there may well be some scatter due mainly to the size and mass of the bulge—changes in the central mass concentration can move the ILR position (see e.g. Hasan & Norman 1990; Thakur et al. 2009). The central mass concentration is not completely decoupled from the $Q_{\rm g}$ measurement, though, and a dense large bulge results in both the ILRs moving outwards and $Q_{\rm g}$ decreasing (with differences up to 50% in bar strength in the case of extremely elliptical bars).

The second scenario to explain the observations is an evolution of the nuclear ring size. It has been well established from numerical modelling that nuclear rings can shrink, mainly

due to the loss of angular momentum in shocks (Knapen et al. 1995; Heller & Shlosman 1996; Regan & Teuben 2003), possibly also by an effect called gas shepherding (Chang 2008; van de Ven & Chang 2009). In this scenario, nuclear rings would form near the maximum radius allowed by their host galaxy's $Q_{\rm g}$ and then evolve down to lower size, thus populating the $Q_{\rm g}$-size diagram. It is not entirely clear, however, whether the speed of this evolution can lead to the uniform spread in size shown in Fig. 3.5, and by how much rings can and do shrink. For instance, the nuclear rings in the paper of Regan & Teuben (2003) evolve so fast (compared to our nuclear ring timescales as discussed in Section 3.12.1) that all but the very youngest would be observed with very small sizes, and thus at the very lower part of our diagram, something which is clearly not the case. A slow evolution would cause rings to linger in the higher regions of the diagram, which is also not the observed case. On the other hand, and causing further uncertainty, Heller & Shlosman (1996) have described the dynamical effects of a gaseous nuclear ring on the stellar orbits in a barred potential, finding that the rings, especially if they are massive, can weaken the bars which host them. It is thus not clear whether time evolution of the nuclear rings leads to systematic changes in their position in the $D_{\rm r}/D_{\rm o}$ vs $Q_{\rm g}$ diagram.

Whatever the exact initial position is of a nuclear ring relative to the ILRs or the extent of the x_2 orbits in a barred galaxy, it is clear that the maximum nuclear ring size is limited by either the outer ILR, or by the extent of the x_2 orbits. Both of these will be related to the bar strength, with stronger bars leaving less physical space for the nuclear ring to form in, and thus hosting smaller rings. This effect has been shown in a number of simulations which aim to reproduce the formation of nuclear rings in different host potentials (e.g. Knapen et al. 1995; Heller & Shlosman 1996; Salo et al. 1999; Rautiainen & Salo 2000; Regan & Teuben 2003). This would lead to a maximum radius for nuclear rings, with stronger bars allowing only smaller rings, as seen in the edge of the distribution of nuclear rings in Fig.3.5.

In conclusion, the existence of a maximum allowed nuclear ring size can be explained by the fact that the radius of the largest x_2-orbits and the outer ILR are larger in weaker bars. The fact that all the space below this maximum is populated with nuclear rings suggests that nuclear rings can form at a variety of radii, limited primarily by the maximum identified above. An additional effect is that the nuclear rings, once formed, evolve with time to become smaller, although evolution of the ring may also stimulate an evolution of the host bar properties. A combination of these effects constitutes the most likely explanation for the observed distribution in Fig. 3.5.

3.12.5 Star-forming nuclear rings in unbarred galaxies: are they different?

We find that 18 not very inclined galaxies with a star-forming nuclear ring do not host a bar. This constitutes a fraction of $19 \pm 4\%$ of the disc galaxies in this sample ($-3 \leq T$), a fraction that is not very different from that of unbarred disc galaxies in the local Universe ($30\%-40\%$; Sandage 1961; de Vaucouleurs et al. 1991; Sellwood & Wilkinson 1993; Knapen et al. 2000; Marinova & Jogee 2007). However, all but three of these unbarred galaxies have evidence for some non-axisymmetry, which should be able to generate ILRs (strong spiral arms as suggested by simulations from Rautiainen & Salo in 2000, oval distortions, counter-rotating components, or interactions with close companions; see Section 3.10 for

details). One of the three remaining galaxies is a blue compact dwarf (NGC 3011), for which Gil de Paz et al. (2003) speculate an origin in terms of a starburst-driven shock interacting with the surrounding interstellar medium.

Nuclear rings in unbarred galaxies usually look indistinguishable from their counterparts in barred hosts, except those found in galaxies with counter-rotating components which tend to be more regular than average. For most of the unbarred host galaxies we could determine (low) $Q_{\rm g}$ values, but a few with strong arm patterns have $Q_{\rm g}$ values that are comparable to those determined for barred galaxies (e.g., $Q_{\rm g} = 0.416$ for NGC 5247, which is the most extreme case). Our sample of unbarred galaxies thus covers a wide range of $Q_{\rm g}$. None of the nuclear rings in unbarred disc galaxies is an outlier in the diagram relating relative ring size to Fig. 3.5, which strongly indicates that their formation mechanism is the same as, or strongly related, to that in barred galaxies, quite possibly involving non-axisymmetry-induced resonances.

In some cases, nuclear rings found in a galaxies without a bar, or with a weak oval, might indicate that a previously existing bar has been destroyed. Simulations have in fact shown that bars can be weakened and/or destroyed by a central mass concentration (e.g. Friedli & Benz 1993), by the transfer of angular momentum from the infalling gas to the stellar bar (e.g. Bournaud et al. 2005), by the buckling instability (e.g., Raha et al. 1991; Martínez-Valpuesta et al. 2004), or a combination of several factors (Berentzen et al. 2007). The mass of a growing nuclear ring itself can weaken the bar which hosts it by increasing the extent of the x_2 orbits and then depopulating the x_1 bar-supporting orbits (Heller & Shlosman 1996). As nuclear rings can last for around a Gyr without gas inflow (Knapen et al. 1995), the nuclear ring could continue to exist even after the bar destruction. We should note, however, that according to Shen & Sellwood (2004), only very centrally concentrated masses could efficiently destroy bars, which suggests that nuclear rings would not be very efficient as bars destructors.

For the few galaxies where no non-axisymmetry has been detected at all, there is the possibility that they have not been studied in enough detail and that further scrutiny may still reveal weak ovals, counter-rotating components or small companions that are disturbing the disc by close flybys, so a resonant origin can hardly be excluded for any of the nuclear rings in our sample.

It is worth noting that the non-axisymmetries in the unbarred galaxies discussed here have been discovered by studying them in above-average detail. If non-barred galaxies in general were subject to the same level of examination, it is likely that many of those would also be found to contain similar non-axisymmetries. Given the substantial number of non-barred nuclear ring hosts found in our Atlas (18, or $19 \pm 4\%$) we are thus led to the conclusion that unbarred nuclear ring hosts are not exceptional cases, as they have often been considered in the past, but instead rather normal. In fact, considering the similar fractions of unbarred galaxies among the nuclear ring host galaxies and among the general disc galaxy population, it is interesting to speculate whether the presence of a bar is at all necessary for the presence of a nuclear ring, especially when realising that nuclear ring hosts are subject to a more detailed search for bars than their counterparts in the wider galaxy population (see Section 3.4.3).

We postulate that nuclear rings are induced by non-axisymmetries in the gravitational potential of the host galaxy, in most but not all cases showing up in the form of a bar.

The fact that only very few disc galaxies will *not* have such a non-axisymmetry leads to the question of why certain galaxies have nuclear rings, whereas most do not. It is possible (as we discussed in Section 3.12.1 about nuclear ring lifetimes) that all discs at some stage form a nuclear ring, but it is also possible that specific combinations of physical parameters in the host potential and interstellar medium are prerequisite to the formation of a nuclear ring.

3.13 Summary

This Chapter presents the most extensive atlas of nuclear rings so far published. It includes 113 rings distributed in 107 galaxies within a distance of 80 Mpc. It includes all *bona fide* nuclear rings that appear in the literature, as well as seven new ones. A total of 17 of the 113 nuclear rings included have been discovered in the framework of the AINUR project (Comerón et al. 2008b and Chapter 2; Comerón et al. 2008c; and the present Chapter).

We investigate how the general structure of non-axisymmetries in galaxies is related to rings, mainly by increasing the statistics and improving the methodology as compared to previous works. Our study is mostly based on the *HST* archive from which we obtain colour index maps, structure maps, Hα, Paα, and/or UV images. Additional images have been collected from the literature or sent by astronomers who have observed those nuclear rings which have not been imaged by *HST*. We have used a complete set of deprojected H-band 2MASS images to perform ellipse fits and to derive the non-axisymmetric torque parameter $Q_{\rm g}$, which were used to study the length, the ellipticity, and the strength of galactic bars and other non-axisymmetric features.

Our main results can be summarized as follows:

- Star-forming nuclear rings are found in $\sim 20 \pm 2\%$ of disc galaxies in the range of morphological types $-3 \leq T \leq 7$. Under the assumption that all spiral galaxies at some stage host a nuclear ring, this number would imply an effective nuclear ring lifetime of 2−3 Gyr, in broad agreement with a large range of other observational and numerical studies.

- Dust nuclear rings are found in $\sim 6 \pm 2\%$ of elliptical galaxies.

- Star-forming rings are predominantly found in galaxies with morphological types ranging from S0 to Sc and dust nuclear rings are found in ellipticals and early lenticulars. Only one nuclear ring in an Sd-type galaxy was found, and none in later types, because the shallow mass distribution of such galaxies is unfavourable to the existence of ILRs, and thus nuclear rings.

- We establish that nuclear rings do not have a strong preference for barred host galaxies. Some $19 \pm 4\%$ of them (18 nuclear rings) occur in non-barred galaxies, though some evidence for non-axisymmetry in the potential can be discerned in most of these hosts. These non-axisymmetries can in principle cause resonances which can lead to ring formation, but we speculate that many non-barred galaxies outside our nuclear ring host sample will also host such non-axisymmetries, and that some additional mechanism is apparently needed to stimulate the formation of a nuclear ring.

- We explore relations between $Q_{\rm g}$ and the geometric parameters of the rings, namely their size relative to the galaxy disc, intrinsic ellipticity, and PA offset between the ring and the bar that hosts it (if present). There is an upper limit to the relative size of a nuclear ring, and this upper limit decreases uniformly with increasing $Q_{\rm g}$. In barred galaxies, this trend can be described as stronger bars hosting smaller rings. Any relative size below the upper limit can and does occur in galaxies. This behaviour is exhibited by both barred and unbarred galaxies, and can be explained in a framework of nuclear rings forming between a set of dynamical resonances. Evolution with time, causing rings to shrink, may play an additional role.

- Nuclear rings are not affected by *local* non-axisymmetric torques, which we measure by the amplitude of the torque parameter at the radius of the nuclear ring (the maximum amplitude of this parameter is $Q_{\rm g}$, and this maximum always occurs outside the nuclear ring). This confirms that the nuclear ring is affected by the non-axisymmetries on larger scales than the ring itself.

- There is a weak correlation between the length and the strength of the bar among the barred host galaxies of the nuclear rings in our Atlas, where bar strength is measured through the non-axisymmetric gravitational torque parameter $Q_{\rm g}$. The bar length relative to the host galaxy disc scale length correlates somewhat better with $Q_{\rm g}$. These results confirm those by Elmegreen et al. (2007) that bars have a specific range of lengths for a given strength when they form, but then evolve into longer bars.

- Nuclear rings in barred galaxies are limited in size to one quarter of the length of the bar.

- There is no strong evidence of any preferred PA offset between rings and bars.

- There is some evidence that the maximum possible ellipticity for a nuclear ring is limited by the bar ellipticity. This conclusion, however, depends on the accuracy of the deprojection of images of strongly barred galaxies, and must thus be taken with caution.

- We have found no correlation between the bulge shape and the properties of nuclear rings.

- We cannot confirm the relation stated in the literature between the presence of nuclear activity and that of nuclear rings.

- Star-forming UCNRs most probably constitute the low-size tail of the nuclear ring size distribution. We have no evidence for the existence of a separate population of such ultra-compact ($< 200\,$pc radius) rings, although the spatial resolution of the *HST* images employed here does not allow us to exclude with certainty the existence of a population of much smaller rings, with radii smaller than $80\,$pc.

- Star-forming nuclear rings are closely related to ILRs and, with very few possible exceptions indeed, are related to dynamical resonances in their host galaxies. Given that they occur rather commonly in galaxies and that they constitute bright, thus

well observable, tracers, this study thus confirms the value of nuclear rings, alongside inner and outer rings, in the observational study of the dynamics and evolution of galaxies.

4

On the curvature of dust lanes in galactic bars

4.1 Introduction

Dust lanes in galactic bars have been observed in nearby galaxies for a long time. Photographic surveys from the beginning of the XX$^{\rm th}$ century already allowed observation of these features. Pease (1917) describes the prominent and nearly straight dust lanes in NGC 5383 as a 'dark streak'. The same paper presents images of NGC 1068 in which a dust lane is clearly visible. The dusty nature of these features was identified at a much later stage. Sandage (1961) writes in his atlas that "one of the major characteristics of the SBb(s) [galaxies] is the presence of two dust lanes leaving the nucleus, one on each side of the bar and extending into the spiral arms".

Dust lanes have been recognised as related to shocks in the gas flow in barred galaxies since Prendergast (1962). Such shocks are usually found in the leading edge of the bar, roughly parallel to its major axis. The location of these shocks also corresponds to the location of areas of high shear, which prevents star formation (Athanassoula 1992; see Zurita et al. 2004 for a graphic illustration in the case of NGC 1530). Simulations show that the dust lanes are nearly straight and near the centre of the bar when the galaxy has no inner Lindblad resonance (ILR), which is known to be quite a rare occurrence. ILRs cause the dust lanes to be offset from the bar major axis, and to be curved with the concavity pointing to the bar major axis (Athanassoula 1992). Simulations by Patsis & Athanassoula (2000) show that the higher the gas sound speed, the smaller is the offset between the dust lane and the major axis of the bar. No dust lanes are expected in nuclear bars (Shlosman & Heller 2002).

Athanassoula (1992) predicted from simulations that dust lanes would have a greater curvature in weaker bars and that dust lanes would be nearly straight in strong bars. This effect has been empirically verified using a set of images of nine barred spiral galaxies by Knapen et al. (2002). The aim of the present Chapter is to improve the statistics compared to the latter study, and to test definitively the prediction from Athanassoula (1992). Because dust lanes can be observed so easily they offer a fundamental handle on

the underlying dynamics of the galaxy and the bar, yet they have hardly been studied observationally. A basic further aim of the present work is thus to explore in a statistical fashion the dependence of dust lane shape on the dynamical properties of the galaxy which hosts them.

4.2 Sample selection and bar strength data

We have selected all galaxies with a published non-axisymmetric maximum torque parameter for the bar, $Q_{\rm b}$, and a published radius at which $Q_{\rm b}$ has been measured, $r(Q_{\rm b})$. Its definition and the values for 266 different galaxies can be found in Laurikainen & Salo (2002); Block et al. (2004), Laurikainen el al. (2004a), Laurikainen et al. (2006), and Comerón et al. (2010) (see also Chapter 3). Some of these authors publish $Q_{\rm g}$, which includes the non-axisymmetries not related to the bars (but to spiral arms). However, $Q_{\rm g}$ and $Q_{\rm b}$ take very similar values in barred galaxies and can be interchanged for our purposes. In several cases $Q_{\rm b}$ has been reported in more than one paper, in which cases we have used the most recent measurement (except for those in Comerón et al. 2010 which are based on shallower images). For NGC 1068 we preferred the value from Comerón et al. (2010) to that from Laurikainen et al. (2004a) because in the latter the authors measure $Q_{\rm b}$ of the nuclear bar, whereas the dust lanes are hosted by the large bar.

There are small variations in the techniques used to determine $Q_{\rm b}$ in the various articles quoted above but we have checked that the $Q_{\rm b}$ determinations are consistent within the error bars. These technical differences cause some scatter in the $Q_{\rm b}$ measurements. The most important source of scatter is the use of different vertical scaleheights when measuring $Q_{\rm b}$ and the large scatter in the observed vertical scaleheight within one single Hubble type. For a detailed discussion see Laurikainen & Salo (2002), where the authors consider that the uncertainties in both the orientation parameters and in the disc scaleheight determination may cause an error of up to 10-15% in $Q_{\rm b}$. As we are mixing data from several sources we take a slightly higher estimate for the overall uncertainty in our $Q_{\rm b}$ values of 20%.

The 266 galaxies with a Q_b determination in the literature have morphological types spanning from S0/a to Sd. For those galaxies in the Sloan Digital Sky Survey (SDSS) DR7 (Abazajian et al. 2009) we examined single-band (g and i) and color-index ($g-i$) images to select galaxies presenting clear dust lanes. For all other galaxies we examined all optical images available in the NASA-IPAC Extragalactic Database (NED). Out of the original 266 galaxies 55 have been found to host dust lanes. This is a lower limit to the true proportion of recognizable bar dust lanes in disc galaxies because for several galaxies only Digital Sky Survey (DSS) images are available, on which bars are often saturated. The final sample for our dust lane study is thus of 55 galaxies. Table 4.1 lists these galaxies, their $Q_{\rm b}$, and its source.

4.3 Measurement of the dust lane curvature

The curvature of the dust lanes was determined directly from the SDSS and NED images using the procedure described by Knapen et al. (2002). We first deprojected the galaxy images using the deprojection parameters listed in Table 4.1. We then measured the change in the angle of the tangent to the dust lane in the range in which its curvature is constant,

Table 4.1: Properties of the host galaxies and dust lanes in our sample.

Galaxy	Dist. (Mpc)	Disc PA (°)	$\epsilon_{\rm d}$	$\Delta\alpha$ (°)	$Q_{\rm b}$	$r(Q_{\rm b})$ (″)	Source
(1)	(2)	(3)	(4)	(5)	(6)	(7)	(8)
N150	20.2	107.6	0.502	10	0.459	26.7	L04
N289	20.7	141.5	0.211	37	0.212	12.8	L04
N613	18.7	121.6	0.228	0	0.401	68.4	L04
N1068	15.3	70.0	0.150	111	0.094	55.0	C10
N1084	18.5	52.7	0.247	35	0.212	35.5	L04
N1097	15.2	130.0	0.320	60	0.279	75.0	L04
N1300	20.2	150.0	0.240	63	0.537	68.4	L04
N1365	20.1	32.0	0.450	64	0.490	164.0	Bl04
N1433	11.6	–	0.000	31	0.430	69.0	Bl04
N1512	9.5	83.0	0.400	27	0.366	79.0	C10
N1530	38.9	–	0.000	4	0.730	49.0	Bl04
N1566	17.4	36.0	0.190	89	0.235	71.0	C10
N1672	15.0	–	0.000	60	0.349	59.0	C10
N2566	21.0	115.8	0.266	3	0.316	54.4	L04
N2964	20.6	96.8	0.434	20	0.310	22.5	L04
N3166	18.8	82.5	0.414	25	0.107	31.5	L04
N3184	14.5	135.0	0.050	95	0.160	45.0	L02
N3351	11.1	9.9	0.400	15	0.225	63.0	C10
N3359	18.0	170.0	0.330	2	0.460	11.0	L02
N3504	23.8	–	0.000	67	0.288	28.5	L04
N3507	15.2	91.9	0.056	11	0.176	19.5	L04
N3583	33.6	119.2	0.256	42	0.246	16.5	L04
N3810	15.2	21.4	0.320	17	0.128	16.5	L04
N3887	16.3	4.6	0.290	51	0.207	31.5	L04
N4123	19.5	125.7	0.323	11	0.677	37.5	L04
N4212	16.8	75.7	0.337	70	0.234	28.5	L04
N4274	15.6	102.0	0.500	36	0.310	45.0	L02
N4303	23.1	146.9	0.139	65	0.259	40.5	L04
N4314	16.4	61.8	0.041	74	0.442	52.5	L04
N4321	24.0	30.0	0.150	73	0.183	61.0	L04
N4457	13.4	80.8	0.117	37	0.089	31.5	L04
N4548	16.4	153.2	0.256	59	0.344	55.5	L04
N4579	23.0	94.8	0.217	50	0.197	34.5	L04
N4593	35.3	98.1	0.258	28	0.309	45.5	L04
N4651	13.0	73.1	0.388	29	0.120	16.5	L04
N4691	16.3	41.2	0.158	11	0.504	13.5	L04
N5020	49.5	84.3	0.110	5	0.365	31.0	C10
N5236	4.5	–	0.000	41	0.294	81.0	C10
N5248	17.9	104.0	0.091	67	0.269	76.5	L04

Table 4.1: (continued).

Galaxy	Dist. (Mpc)	Disc PA (°)	$\epsilon_{\rm d}$	$\Delta\alpha$ (°)	$Q_{\rm b}$	$r(Q_{\rm b})$ (″)	Source
(1)	(2)	(3)	(4)	(5)	(6)	(7)	(8)
N5377	29.2	37.6	0.540	5	0.164	47.0	C10
N5457	6.9	–	0.000	51	0.225	73.0	L04
N5643	14.8	131.2	0.102	12	0.415	33.6	L04
N5728	39.7	14.5	0.410	27	0.350	57.0	C10
N5806	20.5	174.3	0.480	55	0.140	41.0	C10
N5905	52.4	135.0	0.340	11	0.352	23.0	C10
N5921	22.6	130.9	0.295	8	0.416	46.5	L04
N5945	81.3	115.0	0.070	14	0.232	23.0	C10
N6300	12.8	104.8	0.307	59	0.187	33.6	L04
N6782	52.5	34.9	0.102	43	0.165	24.4	L04
N6907	44.4	82.6	0.124	34	0.329	29.0	L04
N6951	24.4	170.0	0.170	9	0.340	43.0	Bl04
N7479	34.9	25.7	0.359	24	0.696	43.5	L04
N7552	20.2	169.9	0.127	14	0.395	45.2	L04
N7582	20.2	152.9	0.529	1	0.436	56.8	L04
N7723	25.2	38.5	0.307	1	0.349	16.5	L04

Notes: galaxy ID (col. 1), distance to the galaxy in Mpc from Comerón et al. 2010 and HyperLEDA (col. 2), galaxy disc PA (col. 3) and disc ellipticity from the literature (col. 4), dust lane curvature as defined in Section 4.3 (col. 5), $Q_{\rm b}$ (col. 6), $r(Q_{\rm b})$ (col. 7), and literature source for the galaxy disc PA, ellipticity, $Q_{\rm b}$, and $r(Q_{\rm b})$ (col. 8). L02: Laurikainen & Salo (2002), Bl04: Block et al. (2004), L04: Laurikainen et al. (2004a), and C10: Comerón et al. (2010).

thus often ignoring the inner parts of the dust lanes where x_2 orbits in the circumnuclear region influence their shape and enhance the curvature (Athanassoula 1992). We also often ignored the outermost parts of the dust lanes, where they are closer to the corotation radius. The measure of dust lane curvature, $\Delta\alpha$, as used here is arrived at by multiplying the change in the tangent angle defined above by the only measure of the bar length that can be reliably derived in both observed and modelled bars, namely the radius at which the torque is maximal ($r(Q_{\rm b})$). $\Delta\alpha$ is thus a quantity which takes into account the size of the host bar. The results are listed in Table 4.1.

The uncertainty in the dust lane curvature is hard to quantify. The error due to galaxy deprojection is most probably not very large ($< 10°$) because in most cases dust lanes are intrinsically rather straight, and thus less sensitive to deprojection than a more strongly curved feature might be. The uncertainty in determining the tangent to the dust lane is larger because the dust lanes are often not too well defined, and sometimes rather fluffy. By repeating our measurements for the same dust lanes, but using slightly different tangent points, we found that the results agree to within a few degrees per kpc. We thus adopt a conservative estimate of uncertainty in the dust lane curvature of $\delta\Delta\alpha \sim 15°$.

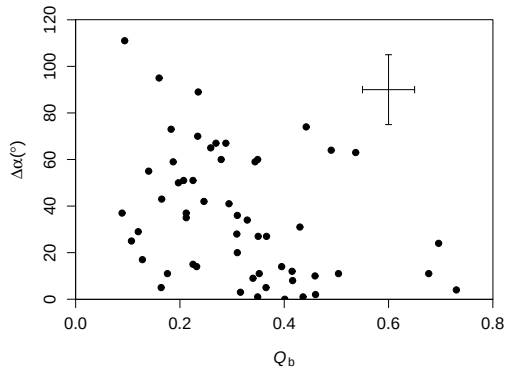

Figure 4.1: Dust lane curvature related to Q_b.

4.4 Results

The relation between the bar strength as described by Q_b, and the dust lane curvature, $\Delta\alpha$, is shown in Fig. 4.1. The plot has the axes flipped with respect to those used in Athanassoula (1992) and Knapen et al. (2002). The most striking feature in the plot is the clear division between a populated lower left and an unpopulated upper right part, separated by a straight and well-defined envelope. This implies that strong bars cannot have curved dust lanes, and that galaxies with smaller bar strengths can have progressively more curved dust lanes. A small unpopulated area appears in the extreme lower left, at the location of galaxies with straight dust lanes and small Q_b. If on the vertical axis of the plot we use the change in the angle of the tangent to the dust lane (in °/kpc) instead of the dust lane curvature the results remain essentially the same.

A similar diagram was presented by Knapen et al. (2002), but they only plotted nine data points. In their figure, the points appear roughly aligned, but in our new version, and thanks to the much larger number of data points, we can see how the relationship has a spread much larger than can be expected from the error bars. It is thus reasonable to suppose that although Q_b limits the allowed dust lane curvature, it does not prescribe it. Other factors must determine the degree of curvature, especially for the weaker bars, and we used numerical simulations to explore which factors might contribute.

4.5 Simulating dust lanes in barred galaxies

We ran a set of 238 3D numerical simulations and studied the dynamical response of the gas within a barred potential using the code FTM 4.4 (updated version) from Heller & Shlosman (1994). In each individual simulation, we used 10^5 isothermal, non-self-gravitating, collisional gas particles. We reproduced the potential of barred galaxies by means of a Miyamoto-Nagai disc, bulge, and halo. The bar is reproduced by a Ferrers potential (Ferrers 1877), which is introduced gradually, in one rotation, in a way that conserves the mass.

We use different parameters for the bar ellipticity, mass, and pattern speed, and for the bulge mass ratio ($B/B+D$) in order to cover the complete range of galaxies in our set of

observations presenting dust lanes.

The Miyamoto-Nagai potential is described by the equation:

$$\Phi_{\rm M}(R,z) = -\frac{GM}{\sqrt{R^2 + (a + \sqrt{z^2 + b^2})^2}} \tag{4.1}$$

For the disc we use $M_{\rm d} = 5 \times 10^{10}\, M_{\odot}$, $a = 5.0$ kpc, and $b = 0.5$ kpc. For the bulge we use $b = 0.05$ varying $B/B+D$ from 0.1 to 0.5 in steps of 0.1 by increasing the bulge mass. For the halo we use $M_{\rm h} = 10^{11}\, M_{\odot}$, $a = 0.0$ kpc, and $b = 10$ kpc.

The Ferrers potential is described by

$$\rho = \frac{15}{8}\frac{M_{\rm b}}{\pi abc}(1 - m^2) \;\text{ for }\; m \leq 1, \rho = 0 \;\text{ for }\; m > 1 \tag{4.2}$$

where $m^2 = \frac{x^2}{a^2} + \frac{y^2}{b^2} + \frac{z^2}{c^2}$, and a is the major, b the minor, and c the vertical axis, taken here in such a way that a/b takes the values $1.5, 2.0, 2.5, 3.0, 3.5, 4.0$, and 4.5 accounting for the ellipticity of the bar. We use $a = 6\,$kpc, $c = b/4$ and two different values for the bar mass: $M_{\rm b} = 5.3 \times 10^{10}\, M_{\odot}$ and $M_{\rm b} = 8 \times 10^{10}\, M_{\odot}$.

The pattern speed is chosen so that in a linear approximation the corotation radius is always greater than the length of the bar. In our set of simulations this means 10, 20, 30, and 40 $\rm km\,sec^{-1}\,kpc^{-1}$.

As dust lanes are found in areas with gas shocks (Prendergast 1962), we inferred dust lane curvature in the simulated galaxies by measuring the curvature of gas density enhancements using the same methodology as used for the dust lanes in real galaxies. This measurement was applied after two bar rotations. Well defined measureable dust lanes appeared in 88 out of 238 simulations. The results can be seen in the left panel of Fig. 4.2, where the symbol coding indicates the ratio between the corotation radius, $r_{\rm CR}$, and the bar radius, $r_{\rm b}$. For convenience, we define in the context of this Chapter that for $r_{\rm CR} < 3.0\, r_{\rm b}$ we have a 'normal' bar and for $3.0\, r_{\rm b} < r_{\rm CR}$ we have a 'very slow' bar (more details on this bar classification can be found in Debattista & Sellwood 2000). $r_{\rm CR}$ was always measured using a linear approximation and $r_{\rm b} = 6\,$kpc was fixed in the simulations. 'Very slow' bars (two out of 88 in the simulations which present dust lanes) are rare in nature (just one is found in the compilation by Rautiainen et al. 2008) and thus are not included in the discussion in the next section because they have a non-standard behaviour.

4.6 Discussion

The observational part of our study confirms that the degree of curvature of dust lanes decreases with increasing bar strength, i.e. stronger bars have straighter dust lanes (Fig. 4.1). This was predicted by Athanassoula (1992) and confirmed in a preliminary way from observations of nine galaxies by Knapen et al. (2002). Here, we find that the relation, in fact, outlines an upper limit to the dust lane curvature allowed for a particular value of $Q_{\rm b}$, in the sense that a bar with low $Q_{\rm b}$ can have either straight or curved dust lanes, but bars with high $Q_{\rm b}$ can only have straight dust lanes.

We performed a series of numerical simulations to explore which parameters may be at the origin of the spread of the data points in the left panel of Fig. 4.2. We tested

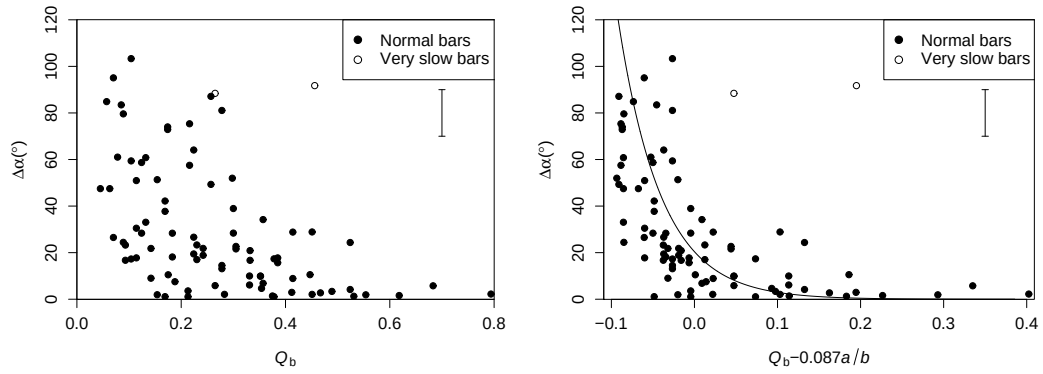

Figure 4.2: Left panel: dust lane curvature related to Q_b in the simulated galaxies. Filled dots stand for 'normal' bars ($r_\mathrm{CR} < 3.0\,r_\mathrm{b}$) and empty dots stand for 'very slow' bars ($r_\mathrm{CR} > 3.0\,r_\mathrm{b}$). Right panel: dust lane curvature related to a combination of Q_b and a/b which minimizes the spread. The line is the best fit to the 'normal' bar data. There is no error bar on Q because it has been calculated from the potentials used in simulations.

whether this spread is caused by different bulge masses, different galaxy masses inside the corotation, and different bar pattern speeds. We find no effect of these parameters on the spread except for the bar pattern speed: the spread for slow bars is higher but this effect is quite small. We found, however, that the data can be organized in a plot with much smaller spread by fitting the logarithm of the dust lane curvature to a linear combination of Q_b and a/b which are parameters that depend only on bar properties. The best fit is

$$Q_\mathrm{b} - 0.087\,a/b = (0.156 \pm 0.020) - (0.119 \pm 0.015)\log_{10}\Delta\alpha \tag{4.3}$$

and it is represented in the right panel of Fig. 4.2. The correlation coefficient of the fit is $\rho = 0.66$, better than when just fitting Q_b and $\log_{10}\Delta\alpha$ ($\rho = 0.58$). This fit shows that Q_b overestimates the effect of the bar ellipticity on the dust lane curvature.

The correlation between the linear combination of Q_b and a/b and the logarithm of $\Delta\alpha$ cannot yet be easily tested with observational data. Measuring the ellipticity of the bar requires an accurate decomposition of high quality images of the galaxy into its different components. Further work is needed in order to obtain these decompositions and refine the comparison with the simulations.

4.7 Conclusions

Using 55 galaxies with published measurements of the bar strength indicator Q_b, and for which we could obtain accurate measurements of the dust lane curvature, $\Delta\alpha$, we confirm the theoretical prediction made by Athanassoula (1992) that the dust lane curvature anticorrelates with the bar strength. Strong bars thus host straight dust lanes, while weaker bars can host more curved dust lanes. We do find that the anticorrelation has a large spread, but from a set of 238 numerical simulations of barred galaxies we show that this spread can be greatly reduced by using an appropriate linear combination of bar parameters (Q_b and the axis ratio a/b).

5

Discovery of a faint thick disc in the galaxy NGC 4244 from S^{4}G imaging

5.1 Introduction

Thick discs are detected as an excess of flux at some distance from the mid-plane, typically at a few thin disc scaleheights, in edge-on and very inclined galaxies. They usually have exponential profiles with a larger scaleheight than 'canonical' or thin discs. They were defined by Burstein (1979) and then found in the Milky Way (Gilmore & Reid 1983) and in basically all kinds of disc galaxies (see the introduction of Yoachim and Dalcanton 2008 and references therein). Several theories of thick disc formation have been proposed, but recent studies suggest that thick discs are formed through mechanisms of internal secular evolution, namely disc heating by gravitational instabilities (Bournaud et al. 2007) and/or stellar scattering by encounters with features such as dark matter subhaloes, spiral arms or giant molecular clouds (Hayashi & Chiba 2006; Haywood 2008; Schönrich & Binney 2009; Bournaud et al. 2009). The formation of thick discs through minor mergers is, in general, discarded by Bournaud et al. (2009) because it would cause thick disc flares much larger than those usually observed. Thus, every old enough (meaning by old that it has existed for a significant fraction of a Hubble time) undisturbed disc galaxy should have traces of a thick disc.

However, this picture could be challenged if a local undisturbed disc galaxy was found not to have a thick disc. A search in the literature yields a candidate, NGC 4244, which has been claimed either to be a doubtful case (Yoachim & Dalcanton 2006), or not to have a thick disc at all (Fry et al. 1999). NGC 4244 is a highly inclined undisturbed Scd galaxy located 4.4 Mpc away (Seth et al. 2005a). At that distance one arcsecond is equivalent to roughly 21 pc in linear scale. NGC 4244 is nearly bulgeless, except for a compact and bright star cluster (bulge-to-disc ratio equal to 0.03 according to Fry et al. 1999). NGC 4244 could be weakly interacting with NGC 4214, which has a similar recession speed and is found at a projected distance of 120 kpc from NGC 4244.

Several studies have been made in order to find the structural components of NGC 4244. Fry et al. (1999) detected only a thin disc. Seth et al. (2005b) found that the scaleheights

of the older stellar components are larger than those of the younger components, which could be an indicator of the existence of a thick disc (however, the difference in scaleheights between the main sequence population and the RGB population is smaller than in all the other galaxies studied in their paper). Tikhonov & Galazutdinova (2005) claimed to have discovered an extended halo in NGC 4244. Seth et al. (2007) found a faint halo component 2.5 kpc above the mid plane at the position of the minor axis.

Hoopes et al. (1999) found that, unlike other edge-on galaxies, NGC 4244 has its ionized gas concentrated in the thin disc. Strickland et al. (2004) found no evidence for a radio, UV, or X-ray emitting halo.

To sum up, previous studies on NGC 4244 show little to no emission at any band outside its well-known thin disc, which goes against the prediction that every old enough undisturbed disc galaxy must have a thick disc.

In this Chapter we present results of a study of NGC 4244 based on the *Spitzer Survey of Stellar Structure in Galaxies* (S^{4}G) 3.6μm images in order to ascertain whether this galaxy has a thick disc. For this purpose we have fitted this galaxy using GALFIT (version 3.0; Peng et al. 2002; Peng et al. 2010) and we have produced luminosity profiles of NGC 4244 at different galactocentric radii.

5.2 Processing of the S^{4}G 3.6μm image of NGC 4244

The *Spitzer Survey of Stellar Structure in Galaxies* (S^{4}G, Sheth et al. 2010) is a survey using the 3.6 μm and 4.5 μm filters of the *Spitzer Space Telescope* Infrared Array Camera (IRAC, Fazio et al. 2004) with the aim of studying the stellar mass distribution in a sample 2331 galaxies which meet the following selection criteria in the HyperLEDA database:

- $V_{\rm radio} < 3000 {\rm km\,s^{-1}}$, which roughly corresponds to a distance $D < 40\,{\rm Mpc}$ using a Hubble constant $H_0 = 70\,{\rm km\,s^{-1}\,Mpc^{-1}}$. This criterion limits the S^{4}G sample to galaxies with derived radio radial velocities in HyperLEDA.
- Integrated blue magnitude $m_{\rm B} < 15.5$.
- Blue light isophotal angular diameter $D_{25} > 1.0'$.
- Galactic latitude $|b| > 30^\circ$ in order to minimize the effect of light contribution from the Milky Way.

All the galaxies in the S^{4}G are mapped out to at least $r = 1.5D_{25}$ with 240 s exposures in the 3.6 μm and 4.5 μm filters. S^{4}G images have a depth of around $\mu_{3.6\mu{\rm m}} = 26.5\,{\rm mag\,arcsec^{-1}}$ which is equivalent to $\mu_{\rm B} = 31.0\,{\rm mag\,arcsec^{-1}}$

The 3.6μm image of NGC 4244 we have used for our study has been processed by the S^{4}G pipelines, resulting in a mosaicked flat-fielded image and in a mask of foreground stars, background galaxies and bad pixels (Sheth et al. 2010). However, as we aim to reach the faintest possible surface brightness level, we have manually refined the mask and we have closely examined the background. We find a systematic background gradient (seen in the top-left panel in Fig. 5.1), which is likely to be caused by zodiacal light. We have modelled this gradient using a third order polynomial fit to all unmasked pixels at a distance of 250

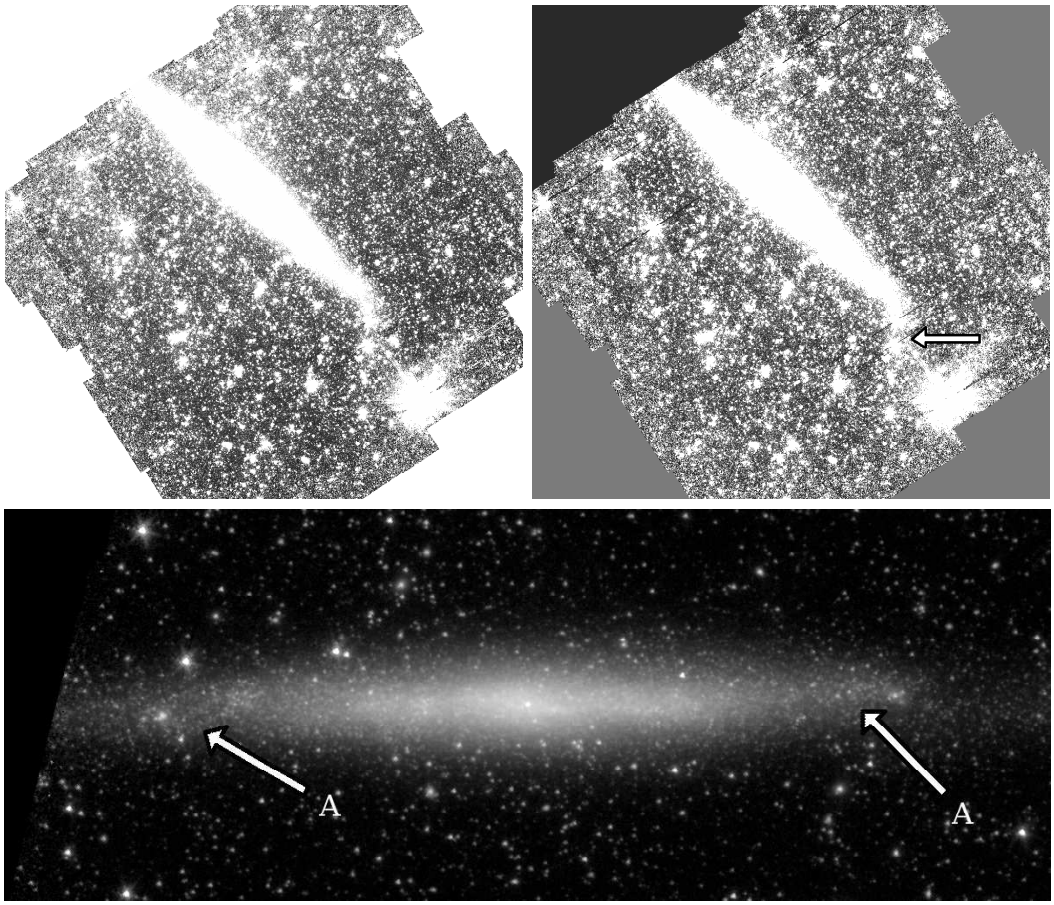

Figure 5.1: Top panels: the 3.6μm S^{4}G image of NGC 4244 before (left) and after (right) removing the gradient in the background. We have used the same histogram equalization display for both images. North is up and East is left. Lower panel: galaxy rotated in such a way that the galaxy plane is horizontal. In this frame North is roughly located at the top-left and East at the bottom-left. The image is 15′ or 19.2 kpc in length. The display is logarithmic. The arrow in the top-right panel indicates a light streak caused by the merger of the light of three foreground stars. The arrows in the bottom panel indicate the location were there is evidence of the spiral structure of the galaxy.

pixels (187.5″) or more from the galaxy mid-plane. In this procedure there is no risk of contamination by any component of the galaxy, because we are going farther than any trace of extended component found by Tikhonov & Galazutdinova (2005) using the RGB star-counting method. We then subtracted the modelled background from the original image (top-right panel in Fig. 5.1).

We rotated the image 43.6° counterclock-wise in order to place the mid-plane of the galaxy horizontally (lower panel in Fig. 5.1). The rotation angle has been calculated finding the mid-plane for all galactocentric distances smaller than $r < 350$ arcsec. The rotation angle value has changes smaller than one degree when reducing the galactocentric range at which it is measured to a half in order to avoid possible disc irregularities at high galactocentric radii. This rotation angle value is slightly different from the 42° used by

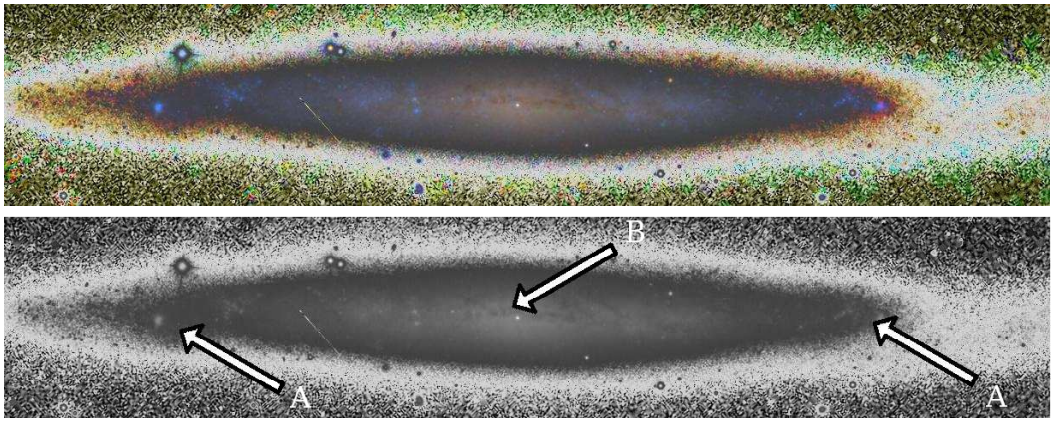

Figure 5.2: SDSS DR7 NGC 4244 image oriented identically and at the same scale as in the bottom panel of Fig. 5.1. The top panel contains a colour version of the image and the bottom panel has a black and white version of it. In the colour image, the blue knots denote star formation and the reddish colours dusty areas. In the bottom panel, the 'A' arrows indicate the location were there is evidence of the spiral structure of the galaxy. The 'B' arrow indicates a dust lane parallel to the mid-plane of the galaxy and slightly above it.

Olling (1996) and Fry et al. (1999). Once the galaxy is rotated, we can define as the *top* part of the galaxy the area extending above its mid-plane and as the *bottom* part of the galaxy the region below it. This definition is arbitrary, but it will be useful because the galaxy is not symmetric with respect to its mid-plane.

The outer half of the bottom panel of Fig. 5.1 and the outer half of Fig. 5.2 (SDSS DR7 image; Abazajian et al. 2009), shows (at galactocentric radii bigger than half the distance between the nuclear cluster and the edge of the image; indicated by the arrow labeled with letter 'A'), possible evidence for the presence of a warp-like feature. In the top images of Fig. 5.1 (the gray-scale distribution is based on a histogram equalization algorithm), the possible 'warp' may be confused with a light streak which goes downwards from the bottom-right extreme of NGC 4244 (opposite to the warp-like feature and indicated by an arrow). This streak is caused by three relatively bright aligned stars whose PSFs merge in the histogram display. The SDSS image (Fig. 5.2) seems to indicate that what could be interpreted as a warp, could also be interpreted as spiral arm structure in this nearly edge-on galaxy. We will from now on favour this interpretation primarily because if it were a warp it would bend in a direction opposite to the H I warp (Olling 1996), and we consider the H I imaging to be less sensitive to disc features in a non-interacting galaxy. Another reason for considering the warp-like feature as spiral arms will be presented in Section 5.3.3 when talking about the residuals after GALFIT modelling.

The warp-like distortion we find coincides with that found in the *R*-band by Fry et al. (1999). The latter authors state that the optical 'warp' they found is coincident with that of Olling (1996), but that was an incorrect statement caused by using an image flipped along the mid-plane of NGC 4244. The warp found in H I by Olling (1996) starts at a galactocentric radius of $r \sim 10'$, which would place it at bigger galactocentric radii than shown in the image in the bottom panel of Fig. 5.1. At these galactocentric radii there is almost no stellar emission.

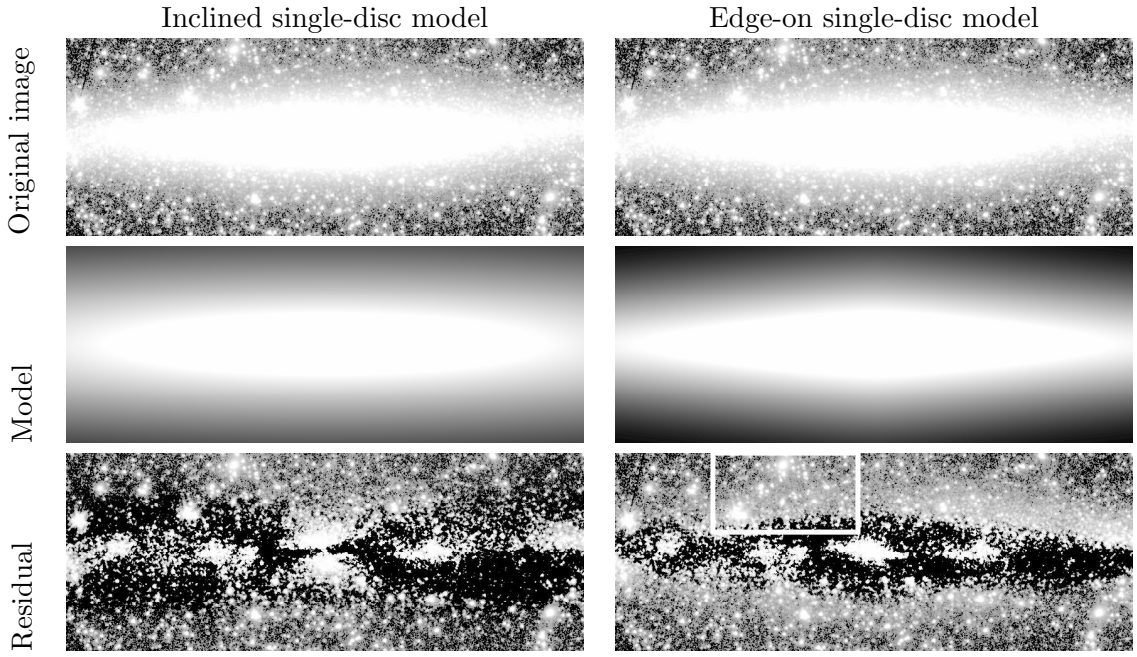

Figure 5.3: The inclined single-disc model is presented at left and the edge-on single-disc model is presented at right. From top to bottom, the images correspond to the original S^{4}G background-subtracted frame, to the GALFIT model, and to the residual image. All the images are in a logarithmic display. The white rectangle indicates an arc-like feature that we could interpret as possibly of tidal origin.

An inspection of the SDSS DR7 image of NGC 4244 (Fig. 5.2; indicated by the arrow labeled with letter 'B') shows a dust lane parallel to the mid-plane and slightly above it. This indicates that what we have defined to be the bottom part of the galaxy is slightly facing us. This was already pointed out by Olling (1996), who found that the inclination of the galaxy is $i = 84.5°$. The dust lane is undetectable in the S^{4}G images, even in a $3.6\,\mu$m $- 4.5\,\mu$m colour-index map.

5.3 GALFIT analysis of NGC 4244

In order to know whether a single-disc description is good enough to account for the structural components of NGC 4244 we have run GALFIT (Peng et al. 2002; Peng et al. 2010) on the S^{4}G NGC 4244 image.

As an input we used the background-subtracted S^{4}G image, the refined mask, and a 'sigma' image, which accounts for the statistical uncertainties of each pixel. We have run an inclined single-disc model and an edge-on single-disc model.

5.3.1 Inclined disc model

To run this model we fixed the centre of the galaxy at the position of the nuclear cluster and the disc PA as 90°. We left as free parameters the disc luminosity, the disc axis ratio, and the disc scalelength. As the galaxy appears to contain no bulge, no further components

are *a priori* needed. The major caveat of modelling a very inclined galaxy this way is that the inclined disc GALFIT model is an infinitely thin circular disc model, which will cause all the vertical extension of the galaxy to be interpreted as caused by the disc inclination. The resulting disc has an axis ratio $d/D = 0.14$, which gives a disc inclination of $i = 82°$. Considering that in our model the disc is infinitely thin, which will automatically cause the disc to be less inclined that it really is, this value is compatible with the inclination of $i = 84.5°$ given by Olling (1996). The inclined disc model and the residual image (the original background-subtracted image at which the model has been subtracted) can be seen in the left column of Fig. 5.3.

5.3.2 Edge-on disc model

To run this model we fixed the centre of the galaxy at the position of the nuclear cluster and the disc PA as 90°. We left as free parameters the disc luminosity, the disc scalelength, and the disc scaleheight. As the galaxy appears to contain no bulge, no further components are *a priori* needed. The major caveat of modelling a not fully edge-on galaxy this way is that we are ignoring the fact that part of the apparent scaleheight is an effect of the galaxy inclination. The edge-on disc model and the residual image can be seen in the right column of Fig. 5.3.

5.3.3 Comparison of the two NGC 4244 GALFIT models

The main difference between the inclined and the edge-on model (see Fig. 5.3) is that in the first case the galaxy isophotes are elliptical and that in the second case they are diamond-shaped. The reason for this is that, in the first case, we are seeing the projection of an infinitely thin disc, which gives as a result a very eccentric ellipse. In the second case we are seeing a diamond shape because the light distribution for an edge-on disc has a cusp at the galactocentric distance $r = 0$. The real galaxy image is more peaked than the inclined disc model for large galactocentric distances (which causes the butterfly-shaped dark areas in the residual image) but has rounder isophotes than the edge-on model near $r = 0$. The residual image shows that, again, the inclined disc model is inaccurate at high galactocentric radii where it predicts a light distribution parallel to the z-axis much wider than observed.

In both models, the residual image shows bright patches close to the mid-plane. In the case of the edge-on model, we may speculate that these patches could correspond to a bar plus spiral arm system seen nearly edge-on. This very same residual image favours the idea that the distortions at high galactocentric radii are caused by spiral arms because they have the same chirality as the spiral residual bright spots. The residual image of the edge-on model also shows an envelope of residual light which may be related to a thick disc. However, that part of this residual emission, especially that at the top-right side of the image, has more to do with the possibly spiral structure of the disc than with the presence of a thick disc as indicated in Fig. 5.2 by the behaviour of blue knots of star formation at high galactocentric radii.

Table 5.1: Fitting parameters and results.

r	$z_{\rm n}$	σ level	Inner exponential fit			Outer exponential fit		
($''$)	($''$)	(mag arcsec^{-2})	range ($''$)	$I_{0\rm t}$ (mag arcsec^{-2})	$H_{\rm zt}$ ($''$)	range ($''$)	$I_{0\rm T}$ (mag arcsec^{-2})	$H_{\rm zT}$ ($''$)
(1)	(2)	(3)	(4)	(5)	(6)	(7)	(8)	(9)
Upper profiles								
-337.5	120	26.55	$15-60$	22.48 ± 0.07	17.5 ± 0.5	–	–	–
-225.0	150	26.68	$20-60$	21.46 ± 0.02	16.9 ± 0.1	–	–	–
-112.5	150	26.91	$15-60$	20.64 ± 0.02	15.4 ± 0.1	–	–	–
0.0	180	27.04	$12-65$	20.27 ± 0.01	15.4 ± 0.1	–	–	–
112.5	150	27.06	$18-65$	20.66 ± 0.02	16.1 ± 0.1	–	–	–
225.5	150	27.08	$27-60$	21.59 ± 0.03	16.4 ± 0.2	–	–	–
337.5	120	27.11	$22-55$	22.76 ± 0.04	17.2 ± 0.2	–	–	–
Lower profiles								
-337.5	120	26.76	$26-50$	22.09 ± 0.03	16.0 ± 0.2	$50-63$	22.74 ± 0.15	19.7 ± 0.9
-225.0	150	26.97	$25-45$	20.92 ± 0.04	13.1 ± 0.2	$50-75$	22.32 ± 0.08	20.4 ± 0.5
-112.5	150	27.07	$27-48$	20.14 ± 0.07	13.1 ± 0.3	$60-100$	22.01 ± 0.09	22.9 ± 0.6
0.0	180	27.14	$23-50$	20.12 ± 0.02	14.2 ± 0.1	$50-75$	20.92 ± 0.08	17.9 ± 0.4
112.5	150	27.24	$22-50$	20.57 ± 0.03	14.6 ± 0.1	$55-80$	21.68 ± 0.08	20.3 ± 0.4
225.5	150	27.11	$22-58$	21.58 ± 0.02	17.0 ± 0.2	$60-80$	22.88 ± 0.09	26.3 ± 0.8
337.5	120	27.12	$25-48$	23.08 ± 0.03	22.6 ± 0.4	$52-75$	23.51 ± 0.06	28.1 ± 0.7

Notes: the uncertainties in this table are statistical errors (3σ). Galactocentric distance (col. 1), z above which noise has been calculated (col. 2), noise level (col. 3), z range at which the fit for the inner exponential has been calculated (col. 4), inner exponential central surface brightness (col. 5), inner exponential scalelength (col. 6), z range at which the fit for the outer exponential has been calculated (col. 7), outer exponential central surface brightness (col. 8), and outer exponential scalelength (col. 9).

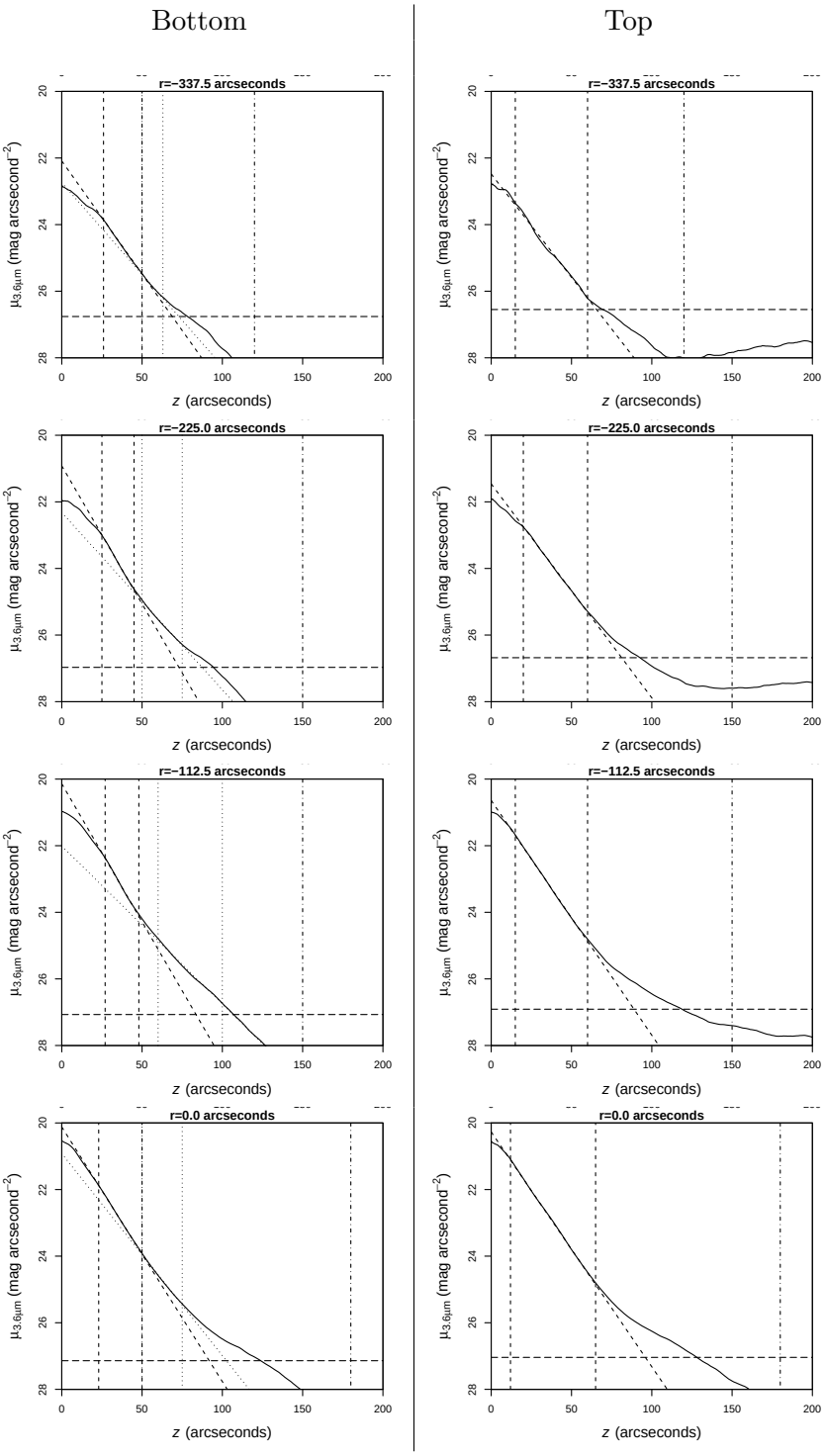

Figure 5.4: Luminosity profiles along z axis at different galactocentric radii (seen in the plot title). Short dashed lines indicate the fits to inner exponentials and the range of radius at which the fit has been done. Point lines indicate the fits to outer exponentials and the range of radius at which the fit has been done. Dash-point lines indicate the minimum radius at which the noise level has been calculated. The horizontal long-dashed line indicates the noise level. The profiles from the bottom part of the galaxy are at left and those from the top part are at right.

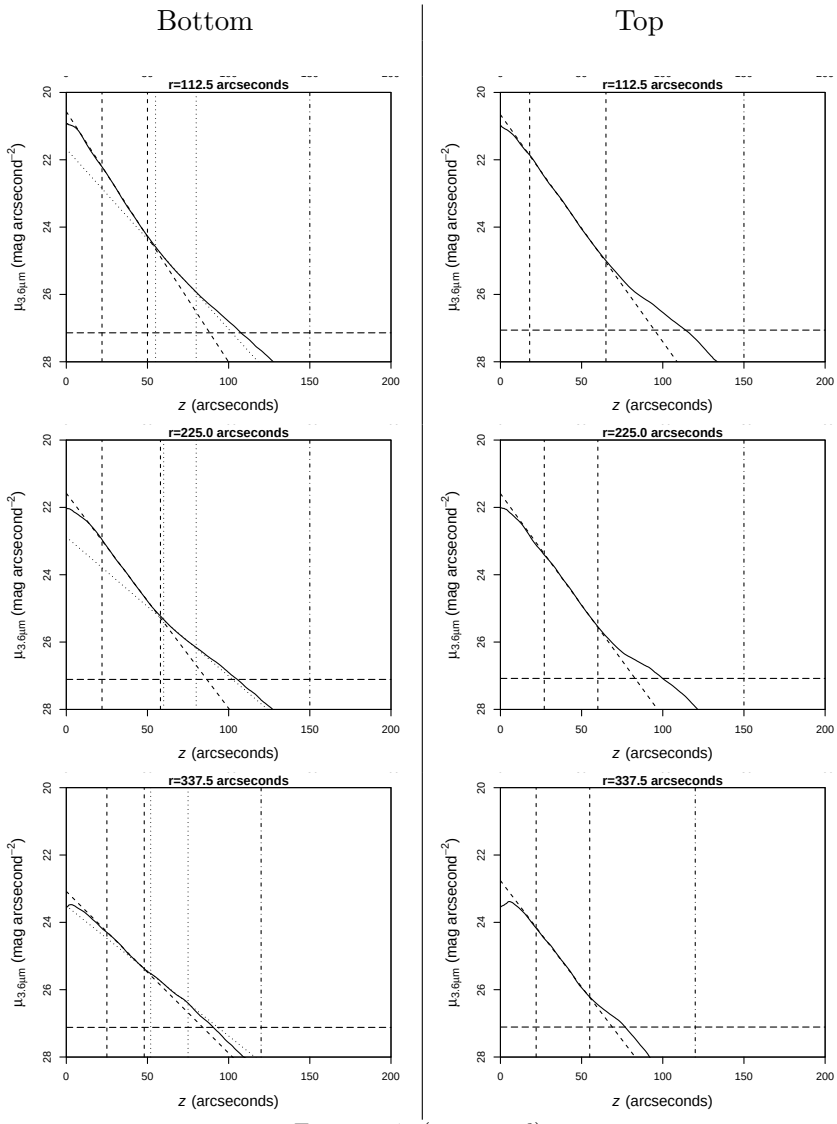

Figure 5.4: (continued).

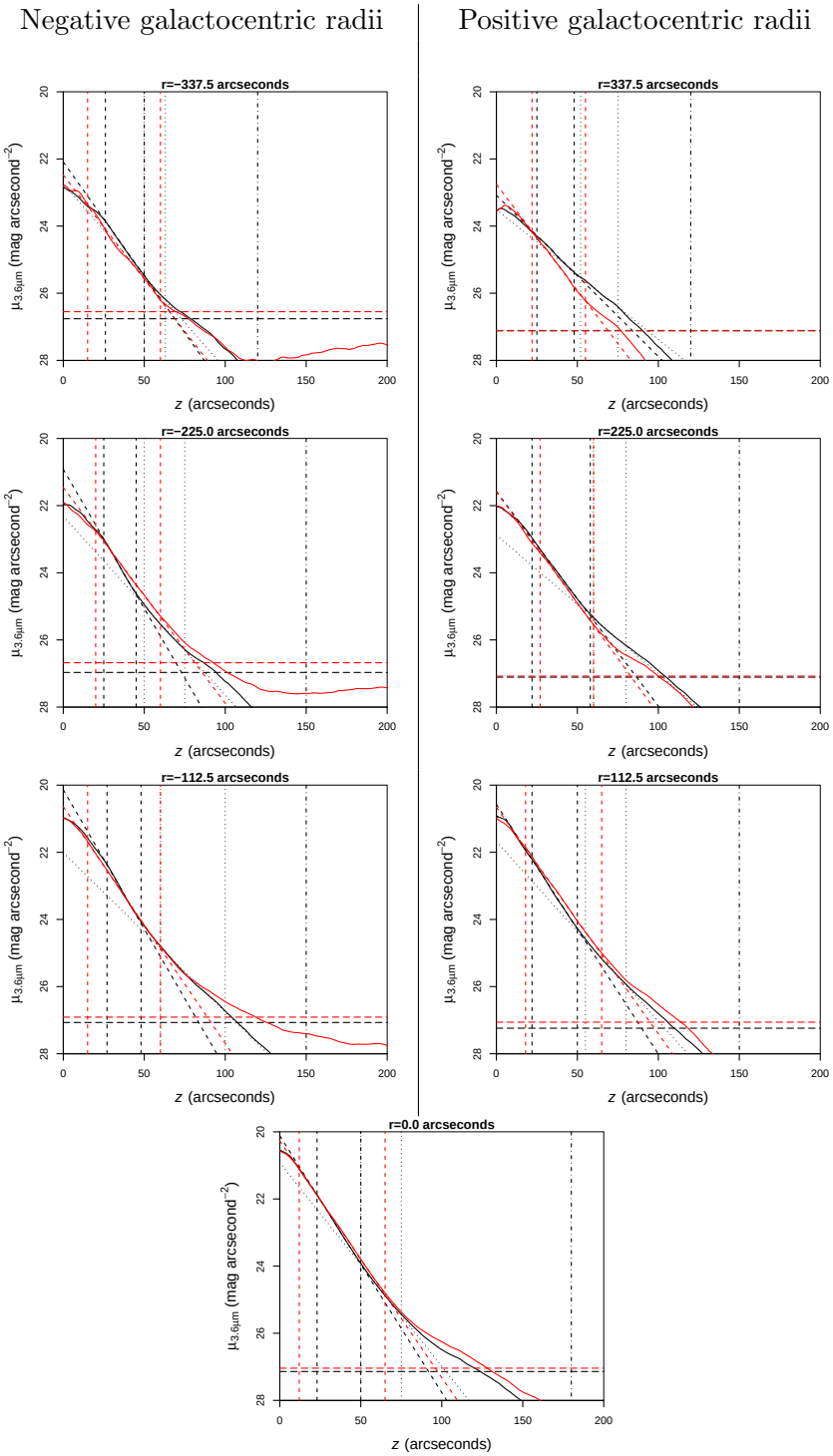

Figure 5.5: Superposition of the profiles shown in Fig. 5.4. Upper profiles are shown in red. The line codification is the same as in Fig. 5.4.

An arc-like feature is visible in the residual images of both models at the top-left side of the frame and at a very low surface brightness. It is more visible in the edge-on model residual image (indicated with a white rectangle) and we speculate that it could be related to some kind of tidal feature. This feature is knotty, which could be explained by the presence of globular clusters in a tidally disrupted galaxy.

Neither of the models we ran reflect accurately the behaviour of the stellar components in NGC 4244. This is mainly because of an intrinsic limitation of GALFIT, namely that it is not designed to fit non-infinitely thin very inclined discs. Even if it is admittedly a somewhat subjective statement, we will consider from now that the model which best matches the galaxy is the edge-on disc galaxy. This is because we consider the butterfly-shaped dark areas in the residual image of the inclined disc model as an indicator that the apparent scaleheight of the disc of NGC 4244 is mostly caused by the real scaleheight of the disc and not by the inclined nature of it. If we consider the edge-on model to be better, and taking into account the light envelope seen in the residual image for this model, we may consider the possibility of the galaxy having a thick disc, which is studied in next Section using photometry.

5.4 Vertical luminosity profiles

We have produced luminosity profiles parallel to the z axis of the galaxy at different galactocentric radii (r). These luminosity profiles are shown in Fig. 5.4.

To produce the luminosity profiles, we first made vertical bins with a width of $225.0''$ (300 pixels), and centred at galactocentric distances $r = -337.5''$, $-225.0''$, $-112.5''$, $0.0''$, $112.5''$, $225.0''$, and $337.5''$. The $225.0''$ bin width has been chosen because it offers a good compromise between spatial resolution and photometric quality. Then, for each bin we made a single vertical luminosity profile by summing all emission, taking into account which pixels were masked. We determined the location of the mid-plane of the galaxy from the profiles obtained in each bin. This was done by folding the profiles and minimizing the difference between the upper and the lower halves of the light profile, with a precision of 0.1 pixel. For each bin we made a visual guess of where the galaxy effectively ends. The noise level was calculated by producing the standard deviation of those pixels at higher z. This is a conservative estimate of the noise, as the profile is produced by averaging all the pixels in the bin. We smoothed the profiles vertically in order to get a higher signal at low surface-brightness areas. This smoothing has been done logarithmically and using a vertical scaleheight of 5 pixels ($3.75''$).

As the top and the bottom part of the galaxy are different, we have fitted them separately. We decided to make exponential fits at ranges in z where the data appear roughly exponential. All the points were given equal weight. We fitted one or two exponentials to each profile depending on whether we detected – by eye – any trace of a thick disc or not. When preparing the fits, we considered all the luminosity values above the noise level to be reliable.

The results of the fits are overlaid on the profiles in Fig. 5.4 and are shown in Table 5.1.

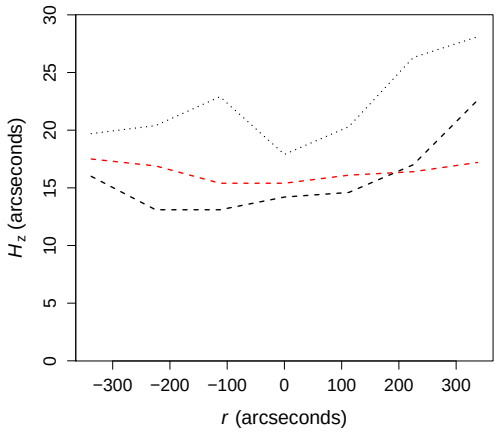

Figure 5.6: Scaleheight of the discs at different galactocentric radii. Dashed lines indicate the thin disc and the dotted line indicates the thick disc. Black lines indicate the measurements of scaleheights in the bottom parts of the galaxy and red lines the measurements in the top parts.

5.5 Results

We find that the top profiles can be fitted with a single exponential profile. There is an extra faint component which cannot be fitted by an exponential component. The bottom profiles are well fitted by two exponential components (Fig. 5.4). The scalelengths of all these fits is roughly stable when changing the galactocentric radii at which we are looking.

5.5.1 Looking for a thick disc in the luminosity profiles

Something that is striking from the luminosity profiles (Fig. 5.4) is the lack of symmetry between the top and the bottom sides of NGC 4244. Once an inner exponential has been fitted, the excess light in the bottom part of the galaxy can be fitted by a second exponential. An excess of light also appears in the top half of the galaxy, but it cannot be so easily fitted by an exponential and, even where we could in principle have done it, the fit would have to be done over a much smaller range in z. In Fig. 5.5 we have plotted in the same frame lower and upper profiles in order to compare them. By comparing lower (black) and upper (red) profiles in this figure, we can see that the concave inflexion points between two exponentials in the bottom profiles (which are especially noticeable for $r = -225.0''$, $-112.5''$, $112.5''$, $225.0''$, and $337.5''$) have no clear counterpart in the top part of the galaxy. This inflexion point is not so evident in the bottom profile at $r = -337.5$, maybe due to the fact that field of view of the image we use does not cover the leftmost part of NGC 4244 (see bottom panel of Fig. 5.1), or maybe due to some effect related with that region being affected by disc spiral arms. The other profile in which there is no obvious inflexion point for the bottom profile is $r = 0.0''$.

One noticeable difference between the top and bottom halves of the galaxy is that the excess light in the top part extends to higher z values for $-225.0'' < r < 0.0''$ (and maybe extending to $r = 112.5''$. This excess corresponds with the arc-like feature in the residual image obtained from GALFIT (indicated with a white rectangle in the bottom-right panel

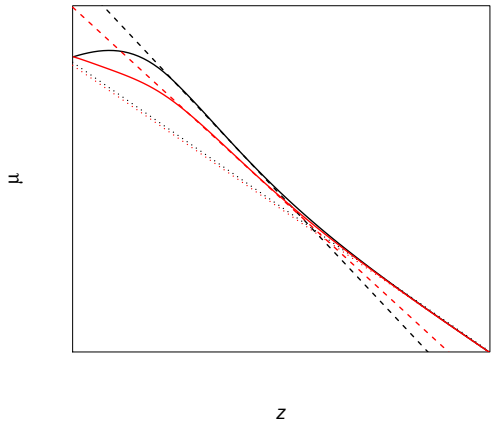

Figure 5.7: Luminosity profiles of a highly inclined modelled galaxy with a semi-transparent thin disc. The top profile is shown in red and the bottom profile is shown in black. Dashed lines indicate the exponential fits to the thin disc and point lines indicate the exponential fits to the thick disc.

in Fig. 5.3) and could be interpreted as a tidal feature, as its shape is somewhat similar to that observed in other very inclined galaxies (such as in NGC 5907 studied by Shang et al. 1998 and Martínez-Delgado et al. 2008 and in NGC 4103 by Martínez-Deglado et al. 2009; these cases are admittedly much more spectacular than that described here). As it has a brightness comparable to that of the second exponential we find in the bottom profile, it could hide part of a thick disc in the top part of the galaxy for radii from $r = -225.0''$ to $r = 112.5''$. However, the lack of traces of a thick disc in the top profiles, even at galactocentric radii not affected by the non-exponential excess of light, indicates that a thick disc there is less obvious than in the bottom parts of the galaxy, if it is present at all.

The scaleheight of the thin disc component is stable from $r = -337.5''$ to $r = 225.0''$. At this point, the bottom part of the disc apparently flares (this can also be seen at the right side of Fig. 5.2). This apparent flare is appears to be related to the spiral structure of the galaxy.

5.5.2 Thin and thick discs and opacities

We have tested whether the fact that NGC 4244 is not totally edge-on ($i = 84.5$ according to Olling 1996), could explain the lack of traces of a thick disc in the top part of the galaxy. In order words, we want to test whether, except for the arc-like feature, the top and bottom parts could be intrinsically symmetric. To do so we have designed a galaxy with two discs, each with the following light (mass) distribution:

$$I(R, z) = I_0\, e^{-R/h_{\rm R}} e^{-z/h_{\rm z}} \tag{5.1}$$

where I_0 is the central surface brightness, R the distance to the rotation axis to the galaxy, z the height above its mid-plane, $h_{\rm R}$ the radial scalelength and $h_{\rm z}$ the vertical scaleheight (not to be confused with the scaleheights which appear in Table 5.1, $H_{\rm z}$, which

are scaleheights of the integrated distribution of light along the line of sight). We created our modelled galaxy with a thin disc and a thick disc (subindices t and T in this section). The galaxy was designed to have $I_{0\mathrm{t}} = 4I_{0\mathrm{T}}$, $h_{\mathrm{Rt}} = h_{\mathrm{RT}}$, and $h_{\mathrm{zt}} = 5h_{\mathrm{zT}}$. We made the thin disc semi-transparent, with a local density of dust proportional to the local light intensity, which means that the dust is assumed to be in equilibrium with the stellar component. The density of dust in the thin disc was a tunable parameter in our model. We assumed that the thick disc is transparent, i.e. contains little or no dust.

We have projected the light emitted by our three-dimensional model galaxy using on inclination $i = 84.5°$. We find that for low thin disc opacities, the two halves of the galaxy are roughly similar, but that an increase of the opacity causes a noticeable effect: as seen in Fig. 5.7, when the thin disc is opaque enough, the break between the two discs is still clearly visible for the bottom profile, but starts to fade out in the top profile. The break (the radius at which the exponential fit for the thin disc has the same surface brightness as the fit for the thick disc) is not only softer, it takes place at a lower surface brightness for the top profile, making it more difficult to detect. As in our model, the luminosity profiles from $r = -337.5''$ to $r = 112.5''$ show a steeper scaleheight for the bottom part of the galaxy. For these galactocentric radii, the arc-like feature may be hiding any trace a softened break radius in the top profiles. At higher galactocentric radii, the galaxy starts to be distorted by, possibly, the presence of spiral arms in the disc, thus making the comparison between NGC 4244 and the model more difficult.

We thus conclude that the luminosity profiles of NGC 4244 are compatible with the galaxy having a thin and a thick disc and being symmetric with respect to its mid-plane except for an arc-like feature on its top side which could be interpreted as a tidal feature.

5.6 NGC 4244 toy model and classification

In order to summarize all the findings we made in NGC 4244 we have made the toy model shown in Fig. 5.8. The features we have included are:

- An unresolved nuclear cluster.
- The well known thin disc with the bottom part slightly facing us as known from the mid-plane dust lane position (Section 5.2).
- A thick disc which has been found using the luminosity profiles of Section 5.4 and with the experiments of Section 5.5.
- A large-scale arm structure which cause the disc to look 'warped' at around $5'$ from the nucleus (Section 5.2).
- A structure made of a small bar (speculative) and small arms as found from the residuals obtained using the GALFIT models (Section 5.3).
- An arc-like feature in the top part of the galaxy. We speculate that this feature could be interpreted as a tidal feature (Section 5.3.3).

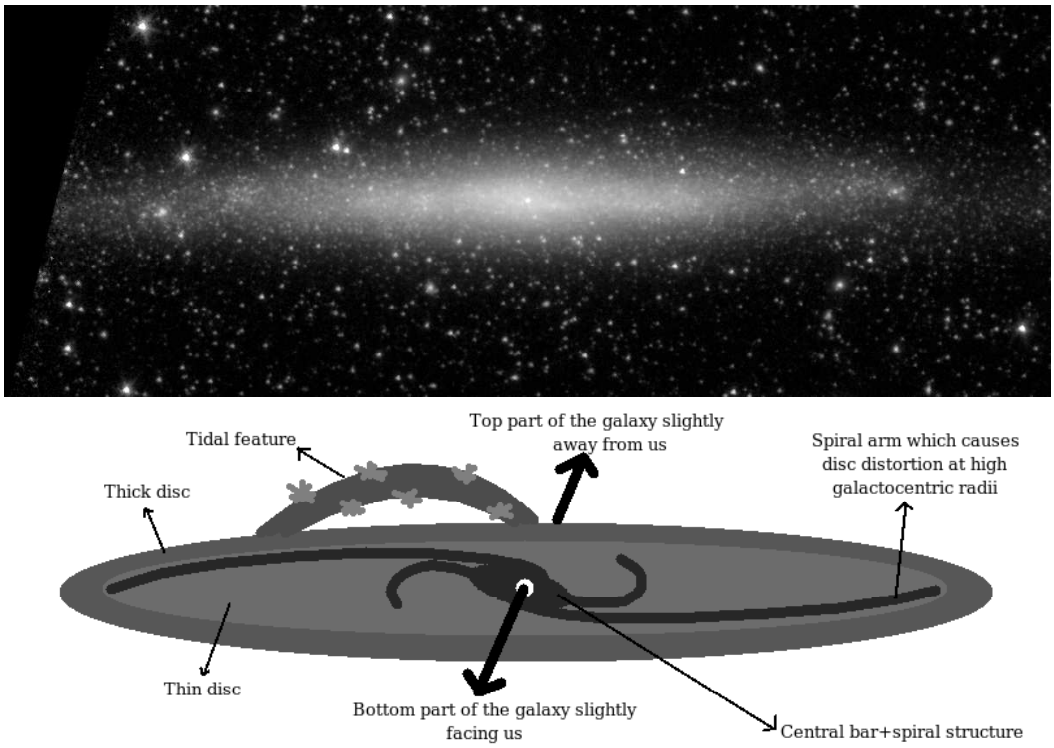

Figure 5.8: Top: S^{4}G 3.6μm image. Bottom: Toy model of NGC 4244 with all the features discussed in this Chapter.

NGC 4244 also has an H I disc which is coplanar with the optical and near-IR one except at large galactocentric radii ($r > 10'$; at this galactocentric radius there is no significant stellar emission) where it has a warp going in the opposite direction to the apparent warp caused by the large-scale spiral arms.

NGC 4244 has been classified as an 'Scd' in the RSA (Sandage & Tamman 1981) an 'SA(s)cd sp' galaxy in the RC3 (de Vaucouleurs et al. 1991; 'sp' stands for 'spindle' or edge-on), and as a 'Sd sp' in Buta et al. (2010; in this case the authors used the same S^{4}G 3.6μm image we use in this Chapter for the classification but they interpreted it using the same morphological criteria as if the image was taken in blue light). Based on our finding we can comment on this classification. An Scd or Sd classification seems correct, as earlier-type galaxies have a significant bulge and later-type ones are usually non-symmetric. As the galaxy is could barred according to our residual images (Fig. 5.3 and Section 5.3.3) and it shows no trace of an inner ring of pseudo-ring, we could classify NGC 4244 as 'SAB(s)d sp'.

5.7 Discussion and conclusions

We find a thick disc in a galaxy which was reported not to have one or as a doubtful case. Fry et al. (1999) did not detect the thick disc when doing surface-brightness photometry because their R-band image was not deep enough (limiting magnitude $\mu_R = 27.5\,\mathrm{mag\,arcsec^{-2}}$, which is equivalent to $\mu_B = 29.5\,\mathrm{mag\,arcsec^{-2}}$; S^{4}G has a depth of around $\mu_{3.6\mu\mathrm{m}} = 26.5\,\mathrm{mag\,arcsec^{-2}}$, which is equivalent to $\mu_B = 31.0\,\mathrm{mag\,arcsec^{-2}}$). Furthermore, they assumed that the galaxy was symmetric with respect to the mid-plane and they summed the top and bottom luminosity profiles in order to make their fits, which diluted even more the effect of the subtle thick disc. Seth et al. (2005b) deduced the presence of an extended component other than the thin disc by finding that the scaleheight of the oldest stars (RGB) is larger than the scaleheight of young main sequence stars. However, their star-counting profiles are made using all galactocentric distances, which does not allow one to determine to what extent this effect is due to the presence of the 'warp' or to the presence of the arc-like feature we have discovered. Furthermore, the sum of all stellar components they have studied (young main sequence stars, Helium-burning stars, AGB stars, and RGB stars) shows no to little trace of a thick disc in their Fig. 3. Tikhonov & Galazutdinova (2005) found an extended feature by counting RGB stars at the location of the arc-like feature. Seth et al. (2007) studied the RGB star distribution in a thin strip along the bottom part of the minor axis of NGC 4244 deep enough to find an halo component undetected by us but they did not notice any trace of the thick disc. This may either be due to the fact that the thick disc has a smaller scaleheight at $r = 0''$ than at other galactocentric radii, or because RGB stars trace a single component. The scaleheight for the disc they fit ($\sim 300\,\mathrm{pc}$ or $\sim 14''$) is exactly the same as the one we find for the thin disc at $r = 0''$.

If thick discs are indeed a product of secular evolution, the subtleness of the thick disc component in NGC 4244 indicates a lack of strong secular evolution. The lack of a pseudobulge – a clear indicator of secular evolution (Kormendy & Kennicutt 2004) – also argues in favour of this. Literature sources report no bar in NGC 4244, which would lead to a smaller secular evolution rate (considering that the galaxy could have been unbarred for a significant amount of time), but in the residual maps made using GALFIT (Fig. 5.3) we have found a feature reminiscent of a small bar. One might argue that a late-type and not very massive galaxy will evolve very little. However, less massive and later-type galaxies, such as NGC 55 (which is an SBm galaxy and is almost one magnitude fainter than NGC 4244 in B), have much clearer thick discs (Seth et al. 2005b). Another possibility is that NGC 4244 has been formed more recently than other galaxies. In this case, NGC 4244 would be a perfect nearby laboratory for the study of galaxy properties at high redshift as it would be at an early stage of galaxy evolution.

To sum up, we have found evidence of a weak thick disc in NGC 4244. The reason of the low density of the thick disc remains unknown and is probably related to a lack of strong secular evolution in this galaxy. Further study is needed to understand the reason for this apparently slow evolution. We would need to know what are the ages of stars in the thick disc in order to constrain the galaxy age. It also would be useful to know the rotation sense of NGC 4244 in order to give more support to the possibility of the apparent disc warp being caused by spiral arms.

6

Structural decomposition of S^{4}G galaxies with outer rings

6.1 Introduction

Model fitting has proven to be useful for identifying the structural components of disc galaxies (see, e.g., Kormendy 1977; Boroson 1981; Prieto et al. 1992; Peng et al. 2002; Laurikainen et al. 2005; Buta et al. 2006; Laurikainen et al. 2006; Peng et al. 2010; Laurikainen et al. 2010a). Our vision on structural components of galaxies has evolved from a relatively simple framework in which a disc galaxy could have a bulge, a bar, and a disc, to a complex picture in which multiple bars can cohabit with oval distortions, lenses, resonance rings and pseudo-rings, bulges, pseudo-bulges, and several kinds of discs.

The first and most obvious galaxy fitting mode is 1D-fitting. One way to get the luminosity profiles for this kind of fit is to take a 1D slice of the galaxy, usually along the major and/or minor axis of the disc or along major and/or minor axis of the bar (Kormendy 1977; Burstein 1979; Kent 1985; Schroder et al. 1990; Acarreta et al. 1996; Baggett et al. 1998). Another possibility is to prepare the luminosity profiles of the galaxy by averaging the number of counts of the pixels in the galaxy image over elliptical annuli (azimuthal averaging). This technique has been used by Boroson (1981), Schild et al. (1985), Ohta et al. (1990), Pastoriza et al. (1991), Prieto et al. (1992), Forbes & DePoy (1992), Saraiva Schröder et al. (1994), Heisler et al. (1996), Patterson & Thuan (1996), Saraiva (1997), Erwin et al. (2005), Pohlen & Trujillo (2006), Erwin et al. (2008), Comerón et al. (2008a), Azzollini et al. (2008), and in Chapter 1, among others. One advantage of the 1D-fitting method is that the light profiles, when averaged over annuli, have a high signal-to-noise ratio. Another advantage is that fitting methods are easy to implement and do not need intensive computing time use. The disadvantage of this method is that, even if it is usually easy to have an estimate of some galaxy parameters such as the disc scalelength, it is much less satisfactory at measuring the properties of non-axisymmetric features and getting a complete picture of the complexity of the galaxy.

The other approach for the identification of structural components in disc galaxies is to make a 2D-fitting directly on a galaxy image. This approach has been used by Shaw &

Gilmore (1989), Scorza & Bender (1990), Monnet et al. (1992), Emsellem et al. (1994), Byun & Freeman (1995), de Jong (1996), Simard (1998), Moriondo et al. (1998), Wadadekar et al. (1999), Khosroshahi et al. (2000), Möllenhoff & Heidt (2001), Ravindranath et al. (2001), Peng et al. (2002), Simard et al. (2002), Laurikainen et al. (2004a), de Souza et al. (2004), Christlein & Zabludoff (2004), Laurikainen et al. (2005), Laurikainen et al. (2006), and Peng et al. (2010), among others. Of these authors, Scorza & Bender (1990), Byun & Freeman (1995), Simard (1998), Moriondo et al. (1998), Wadadekar et al. (1999), Khosroshahi et al. (2000), and Simard et al. (2002) perform exclusively two-component fitting which ignores bars and other non-axisymmetries. This can lead to wrong estimates of some parameters, as discussed in Simard et al. (2002). Two-dimensional multicomponent fitting has clear advantages in describing the complexity of the central components of galaxies, as it uses each pixel for fitting and not just a smoothed azimuthal average. On the other hand, low signal-to-noise ratios may affect the determination of the properties of low surface-brightness areas in images that are not very deep, such as the outskirts of discs and outer rings. Another problem is that the fits require more intensive computation and cannot be made fully automatically. As this method requires human intervention in deciding the number and the nature of the components to be fitted, it has some degree of subjectivity.

In this Chapter we present some preliminary work that has been done at decomposing a number of galaxies in the S^{4}G using GALFIT, and finding the structural components within them. The main purpose of the first phase of this work is to test the quality of S^{4}G images and to detect potential problems when using GALFIT in galaxies with complex structures. A number of caveats that we find when processing this first set of data are discussed in Section 6.5.4.

Another purpose of this Chapter is to make a preliminary study of galaxies with outer rings. Outer rings have first been reported by Perrine (1922) for NGC 1291, although this ring was already visible in a photograph by Keeler (1908). It has been suggested that outer rings are more prevalent in barred (Kormendy 1979) and early-type (de Vaucouleurs 1975; Sandage & Bedke 1994) galaxies. Outer rings are thought to be related to Outer Lindblad Resonances (OLRs; see simulations from Schwarz 1981). In his simulations, Schwarz (1981) showed that outer rings are created by particles outside the corotation which slowly gain angular momentum until they settle in an orbit close to the OLR. Outer rings are closely linked with the spiral pattern of the galaxy and sometimes the ring is a wrapped pair of spiral arms that nearly closes together (Buta & Combes 1996).

We have decomposed 11 galaxies with an outer ring, matched in bar type, morphological type, brightness and axis ratio with a control sample of 11 galaxies with no outer ring, in order to better understand why some galaxies have outer rings when others do not.

6.2 Previous experience

We have obtained experience on decomposing galaxies by participating to the data processing of one of the Near-IR S0 galaxy Survey papers (Laurikainen et al 2010a).

The Near-IR S0 galaxy Survey (NIRS0S; Laurikainen et al. 2005) contains 184 galaxies with the following criteria from the RC3 (de Vaucouleurs et al. 1991):

- $B_{\rm T} \leq 12.5\,{\rm mag}$

- $i \leq 65^{\circ}$
- $-3 \leq T \leq 1$

The NIRS0S observations and data reductions are described in detail in E. Laurikainen et al. (2010b, in preparation). The main motivation of the survey is to derive the properties of S0 galaxy bars, bulges, and discs in order to compare them with the data of the Ohio State University Bright Spiral Galaxy Survey (OSUBSGS, Eskridge et al. 2002). Some results of the NIRS0S papers are:

- The mean shape parameter of the bulges of S0s is more exponential than it was previously thought to be, the Sérsic index parameter of the bulge being $n = 2.1 \pm 0.7$ (Laurikainen et al. 2005).
- Bars show a wide variety of Fourier profiles, ranging from simple symmetric profiles which can be represented by a single Gaussian component to both symmetric and asymmetric profiles which can be represented by two overlapping Gaussians (Buta et al. 2006).
- There is strong evidence that the central components of many S0 galaxies are in fact pseudo-bulges (Laurikainen et al. 2006).

In NIRS0S 2D-multicomponent decompositions were made for 175 galaxies, using BD-BAR (Laurikainen et al. 2004a; Laurikainen et al. 2005) to find the 2D light distribution of galaxies into bulges, discs, bars, ovals, and lenses. The detailed procedure we used can be found in Laurikainen et al. (2005) and the results can be found in Laurikainen et al. (2010a). The main results of this paper are:

- The photometric properties derived for the NIRS0S and the OSUBSGS samples show that the properties of the bulges of S0 galaxies are more similar to those in bulges of spirals than to those in elliptical galaxies.
- The properties of bulges and discs in S0s are coupled in a similar manner as previously found for later type spiral galaxies.
- We find that the ratio between the bulge half-light radius and the galaxy disc scale-length, $r_{\rm eff}/h_{\rm r}$, is around 0.20, 0.15, and 0.10 for S0, S0/a-Sa, and Sab-Sc galaxies respectively. These values are smaller than those predicted in simulations in which bulges are formed in galaxy mergers, and thus indicate an origin possibly due to secular evolution processes.
- The bulge-to-total flux ratio (B/T) for NIRS0S analysed galaxies covers the full range of $B/T < 0.7$. Thirteen per cent of the analysed galaxies from the NIRS0S have $B/T < 0.15$, which are bulge-to-total flux ratios typically seen in late-type galaxies.

Table 6.1: Properties of the sample galaxies with an outer ring and the galaxies without an outer ring. Matched galaxies are side by side.

Galaxies with an outer ring					Galaxies without an outer ring				
Galaxy	Morph.	Dist. (Mpc)	M_B	d/D	Galaxy	Morph.	Dist. (Mpc)	M_B	d/D
(1)	(2)	(3)	(4)	(5)	(1)	(2)	(3)	(4)	(5)
N 1097	.SBS3..	15.2	-21.23	0.21	N 6923	.SBT3*.	39.1	-21.08	0.31
N 1566	.SXS4..	17.5	-21.43	0.16	N 4536	.SXT4..	17.3	-21.79	0.44
N 2633	.SBS3..	34.7	-20.23	0.20	N 2854	.SBS3..	42.3	-19.81	0.36
N 3368	.SXT2..	13.4	-20.89	0.18	N 4450	.SAS2..	29.5	-21.87	0.16
N 3504	RSXS2..	23.9	-20.45	0.04	N 4569	.SXT2..	12.7	-21.10	0.38
N 4245	.SBR0*.	14.9	-18.73	0.20	N 1438	.SBR0*.	19.6	-18.61	0.34
N 4698	.SAS2..	15.5	-19.90	0.39	N 1357	.SAS2..	26.1	-20.11	0.12
N 5248	.SXT4..	17.9	-20.86	0.23	N 1255	.SXT4..	21.4	-20.54	0.26
N 5377	RSBS1..	29.2	-20.60	0.41	N 1015	.SBR1*.	36.5	-19.68	0.07
N 5448	RSXR1..	32.5	-20.81	0.29	N 1367	.SXT1..	18.2	-20.00	0.17
N 6217	RBST4..	23.8	-20.41	0.14	N 289	.SBT4..	20.7	-20.19	0.13

Notes: galaxy ID (col. 1), galaxy morphology from RC3 (col. 2; de Vaucouleurs et al. 1991), galaxy distance calculated from the kinematic distance modulus in HyperLEDA when available and from HyperLEDA's Tully-Fisher distance modulus when not (col. 3; Paturel et al. 2003), galaxy absolute B-band magnitude from HyperLEDA (col. 4; Paturel et al. 2003), and galaxy axis ratio from HyperLEDA (col. 5; Paturel et al. 2003).

Table 6.2: Statistical properties of the outer ring and control samples, showing mean and median values of three of the parameters used for matching the samples.

	Outer ring sample		Control sample	
Property	mean	median	mean	median
Type	2.4	2.1	2.4	2.1
M_B	-20.49	-20.60	-20.44	-20.19
d/D	0.61	0.63	0.59	0.55

6.3 Sample selection

One of the purposes of this Chapter is to study differences in the structural components between a sample of galaxies with outer rings and a control sample of galaxies without outer rings. To do so, we selected a sample of 11 galaxies with an outer ring from those S^{4}G galaxies which had been imaged by 20$^{\text{th}}$ of April 2010. We then made a one-to-one match with other S^{4}G galaxies already imaged in order to prepare a control sample. The outer ring galaxies have all been reported in the literature, except for NGC 4245, whose outer ring has been discovered when processing the S^{4}G image. Galaxies from the control sample were selected from galaxies which have been reported to be unringed in the literature. The pair matching criteria are:

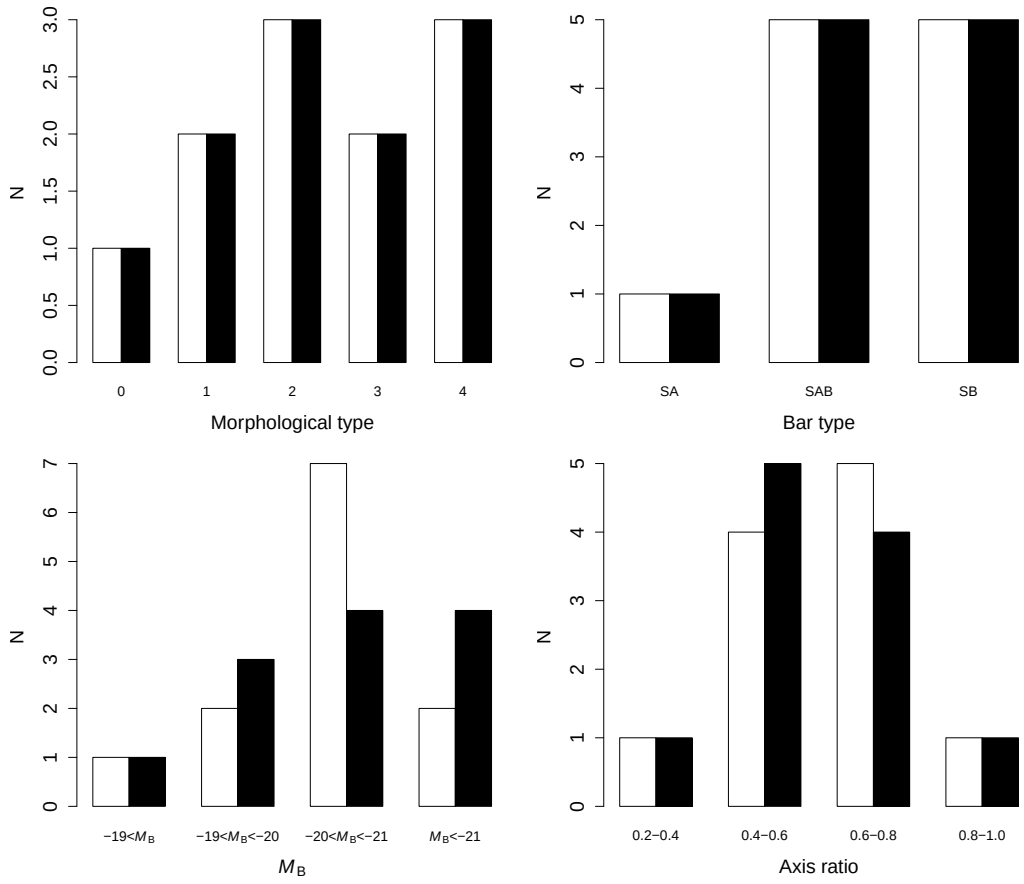

Figure 6.1: Matching of the sample with outer rings and the control sample with respect to four parameters of the host galaxy: morphological type (top left), bar type (top right), absolute M_B magnitude (bottom left), and axis ratio d/D (bottom right). The white bars correspond to the outer ring sample and the black bars denote the control sample without outer rings.

- Both galaxies have the same morphological type according to the RC3 (de Vaucouleurs et al. 1991).
- Both galaxies have the same bar type (SA, SX, or SB) according to the RC3 (de Vaucouleurs et al. 1991).
- The galaxies have an absolute B-band brightness difference smaller than one magnitude according to HyperLEDA (Paturel et al. 2003).
- Once the three preceding matching criteria are fulfilled, we select the galaxy with no outer ring which matches best the axis ratio of the galaxy with outer ring. The axis ratio was taken from HyperLEDA (Paturel et al. 2003).

The matched galaxies and the numerical values of the properties we used for the matching are presented in Table 6.1. Fig. 6.1 and Table 6.2 indicate that the samples indeed are

very similar. The high quality of the matching between the two samples compensates in part the effect of low statistics in the analysis, as illustrated in the following Sections.

Of our eleven outer ring galaxies, eight (namely NGC 1097, NGC 1566, NGC 2633, NGC 3504, NGC 4245, NGC 5248, NGC 5377, NGC 5448, and NGC 6217) have an R'_1 ring morphology, which is defined as resulting from two 180°winding spiral arms with respect to the ends of a bar or oval (Buta 1986; Buta 1989; Buta & Crocker 1991). The remaining ringed galaxies have either R′ or R rings, as there are not enough indications to classify them in one of the main outer ring families (R'_1, R'_2, and $R_1R'_2$). The ring classification comes from Buta et al. (2007), except for NGC 4245, for which the ring has ring has been discovered in this Chapter.

6.4 Model fitting procedure

The galaxies fitted in this Chapter have been processed in the framework of the S^{4}G. They have been fitted using GALFIT (Peng et al. 2002; Peng et al. 2010) and the preliminary version of the software tools developed by H. Salo for Pipeline 4 of S^{4}G (Sheth et al. 2010).

For each galaxy processed for the elaboration of this Chapter we first retrieved the 3.6μm image from the S^{4}G archive. These images are mosaicked, but not always sky-subtracted as S^{4}G is an ongoing survey whose data have not been fully processed yet. In the cases of images which are not sky-subtracted we made an estimate of the sky background by using IRAF's IMEXAM task over several tens of locations outside the galaxy. IMEXAM was run using five by five pixel apertures. We averaged all the background estimates made using IMEXAM in order to obtain a sky value that we subtracted from the frame.

We used the S^{4}G masks when available and produced hand-made masks for all the galaxies which had not been processed yet by S^{4}G pipelines. These masks are used to remove the effect of bad pixels, foreground stars and background galaxies.

For each galaxy, we first found its centre by using IMEXAM. Then we ran a simple model fitting with GALFIT. This model contained only a Sérsic bulge and an exponential disc component and used as a fixed centre the position found with IMEXAM. The aim of running such simple models was to have a first estimate of the two main components of a disc galaxy. We then visually inspected the galaxy in order to find other components such as lenses, bars, oval distortions, and very prominent resonance rings. Then we ran complex GALFIT models including as initial values guesses for these new components and the values obtained for the simple bulge+disc fit in the case of the bulge and disc components. For all these components the centre was fixed. The radial profile functions we used in our fits are:

- A Sérsic function for the bulges, defined as:

$$\Sigma_{\rm Sersic}(r) = \Sigma_{\rm e} \exp\left[-\kappa\left(\left(\frac{r}{r_{\rm e}}\right)^{1/n}\right) - 1\right], \tag{6.1}$$

  where $\Sigma_{\rm Sersic}(r)$ is the surface brightness as a function of the radius, $\Sigma_{\rm e}$ is the surface brightness at the effective radius $r_{\rm e}$, n is the concentration parameter (when n is large the inner profile is steep and the wings are extended and when n is small the inner profile is shallow at small radius and has a steep truncation at large radius), and

the effective radius $r_{\rm e}$ is the radius inside which half of the light of the component is contained. κ is a normalization factor coupled with n in order to keep $r_{\rm e}$ as the radius inside which half of the light of the component can be found. κ can be approximated as $\kappa \simeq 2n - 0.327$ (Ciotti 1991). We left $\Sigma_{\rm e}$, n, and $r_{\rm e}$ as free parameters.

- An exponential function for nuclear, inner, and 'classical' discs, defined as:

$$\Sigma_{\rm Exponential}(r) = \Sigma_0 \exp\left(-\frac{r}{r_{\rm s}}\right), \tag{6.2}$$

where Σ_0 is the surface brightness at $r = 0$ and $r_{\rm s}$ is the disc scalelength. We left Σ_0 and $r_{\rm s}$ as free parameters.

- A Gaussian profile for nuclear point sources. This is a special case of a Sérsic profile in which $n = 0.5$ and where the size parameter is the FWHM instead of $r_{\rm e}$. It is defined as:

$$\Sigma_{\rm Gauss}(r) = \Sigma_0 \exp\left(\frac{-r^2}{2\sigma^2}\right), \tag{6.3}$$

where Σ_0 is the surface brightness at $r = 0$ and the FWHM $= 2.354\sigma$. We left Σ_0 and σ as free parameters.

- A Ferrers profile for bars, nuclear bars, lenses, and oval distortions, defined as:

$$\Sigma_{\rm Ferrer}(r) = \begin{cases} \Sigma_0 \left(1 - (r/r_{\rm out})^2\right)^{\alpha} & \text{for } r < r_{\rm out} \\ 0 & \text{for } r \geq r_{\rm out} \end{cases}, \tag{6.4}$$

where Σ_0 is the surface brightness at $r = 0$, $r_{\rm out}$ is the truncation radius, and α defines the sharpness of the truncation. We left Σ_0 and $r_{\rm out}$ as free parameters. We fix $\alpha = 2$ in order to avoid having too many parameters. Thus, the shape of the radial profile for all the bars in our analysis is the same. As we will show with the quality of the fits displayed in the next Sections, having only Σ_0 and $r_{\rm out}$ as free parameters has proved to be a good enough approximation.

- An annular Sérsic profile to represent prominent nuclear and inner rings. When using GALFIT a Sérsic annulus adopts the following shape:

$$\Sigma_{\rm annulus}(r) = \Sigma_{\rm Sersic}(r) \times P \tag{6.5}$$

where P is a truncation function defined as:

$$P = 0.5 \times \left[1 + \tanh\left((2 - B)\frac{r}{r_{\rm break}} + B\right)\right]. \tag{6.6}$$

In this expression $r_{\rm break}$ is defined as the radius at which, when $r = r_{\rm break}$, the flux is 99% of the untruncated model profile. B is defined as:

$$B = 2.65 - 4.98\left(\frac{r_{\rm break}}{r_{\rm break} - r_{\rm soft}}\right). \tag{6.7}$$

In this expression $r_{\rm soft}$ is defined as the radius at which, when $r = r_{\rm break}$, the flux is 1% of the untruncated model profile. When $r_{\rm break} \gg r_{\rm break} - r_{\rm soft}$ (which is usual for inner rings, as the ring radius is much larger than the ring width; it is not so usual for nuclear rings as the width is increased by resolution effects), $\Sigma(r = 0) \simeq \Sigma_{\rm Sersic}(r = 0)$ and thus $\Sigma_{\rm Sersic}(r = 0)$ could be considered as the surface brightness at the ridge of the ring. We left $r_{\rm break}$, $r_{\rm soft}$, $\Sigma_{\rm e}$, and $r_{\rm e}$ as free parameters and we fixed $n = 0.5$ as we consider that two parameters ($r_{\rm soft}$ and $r_{\rm e}$) are enough to describe properly the radial shape of the brightness profile of a ring.

Once GALFIT has made radial profiles for a component, these are converted to ellipsoidal components, which means we are adding two free parameters to each component, namely a PA and an ellipticity. The only components we have not made elliptical are the Gaussian nuclear components as they are supposed to be related to point-like nuclear sources. When the complex multi-component fit was completed, we looked at the residual image in order to know whether adding more components would be necessary. Components which do not have been fitted are usually easy to detect in the residual image. Nuclear and inner rings appear on it as very bright annuli and bars appear as roughly elliptical bright features. The only components which are not made self-evident when looking at a residual image are nuclei, which are detected as a missing component when the bulge has a Sérsic index which is higher than $n = 5$, and inner and nuclear discs, which are detected when there are truncations and antitruncations in 1D luminosity fits (which are automatically provided by S^{4}G software). We repeated the process of fitting a model until no new component was needed.

In some cases, the fitting procedure crashed, but that was normally solved by changing the initial values. In other cases, the crash was a sign that we missed one or more components. For some galaxies bars (in NGC 1566) and inner rings were not possible to fit, as the algorithm was not converging. In these cases we decided not to fit the problematic component.

For some galaxies, especially strongly barred ones, the disc component is strongly affected by the presence of inner non-axisymmetric components. In these cases we fixed the PA and the ellipticity of the disc with data obtained from outer parts of the disc after running IRAF's ELLIPSE task on the S^{4}G image of the galaxy. In the case of NGC 1097, as the stellar mass of the galaxy is distorted by a companion, we have fixed the disc orientation with data from Lindblad et al. (1997), as we did in Chapter 3.

The images of the processed galaxies, as well as the models, the residual images, and the fits can be found in Fig. C.1 and Fig. C.2 of Appendix C. The fitted properties of discs are summarized in Table 6.3 and in Fig. 6.2, the fitted properties of bulges are summarized in Table 6.4 and in Fig. 6.3, and the fitted properties of bars are summarized in Table 6.5 and in Fig. 6.4.

6.5 Results and discussion

6.5.1 Galaxy discs

When calculating the relative disc mass (Table 6.3) we included the contributions from the inner ring and the oval, except for the case of NGC 289, for which the oval mass was

Table 6.3: Disc properties in our sample galaxies.

Galaxy	Scalelength		PA	$\epsilon_{\rm disc}$	Rel. mass	Fixed?	Inner ring?
	($''$)	(kpc)	($^\circ$)				
(1)	(2)	(3)	(4)	(5)	(6)	(7)	(8)
Galaxies with an outer ring							
NGC 1097	85	6.2	134	0.31	0.48	Y	Y
NGC 1566	302	25.6	95	0.20	0.68	Y	N
NGC 2633	20	3.3	170	0.34	0.45	N	N
NGC 3368	59	3.8	153	0.26	0.73	N	Y
NGC 3504	30	3.5	147	0.06	0.36	Y	Y
NGC 4245	32	2.3	171	0.37	0.56	N	Y
NGC 4698	54	4.1	161	0.51	0.54	N	Y
NGC 5248	87	7.5	105	0.23	0.22	Y	N
NGC 5377	56	8.0	25	0.48	0.32	Y	N
NGC 5448	51	8.0	109	0.57	0.58	Y	Y
NGC 6217	42	4.9	100	0.16	0.50	N	Y
Galaxies without an outer ring							
NGC 289	41	4.1	124	0.26	0.41	N	Y
NGC 1015	22	3.8	20	0.05	0.68	N	Y
NGC 1255	36	3.7	119	0.23	0.92	N	N
NGC 1357	34	4.3	80	0.24	0.85	N	Y
NGC 1367	33	2.9	136	0.29	0.81	N	N
NGC 1438	39	3.7	72	0.38	0.76	N	Y
NGC 2854	9	1.9	48	0.43	0.67	N	N
NGC 4450	46	6.6	175	0.38	0.75	N	N
NGC 4536	53	4.4	111	0.59	0.60	N	N
NGC 4569	60	3.9	22	0.58	0.73	N	N
NGC 6923	18	3.4	74	0.44	0.79	N	N

Notes: Galaxy ID (col. 1), fitted disc scalelength in arcseconds and in kpc (cols. 2 and 3; uncertainties on the order of a 10% of the disc scale-length), disc PA (col. 4; uncertainties on the order 10°), disc ellipticity (col. 5; uncertainties on the order of 0.05; the disc mass may be overestimated as much as a $\sim 10\%$ for galaxies with an inner ring as explained in Section 6.5.4), disc relative mass (col. 6; includes the mass of the disc and eventual inner discs, inner rings and ovals, except for the oval in NGC 289; uncertainties on the order of 0.05), flag which states whether the disc orientation parameters has been fitted or whether they have been fixed as explained in Section. 6.4 (col. 7), and flag which states whether the galaxies has an inner ring (col. 8).

not included. While including inner discs and inner rings in the disc mass is an obvious approach, it is not so evident for the oval mass. However, in most of the galaxies in which we have fitted them, ovals must be interpreted as a mathematical artifice we used to fit a galaxy part. As an example, the ovals in NGC 1255 and NGC 1438 describe a component with an orientation very similar to that of the main disc and which is probably more related to inner

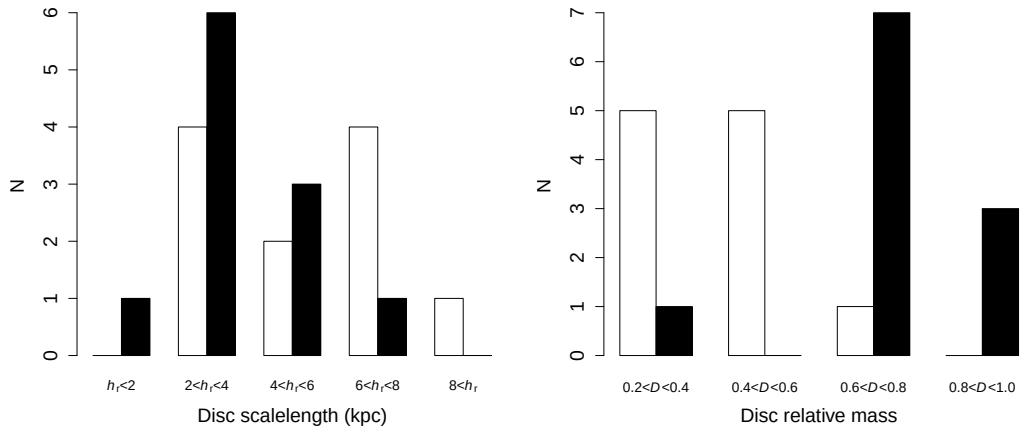

Figure 6.2: Left panel: histogram of fitted disc scalelengths. Right panel: histogram of disc relative masses; this value for disc mass includes the fitted discs, inner discs, inner rings, and ovals. White columns denote galaxies with outer rings and black columns those in the control sample.

discs than to non-axisymmetric components. On the other hand, the oval component we fitted in NGC 289 is very similar to the bar in NGC 1566 and has orientation parameters clearly different from those of the disc of the galaxy, and thus has to be considered together with bars. The inclusion of the mass from the inner ring in the relative disc mass may cause us to overestimate the disc mass as much as a $\sim 10\%$ (see Section 6.5.4 for more details).

We find that the disc scalelengths (h_r) are larger for galaxies with an outer ring than for those without one (left panel in Fig. 6.2). The mean disc scalelength for the discs in ringed galaxies is $h_\mathrm{r} = 7.0 \pm 6.5\,\mathrm{kpc}$, but it is only $h_\mathrm{r} = 3.9 \pm 1.1\,\mathrm{kpc}$ for control galaxies (the uncertainty is at the 1-σ level). We performed a Kolmogorov-Smirnov test on the data and we find that p (the probability that the data forming the two samples comes from the same parent distribution) is $p = 0.21$. We could consider that NGC 1566 is an outlier as its fitted disc scalelength is $h_\mathrm{r} = 25.6\,\mathrm{kpc}$, and when not taking it in consideration, the averaged disc scalelength for ringed galaxies is $h_\mathrm{r} = 5.2 \pm 2.1\,\mathrm{kpc}$. In this case $p = 0.42$ and thus, there is a 58% possibility of the parent distributions being different. As a result we cannot conclude whether the disc scalelengths behave differently in the two samples, given the small number of galaxies included in them. If the measured disc scalelength were really larger for galaxies with an outer ring, it could artificially caused by the effect of outer rings in the fits. These rings are faint, but they occupy a large area in the outskirts of discs, which causes an increase of surface brightness in a wide annulus. The most extreme case is NGC 1566 is which the inner part of the disc is very faint, which causes the fit to result in an enormous disc scalelength. A way to avoid this problem would be to use GALFIT to fit the outer rings, but we decided not to do so, as rings form by far the most complex fitting function we have used in GALFIT (and are thus the most 'unstable' computationally and causes most numerical convergence problems) and the outer rings in our sample have too low surface brightness to get reliable results (however, we have been able to fit brighter outer rings, such as the one in NGC 4736, which is not included in this Chapter due to the lack of any control galaxy which could be matched with it). The picture on disc scalelengths

is even more blurred by the fact that sometimes the inner ring component fits part of the disc. This is especially true for NGC 5448 (see Fig. C.1).

The other difference between the samples that we can identify is that D is smaller for ringed than for non-ringed galaxies ($D = 0.49 \pm 0.15$ and 0.73 ± 0.14 respectively; displayed in the right panel of Fig. 6.2). In this case $p = 0.004$, which makes it very unlikely to have this result by chance. The 'missing' disc mass in ringed galaxies is found partly in bulges and partly in bars, as we will show and discuss in Sections 6.5.2 and 6.5.3. This relative disc mass difference between the two samples is real and, unlike in the case of the possible difference in disc scalelength, not caused by any fitting problem.

We find that the galaxies which need to have the disc orientation fixed in order to get a reasonable fit, tend to be those with a smaller relative disc mass (column 7 in Table 6.3) and thus those with a higher bar mass fraction. As bars can heavily affect the isophotes for inner parts of the disc, it is natural that the most prominent bars imply that extra care is needed when fitting their host galaxies.

To sum up, we find that outer ring galaxies tend to have less massive discs than those in the control sample. We also find very marginal evidence that the fitted scalelengths of discs in galaxies with an outer ring are longer than those in galaxies in the control sample. If this were real, it would due to the effect of the outer ring when fitting the outskirts of the galaxy.

6.5.2 Galaxy bulges

We find no significant difference in the Sérsic index between the ringed and the control samples ($n = 2.7 \pm 1.4$ and $n = 2.1 \pm 1.3$; $p = 0.83$, left panel in Fig. 6.3). However, such a difference cannot be completely ruled out, as the Sérsic index fluctuates considerably with small perturbations in surface brightness and because in some cases the S^{4}G pixel size ($0.75''$) may not sample the nuclear area properly. In addition, in some cases, we may be missing the effect of AGNs, and there is some degeneracy when fitting a bulge in the presence of as many components as we did.

We have calculated the relative mass of the bulge (B) taking in the relative mass of the fitted bulge component plus those of nuclear bars, nuclear rings, and nuclear discs. In the case of NGC 4245, the nuclear bar we have fitted is a small nuclear ring which is blurred by the effect of the pixel size. This nuclear ring has been described in Comerón et al. 2010 and in Chapter 3.

The right panel in Fig. 6.3 shows an histogram of the relative mass of the bulge, B. We find that galaxies with an outer ring tend to have more massive central components than the galaxies from the control sample ($B = 0.30 \pm 0.12$ against $B = 0.13 \pm 0.08$; $p = 0.006$, which implies that the difference is significant). This may be caused, to some extent, by the fact that more than half of the galaxies in our outer ring sample also host a nuclear ring. Actually, of the seven more massive bulges in our outer ring sample, five have a nuclear ring. The intense star formation which is found in a nuclear ring is likely to cause a significant increase in the brightness in the bulge. Thus, the mass of the bulges is affected by nuclear rings and may be overestimated. As an indication of the error we may be making when correlating light with mass, the two nuclear rings we have been able to fit have a mass relative to the galaxy mass of 0.108 (NGC 1097), 0.050 (NGC 4245), and

Table 6.4: Bulge properties in our sample galaxies.

Galaxy	Sérsic index	Rel. mass	Nuclear ring?
(1)	(2)	(3)	(4)
Galaxies with an outer ring			
NGC 1097	1.8	0.33	Y
NGC 1566	1.1	0.06	Y
NGC 2633	0.6	0.36	N
NGC 3368	1.9	0.22	N
NGC 3504	1.3	0.38	Y
NGC 4245	3.2	0.29	Y
NGC 4698	4.8	0.46	N
NGC 5248	3.4	0.37	Y
NGC 5377	3.3	0.40	Y
NGC 5448	3.7	0.22	N
NGC 6217	4.7	0.20	N
Galaxies without an outer ring			
NGC 289	0.7	0.08	N
NGC 1015	1.8	0.20	N
NGC 1255	1.0	0.04	N
NGC 1357	4.3	0.15	N
NGC 1367	1.0	0.10	N
NGC 1438	2.3	0.07	N
NGC 2854	3.6	0.06	N
NGC 4450	1.7	0.12	N
NGC 4536	1.1	0.32	N
NGC 4569	4.2	0.13	N
NGC 6923	1.7	0.15	N

Notes: Galaxy ID (col. 1), fitted disc Sérsic index (col. 2; uncertainties on the order of 1.0), bulge relative mass (col. 3; includes the mass of the bulge and eventual nuclear bars, nuclear discs, and nuclear rings; uncertainties on the order of 0.1 in the case of galaxies with no nuclear ring; in the case of galaxies with a nuclear ring we could be overestimating the relative bulge mass by a value which could be as high as 25% for NGC 1097 and around 10% for the other galaxies; see Section 6.5.4 for more details about the errors), and flag which states whether the galaxy has a nuclear ring (col. 4).

0.058 (NGC 5248). Section 6.5.4 discusses in more detail the uncertainties we introduce by including the nuclear ring mass in the bulge mass. As the nuclear ring in NGC 1097 is the brightest one in our sample (relative ring mass equal to 0.108), the maximum overestimate we make at measuring bulge relative mass is around 0.1. Another possible cause of the higher apparent mass in bulges of galaxies with an outer ring is that, as discs may have longer scalelengths due to the effect of the outer rings, the extrapolation of the disc to smaller radii may underestimate the disc contribution to the light within the bulge radius, thus giving rise to an apparently brighter bulge.

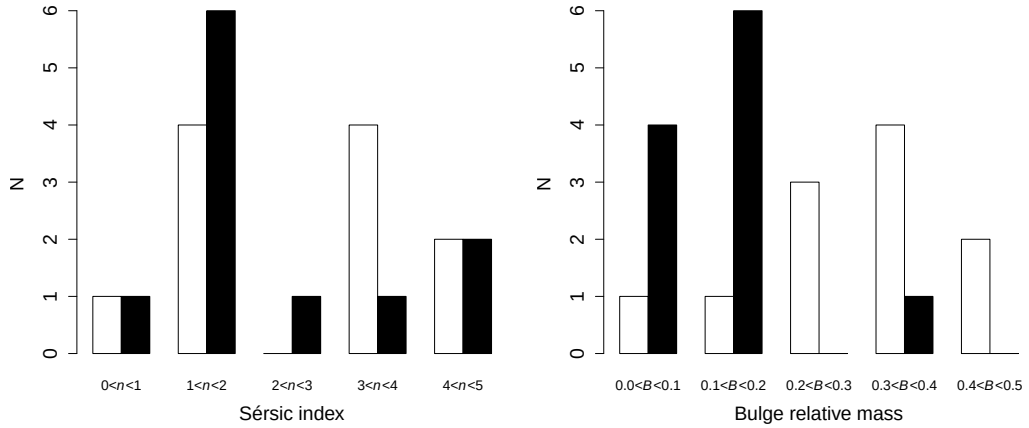

Figure 6.3: Left panel: histogram of fitted bulge Sérsic indexes. Right panel: histogram of bulge relative masses; this value for bulge mass includes the fitted bulges, nuclear discs, nuclear rings, and nuclear bars. White columns denote galaxies with outer rings and black columns those in the control sample.

We find no nuclear rings in galaxies without an outer ring. It thus seem that nuclear rings share the formation mechanisms with outer rings and that they 'prefer' to be in galaxies with an outer ring. However, the correlation between nuclear and outer rings is not one to one as seen in the morphological classification in Table B.1 and the data in Table 6.4. One may also expect that if there is a correlation between the presence of nuclear rings and the presence of outer rings, the presence of outer rings should also correlate with that of inner rings, which is not the case for the galaxies we studied.

In conclusion, we find no evidence for a difference in Sérsic index between the galaxies in the two samples. We find that bulges are more massive in galaxies with outer rings, but this could well be artificial, caused by a combination of the effect of nuclear rings and a lack of central luminosity for the fitted galaxy discs.

6.5.3 Galaxy bars

When fitting NGC 289, we found that it has a bar and an oval distortion. We considered the bar to be the most influential non-axisymmetric feature of the galaxy as the peak of the non-axisymmetric torques is found inside it. Thus the bar length and ellipticity in Table 6.5 for NGC 289 are for the bar and not for the oval. When fitting NGC 1566 we have visually detected two bars within it: a small bar inside the inner pseudo-ring and the large scale bar/oval we have fitted. Unfortunately, we were not able to fit satisfactorily the innermost bar, and thus the fit we present in Fig. C.1 includes only the large scale bar/oval.

We have to note that the bar length measured when fitting a Ferrers component with Galfit is not the same as that measured in Chapter 3. In Chapter 3, we were measuring as the bar length the peak of the ellipticity within it, which is known to be a lower estimate to the bar length (Erwin 2005). What Galfit gives as bar length is the truncation radius of the Ferrers function, which is by definition larger than the maximum ellipticity radius. Furthermore, we find that our fits sometimes slightly overestimate the bar length (compare

Table 6.5: Bar properties in our sample galaxies.

Galaxy	Bar length		r_ϵ	ϵ_b	Rel. mass	Q_g	Source
	($''$)	(kpc)	(kpc)				
(1)	(2)	(3)	(4)	(5)	(6)	(7)	(8)
Galaxies with an outer ring							
NGC 1097	160	11.8	6.7	0.38	0.12	0.279	L04
NGC 1566	272	23.0	11.6	0.50	0.26	0.235	C10
NGC 2633	30	5.1	2.9	0.44	0.19	0.157	New
NGC 3368	55	6.0	4.6	0.66	0.24	0.139	New
NGC 3504	64	7.4	3.6	0.40	0.26	0.288	L04
NGC 4245	60	4.3	3.3	0.54	0.15	0.180	C10
NGC 4698	–	–	–	–	0.00	0.088	L04
NGC 5248	159	13.8	9.5	0.52	0.41	0.100	C10
NGC 5377	128	18.2	10.4	0.44	0.28	0.164	C10
NGC 5448	64	10.0	6.9	0.58	0.21	0.136	New
NGC 6217	66	7.7	4.2	0.35	0.30	0.360	L02
Galaxies without an outer ring							
NGC 289	30	3.0	2.0	0.61	0.50	0.212	L04
NGC 1015	31	5.4	4.1	0.26	0.12	0.247	New
NGC 1255	66	6.9	3.2	0.28	0.04	0.150	L02
NGC 1357	–	–	–	–	0.00	0.067	New
NGC 1367	53	4.6	3.3	0.40	0.07	0.120	L02
NGC 1438	52	5.0	2.9	0.38	0.17	0.393	New
NGC 2854	21	4.4	2.1	0.37	0.24	0.245	New
NGC 4450	77	11.1	6.9	0.59	0.11	0.131	L04
NGC 4536	100	8.4	5.5	0.59	0.08	0.072	New
NGC 4569	115	7.1	4.4	0.53	0.14	0.150	L04
NGC 6923	18	3.5	2.6	0.57	0.06	0.093	New

Notes: Galaxy ID (col. 1), fitted bar length in arcseconds and in kpc (cols. 2 and 3; uncertainties on the order of 20% of the bar length), bar length measured as the radius at which the bar ellipticity is maximum (col. 4; uncertainties on the order of 20% of the bar length) fitted bar ellipticity (col. 5; uncertainties on the order of 0.05), bar relative mass (col. 6; includes the oval mass in the case of NGC 289; uncertainties on the order of 0.1), Q_g (col. 7; uncertainties on the order of 0.05), and literature source for Q_g (col. 8). L02: Laurikainen et al. (2002), L04: Laurikainen et al. (2004a), and C10: Comerón et al. (2010). 'New' means that the Q_b have been calculated by us for this Chapter. The bar length and ellipticity has been calculated after deprojecting the galaxy, considering a circular disc with the orientation parameters in Table. 6.3.

the NGC 1097 model with the real image in Fig. C.1 for an example). We quantified how much larger are the bars in our fits compared to the bar lengths we would get if we had measured them using the method of Chapter 3. To do so, we have downloaded 2MASS H-band images for all our sample galaxies and we have deprojected them using the disc

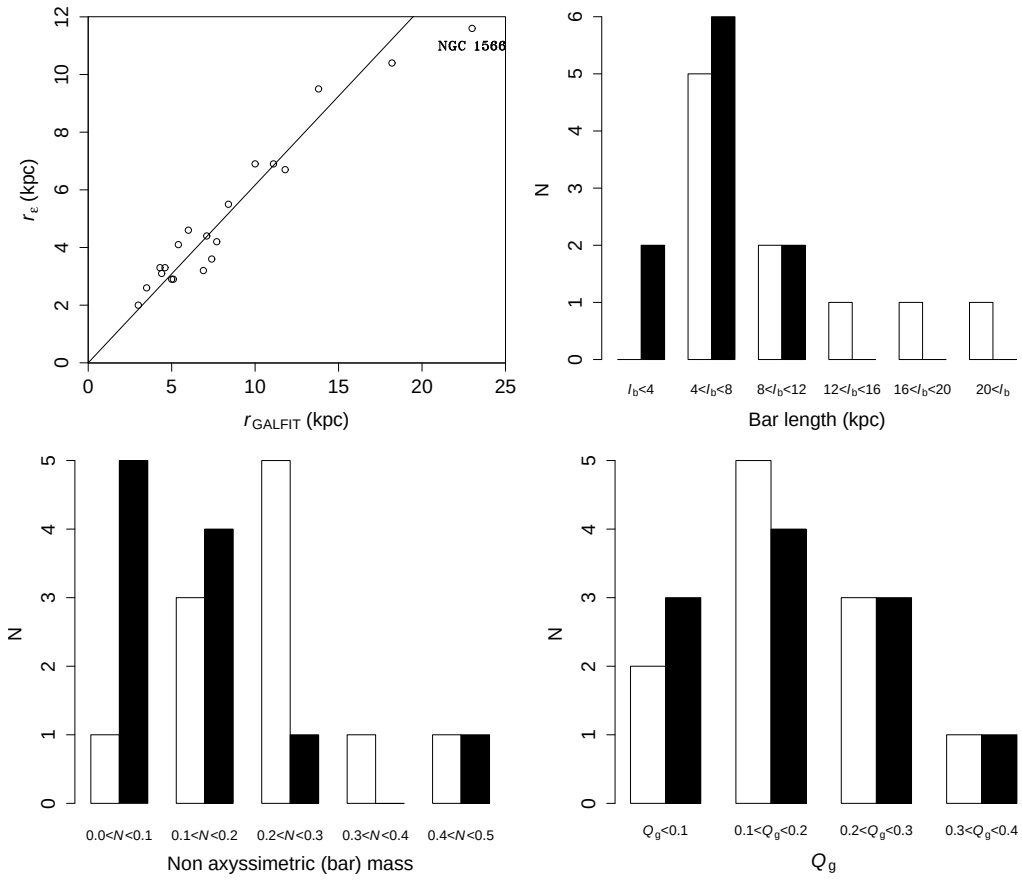

Figure 6.4: Top-left panel: scatter plot whith, in the horizontal axis, the length of the bar as measured using GALFIT and, in the vertical axis, the radius of the bar measured as the ellipticity maximum in an ellipticity profile. The line denotes a linear fit for which NGC 1566 has been discarded as an outlier and the intercept value has been fixed to zero. Top-right panel: histogram of fitted bar length. Bottom-left panel: histogram of bar relative masses; this value for the bar mass includes the fitted bars and the oval component in the case of NGC 289. Bottom-right panel: histogram of the non-axisymmetric torques, Q_g. In the histograms, white columns denote galaxies with outer rings and black columns those in the control sample.

orientation parameters (Table 6.3). We then used IRAF's ELLIPSE task in order to find the peak in the ellipticity. The results are listed in Table 6.5. After doing a linear regression, we find that our bars are 1.60 ± 0.05 times longer when measured using our 2D fits than when measured using ellipticity fits. For this regression, we fixed the intercept equal to zero and we did not use NGC 1566 as it is a clear outlier. The results appear in the top-left panel of Fig. 6.4.

We find that extremely long bars are found only in galaxies with an outer ring (top-right panel in Fig. 6.4). Galaxies with an outer ring have an average bar length of $r = 10.7\,\mathrm{kpc}$, and bars without an outer ring are on average $r = 6.0\,\mathrm{kpc}$ in length (a Kolmogorov-Smirnov test gives $p = 0.17$). A visual inspection of the galaxies in Figs. C.1 and C.2 shows that this difference is caused by several galaxies in which the bar is very long and wide and occupies the whole minor axis of the outer ring. This is the case for NGC 1097, NGC 1566, NGC 2633,

NGC 3504, NGC 5248, NGC 5377, and NGC 5448. They also look visually very extended and massive. In contrast, bars in the control sample galaxies are usually shorter and do not appear so massive. Several of these bars are so wide, and may show such developed embedded spiral arms, that they may be confused with galaxy discs (Jogee et al. 2002). We indeed find that bars in galaxies with an outer ring are in general more massive. We find that the non-axisymmetric mass relative to the galaxy mass is $N = 0.21 \pm 0.11$ for galaxies with an outer ring and $N = 0.14 \pm 0.14$ (bottom-left panel in Fig. 6.4; $p = 0.02$). Although the difference may not appear very significant ('only' a 98% possibility of the difference being true), we have to take into account that N is probably larger than calculated for those galaxies with an outer ring, as the bulge mass, and thus the total galaxy mass, is probably overestimated (see Section 6.5.2).

In order to see whether this larger bar mass in the ringed galaxies is related to the strength of the non-axisymmetries, $Q_{\rm g}$ (at a first approximation equal to the bar strength), we have searched in the literature for $Q_{\rm g}$ values for the 22 studied galaxies. Where there is no $Q_{\rm g}$ value in the literature, we have calculated it using the procedure described in Section 3.4.3. For this calculation we used 2MASS H-band images with the galaxy disc parameters listed in Table 6.3. The $Q_{\rm g}$ values are presented in Table 6.5 and plotted as a histogram in the bottom-right panel of Fig. 6.4. We find that the $Q_{\rm g}$ values are very similar for the two samples ($Q_{\rm g} = 0.19 \pm 0.09$ in the outer ring sample and $Q_{\rm g} = 0.17 \pm 0.10$ in the control sample; $p = 0.83$).

In summary, outer rings 'prefer' to be hosted in galaxies with massive bars which almost completely fill the ring minor axis.

6.5.4 Caveats in this Chapter

As this Chapter constitutes a rather preliminary phase of an ongoing study, we have assumed a constant mass-to-light ratio (M/L) for all the components. This approach is only valid as a very rough approximation. Deducing the mass-to-light ratio of different galaxy areas is an intense field of research (see, e.g., Bell & de Jong 2001; Melena et al. 2009; Zibetti et al. 2009). A recent study on this topic has been made by Kendall et al. (2008) using several observed wavebands, including the two bluest IRAC bands, and there is an ongoing S^{4}G sub-project on this topic (S. Meidt et al. 2010, in preparation). At the wavelengths of the IRAC bands, the potential problems which interfere with the emission from the main sequence stars are the 3.3μm Polycyclic Aromatic Hydrocarbon (PAH) emission, the continuum emission from hot dust, and the lower M/L for post-AGB and red supergiants stars (S. Meidt 2010, in preparation).

The most obvious case of an incorrect use of a constant mass-to-light ratio is that of fitting a nuclear ring, as these features sustain the most intense star formation activity in many starburst galaxies (Elmegreen 1994), and thus are the areas with most contamination by hot dust and red supergiant stars. Knapen et al. (1995) estimated that for the nuclear ring in NGC 4321 the stellar mass-to-light ratio in the K-band is $M/L \sim 0.3 - 0.4 M_{\odot}/L_{\odot}$, when outside the ring it is $M/L > 0.7 M_{\odot}/L_{\odot}$. If we consider NGC 4321 to be a typical nuclear ring and if we consider the behaviour of the 3.6μm-band to be not too far from the K-band, this would imply that we are overestimating the nuclear ring mass by a factor of $2-3$. NGC 1097 hosts by far the most spectacular nuclear ring in our sample, and thus, the

one for which the greatest uncertainty may have been introduced. For NGC 1097, the ring emission accounts for one third of bulge emission. If we consider that assuming a constant mass-to-light ratio leads to an overestimate of the ring mass by a factor of three, we are overestimating the bulge mass by around 25%. In the case of NGC 4245 and NGC 5248, the nuclear ring light constitutes just one sixth of the overall bulge emission, and thus the possible overestimate for the bulge mass is much smaller ($\sim 10\%$). As those galaxies for which we have not explicitly fitted a nuclear ring will not host rings as prominent as in NGC 1097, the overestimate in the relative bulge mass is in those cases likely to be in the order of that in NGC 4245 and NGC 5248, or smaller.

To mitigate the consequences of the use of a constant mass-to-light ratio for nuclear rings, we could either have removed the nuclear rings from the bulge mass, or we could have multiplied their contribution to the bulge mass by a certain factor between zero and one to take into account their difference M/L. But, as we have not been able to fit the nuclear rings in all the galaxies which are known to host one, this would have introduced an unequal treatment of the different galaxies. Furthermore, some of the galaxies in this sample were not included in the survey for nuclear rings of Chapter 3 and thus they could have small nuclear rings yet to be discovered that we would not be taking into consideration. However, as in most of the cases their effect in the relative bulge mass is not expected to be much higher than a 10%, taking them into account would not have changed our mass estimates drastically. This issue remains to be studied in more depth in future work.

A similar problem to that encountered for the nuclear rings occurs when assuming a constant mass-to-light ratio for inner rings. However, as inner rings do not host such a concentrated star formation, the uncertainty when assuming a constant mass-to-light ratio for them is most probably smaller. We could have chosen not to include the mass of those which were fitted when calculating D, but we did not do so for two reasons. The first reason is that, in some cases, the inner ring component fits part of the disc (this is especially true for NGC 5448, where our fit yields a relative emission contribution from the inner ring of 0.256, but it is, to some extent, the case for all the galaxies with a fitted inner ring). This would make removing the ring component incorrect, as we would be removing part of the disc. The second reason is that some rings could not be fitted and their emission is included in the D component of their host galaxies.

We find that seven galaxies with an outer ring also host an inner ring, namely NGC 1097, NGC 3368, NGC 3504, NGC 4245, NGC 4698, NGC 5448, and NGC 6217. Of these, only four inner rings could be included in the fit, namely those in NGC 3368, NGC 4245, NGC 5448, and NGC 6217. In the control sample we find four inner rings, in NGC 289, NGC 1015, NGC 1357, and NGC 1438. Of these, only the ring in NGC 289 has been fitted. As we expect the effect of the inner rings on the overall discs to be similar or smaller than those of nuclear rings on the bulges, we deduce that we are overestimating the mass of the discs by $10 - 20\%$ in galaxies with an inner ring. This would not significantly change the results in Section 6.5.1.

More subtle effects of assuming a constant mass-to-light ratio may be expected when comparing bulge components with discs and bars, as discs and bars host star-forming regions which may have an effect similar to that of nuclear and inner rings. These effects have been ignored here but, again, should be carefully considered and quantified in further work.

Another possible issue with 2D decompositions is that of degeneracies. Outside the

bulge, it is relatively easy to decide which components need to be fitted and whether the resulting fit makes sense. However, for the few central pixels, one may have to fit as much as two or three components, which implies 10 or more fitting parameters. This may lead to degeneracies which have as a consequence a high variability on the final result depending on the initial fitting values. However, Peng et al. (2010), in a long analysis of GALFIT degeneracies, consider the effect small when using their code with a "judicious combination of simplicity and realism". As, except for a couple galaxies which had difficulties at fitting, we have only fitted components which can be seen by eye in the original image, we think that we have met this prescription and, thus, mostly avoided degeneracies. We thus conclude that our decompositions are trustworthy and unique, and that the relative masses derived from them are accurate to the levels of uncertainty described in the preceding paragraphs.

6.6 Conclusions

In this Chapter we have illustrated that the use of GALFIT on S^4G images is indeed a useful approach to studying the components which build up galaxies. However, for producing a deeper study in a larger sample of galaxies we will first need to solve some of the problems which we encountered in this pilot study. First of all, a good mapping of the stellar mass-to-light ratio has to be obtained combining several colours under certain assumptions and using certain prescriptions (Bell & de Jong 2001; Kendall et al. 2008; Melena et al. 2009; Zibetti et al. 2009) in order to improve the quality of our results. Degeneracy effects in the fitting process may also be an issue, although the developers of GALFIT do not consider them to be very important (Peng et al. 2010).

Our preliminary results show that outer rings are found preferentially in galaxies with bars that are more massive, wider, and longer (but not stronger, as measured through a higher Q_g value) than those in the control sample. As the relative bar mass for these galaxies is higher than average, the relative disc mass becomes lower. We also find that bulges in galaxies with outer rings look more massive, but this may be caused by the contributions from bright nuclear rings which, in our sample, are found only in galaxies with an outer ring.

As most of the outer rings in our sample are of the R'_1 variety, it is natural that we find that the bar fills their minor axis: these rings are defined as being made of two 180° winding arms with respect to the ends of a bar or an oval. Outer rings are thought to be related to OLRs (Schwarz 1981), but we see that even though all barred galaxies have an OLR, only for some of these galaxies an outer ring is formed. Our findings seem to indicate that the formation of R'_1 rings is favoured whenever a bar is long and wide enough (with no strong influence of the bar strength). This may be related to the fact that the gain of angular momentum for gas clouds outside the bar corotation orbit is only possible when the corotation radius is placed at low-density disc regions, where there is little risk of a cloud-cloud collision. For shorter bars, deeply embedded in denser regions of the disc, this gain of angular momentum for the gaseous component may be impossible. Thus, only for long bars would the corotation be in areas with low enough density to allow a gas clump to reach the OLR orbits.

We find that of our eleven galaxies with outer rings, seven host an inner ring, and at least six host a nuclear ring. The 11 galaxies with no outer ring only have four inner rings and

no nuclear rings. It thus seem that the very same mechanisms which trigger the formation of an outer ring are also responsible for the creation of nuclear and inner rings. As we have discussed in Chapter 3, nuclear rings are a product of resonances with non-axisymmetric features. As rings preferably occur together, it is thus natural to think they are all a manifestation of the same phenomenon, namely a non-axisymmetric structure which is self-consistent and rotates as a rigid solid at a given pattern speed causing angular momentum redistribution and resonant phenomena at radii varying from a few tens of parsecs for the smallest nuclear rings to 10 kiloparsecs or more for the largest outer rings. As a consequence, the resonance drivers (bars, ovals, and spiral patterns) are the main agents which produce the secular reshaping of galaxies at nearly all scales within the galactic discs.

7

Conclusions

The core of this thesis is a study of star-forming nuclear rings and their origins (Chapters 2 and 3). When preparing it we have also studied some features which may be caused by nuclear rings (such as σ-drops) and features which are caused by bars, as nearly 80% of star-forming nuclear rings are. We have also investigated the highly-inclined galaxy NGC 4244 and have made decompositions of galaxies with an outer ring using GALFIT. We have answered several questions on all these topics, but new questions have appeared. In this Chapter we summarize the answers we have found, as well as the points which remain to be solved.

7.1 Sigma-drops

After comparing the morphological properties of a sample of 20 σ-drop host galaxies with a matched sample of 20 galaxies with no σ-drops we find that:

- There is no significant relation between the presence of a bar and the presence of a σ-drop. Thus bars, at least strong SB bars, are not needed for a galaxy to have a σ-drop.
- Sigma-drops have some correlation with the presence of nuclear dust spirals and nuclear star-forming rings.
- The radius of a σ-drop is independent of other tested parameters of the host galaxy, such as the galaxy size and the bar type.
- Sigma-drop galaxies have a certain tendency to host Seyfert nuclei, while galaxies from the control sample 'prefer' to host LINER nuclei. This correlation is not very strong, presumably because σ-drops and AGN have different time-scales.
- There is no significant relation between the luminosity profiles of the host galaxies and the presence or absence of σ-drops.
- There is no significant relation between the presence or absence of a σ-drop and the H I and CO radio emissions.

We suggest the following model for the creation of a σ-drop. Gas is driven inwards by spiral arms and maybe by bars. The gas is focused by an ILR into a dynamically cold ring where the density increases until it reaches a critical value when star formation starts. These stars are dynamically cold and start to create a σ-drop. Alternatively, if there is no ILR, gas can be focused in a cold nuclear disc that also starts to create stars when it reaches the critical density. In both cases friction causes some gas to lose enough angular momentum to drift inwards to feed the super-massive black hole. This gas can be traced with the dust related to the relatively recent star formation. As a σ-drop is a long-lived feature it would survive long after the ring or the disc has disappeared.

7.2 Nuclear rings

We have produced the most complete atlas of nuclear rings to date, which is called Atlas of Images of NUclear Rings (AINUR). This atlas includes 113 nuclear rings in 107 galaxies. Of those galaxies, six of which are elliptical or early lenticular galaxies, five are highly inclined galaxies, 18 are unbarred disc galaxies, and 78 are barred disc galaxies. The atlas includes imaging of all the nuclear rings, in most of the cases coming from high-resolution frames of the *HST* archive (Appendix B).

7.2.1 Star-forming 'classical' nuclear rings

When starting this thesis, we had encountered two assumptions about star-forming nuclear rings, namely:

- Nuclear rings were assumed to be related to resonances with non-axisymmetries of the galactic potential (Simkin et al. 1980; Combes & Gerin 1985), but that had been proved just for a few individual cases (like in Knapen et al. 1995).
- Nuclear rings were usually linked with large-scale bars and were supposed to be found between the two ILRs (or inside a single ILR in a galaxy with an extremely strong bar).

We find that:

- For rings located in barred galaxies, the maximum possible radius for a star-forming nuclear ring inside a given bar is a quarter of the length of the bar measured as the peak in ellipticity. We also find that the maximum possible size of a ring relative to galaxy radius is inversely proportional to non-axisymmetric torque parameter, $Q_{\rm g}$. These two findings for rings in barred galaxies are exactly what would have been expected if rings were found between the two ILRs, since the size of the outer ILR follows the same trends. Thus, we have statistically shown that star-forming nuclear rings are related to resonances in a non-axisymmetric galactic potential, with very few possible exceptions. This study thus confirms the value of nuclear rings, together with inner and outer rings, in the observational study of the dynamics and evolution of galaxies.

- Star-forming nuclear rings do not have a strong preference for barred host galaxies. Some $19 \pm 4\%$ of them (18 nuclear rings in AINUR) occur in non-barred galaxies, a similar proportion to the fraction of non-barred galaxies in all disc galaxies, though some evidence for non-axisymmetry in the potential can be discerned in most of these hosts. These non-axisymmetries can in principle cause resonances which can lead to ring formation.

In addition, we find that:

- Star-forming nuclear rings are found in $20 \pm 2\%$ of disc galaxies in the range of morphological types $-3 \leq T \leq 7$. Under the assumption that all disc galaxies at some stage host a nuclear ring, this number would imply an effective nuclear ring lifetime of $2-3$ Gyr, in broad agreement with a range of other observational and numerical studies.

- Star-forming rings are predominantly found in galaxies with morphological types ranging from S0 to Sc. Only one nuclear ring was found in an Sd-type galaxy, and none in later types. We infer that the shallow mass distribution of such galaxies is unfavourable to the existence of ILRs, and thus nuclear rings.

- Nuclear rings are not affected by *local* non-axisymmetric torques, which we measure by the amplitude of the torque parameter at the radius of the nuclear ring (the maximum amplitude of this parameter is $Q_{\rm g}$, and this maximum always occurs outside the nuclear ring). This confirms that the nuclear ring is mainly affected by the non-axisymmetries on larger scales than the ring itself.

7.2.2 Star-forming Ultra-Compact Nuclear Rings

When starting this thesis it was unknown whether star-forming UCNRs were just the low-size tail of the nuclear ring size distribution, thus sharing a common origin with 'classical' rings, or whether they were caused by a different physical mechanism such as some kind of interaction of a central SMBH with the surrounding interstellar medium. After studying in detail four star-forming UCNRs in Chapter 2 and studying some more UCNRs in Chapter 3, we find that:

- Star-forming UCNRs are morphologically similar to 'canonical' nuclear rings and, under a visual inspection, scaled-down versions of them. This makes unlikely that they have a formation scenario different to that of other star-forming nuclear rings.

- Star-forming UCNRs are not systematically located at the corotation resonance of a nuclear bar and are often found in galaxies with no nuclear bars. Thus they are related to ILRs of large-scale bars, just as 'canonical' nuclear rings are.

- Star-forming UCNRs are not preferentially found in late-type galaxies with smaller bulges, which would place the ILRs further in.

We conclude that star-forming UCNRs are just 'normal' but small star-forming nuclear rings which for some reason, are located further inside in the galaxy. The only exception is the innermost UCNR in NGC 2787, which is probably caused by the central black hole ionizing the inner part of a polar disc of material.

7.2.3 Dust nuclear rings

- Dust nuclear rings are found in $6 \pm 2\%$ of elliptical galaxies.
- Dust nuclear rings are found in elliptical and early lenticular galaxies and have a different origin than star-forming nuclear rings. Lauer et al. (2005) assert that these rings may be caused by a depletion from inside out of a dust nuclear disc.

7.3 Dust lanes

We have confirmed the theoretical prediction made by Athanassoula (1992) that the dust curvature anticorrelates with the bar strength when using $Q_{\rm b}$ as a bar strength indicator. Strong bars in general host the straightest dust lanes, and weak bars show more curved dust lanes. However, we found that this anticorrelation has a huge spread, which has also been found in a set of 238 numerical simulations of barred disc galaxies which we made. Using the 238 simulated galaxies we have found that the spread in the anticorrelation between the dust curvature and the bar strength can be highly reduced by using as a bar indicator an appropriate linear combination of bar parameters, namely

$$Q_{\rm b} - 0.087\, a/b = (0.156 \pm 0.020) - (0.119 \pm 0.015) \log_{10}\Delta\alpha, \tag{7.1}$$

which shows that $Q_{\rm b}$ is not always an ideal bar strength indicator (a/b stands for the bar axis ratio and $\Delta\alpha$ for the dust lane curvature), and that, in this case, a combination of $Q_{\rm b}$ and the bar ellipticity is superior.

7.4 NGC 4244

NGC 4244 has been reported to be either the only nearby edge-on galaxy for which a thick disc has not been detected or to be a doubtful case. As a galaxy with a lack of a thick disc component would constitute a serious challenge for some galaxy formation models, we have made an in-depth study of NGC 4244. Using data from the S^4G we have found that this galaxy seems to have a tenuous thick disk. We have also found that the asymmetries between the light profiles on either side of the mid-plane of NGC 4244 can be explained by a combination of the galaxy not being perfectly edge-on and a certain degree of opacity of the thin disk. We argue that the subtleness of the thick disk is a consequence of the lack of secular evolution in NGC 4244. We also argue that what is apparently a warp, is actually the effect of spiral arms in a not perfectly edge-on galaxy.

7.5 Galaxies with an outer ring

Using GALFIT decompositions of S^4G images we find that outer rings are found preferentially in galaxies with more massive, wider, and longer bars (but not stronger) than those

bars in the control sample. As the relative bar mass for these galaxies is higher than in the control sample, the relative disc mass becomes lower. We also find that bulges in galaxies with outer rings look more massive, but this is probably artificially caused by bright nuclear rings which, in our sample, are found only in galaxies with an outer ring.

7.6 Open questions

7.6.1 Sigma-drops

- Why do σ-drops have some correlation with Seyfert nuclei if the time-scale of a σ-drop is $\sim 10^9$ years and the time-scale of an AGN is $\sim 10^8$ years?

7.6.2 Nuclear rings

- Star-forming nuclear rings in barred galaxies are located in a wide range of radii, which approximatively matches the extent of the radii at which x_2 orbits are found. At which position between the ILRs is a nuclear ring formed? Do they form at a random position? Could a radial shrinkage with time from a position which is near the outer ILR explain that the whole x_2 region can be populated with star-forming nuclear rings?

- We find that there is no preferred PA offset between the nuclear ring major axis and the bar major axis, even if one may intuitively think that, as nuclear rings are usually found in x_2 orbits, they should be perpendicular to the bar. However, as nuclear rings are nearly round, small errors in the galaxy deprojection parameters could hide any possible correlation.

- We find some hint that indicates that the maximum possible ring ellipticity correlates with the ellipticity of the bar. However, this is unsure, due to the errors introduced in the measurement of ring ellipticity when deprojecting the galaxy.

- We find no correlation between the bulge shape (Sérsic index) and the star-forming nuclear ring properties. However, as the bulge properties were measured in 2MASS images which, in some cases, barely resolve or do not resolve the bulge, further study is needed on this topic with higher resolution near-IR imaging.

- Some literature sources report a correlation between nuclear star-forming rings and AGNs. This is surprising, since nuclear rings have time-scales and spatial scales which are much longer than that of an AGN. In AINUR (Chapter 3) we find no correlation between nuclear rings and the presence of AGNs, which seems to contradict the result of Chapter 1, that σ-drops correlate both with Seyfert galaxies and nuclear rings.

7.6.3 Dust lanes

- We define a new bar strength indicator using data from simulated galaxies. This new indicator should be tested in real galaxies. We have not done it because for calculating this indicator we would need to know the true bar ellipticity of the galaxy. This means

that a bulge/bar/disc decomposition should have been done for a significant sample of galaxies in order to know the bar ellipticity, after removing the influence of the disc and bulge. These decompositions should be done in high-resolution near-IR images in order to avoid the effects of dust and in order to properly resolve the bulge.

7.6.4 NGC 4244

- What causes the subtleness of the thick disc in NGC 4244? Why has secular evolution had so little effect in this galaxy?

7.6.5 Outer ring galaxies

- A larger sample is needed in order to confirm our preliminary findings.
- We need find ways to deal with different mass-to-light ratios in different galaxy components.
- We need to estimate the effect of degenerations in the fits.

8

Conclusiones

El núcleo de esta tesis es el estudio de los anillos nucleares de formación estelar y sus causas (Capítulos 2 y 3). Mientras preparábamos esos Capítulos, hemos estudiado ciertas estructuras que pueden ser causadas por los anillos nucleares (como los σ-drops) y estructuras que han sido causadas por las barras, al igual que el 80% de los anillos nucleares de formación estelar. También hemos estudiado una galaxia muy inclinada, NGC 4244. Hemos contestado a varias preguntas que no se habían resuelto todavía en los temas estudiados, pero nuevas preguntas han aparecido. En este Capítulo resumimos las respuestas que hemos encontrado y también los puntos que requieren más estudio para poder resolverse.

8.1 Sigma-drops

Después de comparar las propiedades morfológicas de una muestra de 20 galaxias con σ-drop con una muestra emparejada de 20 galaxias sin σ-drop hemos descubierto que:

- No hay diferencias significativas entre la distribución de barras en las galaxias con σ-drop y las galaxias sin ellos. Por consiguiente las barras, al menos las SB, no son necesarias para la existencia de un σ-drop.

- Los σ-drops tienen cierta correlación con la presencia de espirales de polvo nucleares y anillos nucleares de formación estelar.

- El radio de un σ-drop es independiente de los demás parámetros que hemos medido en las galaxias huésped, como pueden ser el tamaño de la galaxia y el tipo de la barra.

- Las galaxias con σ-drop tienen cierta tendencia a hospedar núcleos Seyfert y las galaxias de la muestra de control 'prefieren' hospedar un núcleo LINER. La correlación no es muy fuerte, seguramente debido a que los σ-drop y los AGN tienen tiempos de escala distintos.

- No hay ninguna correlación significativa entre el tipo de perfil de luminosidad de la galaxia huésped y la presencia o ausencia de un σ-drop.

- No hay ninguna correlación significativa entre la presencia o ausencia de un σ-drop y las emisiones en H I y en CO.

Sugerimos el siguiente modelo para la creación de σ-drops. El gas es conducido hacia el bulbo de la galaxia por brazos espirales y tal vez por barras. Dicho gas es dirigido por una ILR a un anillo dinámicamente frío hasta que alcanza una densidad crítica para la cuál se inicia la formación estelar. Estas estrellas son dinámicamente frías, lo que empieza a generar un σ-drop. Alternativamente, si no hay ILR, el gas puede condensarse en un disco nuclear frío que también empieza a crear estrellas cuando alcanza una densidad crítica. En ambos casos, parte del gas pierde momento angular debido a procesos de fricción y se mueve radialmente hacia el núcleo donde alimenta el agujero negro super-masivo. Ese gas es trazado por polvo relacionado con los recientes episodios de formación estelar. Como un σ-drop tiene un tiempo de vida largo, sobrevive incluso hasta después de que el anillo o el disco hayan desaparecido.

8.2 Anillos nucleares

Hemos preparado el atlas más completo de anillos nucleares hecho hasta la fecha y lo hemos llamado Atlas of Images of NUclear Rings (AINUR). El atlas incluye 113 anillos nucleares en 107 galaxias, de las cuáles, seis son galaxias elípticas o galaxias lenticulares tempranas, cinco son galaxias con disco muy inclinadas, 18 son galaxias con disco sin barra y 78 son galaxias con disco y con barra. El atlas incluye imágenes de todos esos anillos y, en la mayoría de los casos, éstas tienen alta resolución dado que provienen del archivo del *HST* (Apéndice B).

8.2.1 Anillos nucleares de formación estelar 'clásicos'

Cuando iniciamos esta tesis, existían dos suposiciones sobre los anillos nucleares de formación estelar:

- Se creía que los anillos nucleares estaban relacionados con resonancias debidas a las no-axisimietrías del potencial galáctico (Simkin et al. 1980; Combes & Gerin 1985), pero eso solamente se había demostrado para unos pocos casos concretos (como por ejemplo en Knapen et al. 1995).
- Se relacionaba a los anillos nucleares con barras a gran escala, y se suponía que se encontraban entre las dos ILRs de la barra (o dentro de una única ILR en el caso de galaxias con barras extremadamente fuertes).

Hemos descubierto que:

- Para los anillos que se encuentran en galaxias barradas, el máximo radio posible para un anillo nuclear de formación estelar dentro de la barra es una cuarta parte de la longitud de la barra si ésta se mide como el máximo en elipticidad. También hemos descubierto que el máximo tamaño posible para un anillo (relativo al tamaño de la galaxia) es inversamente proporcional al parámetro de torsión de las estructuras no-axisimétricas, $Q_{\rm g}$. Estos dos descubrimientos son exactamente los que uno esperaría

si los anillos nucleares se encontraran entre las dos ILRs, ya que la ILR externa tiene ese mismo comportamiento. Por consiguiente, hemos demostrado estadísticamente que los anillos nucleares de formación estelar están relacionados con las resonancias en un potencial no axisimétrico, con muy pocas excepciones posibles. En conclusión, este estudio confirma la utilidad de los anillos nucleares, junto con los anillos internos y externos, en el campo del estudio de la dinámica y de la evolución de galaxias.

- Los anillos nucleares de formación estelar no tienen una fuerte preferencia por las galaxias barradas. El $19 \pm 4\%$ de ellos (18 anillos nucleares en AINUR) se encuentran en galaxias no barradas, la cuál es una proporción similar a la de galaxias no barradas con respecto a la población de galaxias con disco. No obstante, en casi todos los casos de anillos nucleares en galaxias no barradas, hemos descubierto evidencias que indican la presencia de no-axisimetrías en el potencial gravitatorio de las galaxias huésped. En principio, dichas no-axisimetrías podrían causar resonancias que tuvieran como consecuencia la creación de anillos.

Además, hemos descubierto que:

- Los anillos nucleares de formación estelar se encuentran en un $20 \pm 2\%$ de las galaxias con disco con tipos morfológicos en el rango $-3 \leq T \leq 7$. Si suponemos que todas galaxias con disco tienen en algún momento de su existencia un anillo nuclear, eso implicaría un tiempo de vida efectivo de los anillos de $2-3$ giga-años, cosa que concuerda con numerosos estudios observacionales y numerosas simulaciones numéricas.

- Los anillos nucleares de formación estelar suelen encontrarse en galaxias con tipos morfológicos que van de S0 a Sc. Únicamente descubrimos una galaxia de tipo Sd con anillo sin encontrar ninguna de tipo más tardío que tuviera uno. A partir de esto, deducimos que la distribución de masa de ese tipo de galaxias no favorece la existencia de ILRs y, en consecuencia, de anillos nucleares.

- Los anillos nucleares no se ven afectados por las no-axisimetrías *locales* que hemos medido usando el parámetro de torsión de las estructuras no-axisimétricas en el radio del anillo nuclear (el máximo en este parámetro es $Q_{\rm g}$, y éste siempre se encuentra en zonas más externas de las galaxia que el anillo nuclear). Esto confirma que los anillos nucleares se ven principalmente afectados por no-axisimetrías a una escala más grande que los propios anillos.

8.2.2 Anillos nucleares de formación estelar Ultra-Compactos

Cuando empezamos esta tesis, se desconocía si los UCNRs de formación estelar era la cola de bajo tamaño de la distribución de anillos nucleares (y en consecuencia compartían origen con los anillos nucleares 'clásicos') o si eran causados por algún tipo de fenómeno distinto como una interacción entre el agujero negro super-masivo central con el medio interestelar circundante. Después de haber estudiado en detalle cuatro UCNRs de formación estelar en el Capítulo 2 y después de estudiar algunos UCNRs más en el Capítulo 3, hemos descubierto que:

- Los UCNRs de formación estelar son morfológicamente parecidos a los anillos nucleares 'canónicos' y, bajo inspección visual, versiones reducidas de los mismos. Eso hace improbable que tengan un origen distinto al de los demás anillos nucleares de formación estelar.

- Los UCNRs de formación estelar no siempre se encuentran en el radio de la resonancia de corotación de una barra nuclear y, a menudo, se encuentran en galaxias sin barra nuclear. En consecuencia, los UCNRs están relacionados con las barras a gran escala, al igual que los anillos nucleares 'canónicos'.

- Los UCNRs de formación estelar no tienen preferencia por galaxias de tipo tardío, que son las que tienen en general bulbos menores y, por lo tanto, tienen las ILRs a menor radio que otras galaxias.

Deducimos que los UCNRs de formación estelar no son mas que anillos nucleares de formación estelar 'normales' que, por algún motivo, son más pequeños. La única excepción es el anillo más interno en NGC 2787 que probablemente tiene su origen en la ionización de la parte interna de un disco de gas por el agujero negro central.

8.2.3 Anillos nucleares de polvo

- Los anillos nucleares de polvo se encuentra en un $6 \pm 2\%$ de las galaxias elípticas.

- Los anillos nucleares de polvo se encuentran en galaxias elípticas y en galaxias lenticulares tempranas y tienen un origen distinto al de los anillos nucleares de formación estelar. Lauer et al. (2005) proponen que estos anillos podrían ser causados por un vaciamiento de dentro hacia fuera de un disco nuclear de polvo.

8.3 Calles de polvo

Hemos confirmado la predicción teórica que hizo Athanassoula (1992) de que la curvatura de una calle de polvo anticorrelaciona con la fuerza de la barra cuando se usa $Q_{\rm b}$ como indicador de la fuerza de la misma. En general, las barras fuertes contienen las calles de polvo más rectas, y las más débiles contienen las más curvadas. Sin embargo, la anticorrelación presenta una gran dispersión. También hemos visto esa dispersión en un conjunto de de 238 simulaciones numéricas de galaxias barradas con disco. Usando esas 238 simulaciones, hemos descubierto que la dispersión en la anticorrelación entre la curvatura de las calles de polvo y la fuerza de la barra se reduce bastante si usamos como fuerza de la barra la siguiente combinación lineal de parámetros:

$$Q_{\rm b} - 0.087\, a/b = (0.156 \pm 0.020) - (0.119 \pm 0.015) \log_{10}\Delta\alpha \qquad (8.1)$$

donde se muestra que $Q_{\rm b}$ no es siempre el mejor indicador de la fuerza de la barra (a/b es el cociente entre los radios mayor y menor de la barra y $\Delta\alpha$ es la curvatura de la calle de polvo), y que, en este caso, una combinación de $Q_{\rm b}$ y la elipticidad de la barra es mejor.

8.4 NGC 4244

Se conoce a NGC 4244 como la única galaxia cercana de canto sin disco grueso o como un caso de dudosa presencia del mismo. Como una galaxia sin disco grueso supondría un serio desafío para algunos modelos de formación de galaxias, hemos hecho un estudio en profundidad de NGC 4244. Hemos usado datos del S^4G y hemos descubierto que esta galaxia parece tener un débil disco grueso. También hemos descubierto que las asimetrías entre los perfiles de luminosidad a ambos lados del plano central de NGC 4244 pueden ser explicadas por una combinación del hecho de que la galaxia no esté exactamente de canto y de un cierto grado de opacidad del disco delgado. Dedujimos que la tenuidad del disco grueso es consecuencia de una falta de evolución secular en NGC 4244. También hemos inferido que lo que aparenta ser un alabeo del disco es en realidad debido a la presencia de brazos espirales en una galaxia que no está perfectamente de canto.

8.5 Galaxias con anillo externo

Hemos descubierto, usando descomposiciones de Galfit en imágenes del S^4G, que los anillos externos suelen 'preferir' galaxias con barras más masivas, más anchas y más largas (pero no más fuertes) que las que se encuentran en la muestra de control. Como la masa relativa de las barras en las galaxias con anillo externo es más grande que en la muestra de control, la masa relativa del disco se hace más pequeña. También hemos visto que la masa del bulbo en las galaxias con anillos externos parece ser mayor que en las galaxias de la muestra de control, pero eso es probablemente debido al incremento de luminosidad en el bulbo causada por anillos nucleares que, de las galaxias estudiadas, solamente se encuentran en las que tienen anillo externos.

8.6 Preguntas que quedan por resolver

8.6.1 Sigma-drops

- ¿Por qué la presencia de σ-drops tiene cierta correlación con la presencia de un núcleo Seyfert si el tiempo de escala de un σ-drop es de $\sim 10^9$ años y el de un AGN es de $\sim 10^8$ años?

8.6.2 Anillos nucleares

- Los anillos estelares de formación estelar en galaxias barradas se pueden encontrar en un amplio rango de radios, que aproximadamente coincide con aquél en el que se encuentran las órbitas x_2. ¿En qué posición entre las ILRs se forman los anillos? ¿Se forman a un radio aleatorio? ¿Puede una reducción radial con el tiempo del tamaño de los anillos desde una posición cercana a la ILR externa explicar que todo el rango de radios en el cuál se encuentran las órbitas x_2 esté poblado con anillos nucleares de formación estelar?

- Hemos descubierto que no hay ninguna diferencia de ángulos privilegiada entre el eje mayor de las barras y el eje mayor de los anillos nucleares. Se podría pensar que, dado

que los anillos se encuentran en órbitas x_2, deberían ser perpendiculares a las barras. Sin embargo, como los anillos son casi circulares, pequeños errores en los parámetros usados para la deproyección de las galaxias podrían estar escondiendo esa relación.

- Hemos descubierto ciertas evidencias que indican que la máxima elipticidad posible para un anillo nuclear correlaciona con la elipticidad de la barra. Sin embargo, eso podría no ser cierto, debido a los errores debidos a la deproyección de la galaxia.
- No hemos descubierto ninguna correlación entre la forma del bulbo (índice de Sérsic) y las propiedades de los anillos nucleares de formación estelar. Sin embargo, al haber sido medidas las propiedades de los bulbos en imágenes de 2MASS que, en algunos casos, apenas si resuelven el bulbo, se necesita profundizar en el tema con imágenes en infrarrojo cercano de más alta resolución.
- Alguna fuentes de la literatura indican que existe cierta correlación entre la presencia de los anillos nucleares de formación estelar y AGNs. Esa posible relación es sorprendente, ya que los anillos nucleares tienen tiempos de escala que son mucho más largos que los de un AGN. En AINUR (Capítulo 3), no hemos descubierto ninguna correlación entre la presencia de un anillo nuclear y la presencia de un AGN, cosa que va en contradicción con un resultado del Capítulo 1 que dice que los σ-drops correlacionan a la vez con la presencia de núcleos Seyfert y la de anillos nucleares.

8.6.3 Calles de polvo

- Hemos definido un nuevo indicador de la fuerza de la barra a partir de galaxias simuladas. Ese nuevo indicador debería ser probado en galaxias reales. No lo hemos hecho ya que, para calcular dicho indicador, hace falta conocer la elipticidad real de la barra de la galaxia. Eso implica que debería haber sido hecha una descomposición bulbo/barra/disco para un número significativo de galaxias para poder conocer la elipticidad de la barra tras haber eliminado el efecto del disco y del bulbo. Esas descomposiciones deberían haberse hecho en imágenes con alta resolución espacial en el infrarrojo cercano para evitar el efecto del polvo y para resolver correctamente el bulbo.

8.6.4 NGC 4244

- ¿Qué causa la tenuidad del disco grueso de NGC 4244? ¿Por qué esta galaxia parece haber tenido tan poca evolución secular?

8.6.5 Galaxias con anillos externos

- Se necesita una muestra mayor que la que hemos usado para poder confirmar nuestros descubrimientos preliminares en este tema.
- Necesitamos encontrar maneras de tratar el problema de las distintas relaciones de masa/luminosidad en las distintas componentes de las galaxias.
- Necesitamos estimar el efecto de las degeneraciones en nuestros ajustes.

9

Bibliography

- Abazajian, K. N., et al. 2009, ApJS, 182, 534
- Acarreta, J. R., Manteiga, M., Pişmiş, P., Mampaso, A., Cruz-González, G. 1996, AJ, 112, 1894
- Adelman-McCarthy, J. K., et al. 2007, ApJS, 172, 634
- Agüero, E. L., Díaz, R. J., Bajaja, E. 2004, A&A, 414, 453
- Aguerri, J. A. L., Beckman, J. E., Prieto, M. 1998, AJ, 116, 2136
- Aguerri, J. A. L., Debattista, V. P., Corsini, E. M. 2003, MNRAS, 338, 465
- Aguerri, J. A. L., Méndez-Abreu, J., Corsini, E. M. 2009, A&A, 495, 491
- Allard, E., Knapen, J. H., Peletier, R. F., Sarzi, M. 2006, MNRAS, 371, 1087
- Allard, E., Peletier, R. F., Knapen, J. H. 2005, ApJ, 633, 25
- Alonso-Herrero, A., Ryder, S. D., Knapen, J. H. 2001, MNRAS, 322, 757
- Andredakis, Y. C., Sanders, R. H. 1994, MNRAS, 267, 283
- Athanassoula, E. 1992, MNRAS, 259, 345
- Athanassoula, E. 1994, in Shlosman, I., ed., Mass-Transfer Induced Activity in Galaxies. Cambridge: Cambridge University Press, Cambridge, p. 143
- Athanassoula, E., Misiriotis, A. 2002, MNRAS, 330, 35
- Azzollini, R., Trujillo, I., Beckman, J. E. 2008, ApJ, 648, 1026
- Baggett, W. E., Baggett, S. M., Anderson, K. S. J. 1998, AJ, 116, 1626
- Ball, R., Sargent, A. I., Scoville, N. Z., Lo, K. Y., Scott, S. L. 1985, ApJ, 298, 21
- Barth, A. J., Ho, L. C., Filippenko, A. V., Rix, H.-W., Sargent, W. L. W. 2001b, ApJ, 546, 205
- Barth, A. J., Sarzi, M., Rix, H.-W., Ho, L. C., Filippenko, A. V., Sargent, W. L. W. 2001a, ApJ, 555, 685
- Becker, R., Mebold, U., Reif, K., van Woerden, H. 1988, A&A, 203, 21
- Bell, E. F., de Jong, R. S. 2001, ApJ, 550, 212
- Benedict, G. F., van Citters, G. W., McGraw, J. T., Rybski, P. M. 1977, BAAS, 9, 629
- Berentzen, I., Shlosman, I., Martínez-Valpuesta, I., Heller, C. H. 2007, ApJ, 666, 189
- Bertola, F., Cinzano, P., Corsini, E. M., Pizzella, A., Persic, M., Salucci, P. 1996, ApJ, 458, 67

- Block, D. L., Buta, R., Knapen, J. H., Elmegreen, D. M., Elmegreen, B. G., Puerari, I. 2004, AJ, 128, 183
- Block, D. L., Puerari, I., Knapen, J. H., Elmegreen, B. G., Buta, R., Stedman, S., Elmegreen, D. M. 2001, A&A, 375, 761
- Binney, J., Tremaine, S. 2008, Galactic Dynamics, 2nd edn. Princeton University Press, Princeton
- Böker, T., Förster-Schreiber, N. M., Genzel, R. 1997, AJ, 114, 1883
- Böker, T. et al. 1999, ApJS, 124, 95
- Boroson, T. A. 1981, ApJS, 46, 177
- van den Bosch, F. C., Emsellem, E. 1998, MNRAS, 298, 267
- Bosma, A., van der Hulst, J. M., Sullivan, III, W. T. 1977, A&A, 57, 373
- Bottema, R. 1993, A&A, 275, 16
- Bottinelli, L., Gouguenheim, L., Paturel, G., Teerikorpi, P. 1995, A&A, 296, 64
- Bournaud, F., Combes, F., Semelin, B. 2005, MNRAS, 364, 18
- Bournaud, F., Elmegreen, B. G., Elmegreen, D. M. 2007, ApJ, 670, 237
- Bournaud, F., Elmegreen, B. G., Martig, M. 2009, ApJ, 707, 1
- Braun, R., Walterbos, R. A. M., Kennicutt, Jr., R. C. 1992, Nature, 360, 442
- Braun, R., Walterbos, R. A. M., Kennicutt, Jr., R. C., Tacconi, L. J. 1994, ApJ, 420, 558
- Burbidge, E. M., Burbidge, G. R. 1962, ApJ, 135, 694
- Burstein, D. 1979, ApJ, 234, 829
- Buta, R. 1983, BAAS, 15, 659
- Buta, R. 1986, ApJSS, 61, 631
- Buta, R. 1988, ApJS, 66, 233
- Buta, R. 1989, The World of Galaxies, edited by H. G. Corwin and L. Botinelli (Springer, New York), p. 29
- Buta, R. 1995, ApJS, 98, 739
- Buta, R., Block, D. L. 2001, ApJ, 550, 243
- Buta, R., Combes, F. 1996, Fund. Cosmic Phys., 17, 95
- Buta, R. J., Corwin, Jr., H. G., Odewahn, S. C. 2007, The de Vaucouleurs Atlas of Galaxies. Cambridge University Press, Cambridge
- Buta, R., Crocker, D. A. 1991, AJ, 102, 1715
- Buta, R., Crocker, D. A. 1993, AJ, 105, 1344
- Buta, R., Crocker, D. A., Byrd, G. G. 1992, AJ, 103, 1526
- Buta, R., Crocker, D. A., Byrd, G. G. 1999, AJ, 118, 2071
- Buta, R. J., Knapen, J. H., Elmegreen, B. G., Salo, H., Laurikainen, E., Elmegreen, D. M., Puerari, I., Block, D. L. 2009, AJ, 137, 4487
- Buta, R., Laurikainen, E., Salo, H., Block, D. L., Knapen, J. H. 2006, AJ, 132, 1859
- Buta, R., Purcell, G. B., Crocker, D. A. 1995, AJ, 110, 1588
- Buta et al. 2010, submitted to ApJS
- Byun, Y. I., Freeman, K. C. 1995, ApJ, 448, 563
- Capetti, A., Balmaverde, B. 2005, A&A, 440, 73
- Carollo, C. M., Stiavelli, M., Mack, J. 1998, AJ, 116, 68
- Chang, P. 2008, ApJ, 684, 236
- Christlein, D., Zabludoff, A. I. 2004, ApJ, 616, 192

- Chung, A., Bureau, M. 2004, AJ, 127, 3192
- Ciotti, L. 1991, A&A, 249, 99
- Colina, L., García-Vargas, M. L., Mas-Hesse, J. M., Alberdi, A., Krabbe, A. 1997, ApJ, 484, 41
- Colina, L., Wada, K. 2000, ApJ, 529, 845
- Combes, F. 2001, in Aretxaga, I., Kunth, D., Mújica, R., eds, Advanced Lectures on the Starburst-AGN, World Scientific, Singapore, p. 223
- Combes, F., Gerin, M. 1985, A&A, 150, 327
- Combes, F., Sanders, R. H. 1981, A&A, 96, 164
- Comerón, S., Knapen, J. H., Beckman, J. E. 2008a, A&A, 485, 695
- Comerón, S., Knapen, J. H., Beckman, J. E. 2008c, JPhCS, 131, 2046
- Comerón, S., Knapen, J. H., Beckman, J. E., Laurikainen, E., Salo, H., Martínez-Valpuesta, I., Buta, R. J. 2010, MNRAS, 402, 2462
- Comerón, S., Knapen, J. H., Beckman, J. E., Shlosman, I. 2008b, A&A, 478, 403
- Comerón, S., Martínez-Valpuesta, I., Knapen, J. H., Beckman, J. E. 2009, ApJ, 706, 256
- Contini, M. 2004, MNRAS, 354, 675
- Contopoulos, G., Papayannopoulos, Th. 1980, A&A, 92, 33
- Corwin, H. G., de Vaucouleurs, A., de Vaucouleurs, G. 1985, Southern galaxy catalogue. A catalogue of 5481 galaxies south of declination -17° found on 1.2 m U. K. Schmidt IIIA-J Plates. University of Texas, Austin
- Curtis, H. D. 1918, Pub. Lick Obs., 13, 9
- Dalcanton, J. J., Yoachim, P., Bernstein, R. A. 2004, ApJ, 608, 189
- Debattista, V. P., Sellwood, J. A. 2000, ApJ, 543, 704
- Díaz, R., Carranza, G., Dottori, H., Goldes, G. 1999, ApJ, 512, 623
- Doi, A., Kameno, S., Kohno, K., Nakanishi, K., Inoue, M. 2005, MNRAS, 363, 692
- van Dokkum, P. G., Franx, M. 1995, AJ, 110, 2027
- Dressler, A., Richstone, D. O. 1990, ApJ, 348, 120
- Dreyer, J. L. E. 1888, MmRAS, 49, 1
- Dreyer, J. L. E. 1895, MmRAS, 51, 185
- Drozdosvky, I. O., Karachentsev, I. D. 2000, A&AS, 142, 425
- Dumas, G., Mundell, C. G., Emsellem, E., Nagar, N. M. 2007, MNRAS, 379, 1249
- Durbala, A., Buta, R., Sulentic, J. W., Verdes-Montenegro, L. 2009, MNRAS, 397, 1756
- Elitzur, M., Shlosman, I. 2006, ApJ, 648, 101
- Elmegreen, B. G. 1994, ApJ, 425, 73
- Elmegreen, B. G., Elmegreen, D. M. 1985, ApJ, 288, 438
- Elmegreen, B. G., Elmegreen, D. M., Knapen, J. H., Buta, R. J, Block, D. L., Puerari, I. 2007, ApJ, 670, 97
- Elmegreen, D. M., Chromey, F. R., Santos, M., Marshall, D. 1997, AJ, 114, 1850
- Elmegreen, D. M., Chromey, F. R., Warren, A. R. 1998, AJ, 116, 2834
- Emsellem, E. 2004, ASSL, 319, 149
- Emsellem, E. 2006, astro-ph/0610834
- Emsellem, E., Fathi, K., Wozniak, H., Ferruit, P., Mundell, C. G., Schinnerer, E. 2006, MNRAS, 365, 367

- Emsellem, E., Greusard, D., Combes, F., Friedli, D., Leon, S., Pécontal, E., Wozniak, H. 2001, A&A, 368, 52
- Emsellem, E., Monnet, G., Bacon, R., Nieto, J. L. 1994, A&A, 285, 739
- Engelbracht, C. W., Rieke, M. J., Rieke, G. H., Kelly, D. M., Achtermann, J. M. 1998, ApJ, 505, 639
- Englmaier, P., Shlosman, I. 2000, ApJ, 528, 677
- Englmaier, P., Shlosman, I. 2004, ApJ, 617, 115
- Erwin, P. 2004, A&A, 415, 941
- Erwin, P. 2005, MNRAS, 364, 283
- Erwin, P., Beckman, J. E., Pohlen, M. 2005, ApJ, 626, 81
- Erwin, P., Pohlen, M., Beckman, J. E. 2008, AJ, 135, 20
- Erwin, P., Sparke, L. S. 1999, ApJ, 521, 37
- Erwin, P., Sparke, L. S. 2002, AJ, 124, 65
- Erwin, P., Sparke, L. S. 2003, ApJSS, 146, 299
- Eskridge, P. B., et al. 2000, AJ, 119, 536
- Eskridge, P. B., et al. 2002, ApJS, 143, 73
- Falcón-Barroso, J., et al. 2006, MNRAS, 369, 529
- Fazio, G. G., et al. 2004, ApJS, 154, 10
- Ferrari, F., Pastoriza, M. G., Macchetto, F., Caon, N. 1999, A&AS, 136, 269
- Ferrers, N. M. 1877, Quart. J. Pure and Appl. Math., 14, 1
- Ferruit, P., Wilson, A. S., Mulchaey, J. 2000, ApJS, 128, 139
- Fisher, D. 1997, AJ, 113, 950
- Forbes, D. A., DePoy, D. L. 1992, A&A, 259, 97
- Forbes, D. A., Norris, R. P., Williger, G. M., Smith, R. C. 1994, AJ, 107, 984
- Freeman, K. C. 1970, ApJ, 160, 811
- Friedli, D., Benz, W. 1993, A&A, 268, 65
- Friedli, D., Wozniak, H., Rieke, M., Martinet, L., Bratschi, P. 1996, A&AS, 118, 461
- Fry, A. M., Morrison, H. L., Harding, P., Boroson, T. A. 1999, AJ, 118, 1209
- Fuentes-Carrera, I., et al. 2004, A&A, 415, 451
- Fukuda, H., Wada, K., Habe, A. 1998, MNRAS, 295, 463
- Gadotti, D. A. 2008, MNRAS, 384, 420
- Galliano, E., Alloin, D., Granato, G. L., Villar-Martín, M. 2003, A&A, 412, 615
- Ganda, K., Falcón-Barroso, J., Peletier, R. F., Capellari, M., Emsellem, E., McDermid, R. M., de Zeeuw, P. T., Carollo, C. M. 2006, MNRAS, 367, 46
- García-Barreto, J. A., Dettmar, R.-J., Combes, F., Gerin, M., Koribalski, B. 1991a, RMxAA, 22, 197
- García-Barreto, J. A., Downes, D., Combes, F., Gerin, M., Magri, C., Carrasco, L., Cruz-Gonzalez, I. 1991b, A&A, 244, 257
- García-Barreto, J. A., Franco, J., Carrillo, R., Venegas, S., Escalante-Ramírez, B. 1996, RMxAA, 32, 89
- García-Burillo, S., Combes, F., Schinnerer, E., Boone, F., Hunt, L. K. 2005, A&A, 441, 1011
- Gil de Paz, A., Madore, B. F., Noeske, K., Cairós, L. M., Papaderos, P., Silich, S. A. 2003, ApJ, 596, 179
- Gilmore, G., Reid, N. 1983, MNRAS, 202, 1025

- González Delgado, R. M., Heckman, T., Leitherer, C., Meurer, G., Krolik, J., Wilson, A. S., Kinney, A., Koratkar, A. 1998, ApJ, 505, 174
- González Delgado, R. M., Pérez, E., Tadhunter, C., Vilchez, J. M., Rodríguez-Espinosa, J. M. 1997, ApJS, 108, 155
- Greene, J. E., Ho, L. C., Ulvestad, J. S. 2006, ApJ, 636, 56
- de Grijs, R. 1998, MNRAS, 299, 595
- Gutiérrez, L., et al. 2010, in preparation
- Harris, J., Calzetti, D., Gallagher, J. S., III, Conselice, C. J., Smith, D. A. 2001, AJ, 122, 3046
- Hasan, H., Norman, C. 1990, ApJ, 361, 69
- Hawarden, T. G., van Woerden, H., Goss, W. M., Mebold, U., Peterson, B. A. 1979, A&A, 76, 230
- Hayashi, H., Chiba, M. 2006, PASJ, 58, 835
- Haywood, M. 2008, MNRAS, 338, 1175
- Heckman, T. M. 1978, PASP, 90, 241
- Heisler, C. A., de Robertis, M. M., Nadeau, D. 1996, MNRAS, 280, 579
- Helfer, T. T., Thornley, M. D., Regan, M W., Wong, T., Sheth, K., Vogel, S. N., Blitz, L., Bock, D. C.-J. 2003, ApJS, 145, 259
- Heller, C. H., Shlosman, I. 1996, ApJ, 471, 143
- Héraudeau, Ph., Simien, F. 1998, A&A, 133, 317
- Héraudeau, Ph., Simien, F., Maubon, G., Prugniel, P. 1999, A&AS, 136, 509
- Hernquist, L. 1989, Nature, 340, 687
- Hernquist, L., Mihos, J. C. 1995, ApJ, 448, 41
- Ho, L. C. 2002, ApJ, 564, 120
- Ho, L. C., Filippenko, A., Sargent, W. L. W. 1995, ApJS, 98, 477
- Ho, L. C., Filippenko, A., Sargent, W. L. W. 1997a, ApJ, 487, 568
- Ho, L. C., Filippenko, A., Sargent, W. L. W. 1997b, ApJS, 112, 315
- Hoopes, C. G., Walterbros, R. A. M., Rand, R. J. 1999, ApJ, 522, 669
- Hummel, E., Jörsäter, S., Lindblad, P. O., Sandqvist, A. 1987, A&A, 172, 51
- Ishizuki, S., Kawabe, R., Ishiguro, M., Okumura, S. K., Morita, K.-I. 1990, Nature, 344, 224
- Jarvis, B. J., Dubath, P., Martinet, L., Bacon, R. 1988, Msngr, 53, 19
- Jarvis, B. J., Peletier, R. F. 1991, A&A, 247, 315
- Jensen, J. B., Tonry, J. L., Barris, B. J., Thompson, R. I., Liu, M. C., Rieke, M. J., Ajhar, E. A., Blakeslee, J. P. 2003, ApJ, 583, 712
- Jogee, S., Shlosman, I., Laine, S., Englmaier, P., Knapen, J. H., Scoville, N., Wilson, C.D. 2002, ApJ, 575, 156
- de Jong, R. S. 1996, A&AS, 118, 557
- Jore, K. P., Broeils, A. H., Haynes, M. P. 1996, AJ, 112, 2
- Karachentsev, I. D., Sharina, M. E. 1997, A&A, 324, 457
- Karachentsev, I. D., Sharina, M. E., Dolphin, A. E., Grebel, E. K. 2003, A&A, 408, 111
- Karachentseva, V. E., Karachentsev, I. D., Richter, G. M., von Berlepsch, R., Fritze, K. 1987, AN, 308, 247
- Keeler, J. E. 1908, Pub. Lick Observatory, VIII

- Kendall, S., Kennicutt, R. C., Clarke, C., Thornley, M. D. 2008, MNRAS, 387, 1007
- Kennicutt, R. C., Jr. 1998, ARA&A, 36, 189
- Kennicutt, R. C., Lee, J. C., Akiyama, S., Funes, J. G., Sakai, S. 2005, AIP Conf. Ser. Vol. 783, The Evolution of Starbursts, The 331st Wilhelm and Else Heraeus Seminar. p. 3
- Kent, S. M. 1985, ApJS, 59, 115
- Khosroshahi, H., Wadadekar, Y., & Kembhavi, A. 2000, ApJ, 533
- Knapen, J. H. 2005, A&A, 429, 141
- Knapen, J. H., Beckman, J. E., Heller, C. H., Shlosman, I., de Jong, R. S. 1995, ApJ, 454, 623
- Knapen, J. H., Beckman, J. E., Shlosman, I., Peletier, R. F., Heller, C. H., de Jong, R. S. 1995, ApJ, 443, 73
- Knapen, J. H., Mazzuca, L. M., Böker, T., Shlosman, I., Colina, L., Combes, F., Axon, D. J. 2006, A&A, 448, 489
- Knapen, J. H., Pérez-Ramírez, D., Laine, S. 2002, MNRAS, 337, 808
- Knapen, J. H., Shlosman, I., Peletier, R. F. 2000, ApJ, 529, 93
- Knapen, J. H., Whyte, L. F., de Blok, W. J. G., van der Hulst, J. M. 2004, A&A, 423, 481
- Kohno, K., Kawabe, R., Tosaki, T., Okumura, S. K. 1996, ApJ, 461, 29
- Kormendy, J. 1977, ApJ, 217, 406
- Kormendy, J. 1979, ApJ, 227, 714
- Kormendy, J., Kennicutt, R. C. Jr. 2004, ARA&A, 42, 603
- Krist, J. E., Hook, R. N. 1999, The Tiny Tim User's Guide ver. 5.0. STSCI, Baltimore
- Laine, S., Knapen, J. H., Pérez-Ramírez, D., Doyon, R., Nadeau, D. 1999, MNRAS, 302, 33
- Laine, S., Knapen, J. H., Pérez-Ramírez, D., Englmaier, P., Matthias, M. 2001, MNRAS, 324, 891
- Laine, S., Shlosman, I., Knapen, J. H., Peletier, R. F. 2002, ApJ, 567, 97
- Lauer, T. R., et al. 2005, AJ, 129, 2138
- Laurikainen et al. 2010b, in preparation
- Laurikainen, E., Salo, H. 2002, MNRAS, 337, 1118
- Laurikainen, E., Salo, H., Buta, R. 2004b, ApJ, 607, 103
- Laurikainen, E., Salo, H., Buta, R. 2005, MNRAS, 362, 1319
- Laurikainen, E., Salo, H., Buta, R., Knapen, J. H. 2009, ApJ, 692, 34
- Laurikainen, E., Salo, H., Buta, R., Knapen, J. H., Comerón, S. 2010a, MNRAS, 405, 1089
- Laurikainen, E., Salo, H., Buta, R., Knapen, J. H., Speltincx, T., Block, D. 2006, AJ, 132, 2634
- Laurikainen, E., Salo, H., Buta, R., Vasylyev, S. 2004a, MNRAS, 355, 1251
- Laurikainen, E., Salo, H., Rautiainen, P. 2002, MNRAS, 331, 880
- Lindblad, B. 1961, Stockholms Obs. Ann., 21, 8
- Lindblad, P. A. B., Kristen, H., Jörsäter, S., Högbom, J. 1997, A&A, 317, 36
- Lintott, C. J., et al. 2008, MNRAS, 389, 1179
- Maciejewski, W. 2003, in Boily, C. H., Patsis, P., Portegies Zwart, S., Spurzem, R., Theis, C., eds, EAS Publ. Ser. Vol. 10, Galactic and Stellar Dynamics. EDP Sciences,

Les Ulis, p. 3
- Maiolino, R., Ruiz, M., Rieke, G. H., Papadopoulos, P. 1997, ApJ, 485, 552
- Maoz, D., Barth, A. J., Ho, L. C., Sternberg, A., Filippenko, A. V. 2001, AJ, 121, 3048
- Maoz, D., Barth, A. J., Sternberg, A., Filippenko, A. V., Ho, L. C., Macchetto, F. D., Rix, H.-W., Schneider, D. P. 1996, AJ, 111, 2248
- Maoz, D., Nagar, N. M., Falcke, H., Wilson, A. S. 2005, ApJ, 625, 699
- van der Marel, R. P. 1994, MNRAS, 270, 271
- Marinova, I., Jogee S. 2007, ApJ, 659, 1176
- Márquez, I., Masegosa, J., Durret, F., González Delgado, R. M., Moles, M., Maza, J., Pérez, E., Roth, M. 2003, A&A, 409, 459
- Martin, P. 1995, AJ, 109, 2428
- Martínez-Valpuesta, I., Shlosman, I. 2004, ApJ, 613, 29
- Martínez-Valpuesta, I., Shlosman, I., Heller, C. 2006, ApJ, 637, 214
- Martini, P., Regan, M. W., Mulchaey, J. S., Pogge, R. W. 2003, ApJS, 146, 353
- Martinet, L., Friedli, D. 1997, A&A, 323, 363
- Martínez-Delgado, D., Peñarrubia, J., Gabany, R. J., Trujillo, I., Majewski, S. R., Pohlen, M. 2008, ApJ, 689, 184
- Martínez-Delgado, D., Pohlen, M., Gabany, R. J., Majewski, S. R., Peñarrubia, J. 2009, ApJ, 692, 955
- Mazzuca, L. M., Sarzi, M., Knapen, J. H., Veilleux, S., Swaters, R. 2006, ApJ, 649, 79
- Mediavilla, E., Guijarro, A., Castillo-Morales, A., Jiménez-Vicente, J., Florido, E., Arribas, S., García-Lorenzo, B., Battaner, E. 2005, A&A, 433, 79
- Mei, S., et al. 2007, ApJ, 655, 144
- Meidt, S. 2010, in preparation
- Melena, N. W., Elmegreen, B. G., Hunter, D. A., Zernow, L. 2009, AJ, 138, 1203
- Menéndez-Delmestre, K., Sheth, K., Schinnerer, E., Jarrett, T. H., Scoville, N. Z. 2007, ApJ, 657, 790
- Merrifield, M. R., Kuijken, K. 1994, ApJ, 432, 575
- Möllenhoff, C., Heidt, J. 2001, A&A, 368, 16
- Monnet, G., Bacon, R., Emsellem, E. 1992, A&A, 253, 366
- Morgan, W. W. 1958, PASP, 70, 364
- Moriondo, G., Giovanardi, C., Hunt, L. K. 1998, A&AS, 130, 81
- Mulchaey, J. S., Regan, M. W. 1997, ApJ, 482, 135
- Mulder, P. S., van Driel, W., Braine, J. 1995, A&A, 300, 687
- Nilson, P. 1973, Uppsala General Catalogue of Galaxies, Acta Universitatis Upsalienis, Nova Regiae Societatis Upsaliensis
- Noordermeer, E., van der Hulst, J. M., Sancisi, R., Swaters, R. A., van Albada, T. S. 2005, A&A, 442, 137
- Olling, R. P. 1996, AJ, 112, 457
- Ondrechen, M. P., van der Hulst, J. M., Hummel, E. 1989, ApJ, 342, 39
- Ohta, K., Hamabe, M., Wakamatsu, K.-I. 1990, 357, 71
- Pastoriza, M. G., Bica, E., Bonatto, Ch., Mediavilla, E., Perez, E. 1991, AJ, 102, 1696

- Patsis, P. A., Athanassoula, E. 2000, A&A, 358, 45
- Patterson, R. J., Thuan, T. X., 1996, ApJS, 107, 103
- Paturel, G., Petit, C., Prugniel, Ph., Theureau, G., Rousseau, J., Brouty, M., Dubois, P., Cambrésy, L. 2003, A&A, 412, 45
- Pease, F. G. 1917, ApJ, 46, 24
- Peeples, M., Martini, P. 2006, ApJ, 652, 1097
- Peng, C. Y., Ho, L. C., Impey, C. D., Rix, H.-W. 2002, AJ, 124, 266
- Peng, C. Y., Ho, L. C., Impey, C. D., Rix, H.-W. 2010, AJ, 139, 2097
- Pérez-Ramírez, D., Knapen, J. H., Peletier, R. F., Laine, S., Doyon, R., Nadeau, D. 2000, MNRAS, 317, 234
- Perrine, C. D. 1922, MNRAS, 82, 486
- Peterson, C. J., Huntley, J. M. 1980, ApJ, 242, 913
- Pogge, R. W. 1989, ApJS, 71, 433
- Pogge, R. W., Martini, P. 2002, ApJ, 569, 624
- Pohlen, M., Trujillo, I. 2006, A&A, 454, 759
- Prendergast, K. H. 1962, *Distribution and Motion of ISM in Galaxies, ed L. Woltjer* (New York: Benjamin)
- Prieto, M., Beckman, J. E., Cepa, J., Varela, A. M. 1992, A&A, 257, 85
- Raha, N., Sellwood, J. A., James, R. A., Kahn, F. D. 1991, Nature, 352, 411
- Rautiainen, P., Salo, H. 2000, A&A, 362, 465
- Rautiainen, P., Salo, H., Laurikainen, E. 2008, MNRAS, 388, 1803
- Ravindranath, S., Ho, L. C., Peng, C. Y., Filippenko, A. V., Sargent, W. L. W. 2001, AJ, 122, 653
- Regan, M. W., Elmegreen, D. M. 1997, AJ, 114, 965
- Regan, M. W., Teuben, P. 2003, ApJ, 582, 723
- Regan, M. W., Teuben, P. 2004, ApJ, 600, 595
- Roberts, Jr., W. W., Huntley, J. M., van Albada, G. D. 1979, ApJ, 233, 67
- Ryder, S. D., Buta, R. J., Toledo, H., Shukla, H., Staveley-Smith, L., Walsh, W. 1996, ApJ, 460, 665
- Ryder, S. D., Illingworth, S. M., Sharp, R. G., Farage, C. L. 2010, PASA, 27, 56
- Saha, A., Thim, F., Tammann, G. A., Reindl, B., Sandage, A. 2006, ApJS, 165, 108
- Sakamoto, K., Okumura, S. K., Ishizuki, S., Scoville, N. Z. 1999, ApJS, 124, 403
- Salo, H., Rautiainen, P., Buta, R., Purcell, G. B., Cobb, M. L., Crocker, D. A., Laurikainen, E. 1999, AJ, 117, 792
- Sandage, A. 1961, The Hubble atlas of galaxies. Carnegie Institution, Washington
- Sandage, A., Bedke, K. 1994, The Carnegie Atlas of Galaxies, Carnegie Inst. of Wash. Publ. No. 618
- Sandage. A., Tammann, G. A. 1981, A revised Shapley-Ames Catalog of bright galaxies. Carnegie Institution, Washington
- Saraiva, M. F. 1997, AJ, 113, 1607
- Saraiva Schröder, M. F., Pastoriza, M. G., Kepler, S. O., Puerari, I. 1994, A&AS, 108, 41
- Sarzi, M., Allard, E. L., Knapen, J. H., Mazzuca, L. M. 2007, MNRAS, 380, 949
- Sarzi, M., Rix, H.-W., Shields, J. C., Rudnick, G., Ho, L. C., McIntosh, D. H., Filippenko, A. V., Sargent, W. L. W. 2001, ApJ, 550, 65

- Schild, R., Tresh-Fienberg, R., Huchra, J. 1985, 90, 441
- Schönrich, R., Binney, J. 2009, MNRAS, 396, 203
- Schroder, M. F. S., Pastoriza, M. G., Mediavilla, E. 1990, RMxAA, 21, 158
- Schwarz, M. P. 1981, ApJ, 247, 77
- Schwarz, M. P. 1984b, Proc. Astron. Soc. Australia, 5, 464
- Schwarz, M. P. 1984a, MNRAS, 209, 93
- Schweizer, F. 1980, ApJ, 237, 303
- Scorza, C., Bender, R. 1990, A&A, 235, 49
- Scoville, N. Z., Matthews, K., Carico, D. P., Sanders, D. B. 1988, ApJ, 327, 61
- Sellwood, J. A., Wilkinson, A. 1993, RPPh, 56, 173
- Sérsic, J. L. 1958, Observatory, 78, 123
- Sérsic, J. L., Pastoriza, M. 1965, PASP, 77, 287
- Seth, A. C., Dalcanton, J. J., de Jong, R. S. 2005a, AJ, 129, 1331
- Seth, A. C., Dalcanton, J. J., de Jong, R. S. 2005b, AJ, 130, 1574
- Seth, A. C., de Jong, R., Dalcanton, J., The Ghosts Team 2007, in Proc. IAU Symp. 241, Detection of a Stellar Halo in NGC 4244, Kluwer, Dordrecht, p. 523
- Shang, Z., et al. 1998, ApJ, 504, 23
- Shapiro, K. L., Gerssen, J., van der Marel, R. P. 2003, AJ, 126, 2707
- Shaw, M. A., Gilmore, G. F. 1989, MNRAS, 237, 903
- Shen, J., Sellwood, J. A. 2004, ApJ, 604, 614
- Sheth et al. 2010, submitted to ApJ
- Shlosman, I. 1999, in Beckman, J. E., Mahoney, T. J., eds, ASP Conf. Ser. Vol. 187, The Evolution of Galaxies on Cosmological Timescales. Astron. Soc. Pac., San Francisco, p. 100
- Shlosman, I. 2001, in Knapen, J. H., Beckman, J. E., Shlosman, I., Mahoney, T. J., eds, ASP Conf. Ser. Vol. 249, The Central Kiloparsec of Starbursts and AGN: The La Palma Connection. Astron. Soc. Pac., San Francisco, p. 55
- Shlosman, I., Begelman, M. C., Frank, J. 1990, Nature, 345, 679
- Shlosman, I., Heller C. H. 2002, ApJ, 565, 921
- Simard, L. 1998, in ASP Conf. Ser. 145, Astronomical Data Analysis Software and Systems VII, ed. R. Albrecht, R. N. Hook, & H. A. Bushouse (San Francisco: ASP), 108
- Simard, L., et al. 2002, ApJS, 142, 1
- Simien, F., Prugniel, Ph. 1997a, A&AS, 122, 521
- Simien, F., Prugniel, Ph. 1997b, A&AS, 126, 15
- Simien, F., Prugniel, Ph. 1997c, A&AS, 126, 519
- Simien, F., Prugniel, Ph. 1998, A&AS, 131, 287
- Simien, F., Prugniel, Ph. 2000, A&AS, 145, 263
- Simien, F., Prugniel, Ph. 2002, A&A, 384, 371
- Simkin, S. M., Su, H. J., Schwarz, M. P. 1980, ApJ, 237, 404
- Sil'chenko, O. K., Afanasiev, V. L. 2004, AJ, 127, 2641
- Sil'chenko, O. K., Moiseev, A. V. 2006, AJ, 131, 1336
- Smith, D. A., Herter, T., Haynes, M. P., Neff, S. G. 1999, ApJ, 510, 669
- Sofue, Y., Koda, J., Nakanishi, H., Onodera, S., Takamiya, T., Kohno, K., Okumura, S. 2004, In "Studies of Galaxies in the Young Universe with New Generation

Telescope", Eds. N. Arimoto, W. Duschl, p. 171
- Sofue, Y., Rubin, V. 2001, ARA&A, 39, 137
- de Souza, R. E., Gadotti, D. A., dos Anjos, S. 2004, ApJS, 153, 411
- Springob, C. M., Haynes, M. P., Giovanelli, R., Kent, B. R. 2005, ApJS, 160, 149
- Statler, T. S. 2001, AJ, 121, 244
- Strickland, D. K., Heckman, T. M., Colbert, E. J. M., Hoopes, C. G., Weaver, K. A. 2004, ApJS, 151, 193
- Telesco, C. M., Gatley, I. 1984, ApJ, 284, 557
- Terashima, Y., Wilson, A. S. 2003, ApJ, 583, 145
- Thakur, P., Ann, H. B., Jiang, I.-G. 2009, ApJ, 693, 586
- Thronson, Jr., H. A., Hereld, M., Majewski, S., Greenhouse, M., Johnson, P., Spillar, E., Woodward, C. E., Harper, D. A., Rauscher, B. J. 1989, ApJ, 343, 158
- Tikhonov, N. A., Galazutdinova, O. A. 2005, Astrophysics, 48, 221
- Tonry, J. L., Dressler, A., Blakeslee, J. P., Ajhar, E. A., Fletcher, A. B., Luppino, G. A., Metzger, M. R., Moore, C. B. 2001, APJ, 546, 681
- Tran, H. D., Tsvetanov, Z., Ford, H. C., Davies, J., Jaffe, W., van den Bosch, F. C., Rest, A. 2001, AJ, 121, 2928
- Trujillo, I., Martínez-Valpuesta, I., Martínez-Delgado, D., Peñarrubia, J., Gabany, R. J., Pohlen M. 2009, ApJ, 704, 618
- Tsvetanov, Z. I., Petrosian, A. R. 1995, ApJS, 101, 287
- Tully, R. B. 1988, Nearby galaxies catalog. Cambridge University Press, Cambridge and New York
- de Vaucouleurs, G. 1957, HPh, 53, 275
- de Vaucouleurs, G. 1963, ApJS, 8, 31
- de Vaucouleurs, G. 1975, ApJS, 29, 193
- de Vaucouleurs, G., Buta, R. 1980, AJ, 85, 637
- de Vaucouleurs, G., de Vaucouleurs, A., Corwin, Jr., H. G. 1976, The Second Reference Catalogue of Bright Galaxies. University of Texas Press, Austin
- de Vaucouleurs, G., de Vaucouleurs, A., Corwin, H. G., Jr., Buta, R. J., Paturel, G., Fouque, P. 1991, Third Reference Catalogue of Bright Galaxies. Springer Verlag, New York (RC3)
- van de Ven, G., Chang, P. 2009, ApJ, 697, 619
- Véron-Cetty, M.-P., Véron, P. 1988, A&A, 204, 28
- Wadadekar, Y., Robbason, B., Kembhavi, A. 1999, AJ, 117, 1219
- Walker, M. F., Chincarini G. 1967, ApJ, 147, 416
- Whitmore, B. C., Lucas, R. A., McElroy, D. B., Steiman-Cameron, T. Y., Sackett, P. D., Olling, R. P. 1990, AJ, 100, 1489
- Wilner, S. P., Elvis, M., Fabbiano, G., Lawrence, A. Ward, M. J. 1985, ApJ, 299, 433
- Wilson, A. S., Shopbell, P. L., Simpson, C., Storchi-Bergmann, T., Barbosa, F. K. B., Ward, M. J. 2000, AJ, 120, 1325
- Worden, S. P. 1974, PASP, 86, 92
- Wozniak, H., Champavert, N. 2006, MNRAS, 369, 853
- Wozniak, H., Combes, F., Emsellem, E., Friedli, D. 2003, ASPC, 290, 563
- Wozniak, H., Fiedli, D., Martinet, L., Martin, P., Bratschi, P. 1995, A&AS, 111, 115
- Yoachim, P., Dalcanton, J. J. 2006, AJ, 131, 226

- Yoachim, P., Dalcanton, J. J. 2008, ApJ, 683, 707
- Young, J. S., et al. 1995, ApJS, 98, 219
- de Zeeuw, P. T., et al. 2002, MNRAS, 329, 513
- Zibetti, S., Charlot, S., Rix, H.-W. 2009, MNRAS, 400, 1181
- Zurita, A., Relaño, M., Beckman, J. E., Knapen, J. H. 2004, A&A, 413, 73
- Zwicky, F., Zwicky, M. A. 1971, Catalogue of selected compact galaxies and of post-eruptive galaxies. Zwicky, Guemligen

A

Aditional material to Chapter 1

This appendix includes aditional material to Chapter 1.

A.1 Structure maps and Hα images of the σ-drop sample galaxies

Where two images for one galaxy are given on a row, the structure map is shown on the left, and the continuum-subtracted Hα image on the right; where only one image is shown there is no Hα image available. The orientation of the images is shown with pairs of arrows, where the longer indicates north and the shorter one east. The small ellipse indicates $r_{\rm c}$, as defined in the text, and the large one is at 1 kpc radius. Where one ellipse is drawn it indicates $r_{\rm c}$—in those cases the image scale is such that the 1 kpc radius falls outside the image. Grey-scales are such that dark indicates more dust (less emission) in the structure maps, and more Hα emission in the Hα images. Each image has at the top left the name of the galaxy, the morphological classification given in NED and the activity, also given in NED.

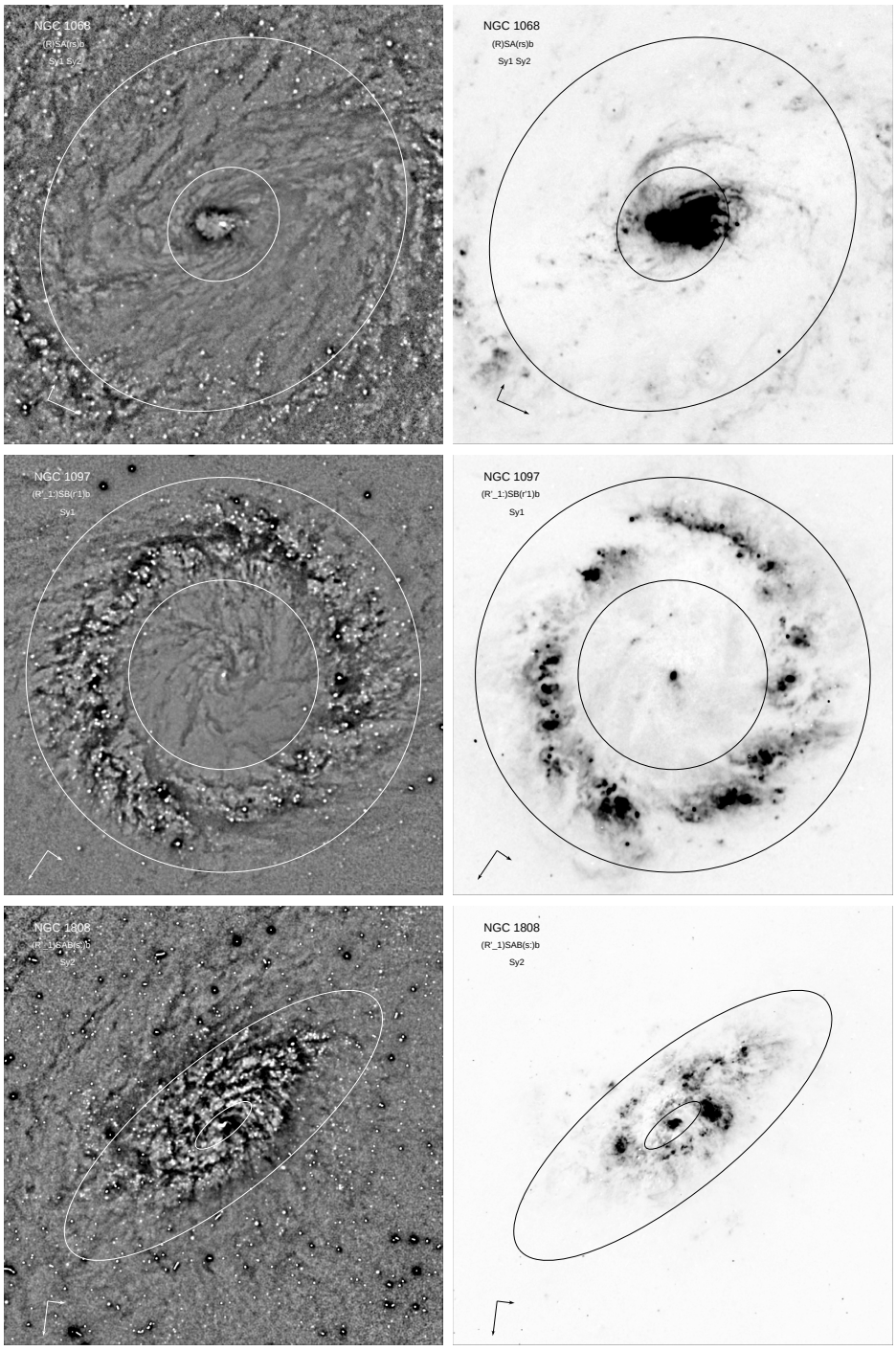

Figure A.1: Structure maps and Hα images of the central kiloparsec of σ-drop galaxies.

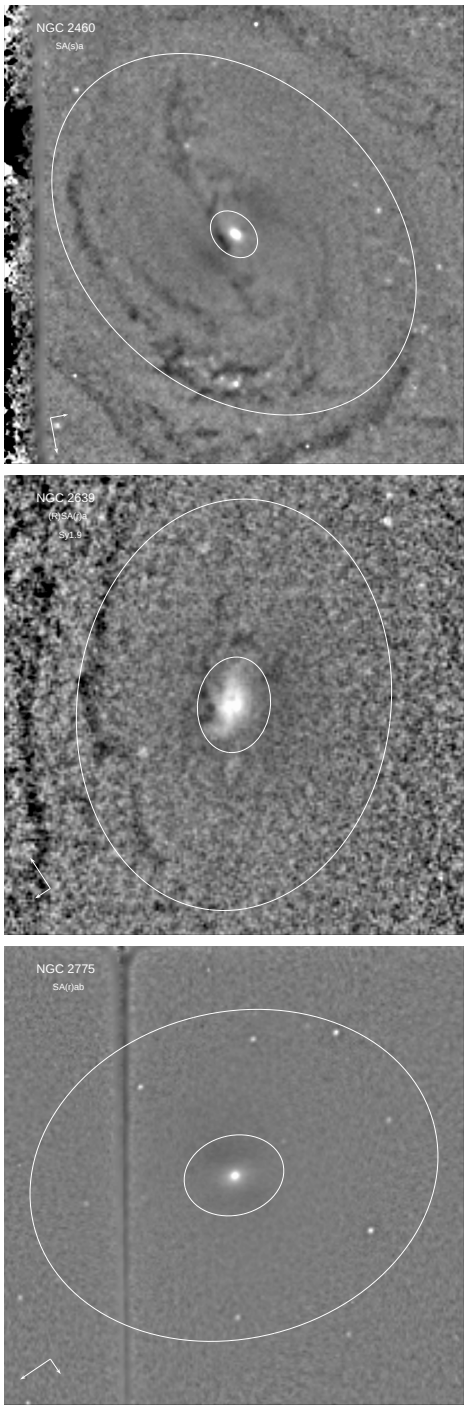

Figure A.1: (continued)

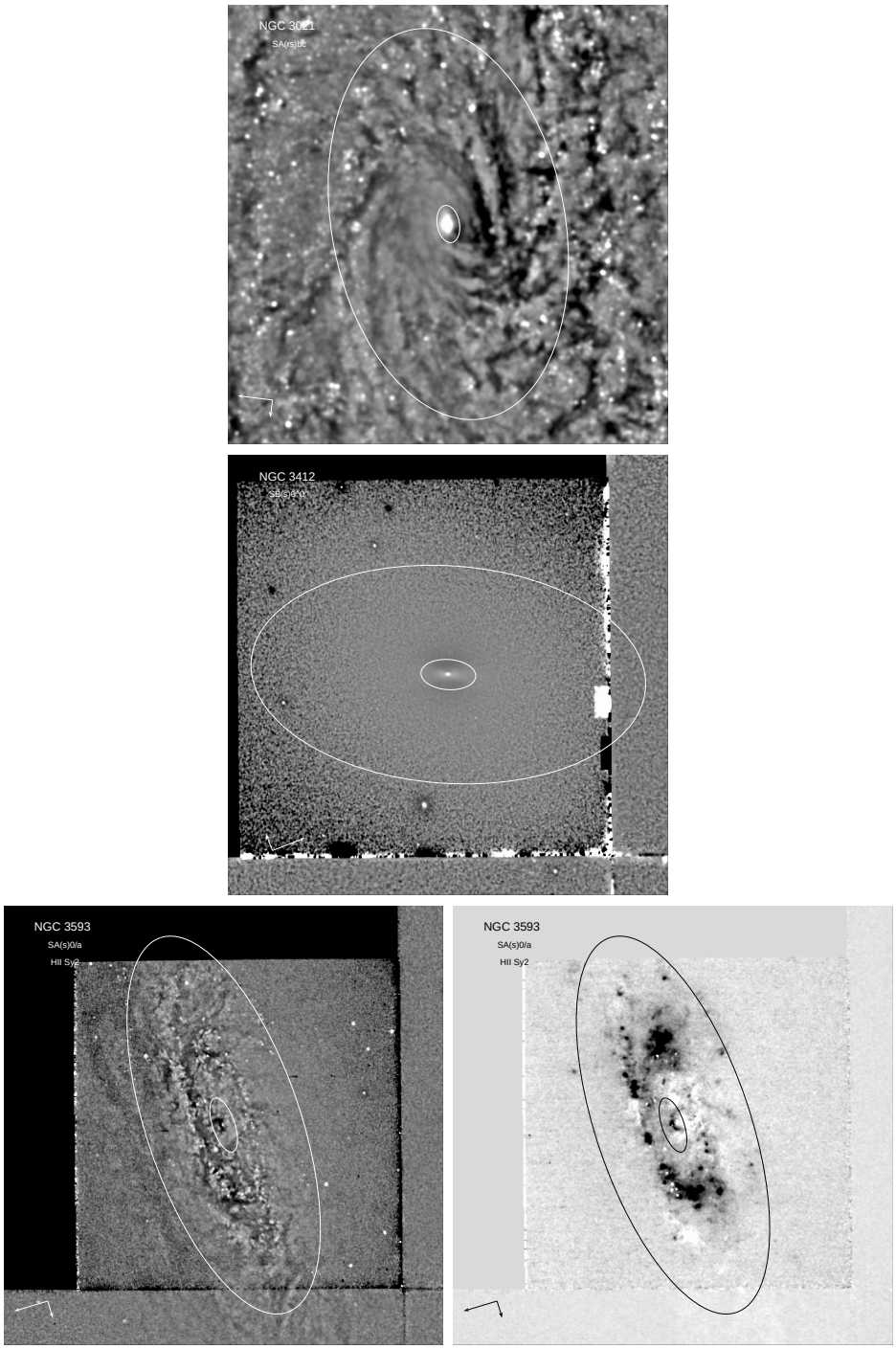

Figure A.1: (continued)

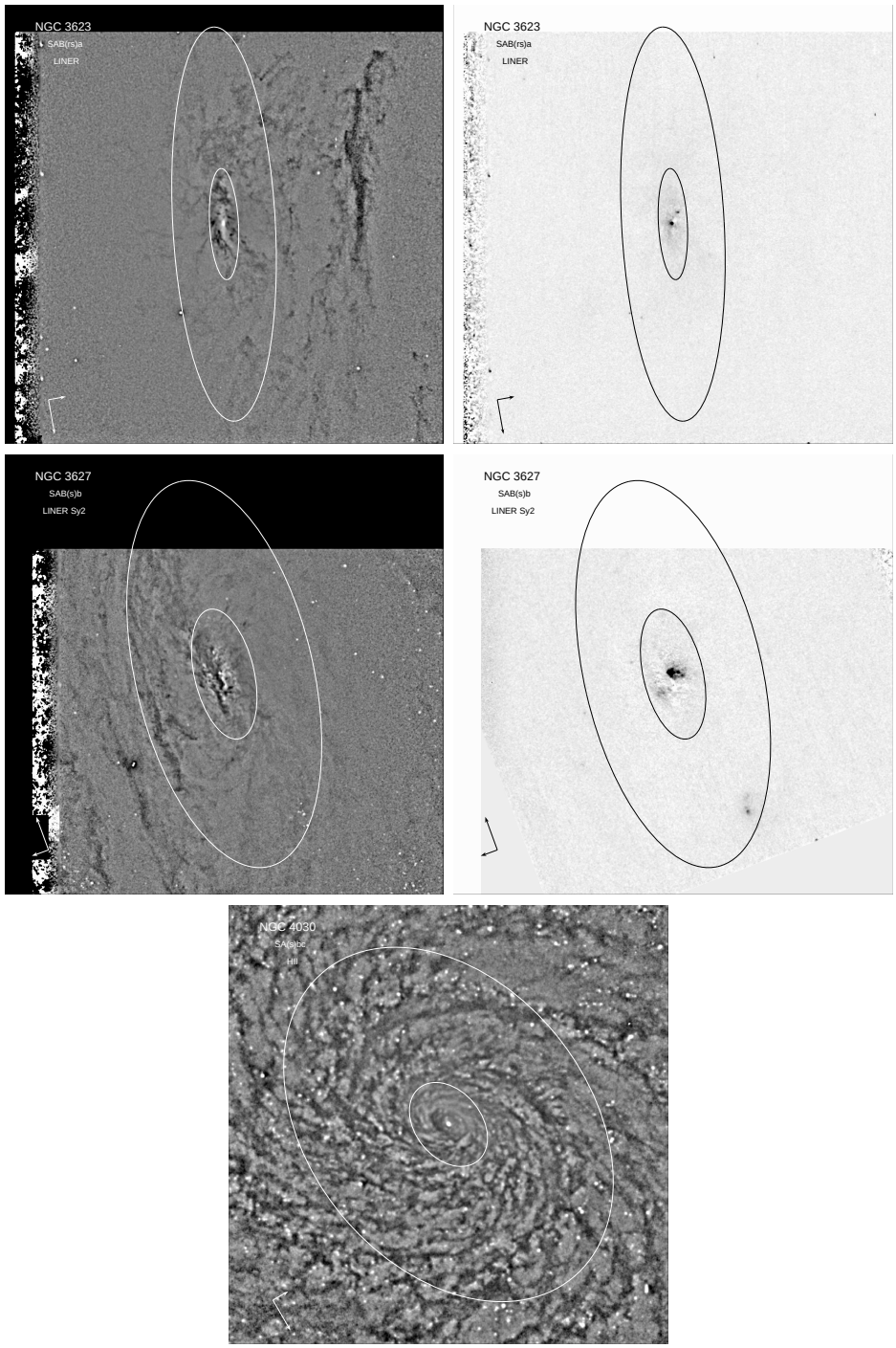

Figure A.1: (continued)

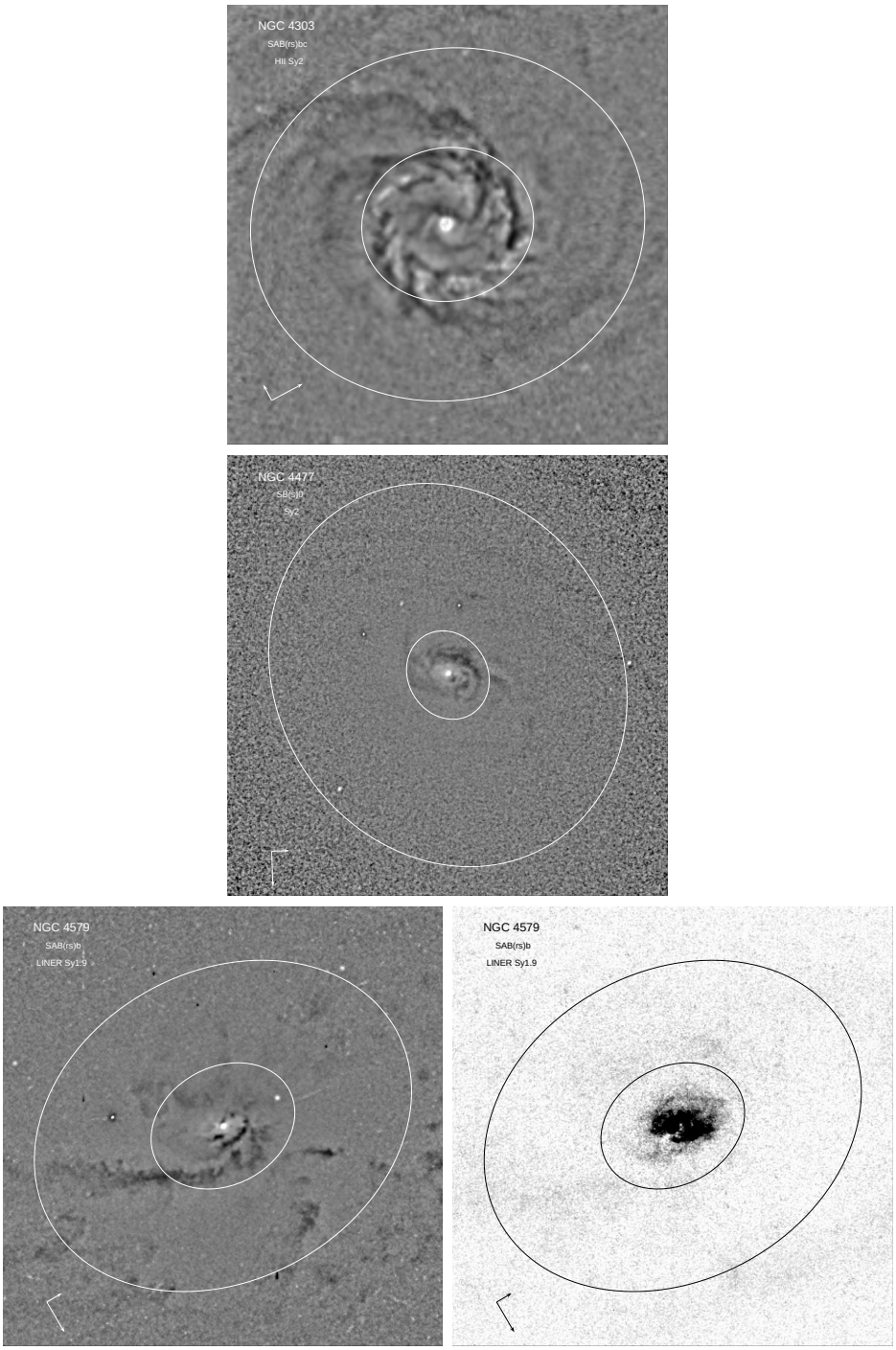

Figure A.1: (continued)

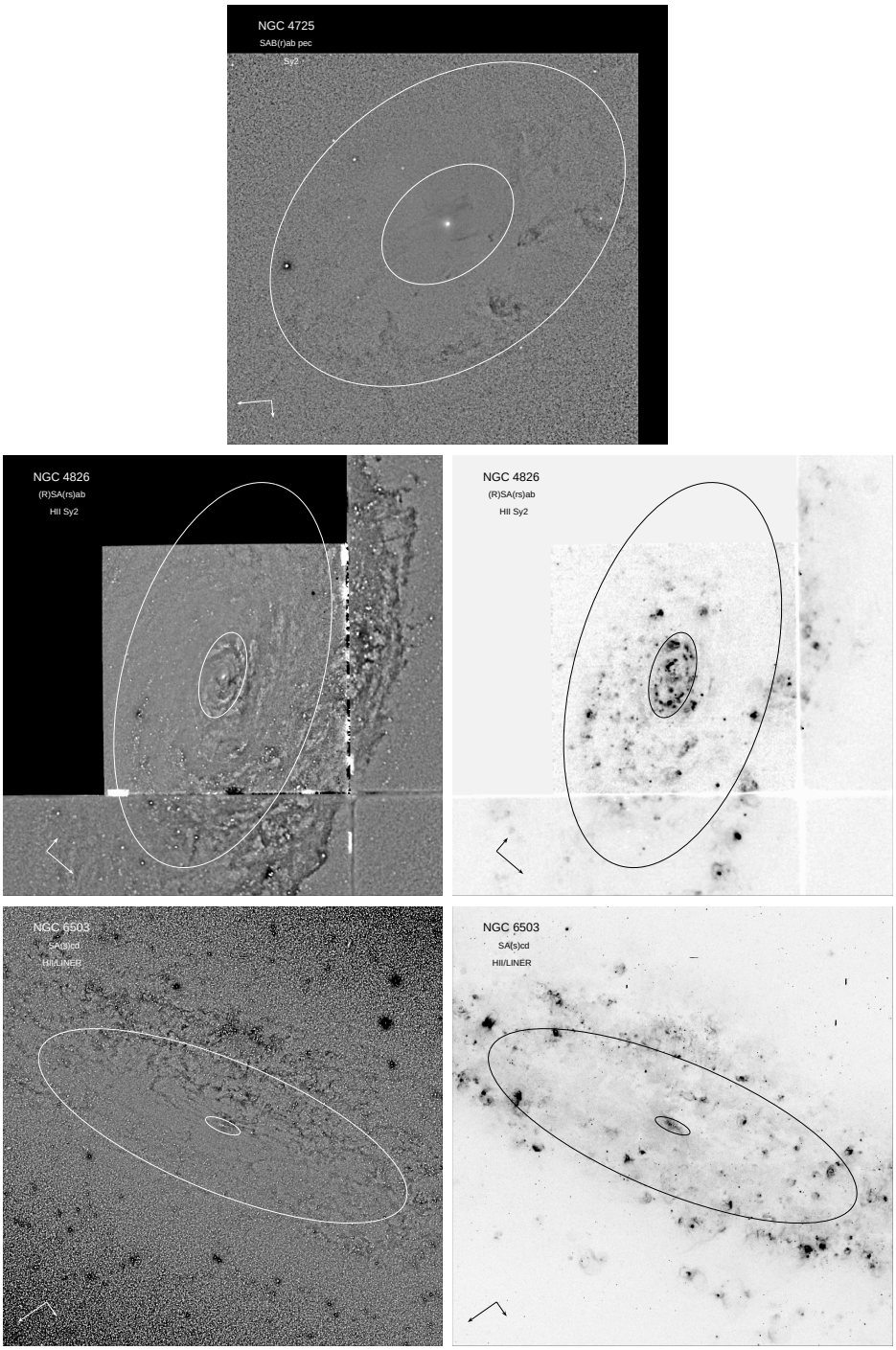

Figure A.1: (continued)

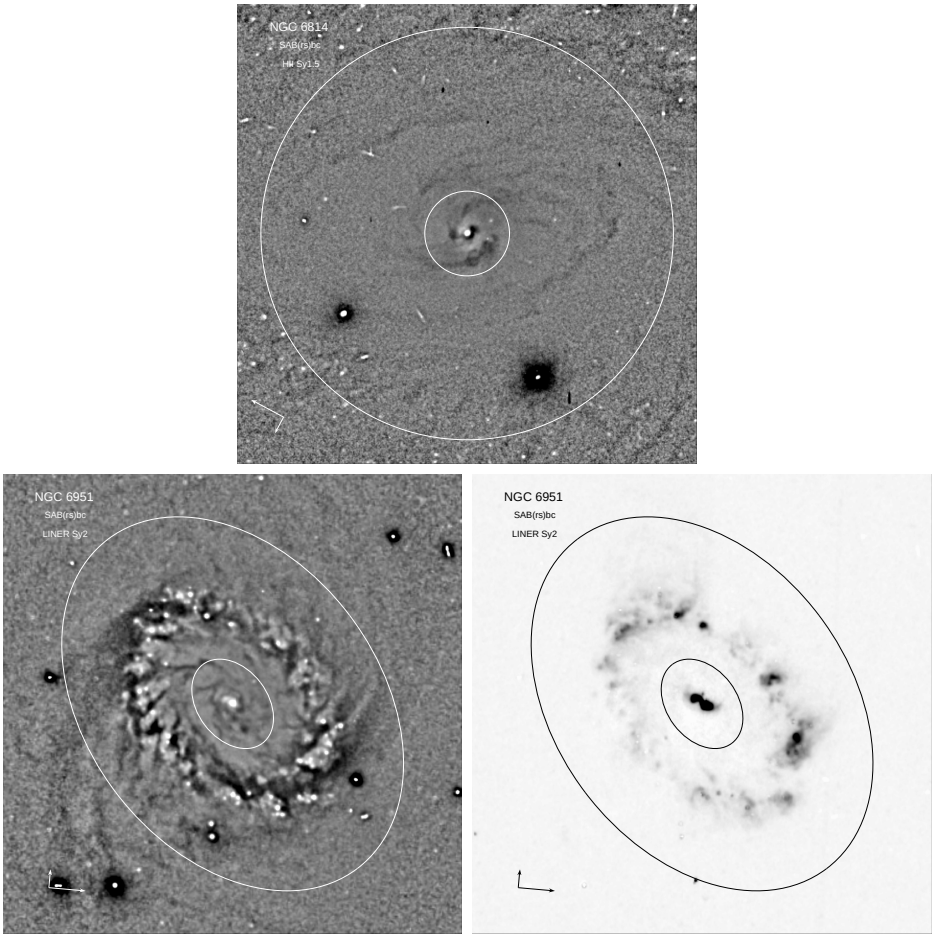

Figure A.1: (continued)

A.2 Structure maps and Hα images of the control sample galaxies

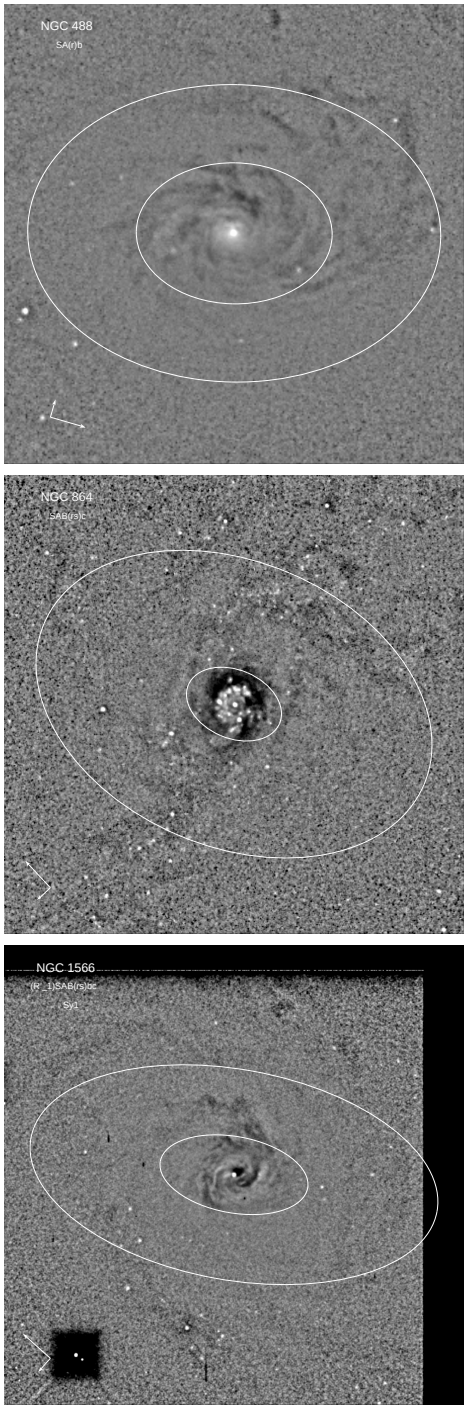

Figure A.2: Structure maps and Hα images of the central kiloparsec of control galaxies.

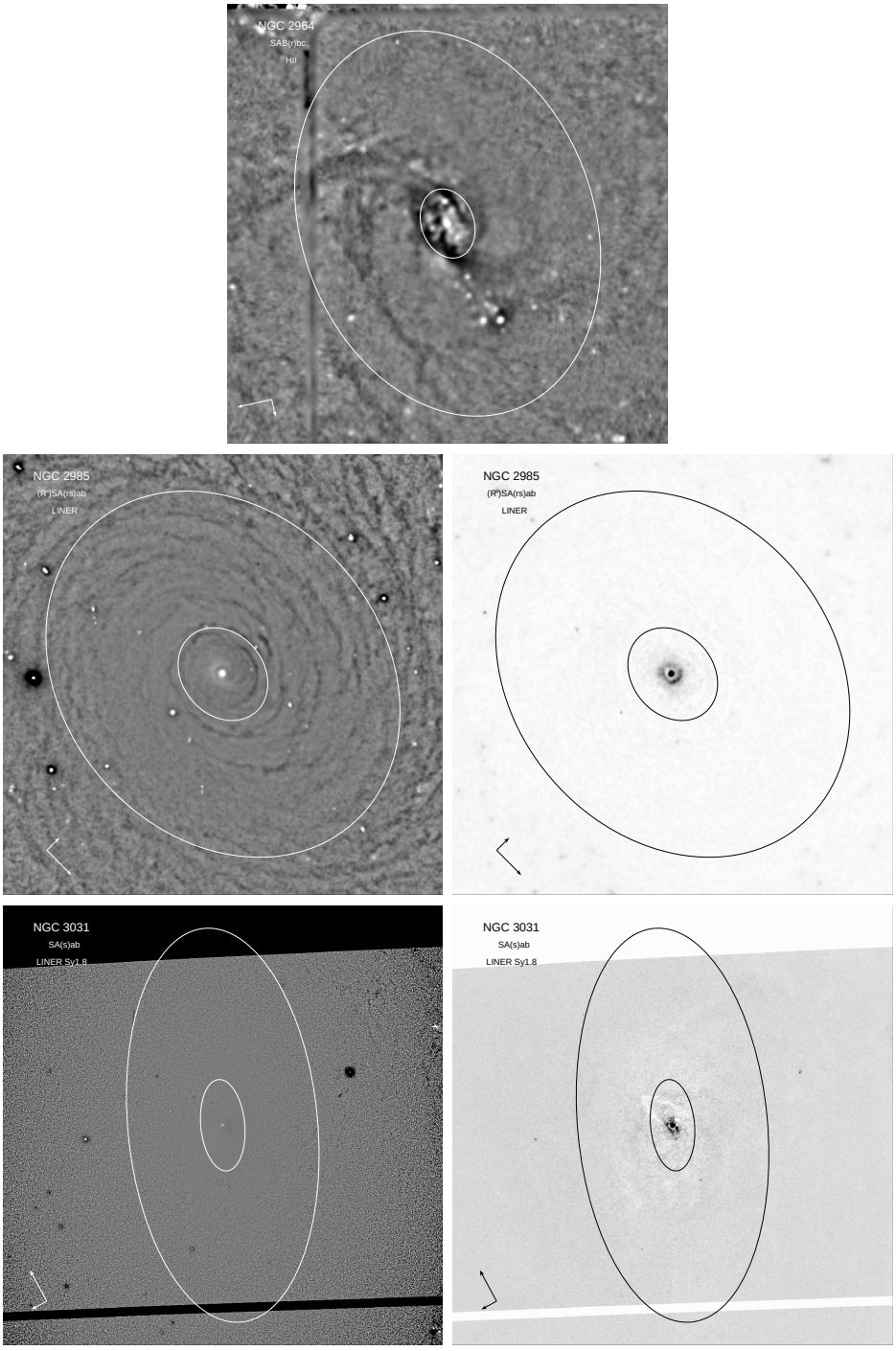

Figure A.2: (continued)

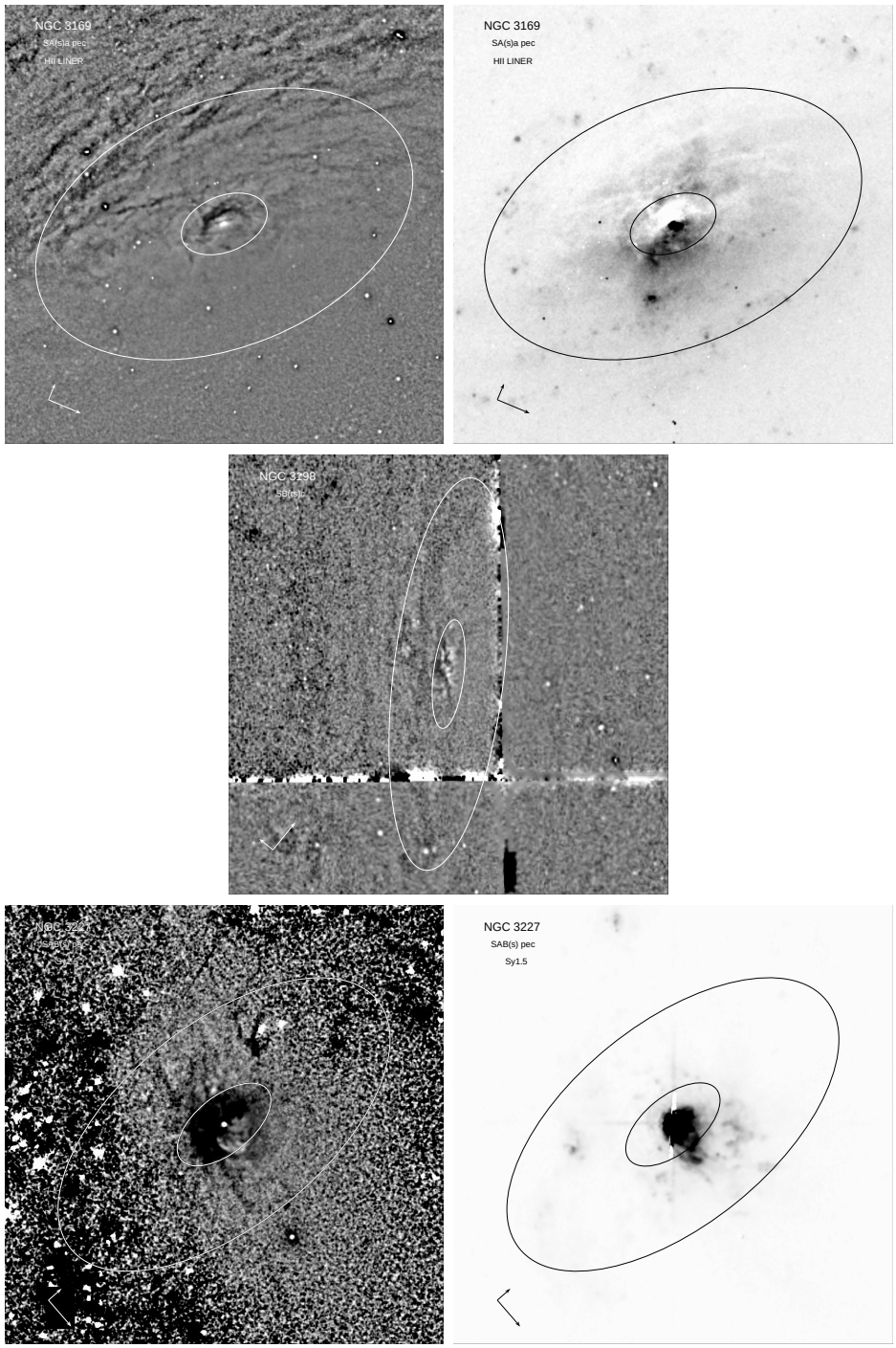

Figure A.2: (continued)

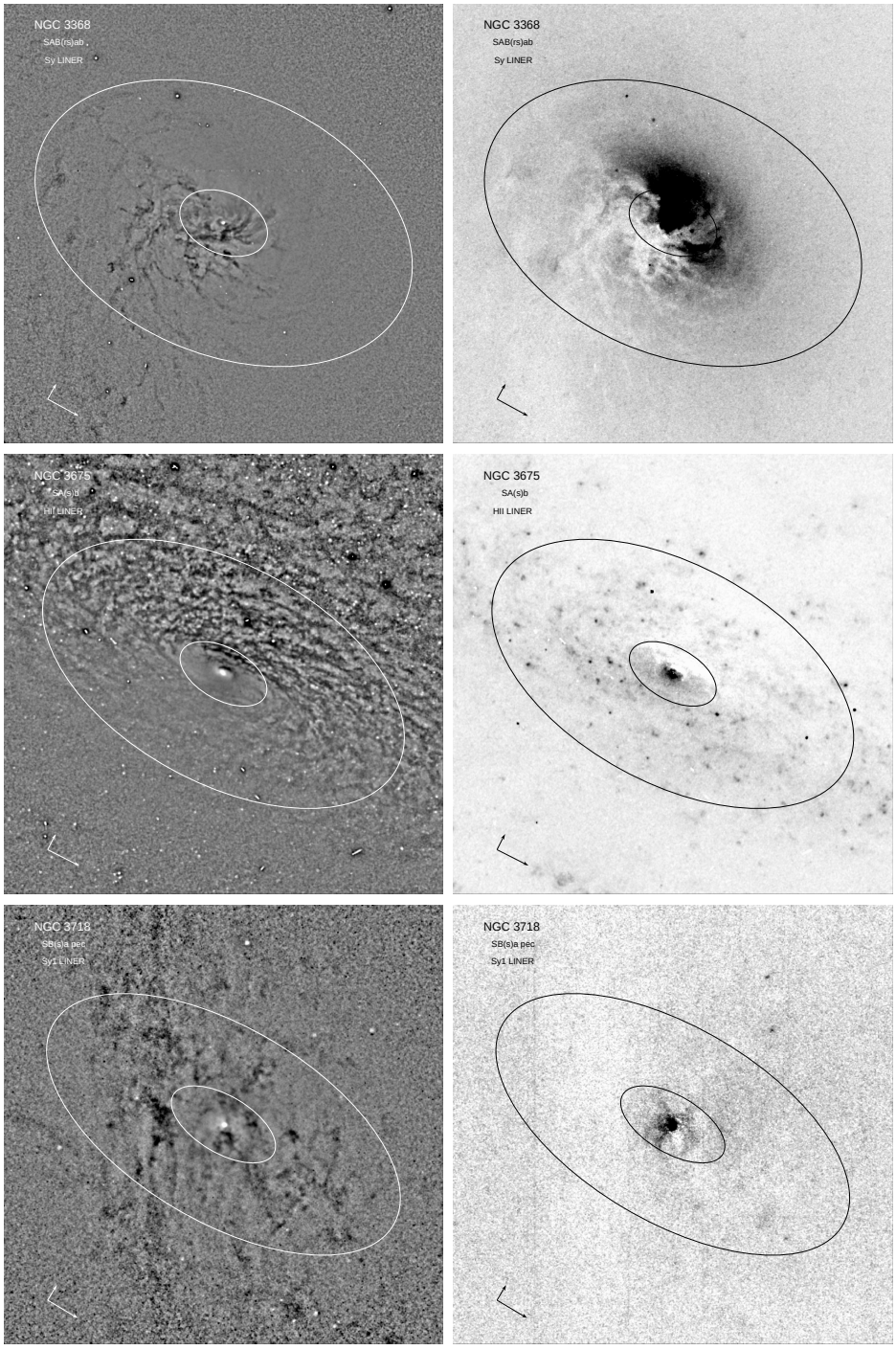

Figure A.2: (continued)

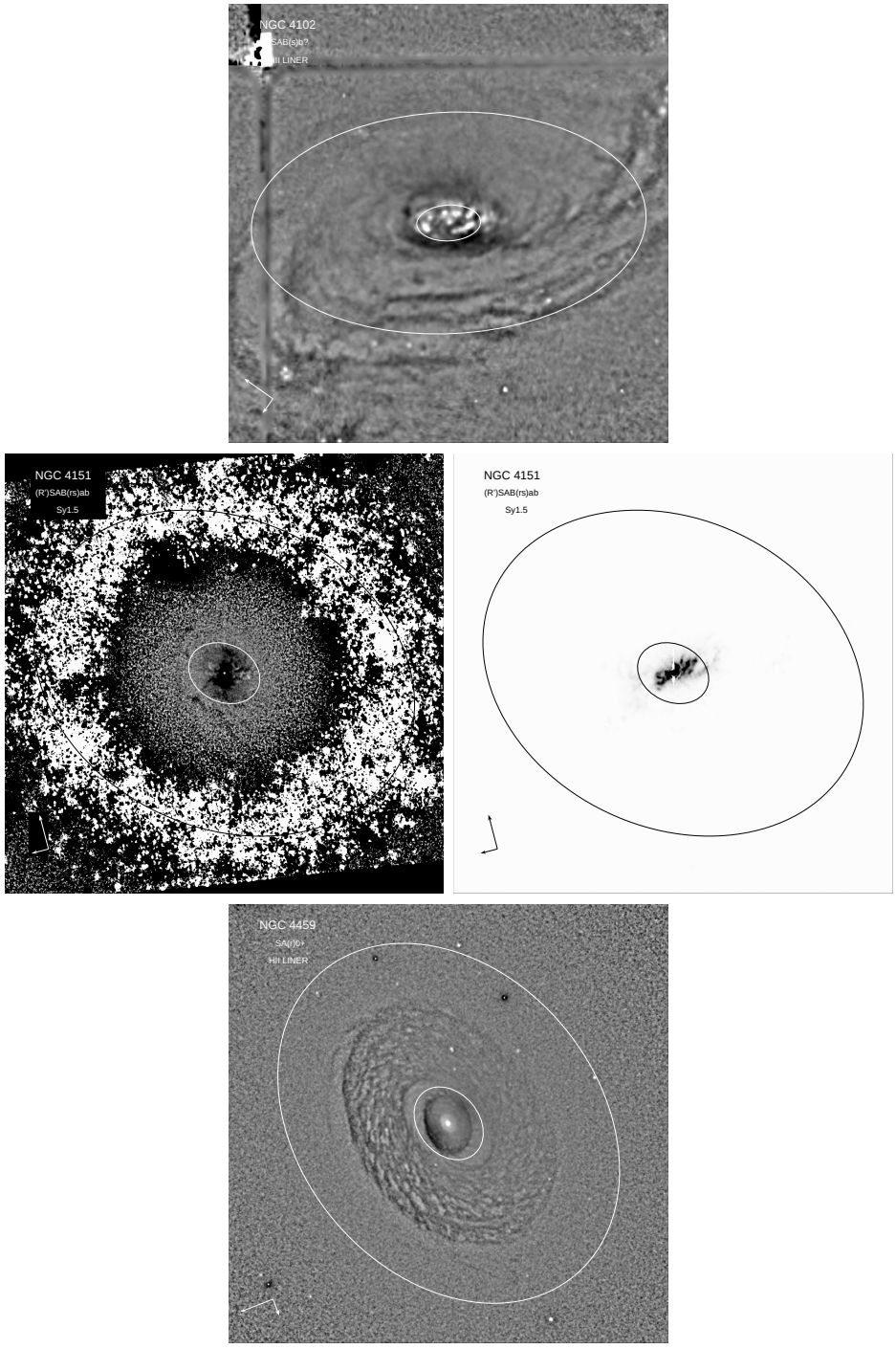

Figure A.2: (continued)

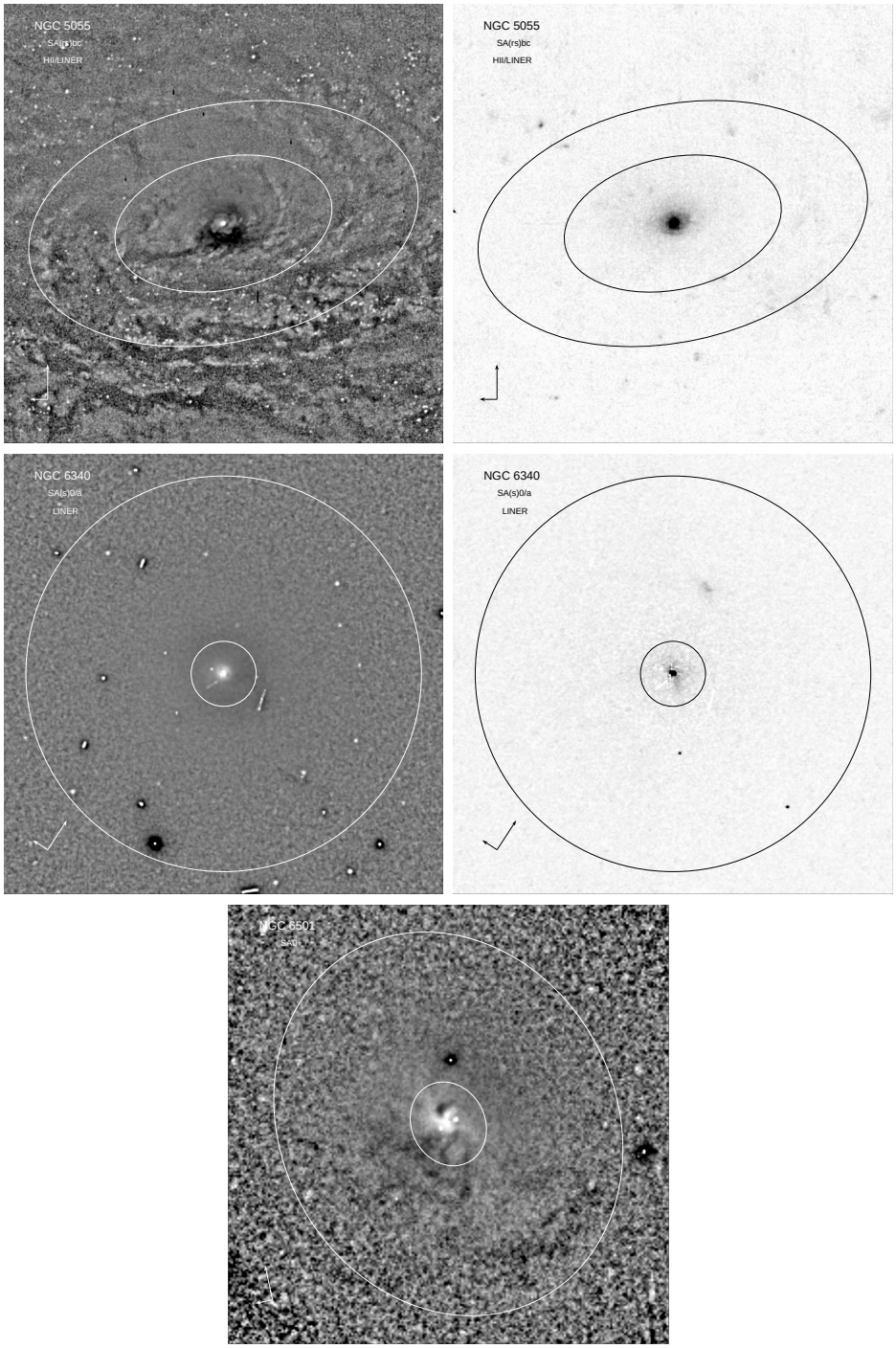

Figure A.2: (continued)

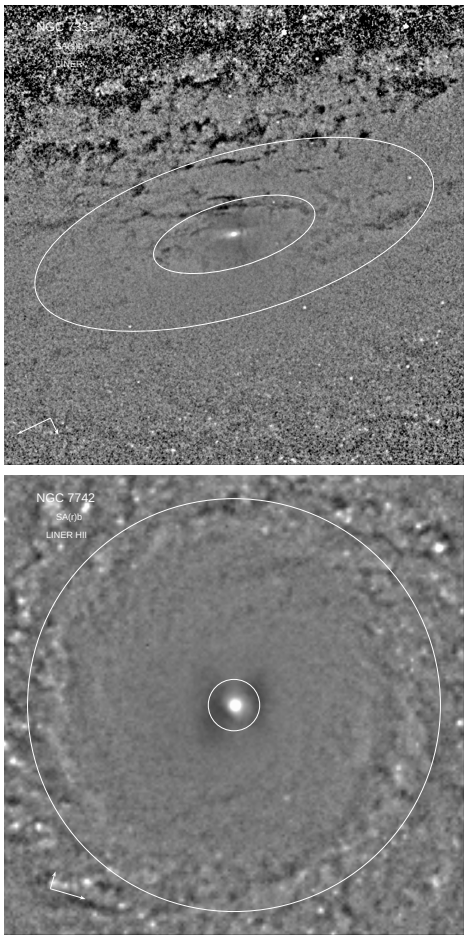

Figure A.2: (continued)

A.3 Radial surface brightness profiles of the σ-drop sample galaxies

Exponential fits are indicated with dashed lines, while the dotted lines indicate the sky level for each galaxy. Vertical dashed-dotted lines correspond to the end of the bar. Where there are two vertical lines, they indicate the lower and the upper limit to the end of the bar. The squares show the limits of the intervals that we have used to fit the exponential discs.

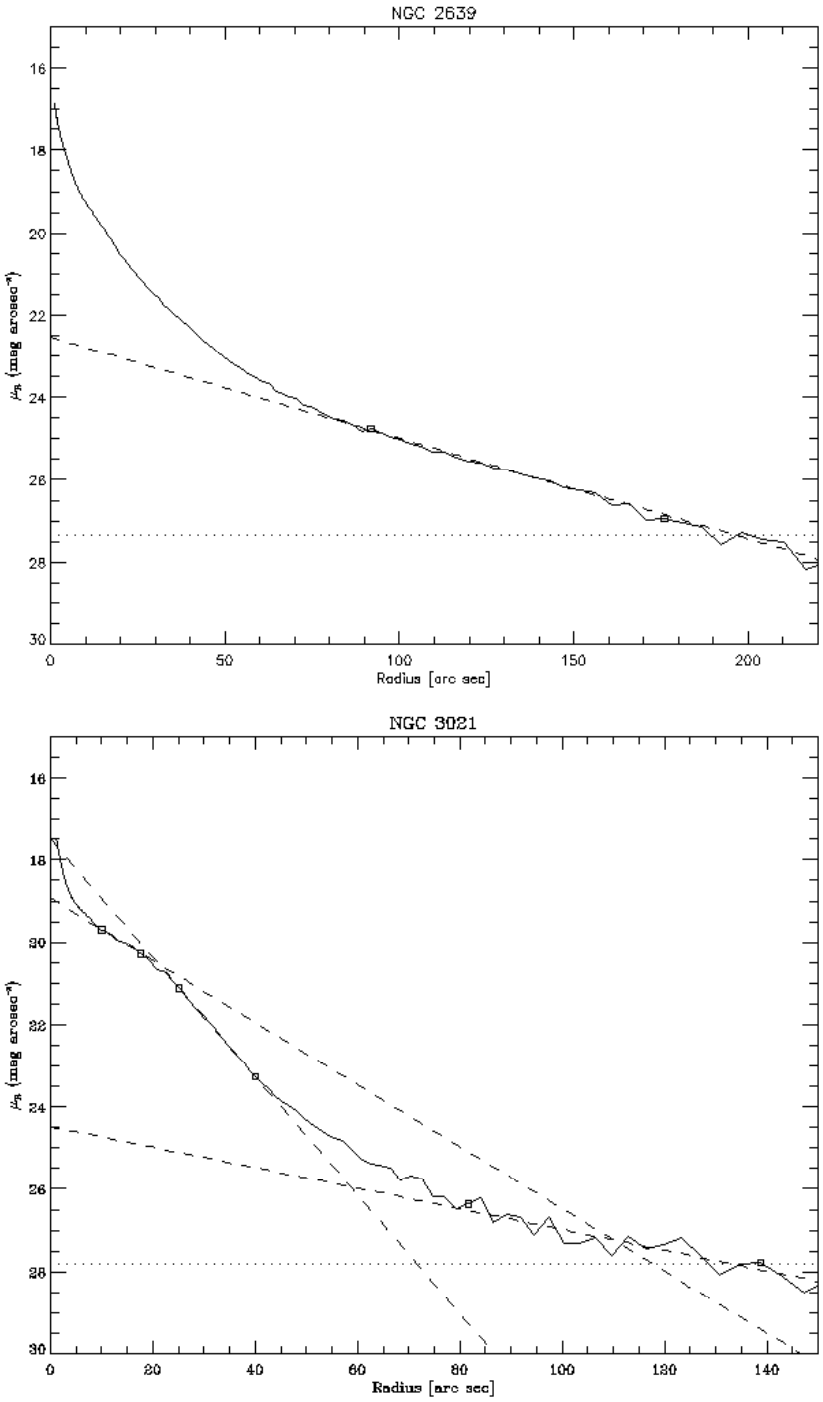

Figure A.3: Luminosity profiles of σ-drop galaxies.

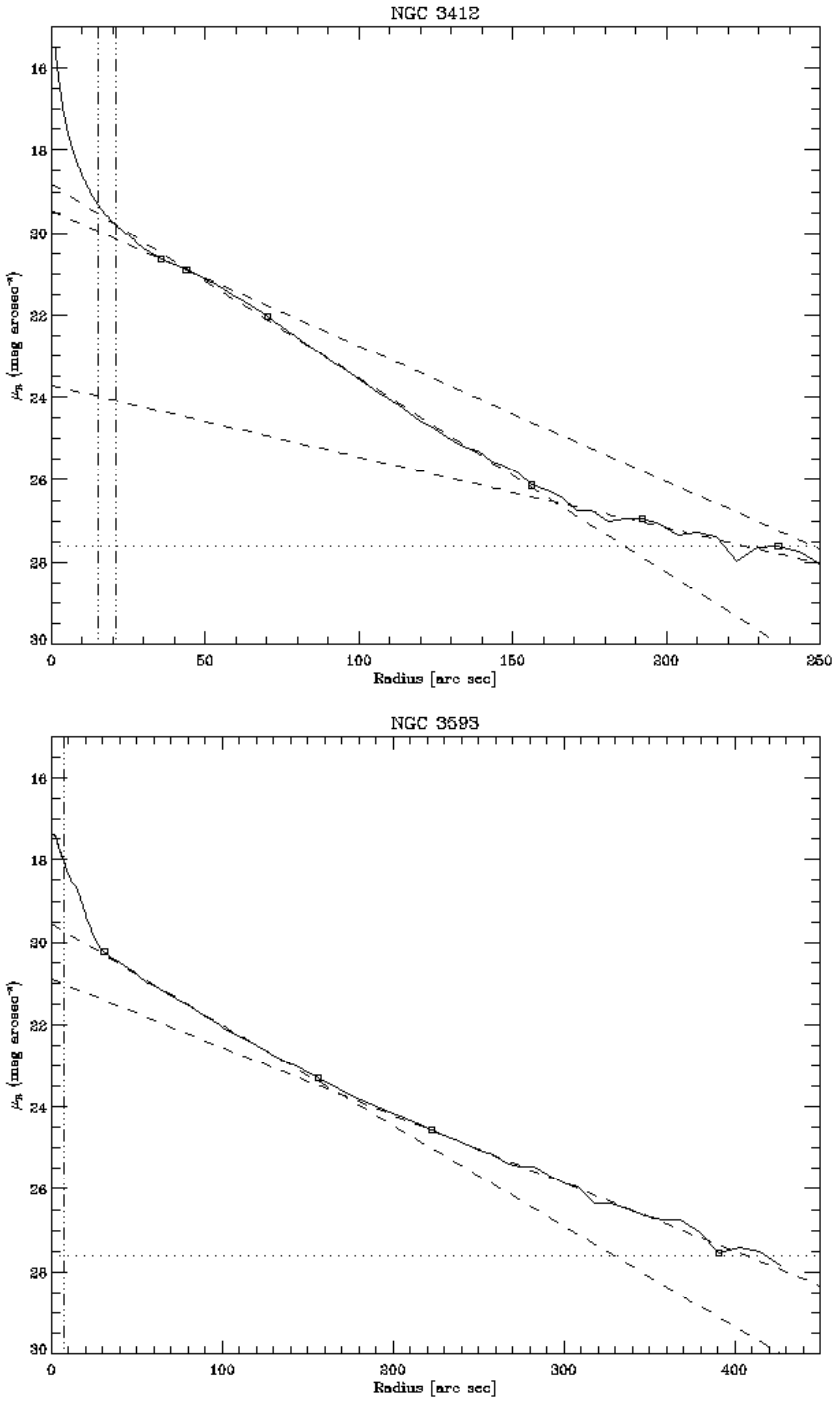

Figure A.3: (continued)

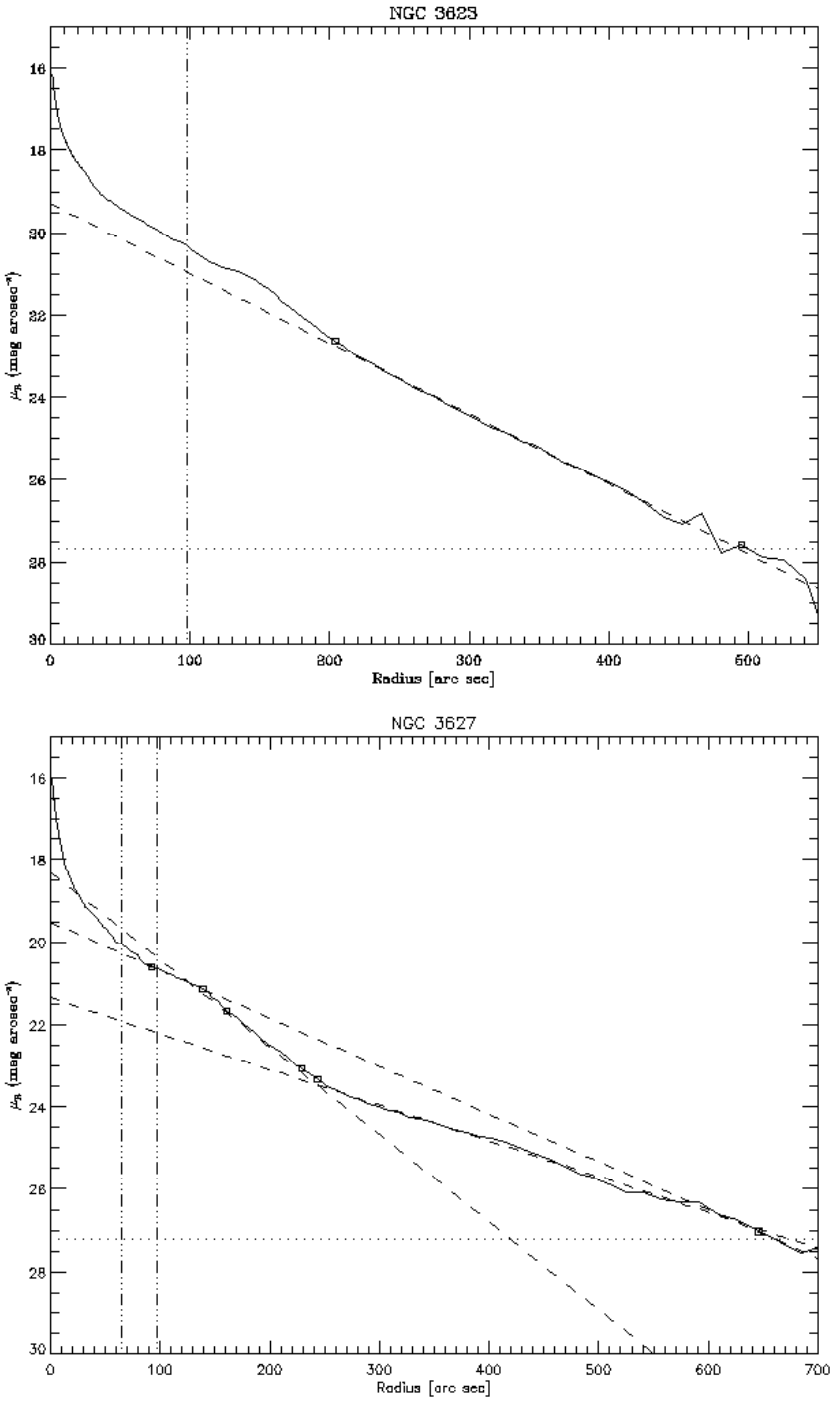

Figure A.3: (continued)

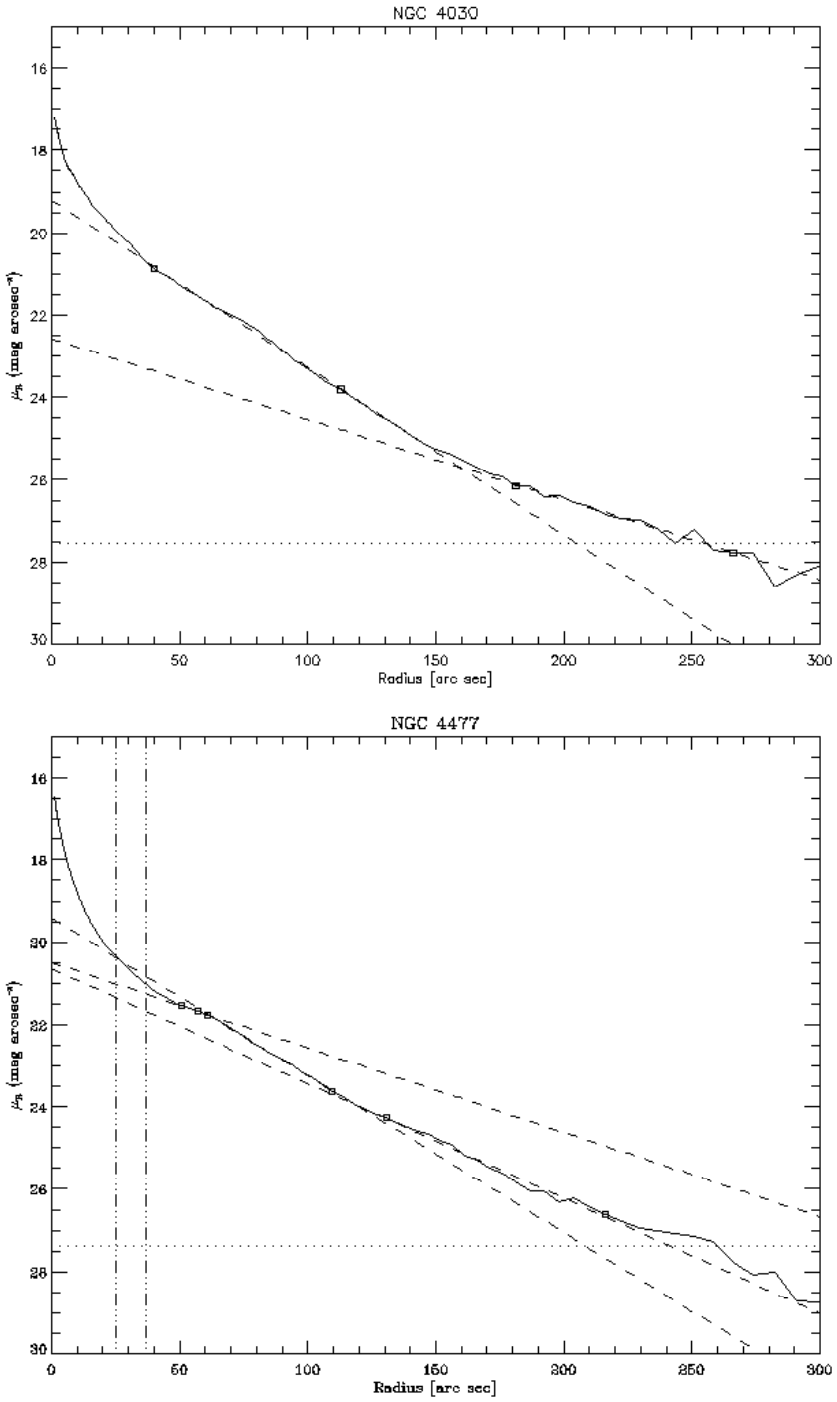

Figure A.3: (continued)

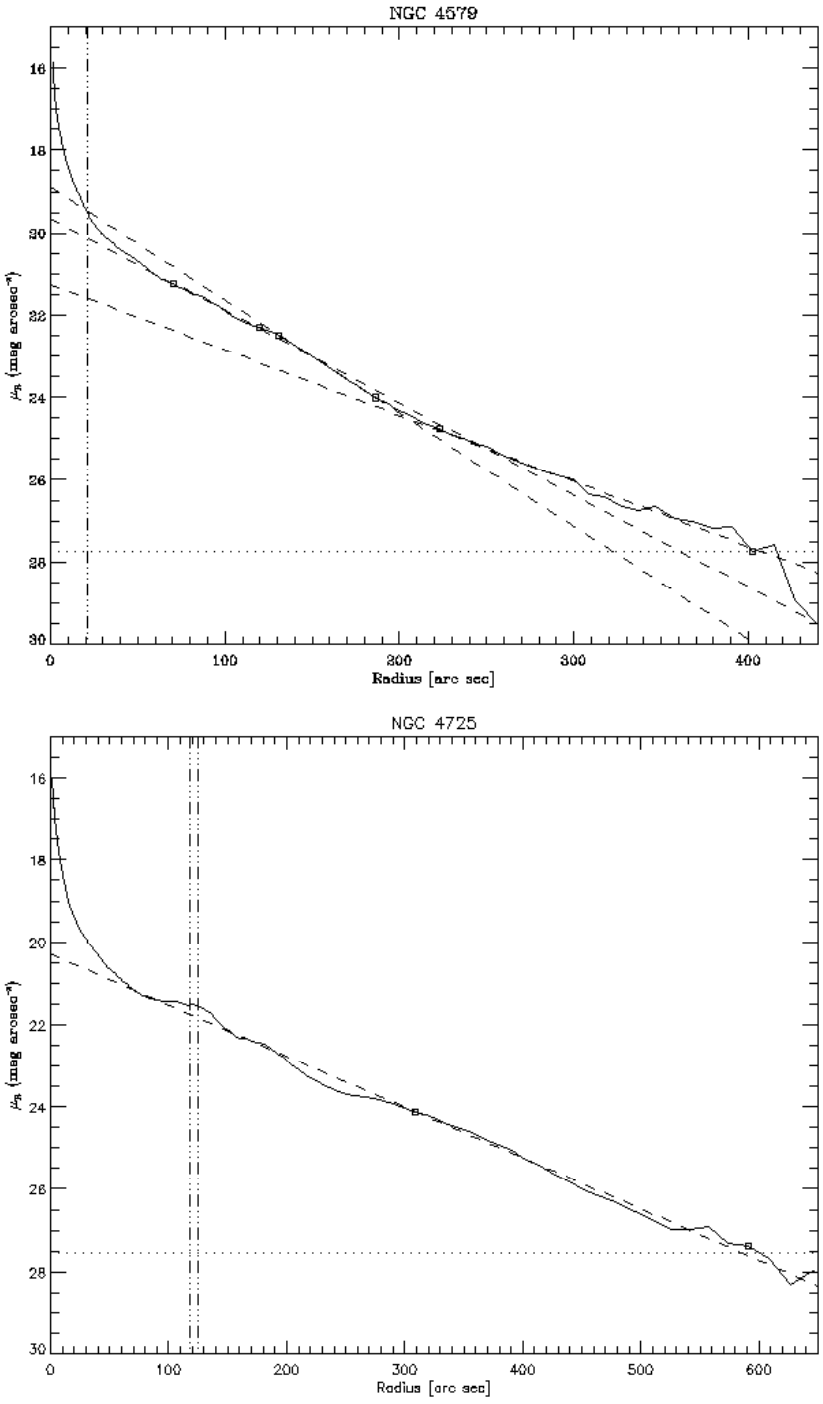

Figure A.3: (continued)

A.4 Radial surface brightness profiles of the control sample galaxies

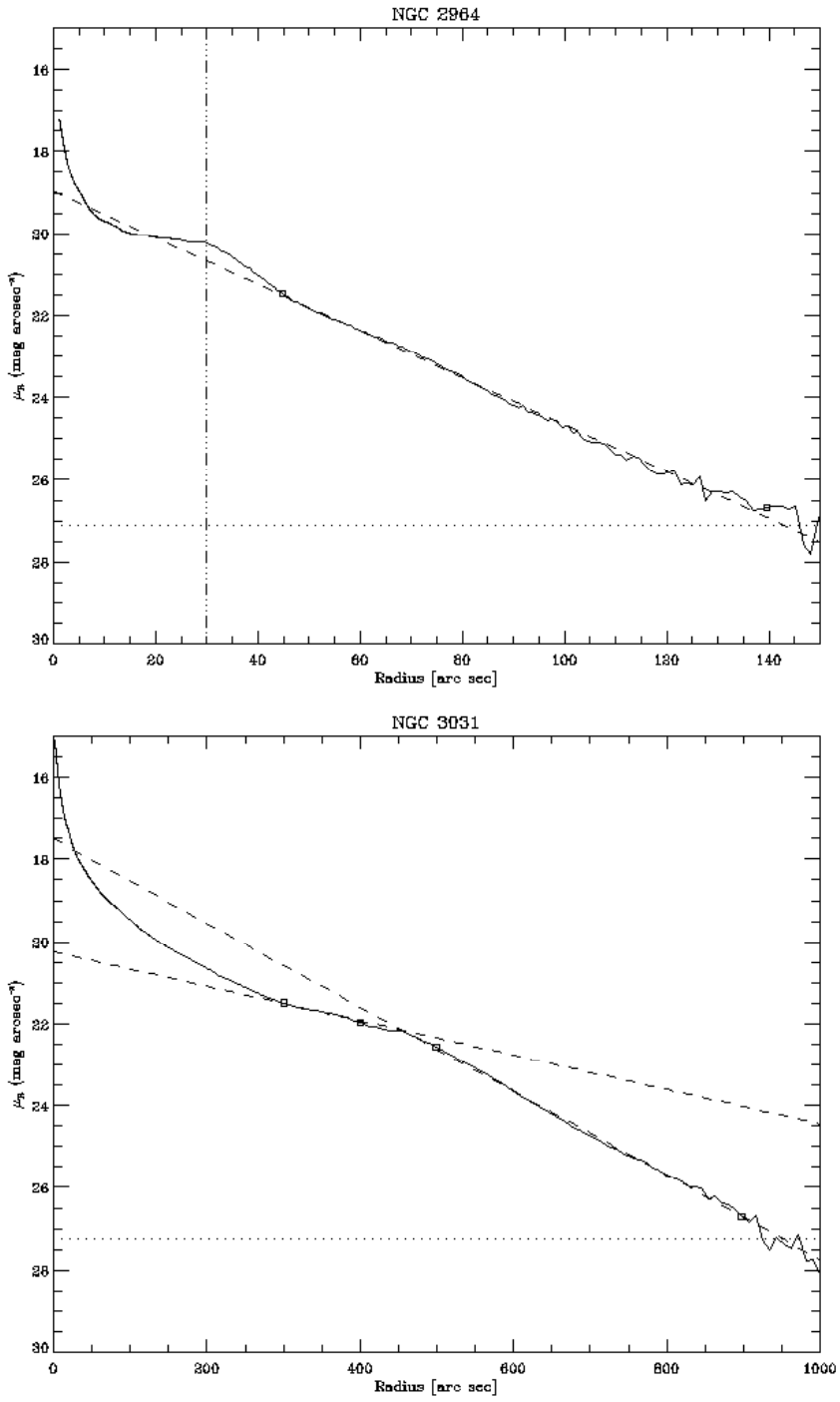

Figure A.4: Luminosity profiles of control galaxies.

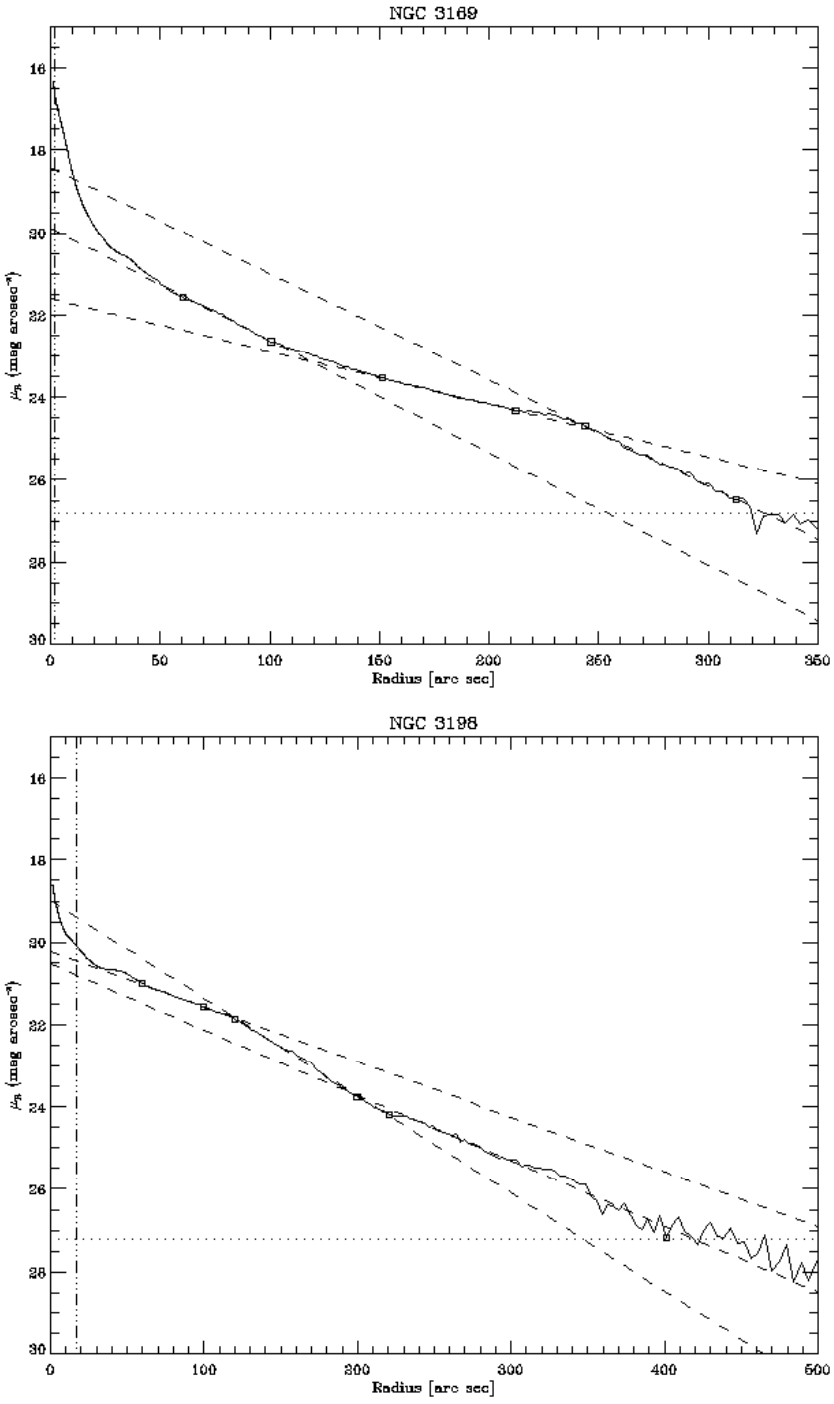

Figure A.4: (continued)

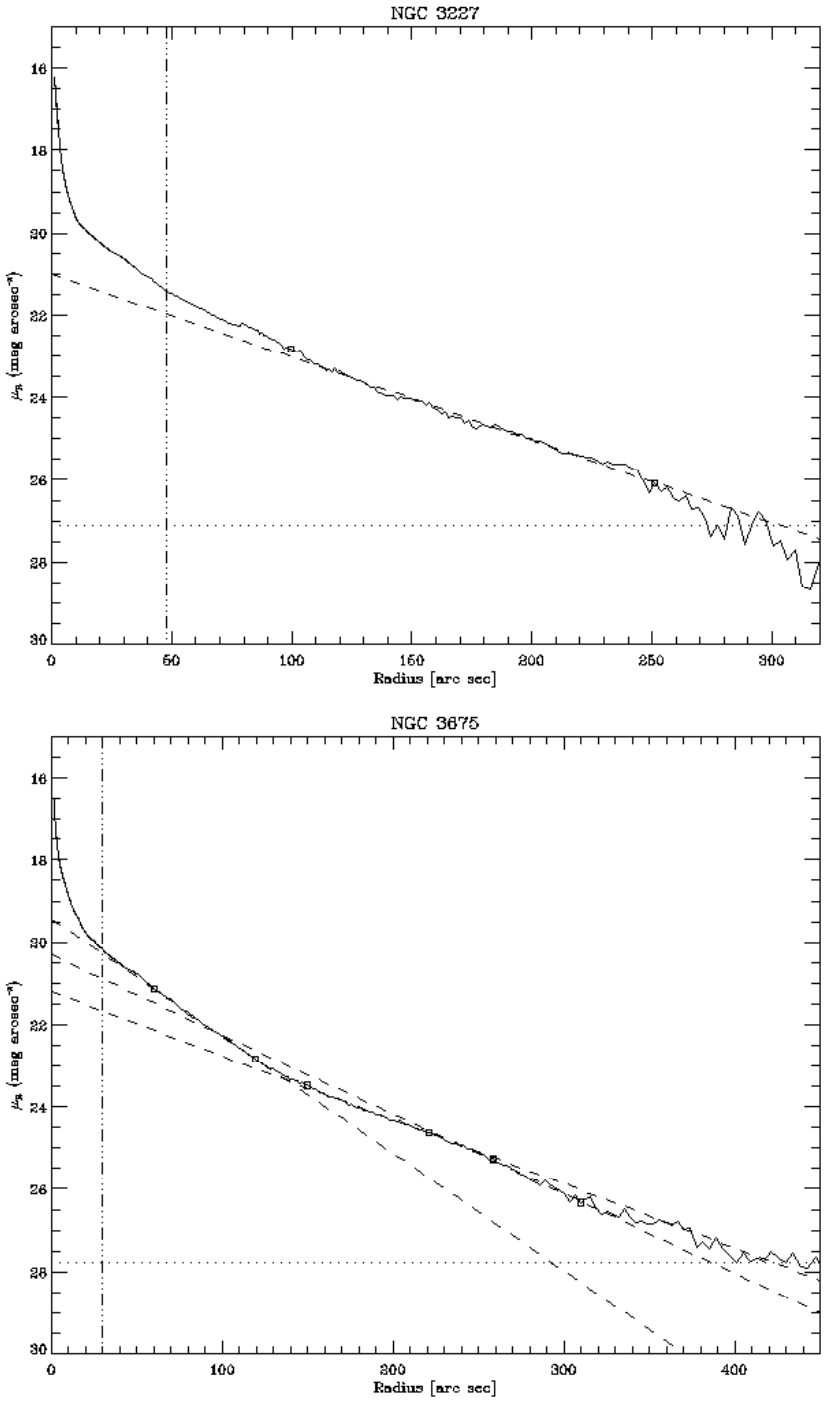

Figure A.4: (continued)

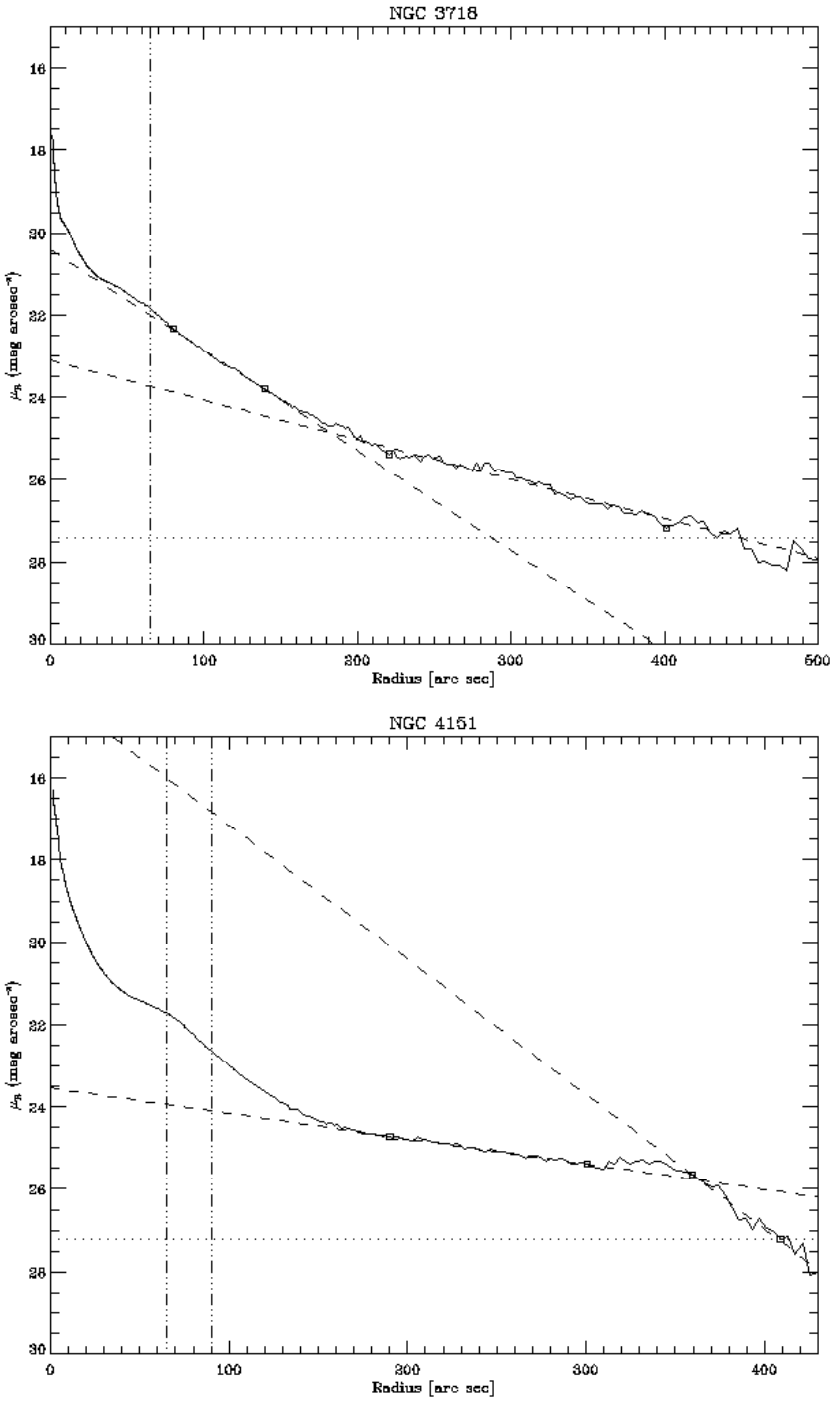

Figure A.4: (continued)

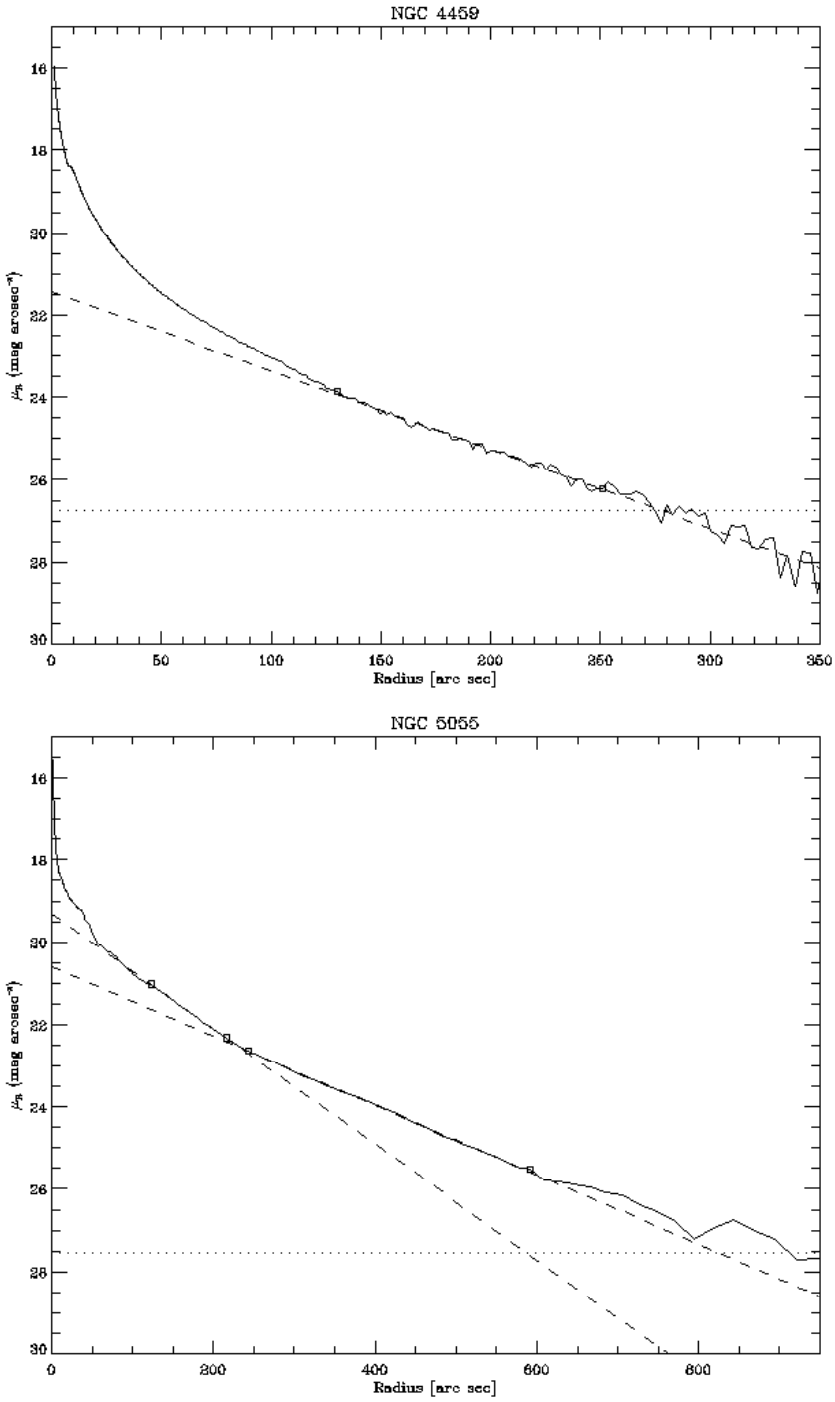

Figure A.4: (continued)

B

Aditional material to Chapter 3

This appendix includes aditional material to Chapter 3.

B.1 Tables

Table B.1: Properties of the nuclear ring host galaxies.

Galaxy	RA (hh mm)	dec (°')	Distance (Mpc)	Refs.	Morph. type	Nuclear activity	Disc scale-length (kpc)	Disc PA (°)	ϵ_d
(1)	(2)	(3)	(4)	(5)	(6)	(7)	(8)	(9)	(10)
ESO 198-13	02 29	−48 29	74.2	(1)	(R)SA(r)ab	–	–	119.7	0.26
ESO 437-33	10 40	−30 12	43.5	(1)	(R'_1)SAB(rl)a	–	5.7	15.6	0.32
ESO 437-67	10 52	−32 40	43.3	(1)	(R'_1)SB(r)ab	–	2.8	–	0.00
ESO 565-11	09 29	−20 23	66.5	(1)	(R'_1)SB(rs)a	–	5.9	156.1	0.28
IC 342	03 47	+68 06	3.3	(2)	SAB(rs)cd	H II	2.5	–	0.05
IC 1438	22 16	−21 26	36.2	(1)	$(R_1R'_2)$SAB(r)a	–	3.7	–	0.07
IC 4214	13 18	−32 06	31.4	(1)	(R'_1)SAB(r)a	–	3.1	165.4	0.38
IC 4933	20 03	−54 59	67.3	(1)	SB(rs)bc	–	6.1	9.0	0.38
NGC 278	00 52	+47 33	11.7	(1)	SAB(rs)b	H II	0.7	65.8	0.07
NGC 473	01 20	+16 33	31.0	(1)	SAB(r)0/a	–	1.7	153.3	0.42
NGC 521	01 25	+01 44	71.2	(1)	SB(r)bc	Transition 2	7.5	–	0.07
NGC 613	01 34	−29 25	18.7	(1)	SB(rs)bc	–	2.8	121.6	0.23
NGC 718	01 53	+04 12	24.1	(1)	(R′)SAB(rs)a	LINER 2	2.4	7.4	0.15
NGC 864	02 15	+06 00	21.8	(1)	SAB(rs)c	H II	2.9	28.7	0.16
NGC 936	02 28	−01 09	23.0	(3)	SB(rs)0^+	–	4.0	122.7	0.26
NGC 1068	02 43	−00 01	15.3	(1)	(R)SA(rs)b	Sy 1.8	2.9	72.5	0.13
NGC 1079	02 44	−29 00	17.7	(1)	$(R_1R'_2)$SAB(rs)a	–	3.0	78.0	0.41
NGC 1097	02 46	−30 17	15.2	(1)	(R'_1)SB(rs)b pec	–	5.1	134.0	0.31
NGC 1241	03 11	−08 55	55.8	(1)	SAB(rs)b	–	5.2	147.5	0.42
NGC 1300	03 20	−19 25	20.2	(1)	SB(rs)b	–	5.3	87.0	0.18
NGC 1317	03 23	−37 06	23.9	(1)	(R′)SAB(rl)a	–	2.7	64.5	0.11
NGC 1326	03 24	−36 28	16.1	(1)	(R_1)SAB(r)0/a	–	2.5	73.4	0.25
NGC 1343	03 38	+72 34	35.1	(1)	SAB(s)b pec	–	4.9	77.5	0.45
NGC 1386	03 37	−36 00	16.5	(3)	SB(s)0^+	–	1.8	24.6	0.65
NGC 1387	03 37	−35 30	18.9	(4)	$SB0^-$	–	2.0	–	0.00
NGC 1415	03 41	−22 34	19.6	(1)	(R)SAB(s)a	–	2.1	151.7	0.61

Table B.1: (continued).

Galaxy	RA (hh mm)	dec (°')	Distance (Mpc)	Refs.	Morph. type	Nuclear activity	Disc scale-length (kpc)	Disc PA (°)	ϵ_d
(1)	(2)	(3)	(4)	(5)	(6)	(7)	(8)	(9)	(10)
NGC 1433	03 42	−47 13	11.6	(1)	(R'_1)SB(r)ab	–	3.0	159.0	0.16
NGC 1512	04 04	−43 21	9.5	(5)	(R′)SB(r)ab pec	–	1.7	83.0	0.40
NGC 1566	04 20	−54 56	17.4	(1)	(R'_1)SAB(s)bc	–	2.7	36.0	0.19
NGC 1672	04 46	−59 15	15.0	(1)	$(R'_1$:)SB(r)bc	–	2.9	–	0.13
NGC 1808	05 08	−37 31	10.9	(1)	(R_1)SAB(s)b pec	–	1.6	119.5	0.26
NGC 1819	05 12	+05 12	63.2	(1)	SB0	–	3.8	116.2	0.32
NGC 2273	06 50	+60 51	29.4	(1)	(RR)SAB(rs)a	Sy 2	2.9	59.3	0.40
NGC 2595	08 28	+21 29	62.6	(1)	SAB(rs)c	–	4.6	11.8	0.32
NGC 2787	09 19	+69 12	7.5	(3)	SB(r)0^+	LINER 1.9	0.8	113.5	0.45
NGC 2859	09 24	+34 31	25.9	(1)	(R)SB(rl)0^+	Transition 2	2.1	85.0	0.13
NGC 2903	09 32	+21 30	8.9	(6)	SAB(rs)bc	H II	1.9	23.0	0.54
NGC 2935	09 37	−21 08	30.6	(1)	(R'_2)SAB(s)b	–	5.2	171.0	0.24
NGC 2950	09 43	+58 51	22.2	(1)	(R)SB(r)0^o	no activity	2.3	140.0	0.37
NGC 2985	09 50	+72 17	22.6	(1)	(R′)SA(rs)ab	Transition 1.9	4.0	175.5	0.19
NGC 2997	09 46	−31 11	13.1	(1)	S$\underline{\text{A}}$B(s)c	–	3.7	96.6	0.40
NGC 3011	09 50	+32 13	23.8	(1)	S0/a	–	0.7	59.5	0.17
NGC 3081	09 59	−22 50	31.8	(1)	$(R_1R'_2)$SAB(r)0/a	–	2.6	97.0	0.16
NGC 3185	10 18	+21 41	18.9	(1)	(R)SB(r)a	Sy 2	2.1	130.2	0.42
NGC 3245	10 27	+28 30	21.1	(1)	SA(l)0^o	Transition 2	2.0	176.0	0.44
NGC 3258	10 29	−35 36	37.5	(1)	E1	–	–	–	–
NGC 3268	10 30	−35 20	37.5	(1)	E2	–	–	–	–
NGC 3310	10 39	+53 30	17.4	(1)	SA(rs)bc pec	H II	2.8	167.0	0.38
NGC 3313	10 37	−25 19	51.1	(1)	SB(r)b	–	9.1	55.0	0.19
NGC 3351	10 44	+11 42	11.1	(7)	SB(r)b	H II	3.0	9.9	0.40
NGC 3379	10 47	+12 35	10.6	(3)	E1	LINER 2	–	–	–
NGC 3414	10 51	+27 59	22.1	(1)	$S0^o$ pec	LINER 2	2.5	22.7	0.14

Table B.1: (continued).

Galaxy	RA (hh mm)	dec (°')	Distance (Mpc)	Refs.	Morph. type	Nuclear activity	Disc scale-length (kpc)	Disc PA (°)	ϵ_d
(1)	(2)	(3)	(4)	(5)	(6)	(7)	(8)	(9)	(10)
NGC 3486	11 00	+28 58	11.6	(1)	SAB(r)c	Sy 2	3.0	80.0	0.29
NGC 3504	11 03	+27 58	23.8	(1)	(R'_1)SA$\underline{B}$(rs)ab	H II	1.9	–	0.02
NGC 3593	11 15	+12 49	9.9	(1)	S0/a pec	H II	2.0	86.2	0.51
NGC 3945	11 53	+60 41	21.4	(1)	(R)SB(rl)0^+	LINER 2	7.3	158	0.43
NGC 3982	11 56	+55 08	23.6	(1)	SAB(r)b	Sy 1.9	1.2	–	0.13
NGC 4100	12 06	+49 35	18.6	(1)	(R')SA(s)bc	H II	2.9	165.0	0.72
NGC 4102	12 06	+52 43	18.6	(5)	SAB(s)b?	H II	1.8	38.0	0.44
NGC 4138	12 09	+43 41	13.8	(3)	SA(r)a	Sy 1.9	1.3	148.2	0.40
NGC 4245	12 18	+29 36	15.0	(1)	SB(r)0/a	H II	1.5	174.1	0.18
NGC 4262	12 20	+14 53	20.9	(1)	SB(s)0^-?	no activity	1.2	145.0	0.11
NGC 4274	12 19	+29 37	15.6	(1)	(R')SB(r)ab	H II	2.8	102.5	0.53
NGC 4303	12 22	+04 28	23.1	(1)	SAB(rs)bc	H II	4.2	146.9	0.14
NGC 4314	12 23	+29 54	16.4	(1)	(R'_1)SB(r'l)a	LINER 2	3.3	61.8	0.04
NGC 4321	12 23	+15 49	24.0	(1)	SAB(s)bc	Transition 2	6.6	–	0.09
NGC 4340	12 24	+16 43	15.1	(1)	SB(r)0^+	no activity	2.2	98.6	0.44
NGC 4371	12 25	+11 42	14.3	(8)	SB(r)0^o	no activity	2.3	96.5	0.53
NGC 4448	12 28	+28 37	11.7	(1)	(R)SB(r)ab	H II	1.2	91.8	0.69
NGC 4459	12 29	+13 59	16.1	(8)	SA(r)0^+	Transition 2	2.5	108.3	0.24
NGC 4494	12 31	+25 46	20.9	(1)	E1-2	LINER 2	–	–	–
NGC 4526	12 34	+07 42	14.7	(3)	SAB0^o sp	H II	3.1	113.0	0.65
NGC 4571	12 37	+14 13	16.8	(5)	SA(r)c	–	3.2	34.9	0.18
NGC 4579	12 38	+11 49	23.0	(1)	SA$\underline{B}$(r$\underline{s}$)ab	Sy 1.9	5.0	94.8	0.22
NGC 4593	12 40	−05 21	35.3	(1)	(R')SB(rs)ab	–	5.4	98.1	0.26
NGC 4736	12 51	+41 07	5.2	(3)	(R)S$\underline{A}$B($\underline{r}$s)ab	LINER 2	1.2	105.0	0.13
NGC 4800	12 55	+46 32	14.5	(1)	SA(rs)b	H II	0.8	19.4	0.29
NGC 4826	12 57	+21 41	7.5	(3)	(R')SA(r)$\underline{a}$b pec	Transition 2	2.1	115.0	0.50

Table B.1: (continued).

Galaxy	RA (hh mm)	dec (°')	Distance (Mpc)	Refs.	Morph. type	Nuclear activity	Disc scale-length (kpc)	Disc PA (°)	ϵ_d
(1)	(2)	(3)	(4)	(5)	(6)	(7)	(8)	(9)	(10)
NGC 5020	13 13	+12 36	49.5	(1)	SAB(rs)bc	–	5.9	84.3	0.11
NGC 5033	13 13	+36 36	15.4	(1)	SA(s)c	Sy 1.5	5.2	171.0	0.55
NGC 5135	13 26	−29 50	57.4	(1)	SB(l)ab	–	13.9	–	0.09
NGC 5194	13 30	+47 12	7.7	(3)	SA(s)bc	Sy 2	4.3	163.0	0.21
NGC 5236	13 37	−29 52	4.5	(7)	SAB(s)c	–	2.0	–	0.07
NGC 5247	13 38	−17 53	18.9	(1)	SA(s)c	–	4.6	40.0	0.17
NGC 5248	13 38	+08 53	17.9	(1)	(R′)SAB(rs)bc	H II	2.9	125.0	0.41
NGC 5377	13 56	+47 14	29.2	(1)	(R'_1)SA$\underline{B}$(rs)a	LINER 2	3.8	37.6	0.54
NGC 5427	14 03	−06 02	39.4	(1)	SA(rs)b$\underline{c}$	–	3.9	154.0	0.07
NGC 5728	14 42	−17 11	39.7	(1)	(R_1)SA$\underline{B}$(r)a	–	4.2	14.5	0.41
NGC 5806	15 00	+01 53	20.5	(1)	SAB(s)b	H II	2.0	174.3	0.48
NGC 5812	15 01	−07 27	28.0	(1)	E0	–	–	–	–
NGC 5905	15 15	+55 31	52.4	(1)	SB($\underline{r}$s)bc	H II	3.4	128.9	0.19
NGC 5945	15 30	+42 55	81.3	(1)	(R_1)SB(rs)ab	–	8.1	115.0	0.07
NGC 6503	17 49	+70 09	5.2	(9)	SA(s)cd	Transition 2	0.8	122.3	0.67
NGC 6753	19 11	−57 93	41.8	(1)	(R)SA(r)b	–	3.4	29.3	0.15
NGC 6782	19 24	−59 55	52.5	(1)	$(R_1R'_2)$SB(r)a	–	3.9	34.9	0.10
NGC 6861	20 07	−48 22	38.0	(1)	SA(s)0^-	–	4.3	133.1	0.36
NGC 6951	20 37	+66 06	24.4	(1)	SA$\underline{B}$(rs)bc	Sy 2	5.0	132.2	0.29
NGC 6958	20 49	−38 00	37.1	(1)	E^+	–	–	–	–
NGC 7049	21 19	−48 33	30.2	(1)	SA(s)0^o	–	2.7	63.7	0.32
NGC 7217	22 08	+31 22	16.0	(1)	(R)SA(r)ab	LINER 2	2.0	93.0	0.14
NGC 7469	23 03	+08 52	70.7	(1)	(R′)SAB(rs)a	–	10.2	126.5	0.13
NGC 7552	23 16	−42 35	20.2	(1)	(R'_1)SB(s)ab	–	1.7	169.9	0.13
NGC 7570	23 17	+13 29	68.1	(1)	SBa	–	3.9	152.0	0.12
NGC 7716	23 37	+00 18	36.6	(1)	SAB(r)b	–	2.5	30.4	0.31

Table B.1: (continued).

Galaxy	RA (hh mm)	dec (°')	Distance (Mpc)	Refs.	Morph. type	Nuclear activity	Disc scale-length (kpc)	Disc PA (°)	ϵ_d
(1)	(2)	(3)	(4)	(5)	(6)	(7)	(8)	(9)	(10)
NGC 7742	23 44	+10 46	24.2	(1)	SA(r)ab	Transition 2	1.3	–	0.05
NGC 7771	23 51	+20 07	62.5	(7)	SB(s)a pec	–	5.1	67.0	0.50
UGC 10445	16 34	+28 59	16.8	(1)	SBc	–	–	143.1	0.29

Notes: galaxy ID (col. 1), position on the sky in J2000.0 coordinates (cols. 2 and 3), distance (col. 4, from the literature for galaxies with radial velocity $v \leq 1400$ where possible; In other cases from the radial velocity from HyperLEDA, with $H_0 = 70$km/s Mpc), reference of the distance measurement (col. 5), morphological type (col. 6, from Buta et al. 2007 when available and from NED for the other galaxies), presence and type of nuclear activity (col. 7, from Ho et al. 1997b), scalelength of the exponential disc in kpc (col. 8), PA of the major axis of the outer disc (col. 9), and outer disc ellipticity (col. 10). Orientation parameters come different sources described in Section 3.4.3. Distance references: (1) Paturel et al. (2003) (HyperLEDA), (2) Karachentsev et al. (2003), (3) Tonry et al. (2001), (4) Jensen et al. (2003), (5) Tully et al. (1988), (6) Drozdovsky & Karachentsev (2000), (7) Saha et al. (2006), (8) Mei et al. (2007), and (9) Karachentsev & Sharina (1997).

Table B.2: Properties of the nuclear rings and the bars in our sample galaxies.

Galaxy	Ring semi-major axis		Rel. Ring	$\epsilon_{\rm r}$	PA offset (°)	Bar length	$\epsilon_{\rm b}$	$Q_{\rm g}$	$r_{Q_{\rm g}}$		Ring0
	(″)	(pc)	size	Deproj. (°)	Deproj.	(kpc)	Deproj.		(″)	(kpc)	type
(1)	(2)	(3)	(4)	(5)	(6)	(7)	(8)	(9)	(10)	(11)	(12)
ESO 198-13	9.7	3490	0.234	0.05	–	–	–	–	–	–	sf
ESO 437-33	3.5	730	0.071	0.18	66	2.7	0.16	0.056	15	3.2	sf
ESO 437-67	3.4	710	0.044	0.10	29	5.5	0.61	0.403	23	4.8	sf
ESO 565-11	11.1	3560	0.212	0.55	39	11.6	0.62	0.316	29	9.3	sf
IC 342	2.9	50	0.002	0.31	59	2.0	0.39	0.177	225	3.6	sf
IC 1438	3.9	680	0.054	0.36	44	3.5	0.49	0.155	17	3.0	sf
IC 4214	7.6	1150	0.081	0.21	31	4.4	0.36	0.127	27	4.1	sf
IC 4933	2.6	850	0.041	0.19	70	8.8	0.60	0.239	21	6.9	sf
NGC 278	4.7	260	0.057	0.18	14	0.8	0.22	0.090	27	1.5	sf
NGC 473	11.3	1690	0.201	0.06	–	–	–	0.119	25	3.8	sf
NGC 521	4.3	1470	0.049	0.24	85	6.2	0.45	0.146	13	4.5	sf
NGC 613	4.5	400	0.027	0.26	70	7.0	0.65	0.442	47	4.3	sf
NGC 718	2.9	330	0.034	0.17	59	2.6	0.44	0.133	21	2.5	sf
NGC 864	0.8	90	0.007	0.08	84	3.5	0.53	0.376	19	2.0	sf
NGC 936	8.5	940	0.062	0.12	53	5.1	0.52	0.201	39	4.3	sf
NGC 1068	16.0	1190	0.077	0.31	28	4.6	0.31	0.094	55	4.1	sf
NGC 1079	1.6	130	0.019	0.20	87	3.8	0.51	0.238	37	3.2	sf
NGC 1097	13.2	970	0.041	0.32	56	6.7	0.51	0.241	75	5.5	sf
NGC 1241	2.9	790	0.033	0.08	83	7.8	0.62	0.279	21	5.7	sf
NGC 1300	4.1	400	0.022	0.15	10	7.3	0.71	0.541	63	6.2	sf
NGC 1317	12.5	1450	0.163	0.15	90	5.9	0.36	0.097	35	4.1	sf
NGC 1326	6.2	480	0.048	0.14	75	3.1	0.50	0.163	39	3.0	sf
NGC 1343	11.6	1970	0.122	0.30	69	9.7	0.31	0.152	47	8.0	sf
NGC 1386	16.8	1340	0.138	0.18	–	–	–	–	–	–	sf
NGC 1387	7.3	660	0.080	0.06	0	2.2	0.31	0.078	19	1.7	sf
NGC 1415	9.9	940	0.089	0.25	19	5.1	0.54	0.190	47	4.5	sf

Table B.2: (continued).

Galaxy	Ring semi-major axis		Rel. Ring	$\epsilon_{\rm r}$	PA offset (°)	Bar length	$\epsilon_{\rm b}$	$Q_{\rm g}$	$r_{Q_{\rm g}}$		Ring
	(″)	(pc)	size	Deproj.	Deproj. (°)	(kpc)	Deproj.		(″)	(kpc)	type
(1)	(2)	(3)	(4)	(5)	(6)	(7)	(8)	(9)	(10)	(11)	(12)
NGC 1433	9.8	550	0.053	0.32	55	5.6	0.67	0.390	67	3.8	sf
NGC 1512	10.4	480	0.052	0.20	45	5.0	0.69	0.366	79	3.6	sf
NGC 1566	9.7	820	0.047	0.23	7	3.0	0.42	0.235	71	6.0	sf
NGC 1672	5.8	420	0.031	0.23	4	5.2	0.64	0.349	59	4.3	sf
NGC 1808	5.4	280	0.033	0.20	5	3.9	0.61	0.388	73	3.9	sf
NGC 1819	2.9	870	0.055	0.33	86	8.3	0.29	0.123	23	7.0	sf
NGC 2273	2.5	360	0.035	0.41	27	3.7	0.52	0.218	21	3.0	sf
NGC 2595	5.4	1640	0.106	0.29	55	11.8	0.64	0.392	29	8.8	sf
NGC 2787	2.8	100	0.026	–	–	1.7	0.47	0.137	37	1.3	p
	2.8	100	0.026	–	–	1.7	0.47	0.137	37	1.3	p
NGC 2859	6.8	850	0.059	0.34	61	4.8	0.44	0.156	33	4.1	sf
NGC 2903	3.7	160	0.011	0.32	70	2.9	0.56	0.273	61	2.6	sf
NGC 2935	3.6	530	0.027	0.10	88	3.9	0.48	0.196	25	3.7	sf
NGC 2950	4.7	510	0.059	0.26	64	2.8	0.27	0.066	23	2.5	sf
NGC 2985	0.5	60	0.004	0.18	5	8.1	0.29	0.061	23	2.5	sf
NGC 2997	5.5	350	0.016	0.15	–	–	–	0.306	99	6.3	sf
NGC 3011	5.4	620	0.216	0.08	–	–	–	0.055	15	1.7	sf
NGC 3081	7.8	1200	0.094	0.43	47	5.7	0.55	0.194	35	5.4	sf
NGC 3185	2.2	200	0.033	0.37	89	3.3	0.43	0.138	27	2.5	sf
NGC 3245	1.1	110	0.011	0.10	–	–	–	0.088	13	1.3	sf
NGC 3258	1.1	190	0.011	–	–	–	–	–	–	–	d
NGC 3268	0.7	130	0.006	–	–	–	–	–	–	–	d
NGC 3310	8.2	690	0.119	0.13	8	2.1	0.44	0.128	19	1.6	sf
NGC 3313	5.0	1230	0.053	0.12	35	12.9	0.66	0.321	33	8.2	sf
NGC 3351	7.7	410	0.036	0.25	66	5.5	0.67	0.225	63	3.4	sf
NGC 3379	1.5	80	0.009	–	–	–	–	–	–	–	d

Table B.2: (continued).

Galaxy	Ring semi-major axis		Rel. Ring	$\epsilon_{\rm r}$	PA offset	Bar length	$\epsilon_{\rm b}$	$Q_{\rm g}$	$r_{Q_{\rm g}}$		Ring
	($''$)	(pc)	size	Deproj.	Deproj. ($^\circ$)	(kpc)	Deproj.		($''$)	(kpc)	type
(1)	(2)	(3)	(4)	(5)	(6)	(7)	(8)	(9)	(10)	(11)	(12)
NGC 3414	8.2	880	0.102	0.04	84	4.4	0.23	0.097	33	3.5	sf
NGC 3486	22.2	1250	0.122	0.14	88	4.6	0.32	0.087	81	4.6	sf
NGC 3504	1.8	200	0.022	0.19	20	3.7	0.60	0.311	31	3.6	sf
NGC 3593	7.0	330	0.048	0.21	–	–	–	–	–	–	sf
NGC 3945	5.3	550	0.031	0.23	81	6.3	0.58	0.163	53	5.5	sf
NGC 3982	10.2	1160	0.159	0.20	26	4.0	0.23	0.126	13	1.5	sf
NGC 4100	5.4	490	0.040	0.33	–	–	–	–	–	–	sf
NGC 4102	1.6	140	0.018	0.15	71	1.3	0.37	0.108	13	1.2	sf
NGC 4138	19.9	1330	0.221	0.20	–	–	–	0.037	35	2.3	sf
NGC 4245	4.6	330	0.059	0.06	41	2.8	0.50	0.194	29	2.1	sf
NGC 4262	2.9	290	0.051	0.09	66	1.4	0.34	0.083	11	1.1	sf
NGC 4274	9.0	680	0.083	0.37	81	5.0	0.59	0.231	49	3.7	sf
NGC 4303	3.2	350	0.016	0.11	83	5.8	0.11	0.285	41	4.6	sf
NGC 4314	7.1	560	0.061	0.31	11	5.7	0.66	0.432	49	3.9	sf
NGC 4321	7.5	870	0.041	0.32	22	6.7	0.51	0.221	85	9.9	sf
NGC 4340	8.6	630	0.103	0.14	22	4.7	0.63	0.290	57	4.2	sf
NGC 4371	0.7	50	0.006	0.07	55	4.9	0.60	0.175	63	4.4	d/sf?
	10.6	740	0.090	0.22	55	4.9	0.60	0.175	63	4.4	sf
NGC 4448	1.4	80	0.025	0.18	46	2.6	0.70	0.192	29	1.6	sf
NGC 4459	2.1	160	0.015	0.18	–	–	–	0.043	21	1.6	sf
	8.1	630	0.061	0.06	–	–	–	0.043	21	1.6	sf
NGC 4494	0.6	60	0.004	–	–	–	–	–	–	–	d
NGC 4526	10.6	760	0.052	0.29	–	–	–	–	–	–	sf
NGC 4571	15.5	1260	0.140	0.06	–	–	–	0.192	37	3.0	sf
NGC 4579	1.6	170	0.009	0.04	54	5.1	0.47	0.200	33	3.7	sf
NGC 4593	5.2	880	0.070	0.09	71	10.3	0.61	0.356	43	7.4	sf

Table B.2: (continued).

Galaxy	Ring semi-major axis		Rel. Ring	ϵ_r	PA offset	Bar length	ϵ_b	Q_g	r_{Q_g}		Ring
	($''$)	(pc)	size	Deproj.	Deproj. (°)	(kpc)	Deproj.		($''$)	(kpc)	type
(1)	(2)	(3)	(4)	(5)	(6)	(7)	(8)	(9)	(10)	(11)	(12)
NGC 4736	50.1	1260	0.165	0.22	–	–	–	0.054	139	3.5	sf
NGC 4800	0.4	30	0.007	0.12	67	3.4	0.14	0.087	19	1.3	sf
	1.7	120	0.031	0.08	24	3.4	0.14	0.087	19	1.3	sf
	10.0	700	0.187	0.02	82	3.4	0.14	0.087	19	1.3	sf
NGC 4826	4.0	150	0.013	0.21	–	–	–	0.069	25	0.9	sf
NGC 5020	4.3	1020	0.051	0.22	2	8.6	0.68	0.365	31	7.4	sf
NGC 5033	12.9	960	0.046	0.06	–	–	–	0.246	29	2.2	sf
NGC 5135	2.2	610	0.029	0.21	80	9.5	0.57	0.244	27	7.5	sf
NGC 5194	16.1	600	0.054	0.24	43	1.5	0.29	0.246	135	5.0	sf
NGC 5236	6.1	130	0.012	0.18	87	2.5	0.57	0.294	81	1.8	sf
NGC 5247	4.6	420	0.026	0.22	–	–	–	0.416	75	6.9	sf
NGC 5248	1.7	150	0.012	0.19	19	4.6	0.44	0.100	43	3.7	sf
	7.5	650	0.052	0.20	4	4.6	0.44	0.100	43	3.7	sf
NGC 5377	5.6	790	0.052	0.24	76	9.2	0.36	0.164	47	6.7	sf
NGC 5427	3.2	600	0.028	0.08	–	–	–	0.228	37	7.1	sf
NGC 5728	5.7	1100	0.056	0.23	54	12.7	0.58	0.350	57	11.0	sf
NGC 5806	4.2	420	0.045	0.24	64	3.7	0.30	0.140	41	4.1	sf
NGC 5812	0.1	10	0.001	–	–	–	–	–	–	–	d
NGC 5905	1.6	390	0.016	0.14	53	9.4	0.61	0.352	23	5.8	sf
NGC 5945	3.3	1280	0.065	0.18	65	12.6	0.58	0.232	23	9.1	sf
NGC 6503	47.0	1190	0.266	0.09	–	–	–	–	–	–	sf
NGC 6753	8.5	1720	0.089	0.05	–	–	–	0.045	13	2.6	sf
NGC 6782	4.5	1150	0.060	0.06	3	6.4	0.45	0.205	23	5.9	sf
NGC 6861	1.3	230	0.013	0.36	–	–	–	0.152	15	2.8	sf
NGC 6951	4.7	560	0.034	0.17	78	5.9	0.57	0.275	39	4.6	sf
NGC 6958	1.1	190	0.014	–	–	–	–	–	–	–	d

Table B.2: (continued).

Galaxy	Ring semi-major axis		Rel. Ring	$\epsilon_{\rm r}$	PA offset	Bar length	$\epsilon_{\rm b}$	$Q_{\rm g}$	$r_{Q_{\rm g}}$		Ring
	($''$)	(pc)	size	Deproj.	Deproj. ($^\circ$)	(kpc)	Deproj.		($''$)	(kpc)	type
(1)	(2)	(3)	(4)	(5)	(6)	(7)	(8)	(9)	(10)	(11)	(12)
NGC 7049	2.7	400	0.022	0.13	–	–	–	0.076	15	2.2	d/sf?
NGC 7217	10.8	840	0.082	0.08	–	–	–	0.026	41	3.2	sf
NGC 7469	2.1	700	0.047	0.31	63	5.5	0.25	0.049	13	4.5	sf
NGC 7552	3.5	340	0.029	0.15	47	5.0	0.66	0.513	47	4.6	sf
NGC 7570	3.7	1220	0.076	0.14	72	11.2	0.63	0.424	29	9.6	sf
NGC 7716	6.8	1200	0.121	0.04	45	4.3	0.13	0.096	33	5.9	sf
NGC 7742	9.0	1050	0.163	0.05	–	–	–	0.055	21	2.5	sf
NGC 7771	2.8	830	0.035	0.11	25	10.3	0.58	0.399	27	8.2	sf
UGC 10445	1.5	120	0.025	0.04	–	–	–	–	–	–	sf

Notes: galaxy ID (col. 1), nuclear ring semi-major axis in arcsecs and in pc (cols. 2 and 3), relative size of the nuclear ring, ring diameter divided by $D_{\rm o}$ (col. 4), nuclear ring ellipticity (col. 5), PA offset between the nuclear ring major axis and the bar major axis (col. 6), bar length in kpc (col. 7), bar maximum ellipticity (col. 8), $Q_{\rm g}$ measurement (col. 9), radius at which the maximum non-axisymmetric torque is found in arcsec and in pc (col. 10 and 11), type of nuclear ring, where 'd' stands for dust nuclear ring, 'p' stands for polar nuclear ring, and 'sf' stands for star-forming nuclear ring (col. 12). All the measurements have been done after deprojecting the galaxy using parameters found in Table B.1.

B.2 Nuclear ring images

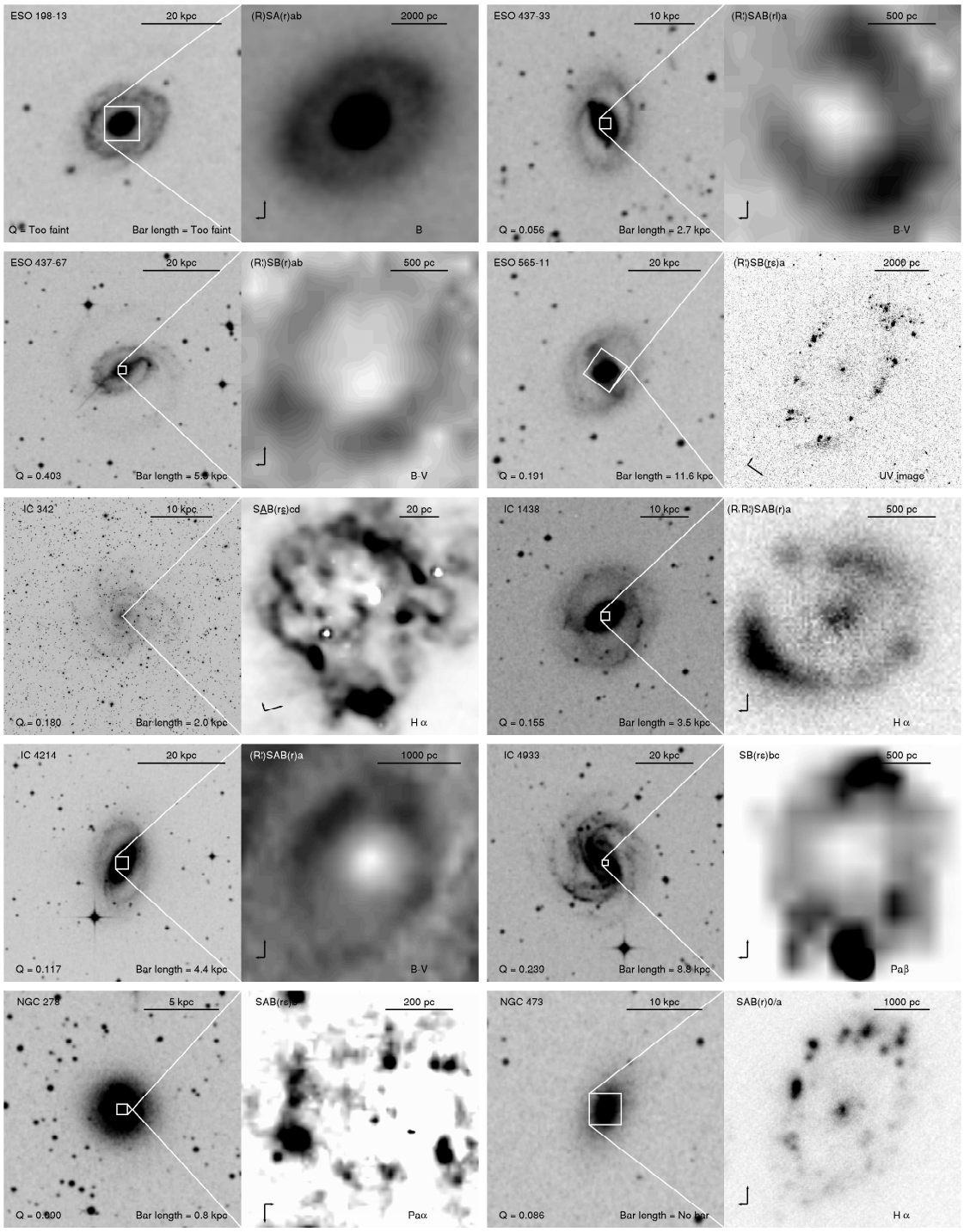

Figure B.1: At the left of each pair of images, we present a DSS images whose size is twice D_{25}. At the right we present ring images, where the ring diameter is scaled to be $\sim 80\%$ of the image side and where darker areas indicate star formation. From left to right and top to bottom, the labels correspond to: galaxy name, DSS image scale, galaxy classification from NED, scale of the nuclear ring image, value of the bar non-axisymmetric torque parameter $Q_{\rm g}$ of the galaxy, bar length after galaxy deprojection, orientation of the nuclear ring image with the large arrow indicating north and the small one east, and kind of nuclear ring image.

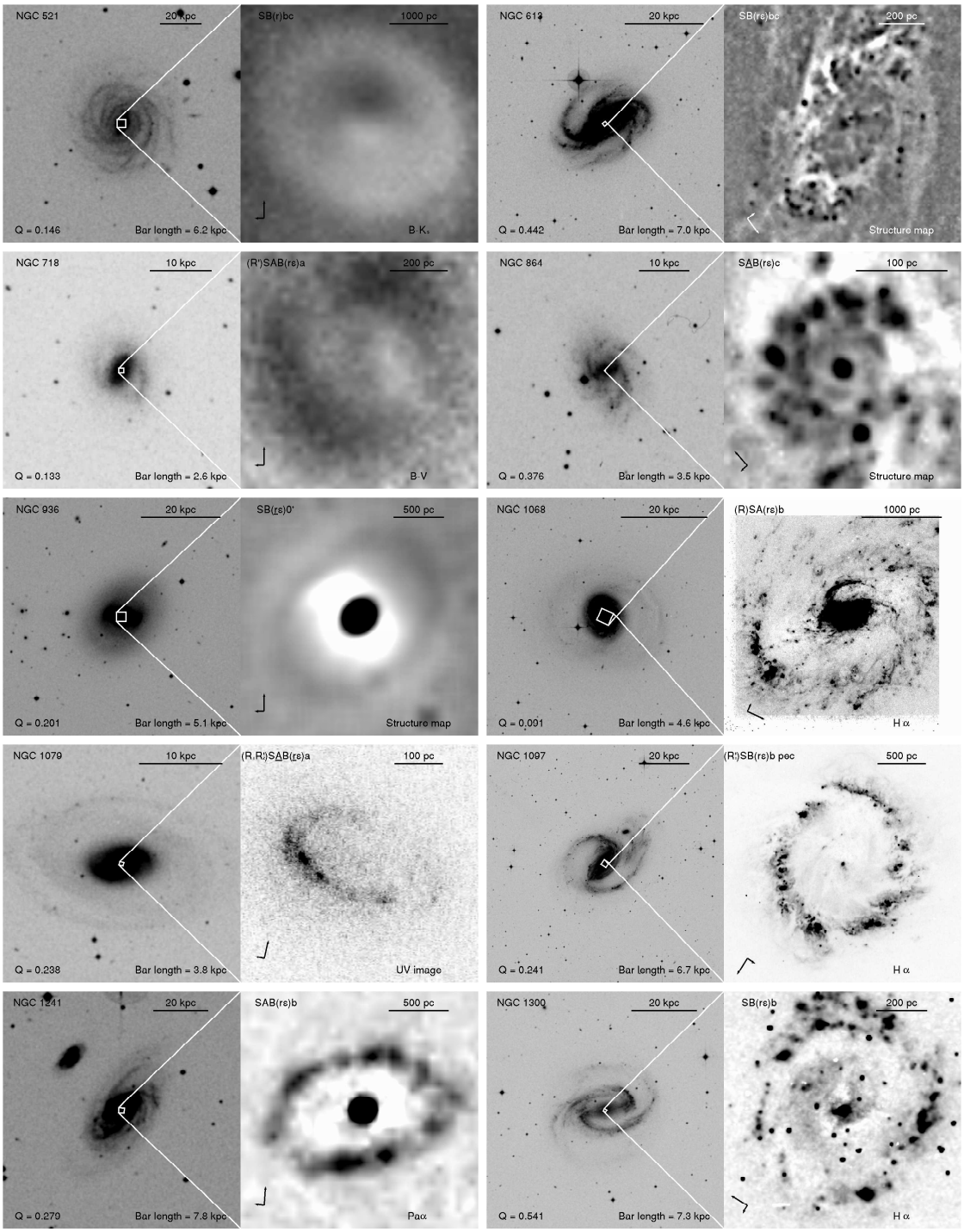

Figure B.1: (continued).

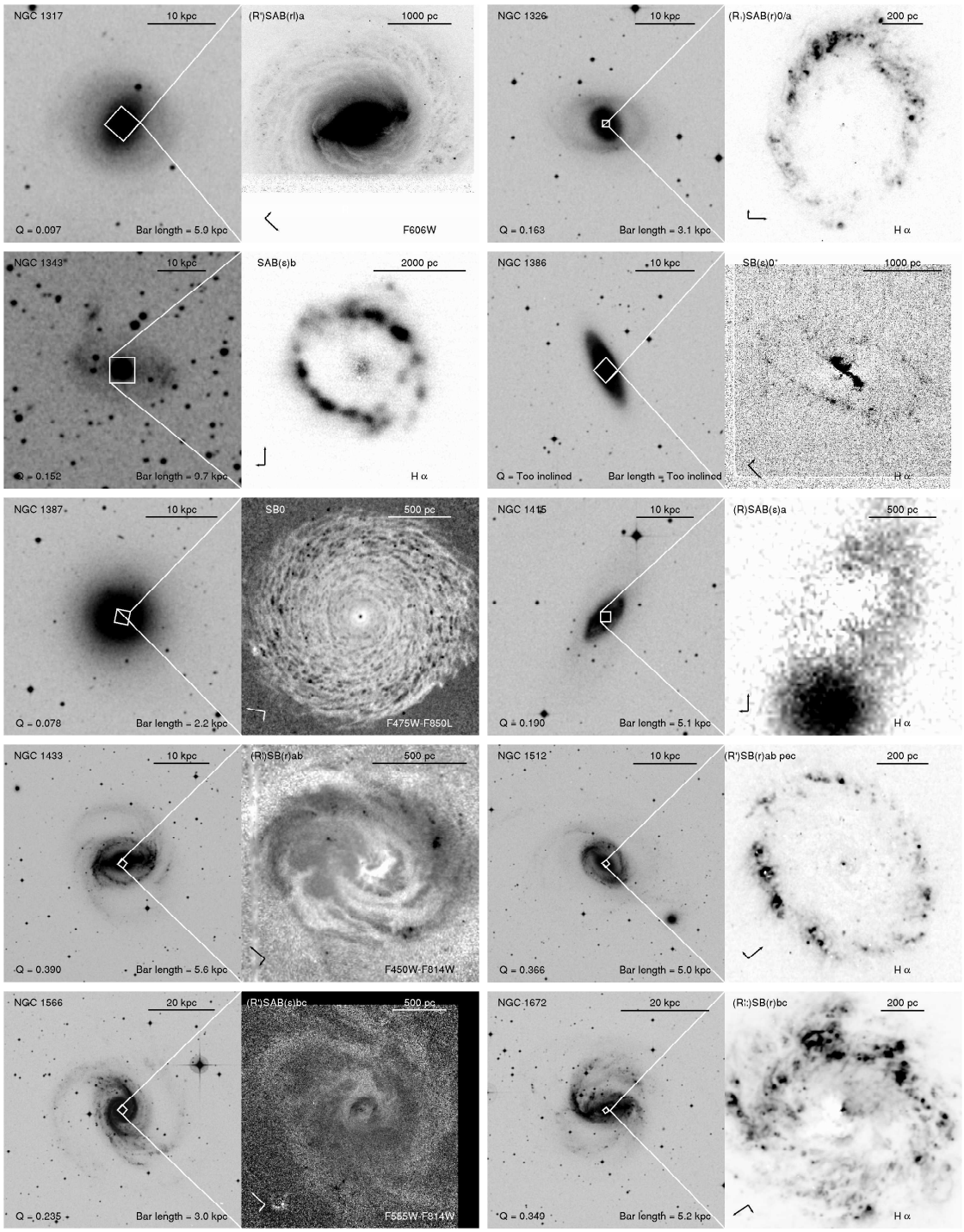

Figure B.1: (continued).

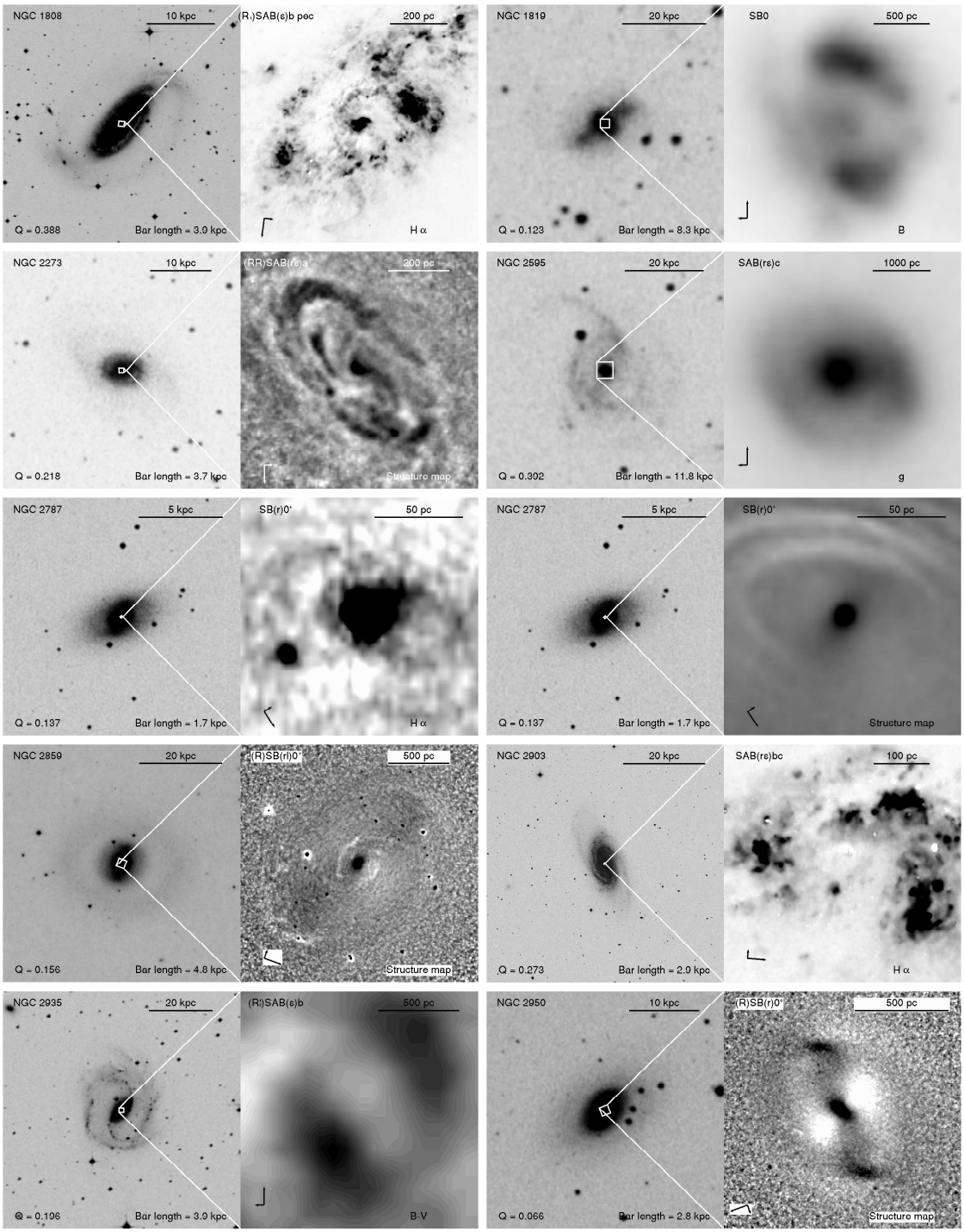

Figure B.1: (continued).

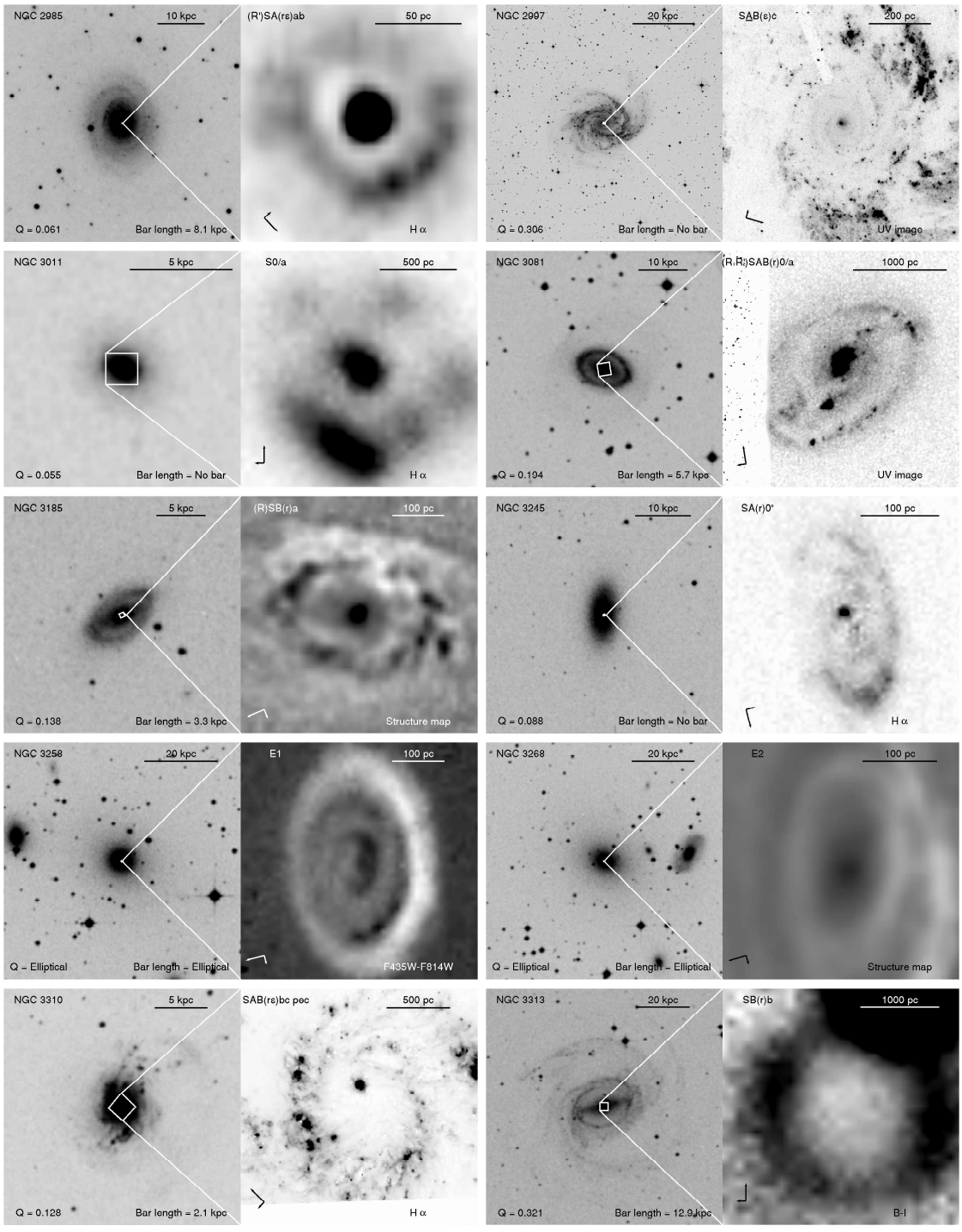

Figure B.1: (continued).

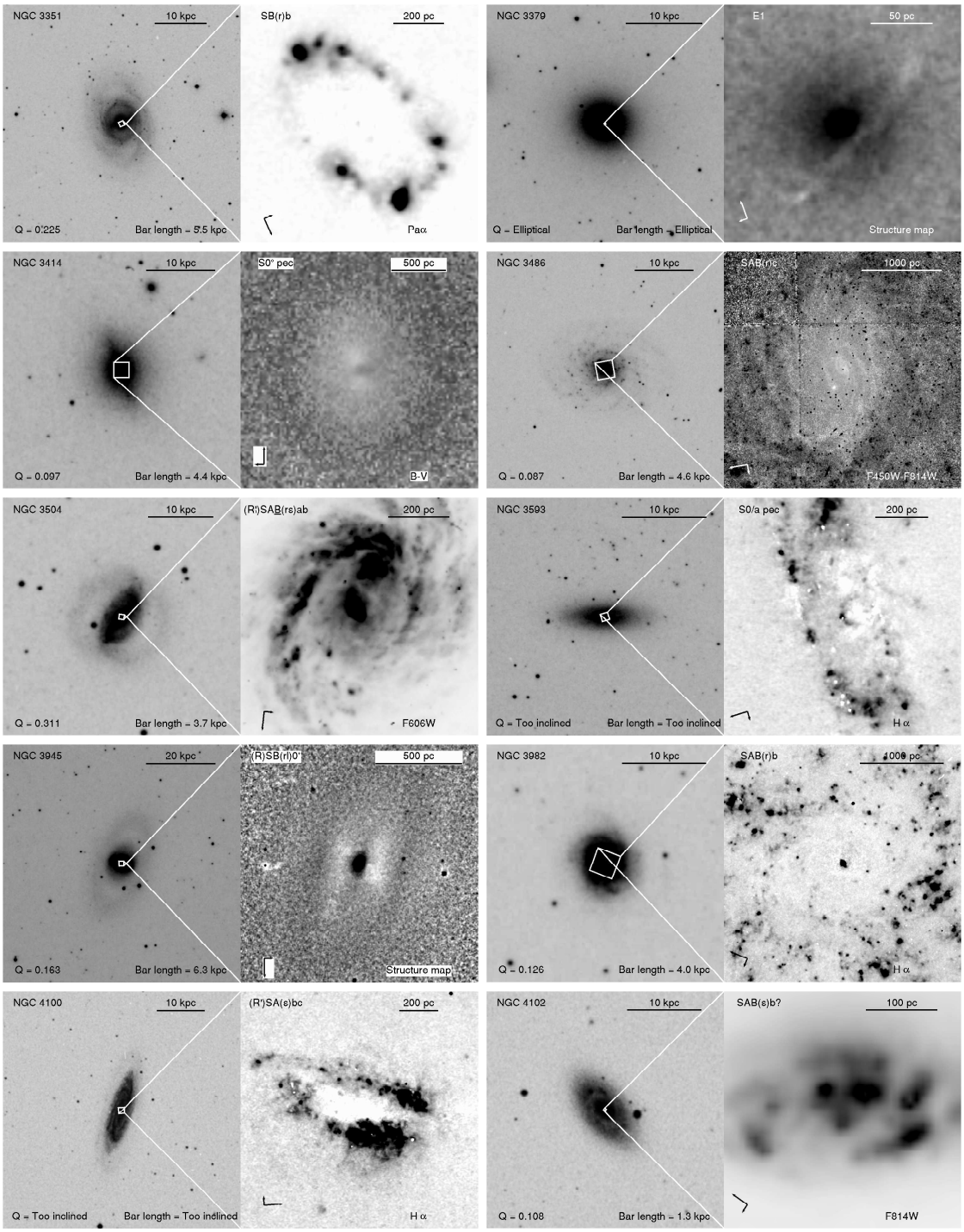

Figure B.1: (continued).

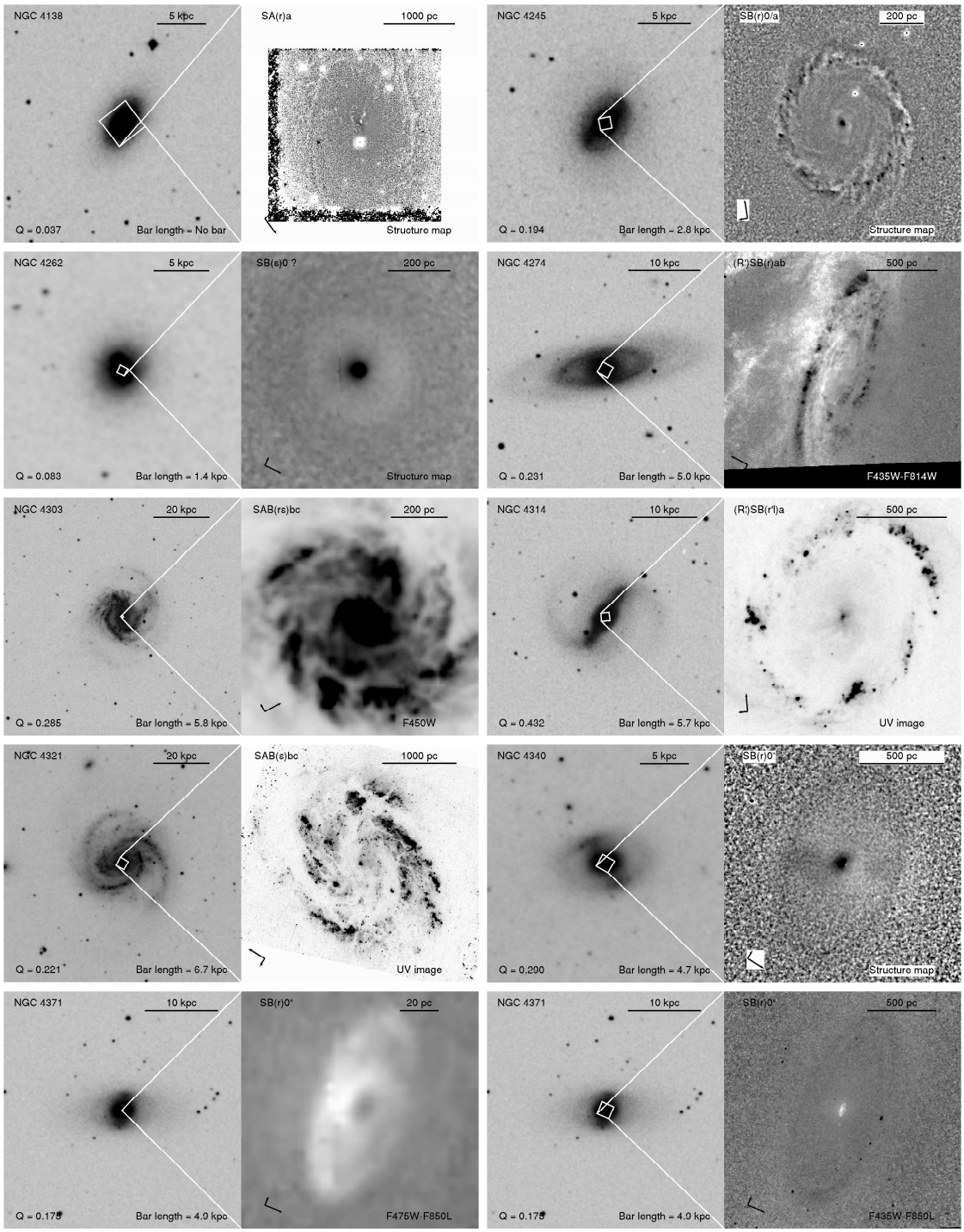

Figure B.1: (continued).

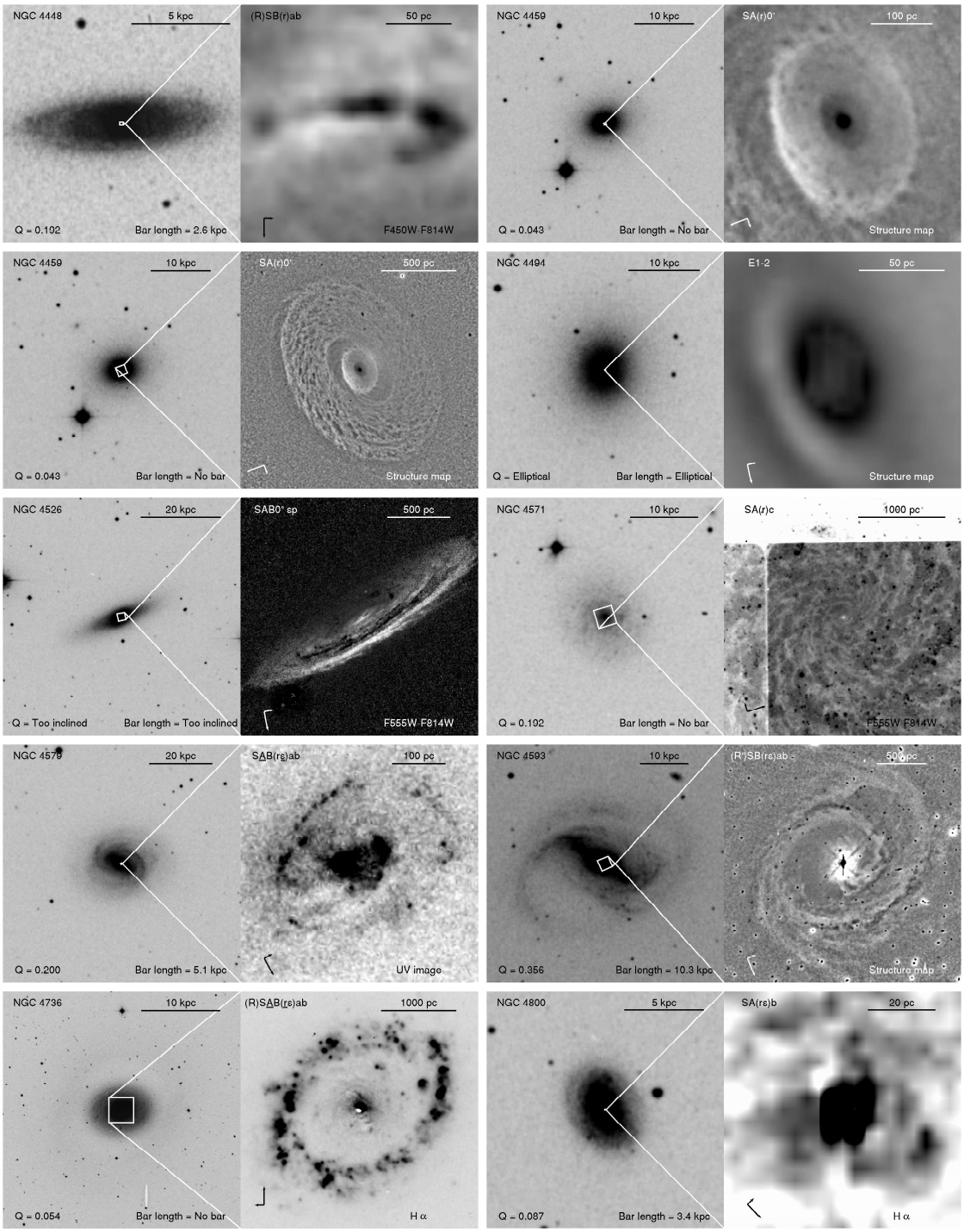

Figure B.1: (continued).

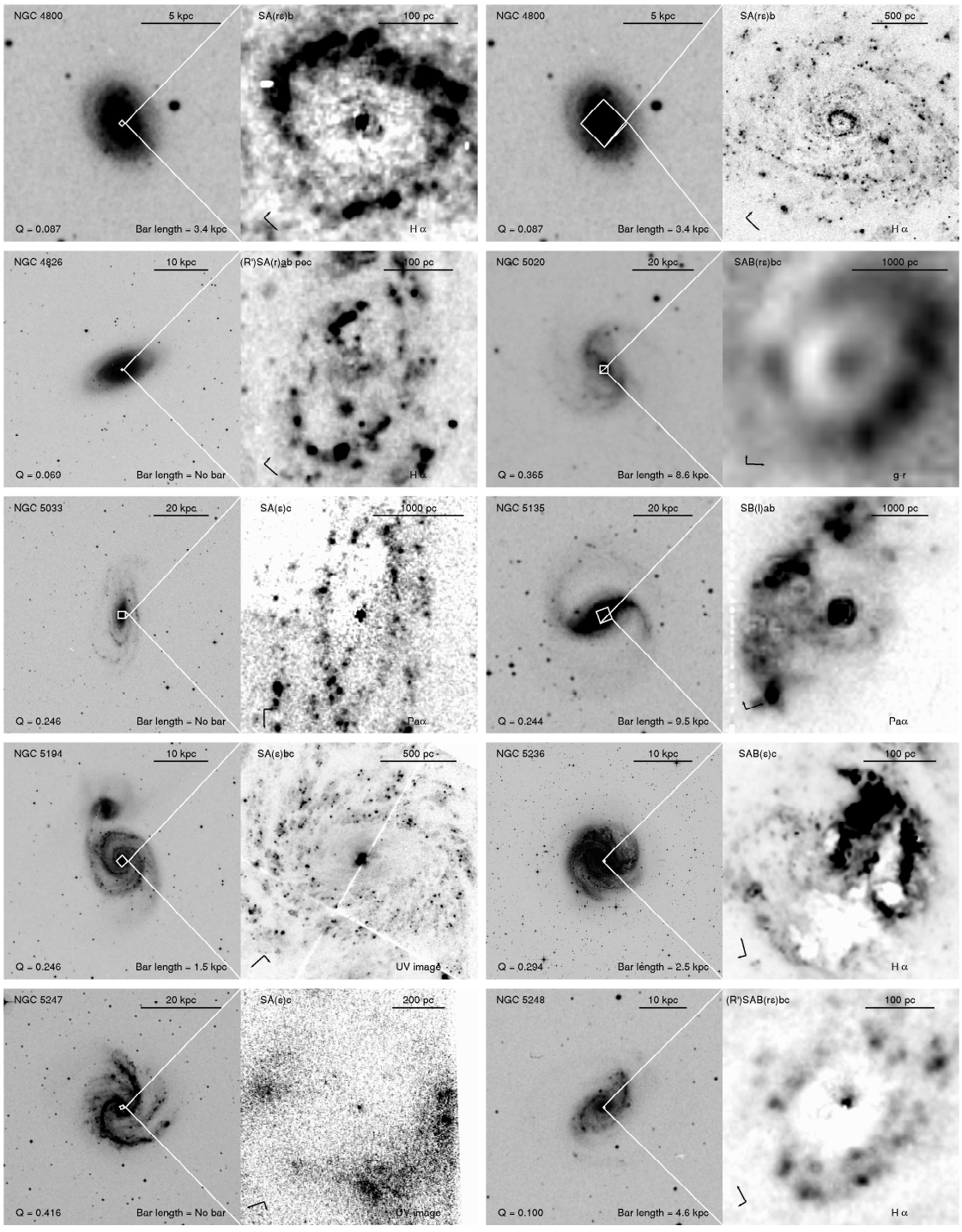

Figure B.1: (continued).

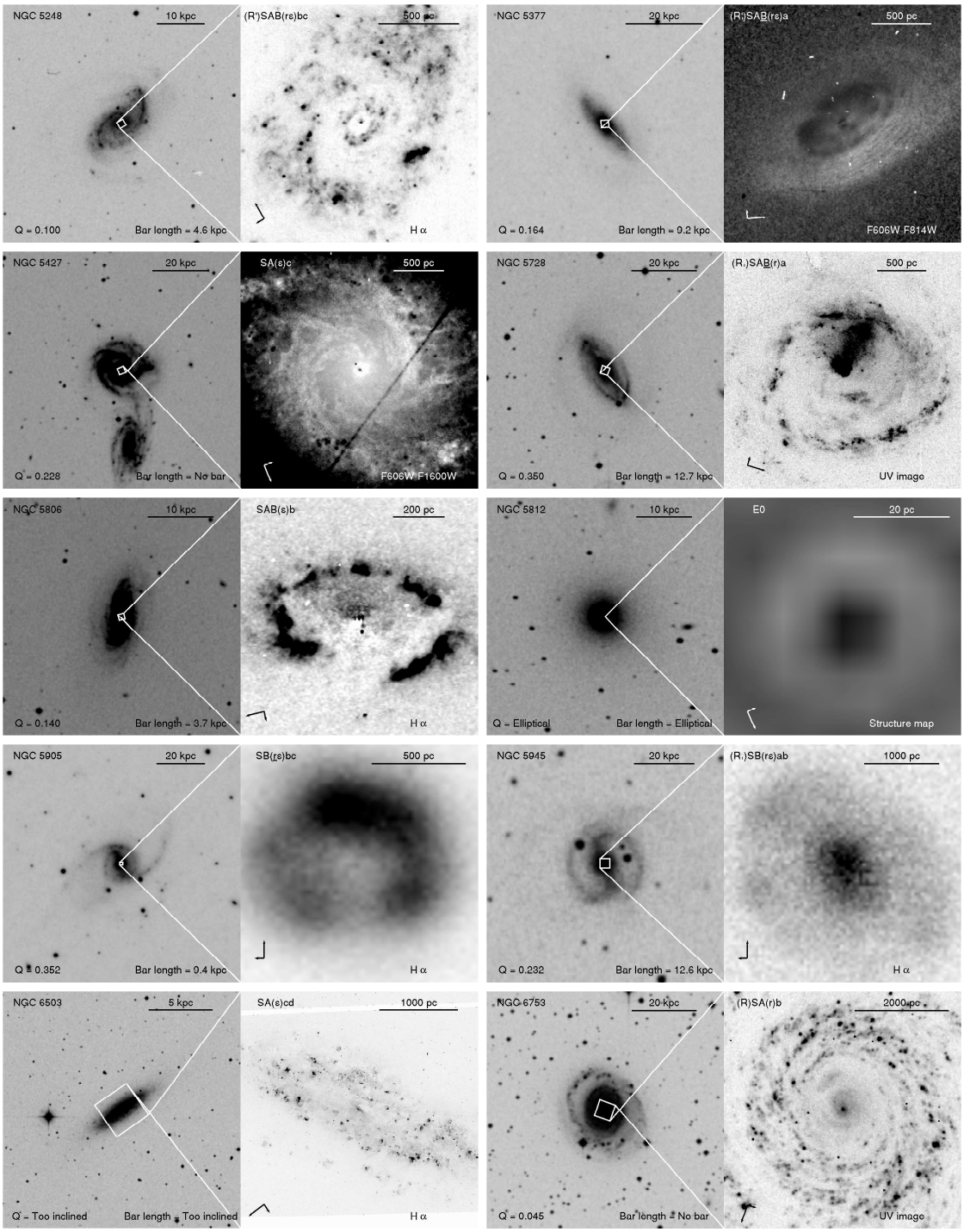

Figure B.1: (continued).

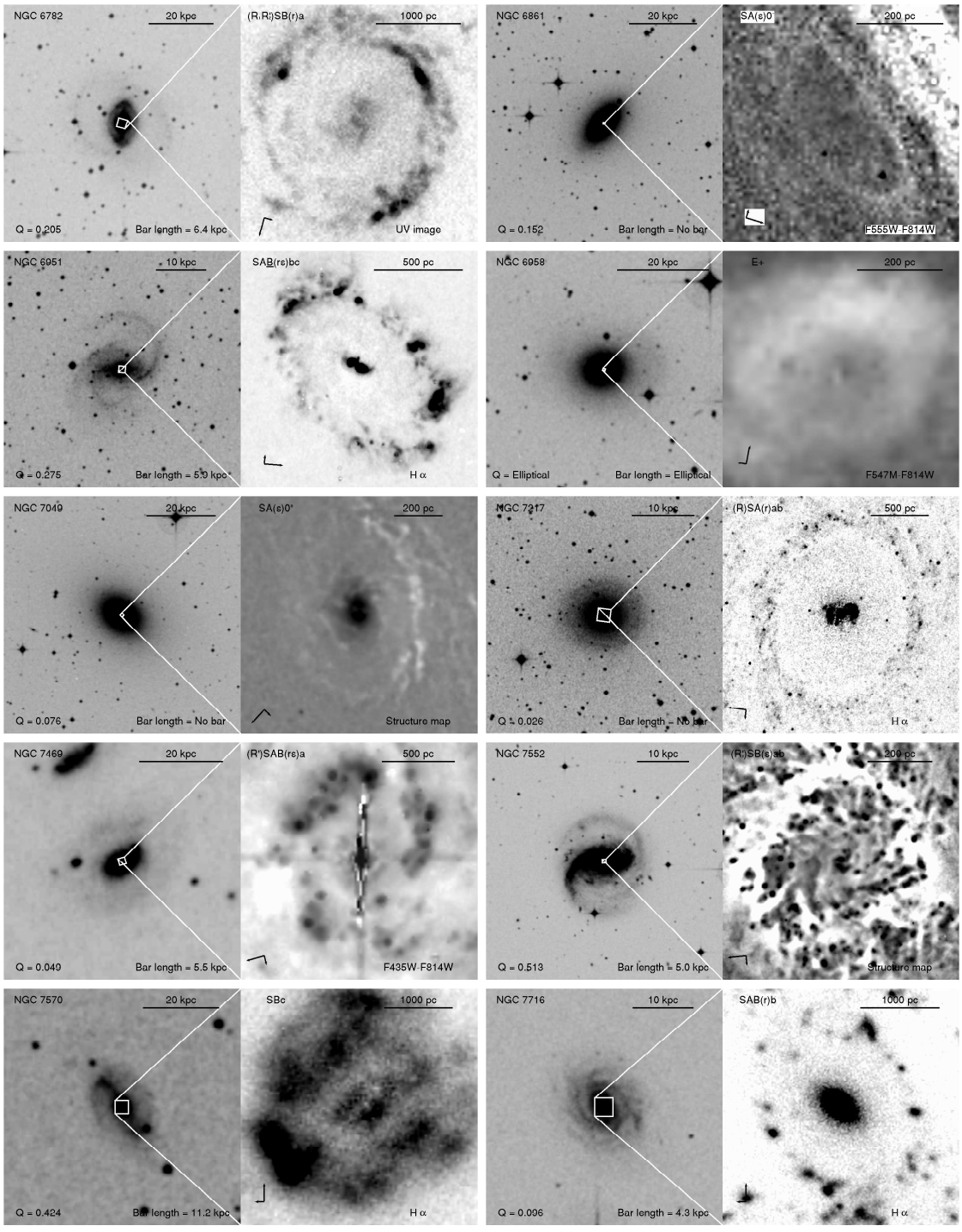

Figure B.1: (continued).

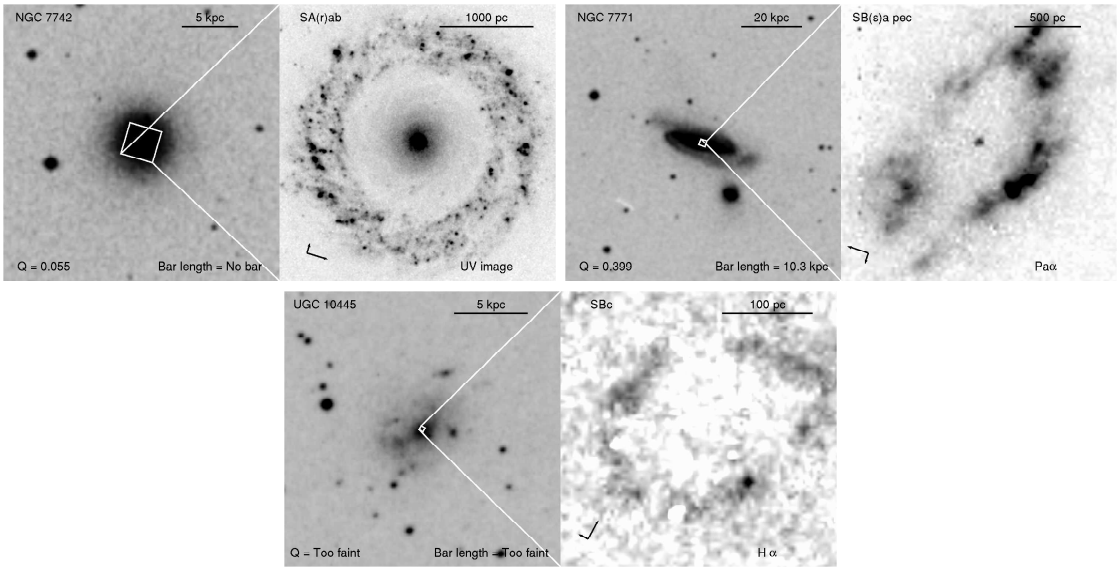

Figure B.1: (continued).

C

Aditional material to Chapter 6

This Appendix includes additional material to Chapter 6.

For all the galaxies, both in the outer ring and in the control sample, the top-left panel shows the original sky-subtracted S^4G image, the top-right panel shows the image after masking, the middle-left panel shows the model of the galaxy obtained with GALFIT, and the middle-right panel shows the residual image. The bottom panel shows the decomposition of the galaxy. In the bottom panel the grey dots denote the data points of the 2D surface brightness distribution (the brightness of each pixel as a function of the sky-plane radius from the galaxy centre), and the white dots indicate the sum of all the modelled components in the same way. The fitted components are shown in colours an their brightness relative to the total modelled galaxy brightness is shown, along with the nature of the component at the top-right section of the panel. The visualization of GALFIT results are made with the GALFIDL software written by H. Salo for the S^4G.

C.1 Galaxies from the outer ring sample

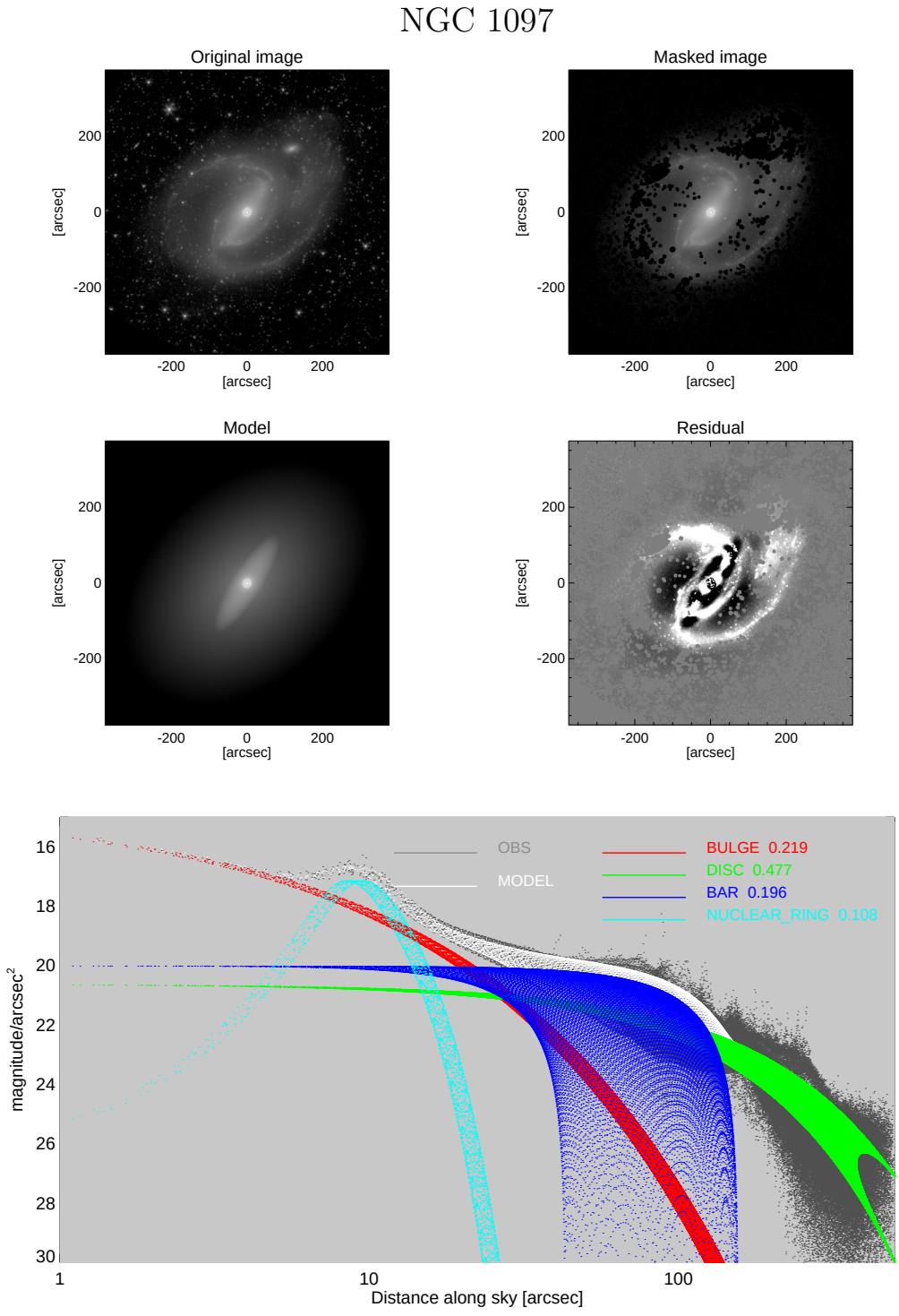

Figure C.1: Results from the GALFIT fitting to the sample of galaxies with outer rings.

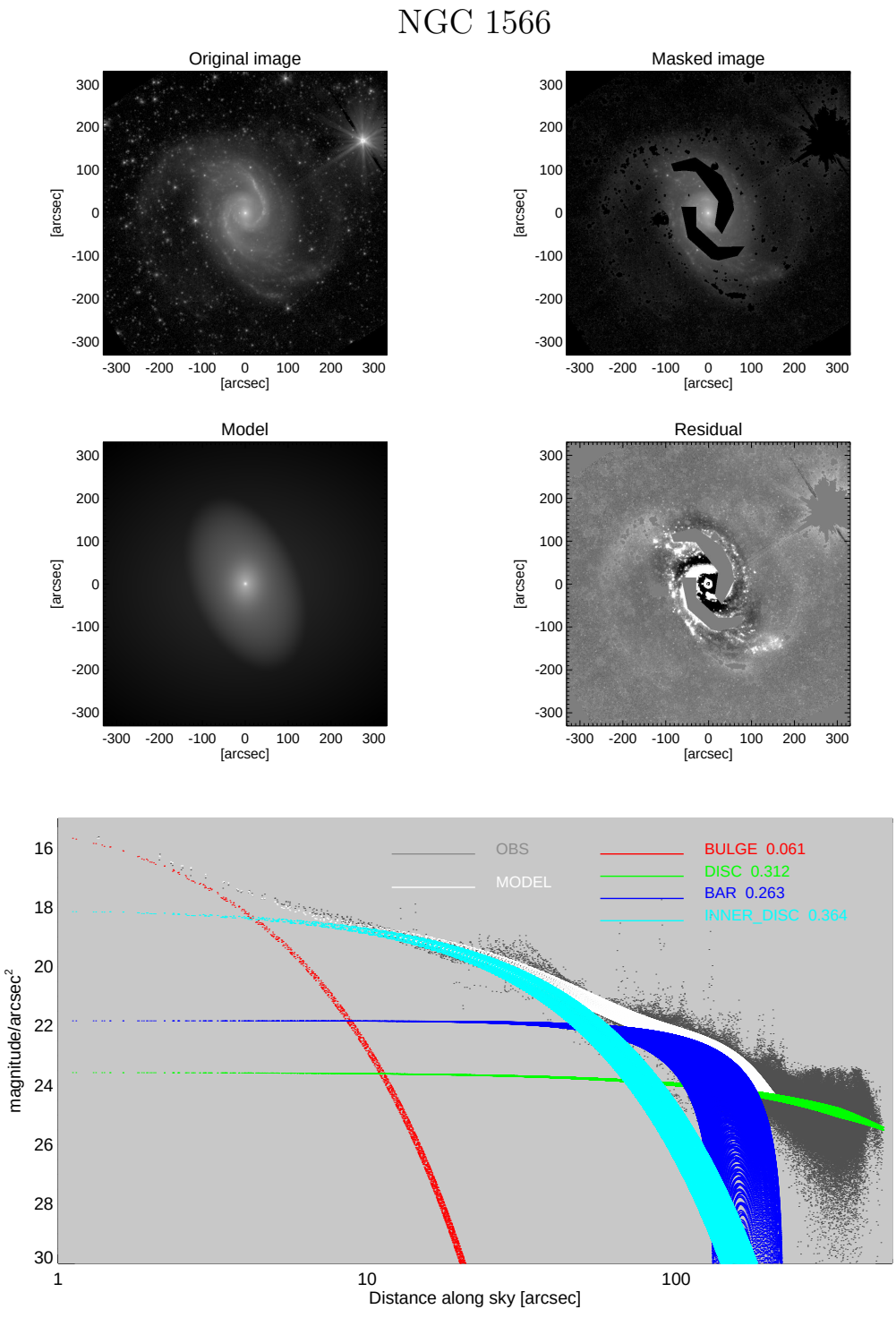

Figure C.1: (continued).

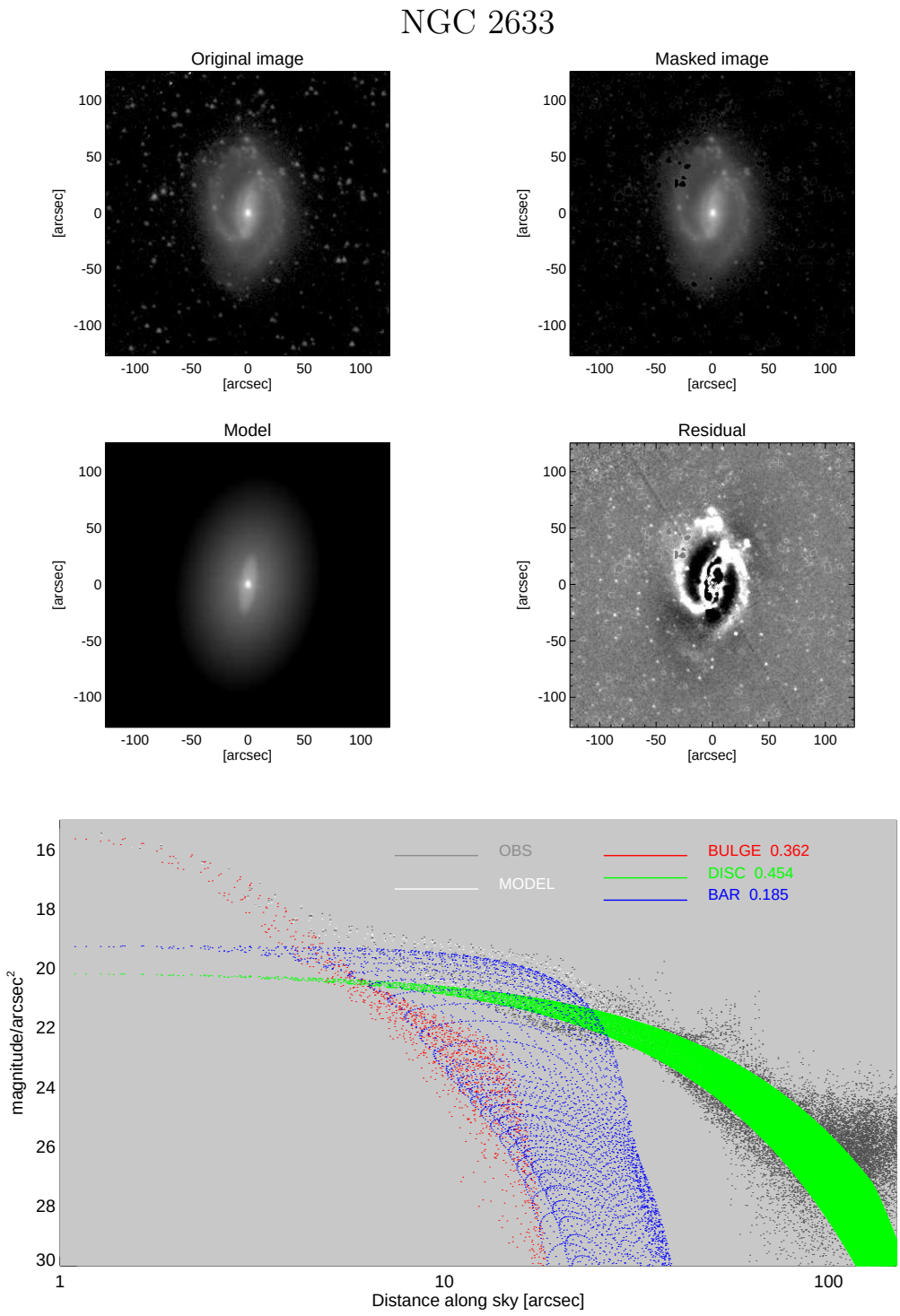

Figure C.1: (continued).

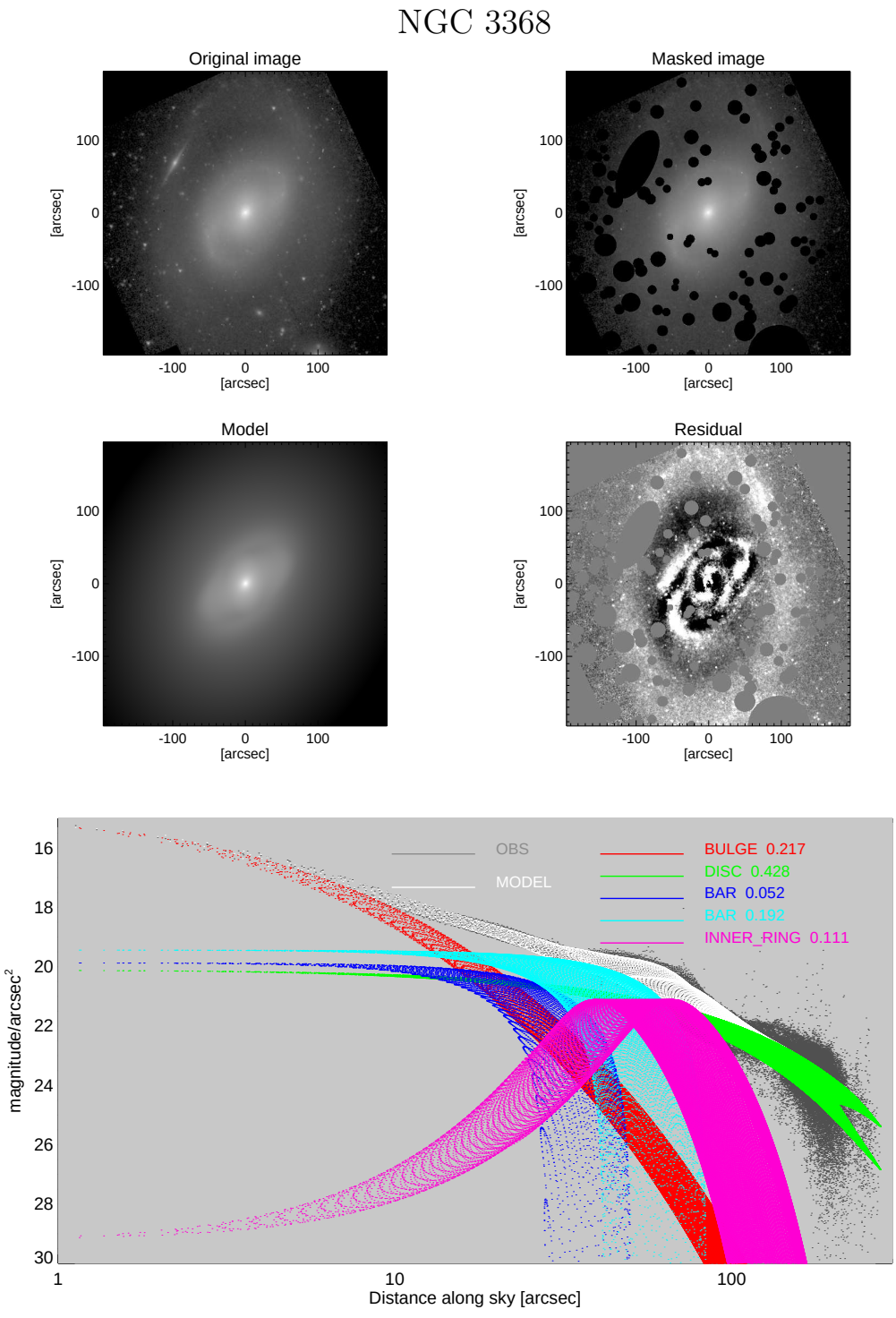

Figure C.1: (continued).

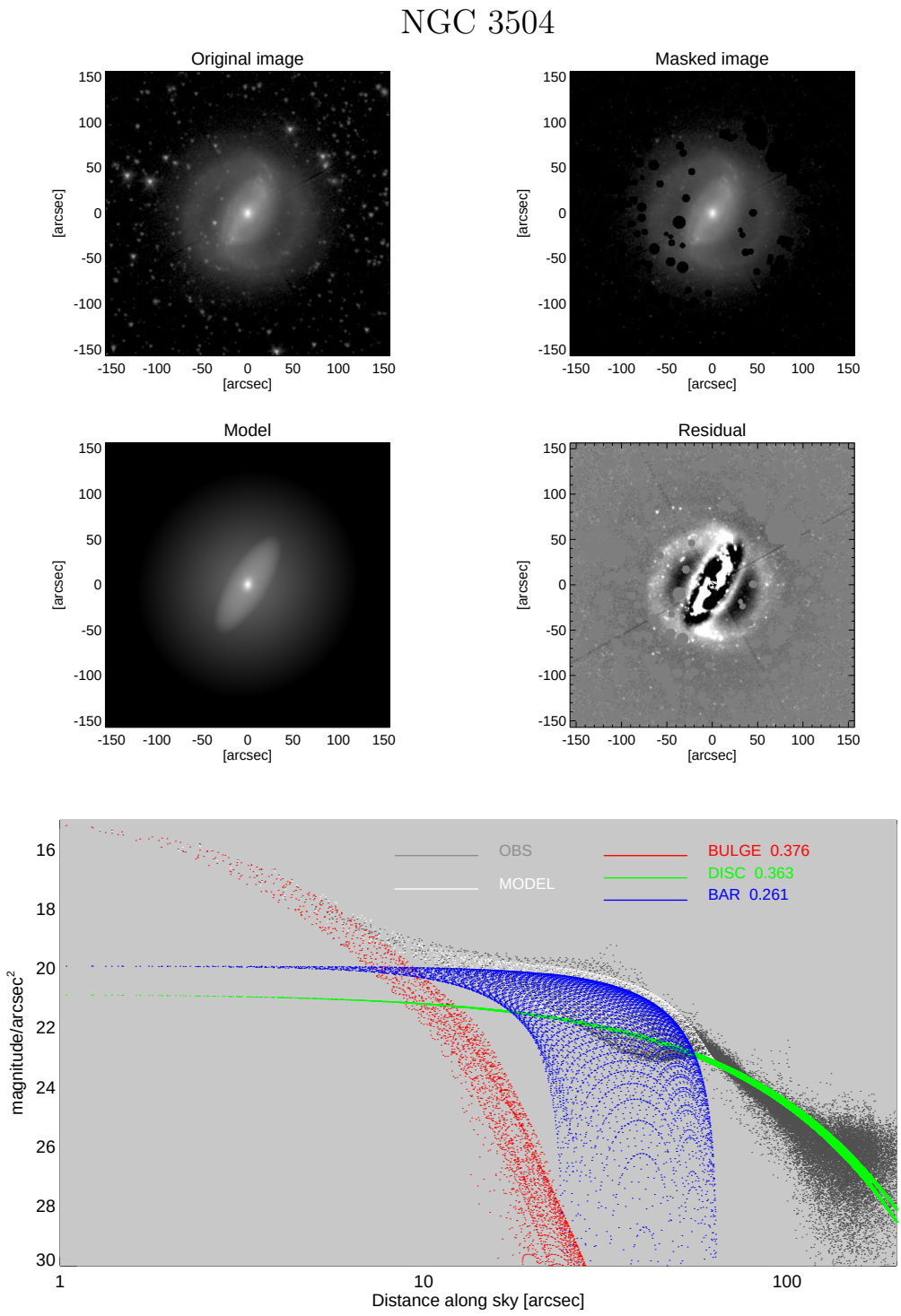

Figure C.1: (continued).

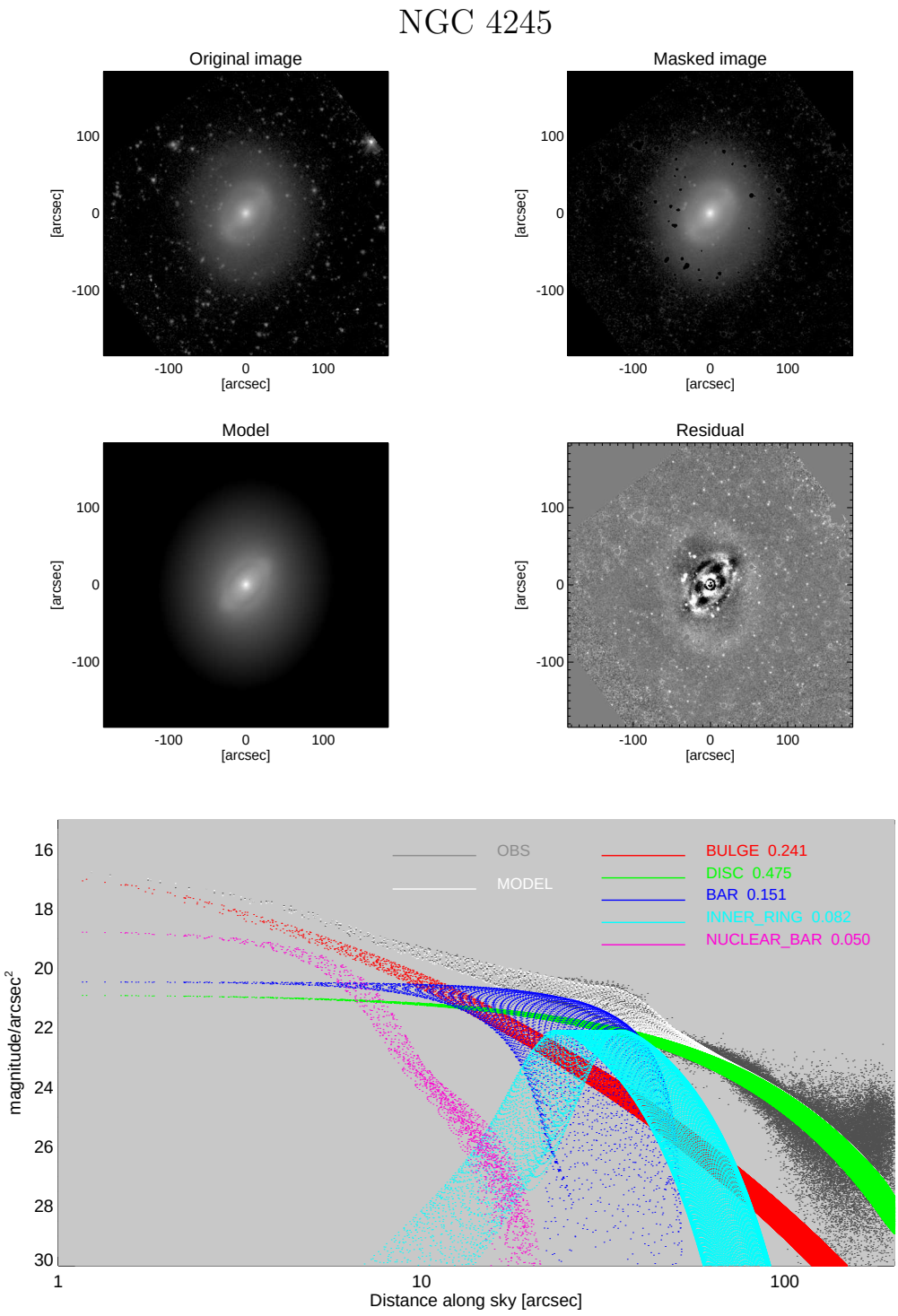

Figure C.1: (continued).

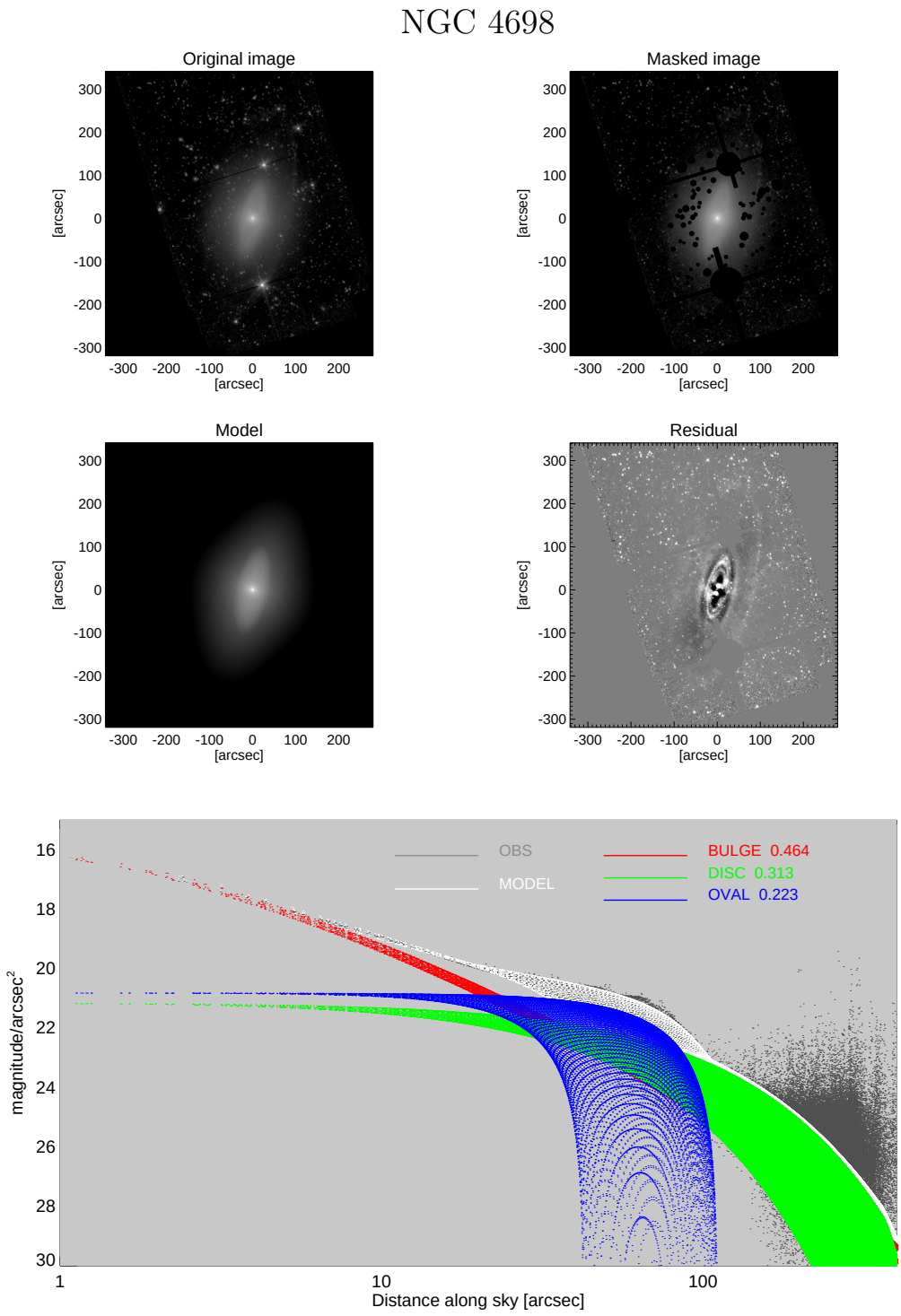

Figure C.1: (continued).

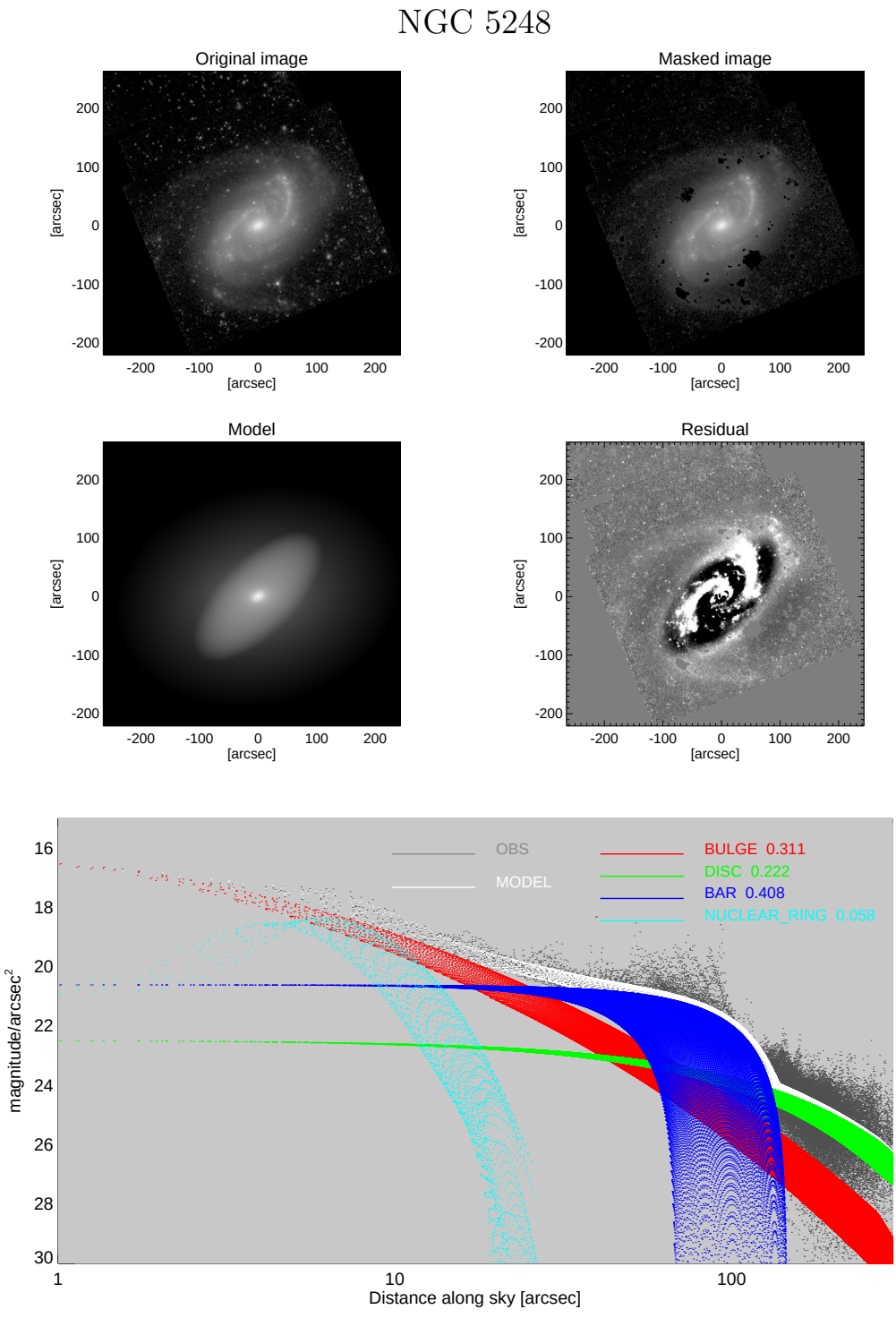

Figure C.1: (continued).

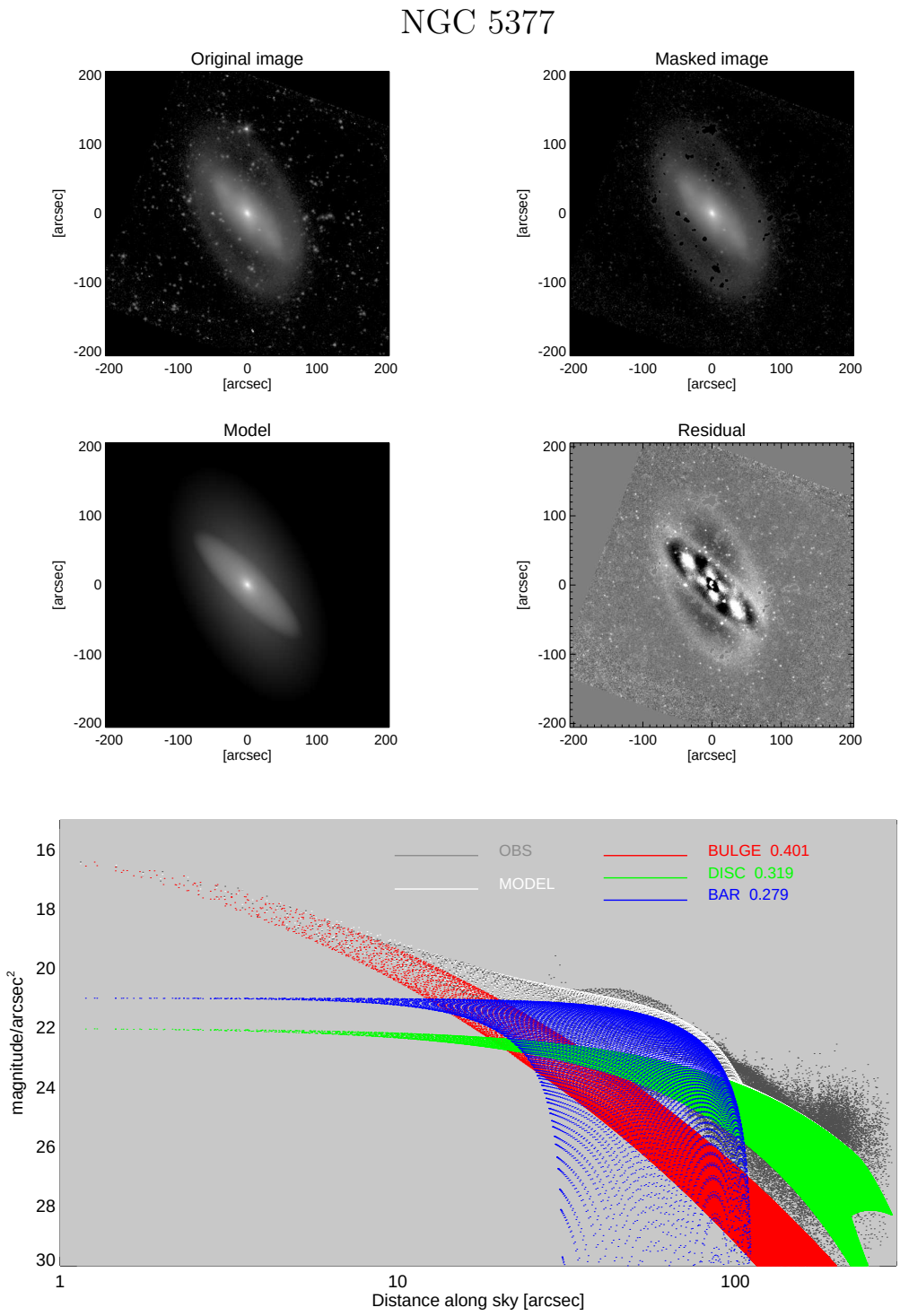

Figure C.1: (continued).

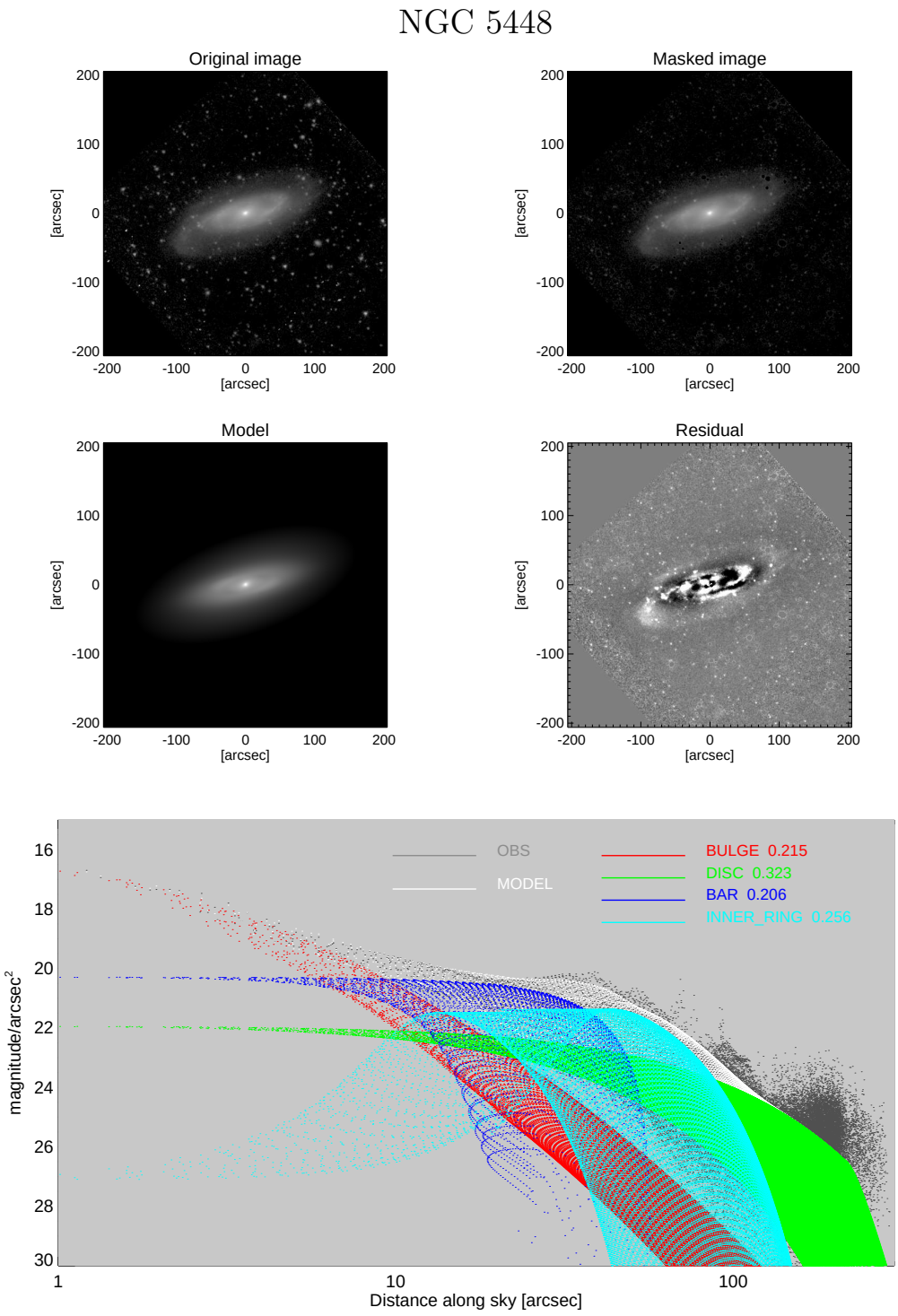

Figure C.1: (continued).

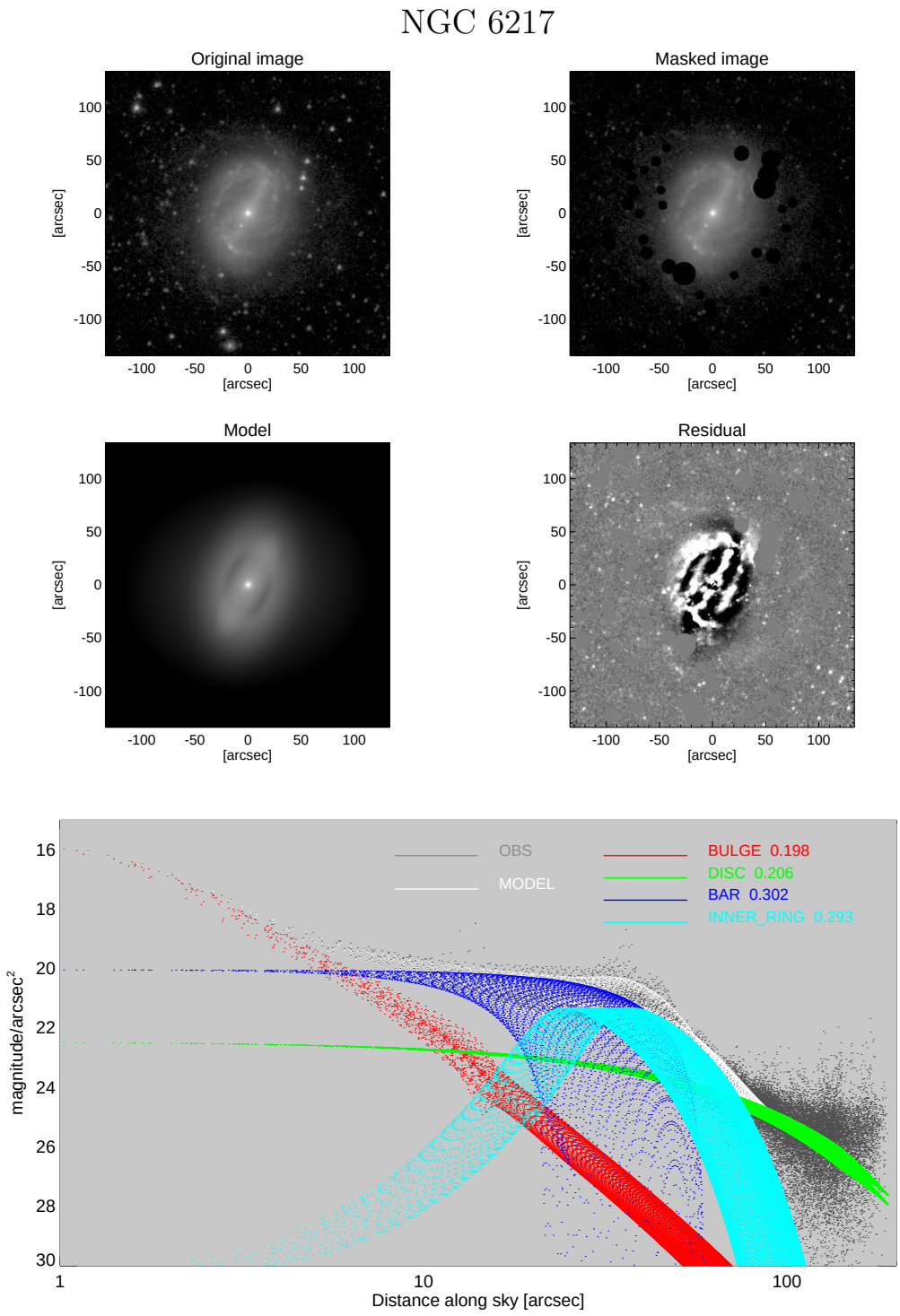

Figure C.1: (continued).

C.2 Galaxies from the control sample

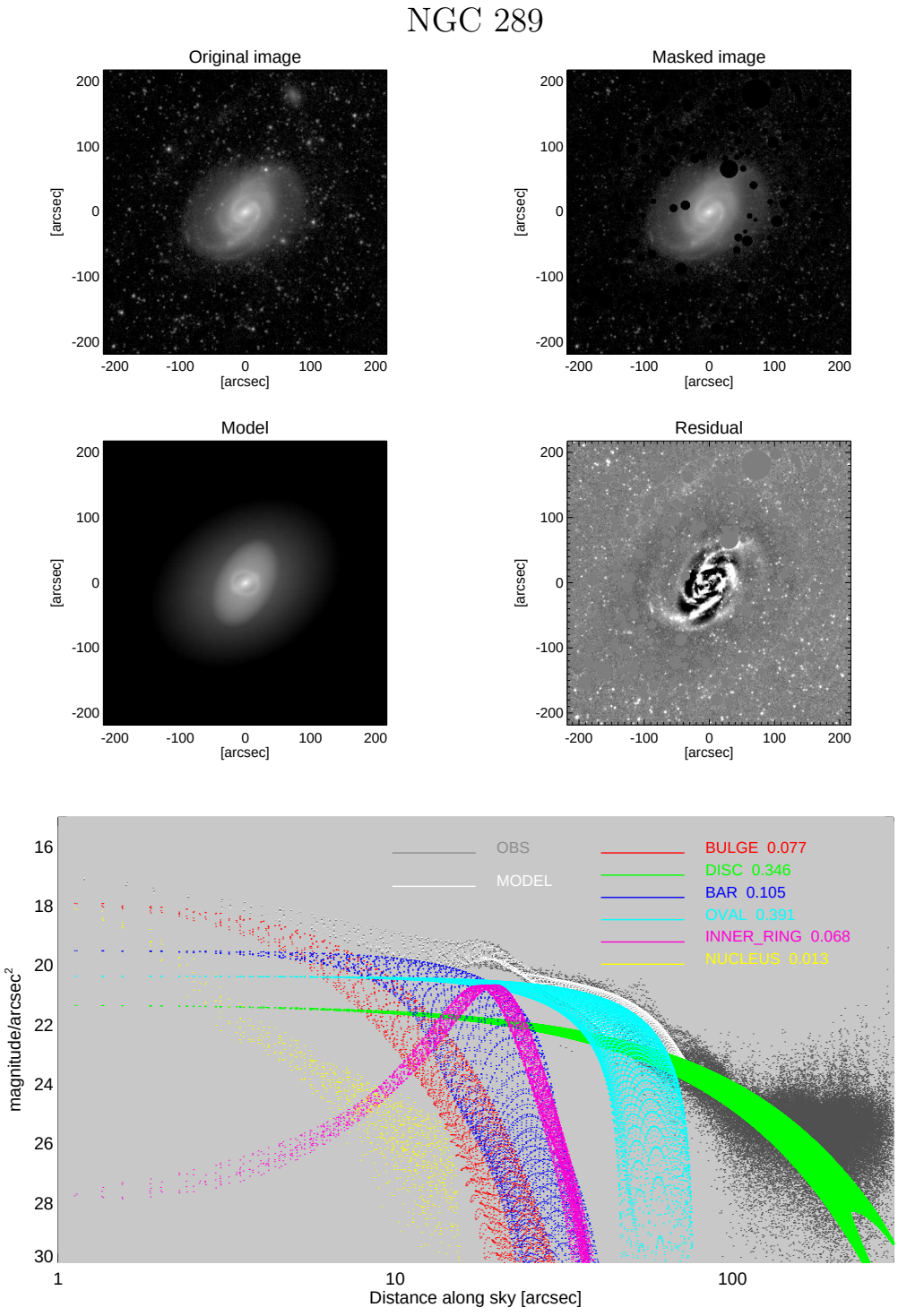

Figure C.2: Results from the GALFIT fitting to the sample of control galaxies.

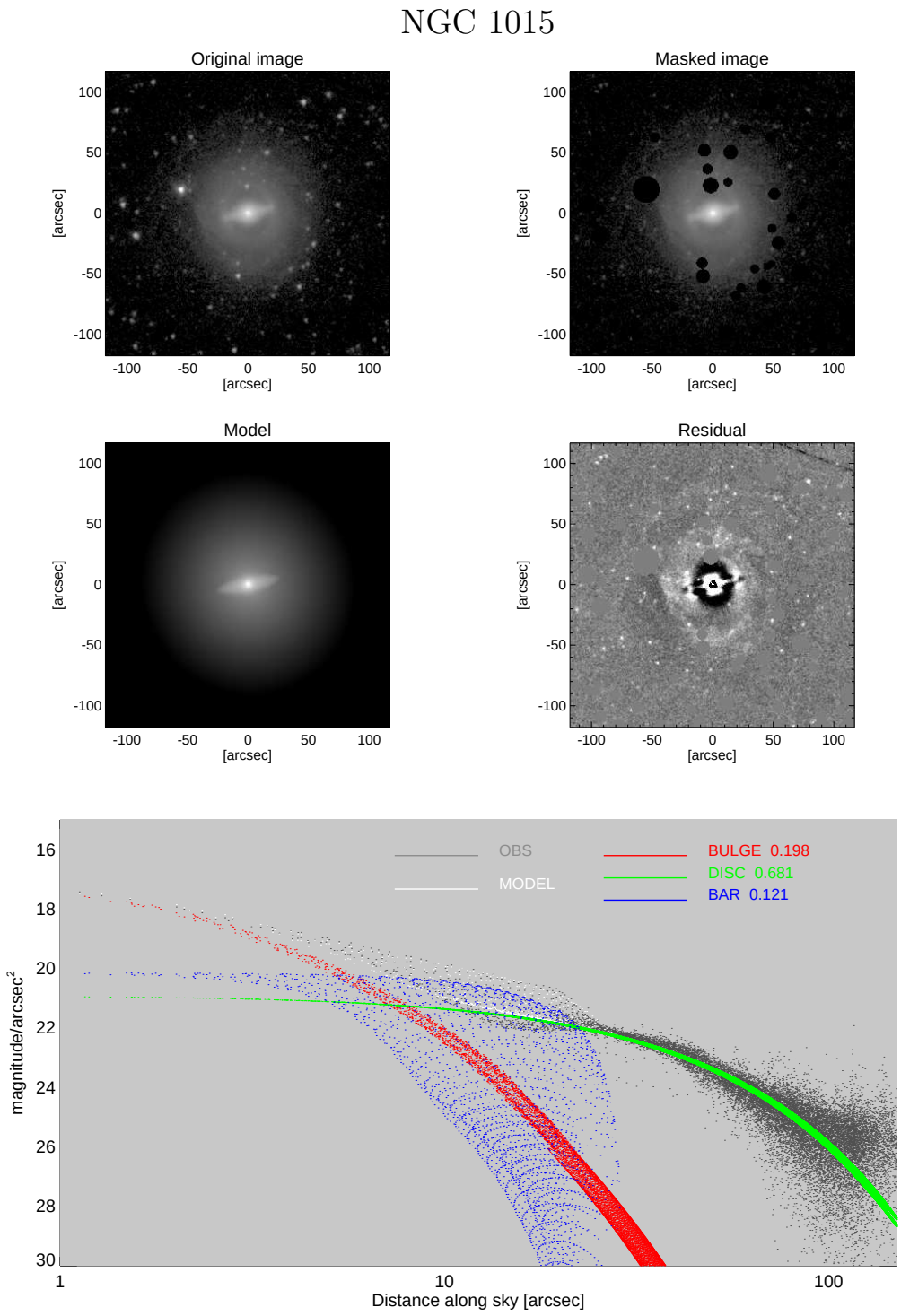

Figure C.2: (continued).

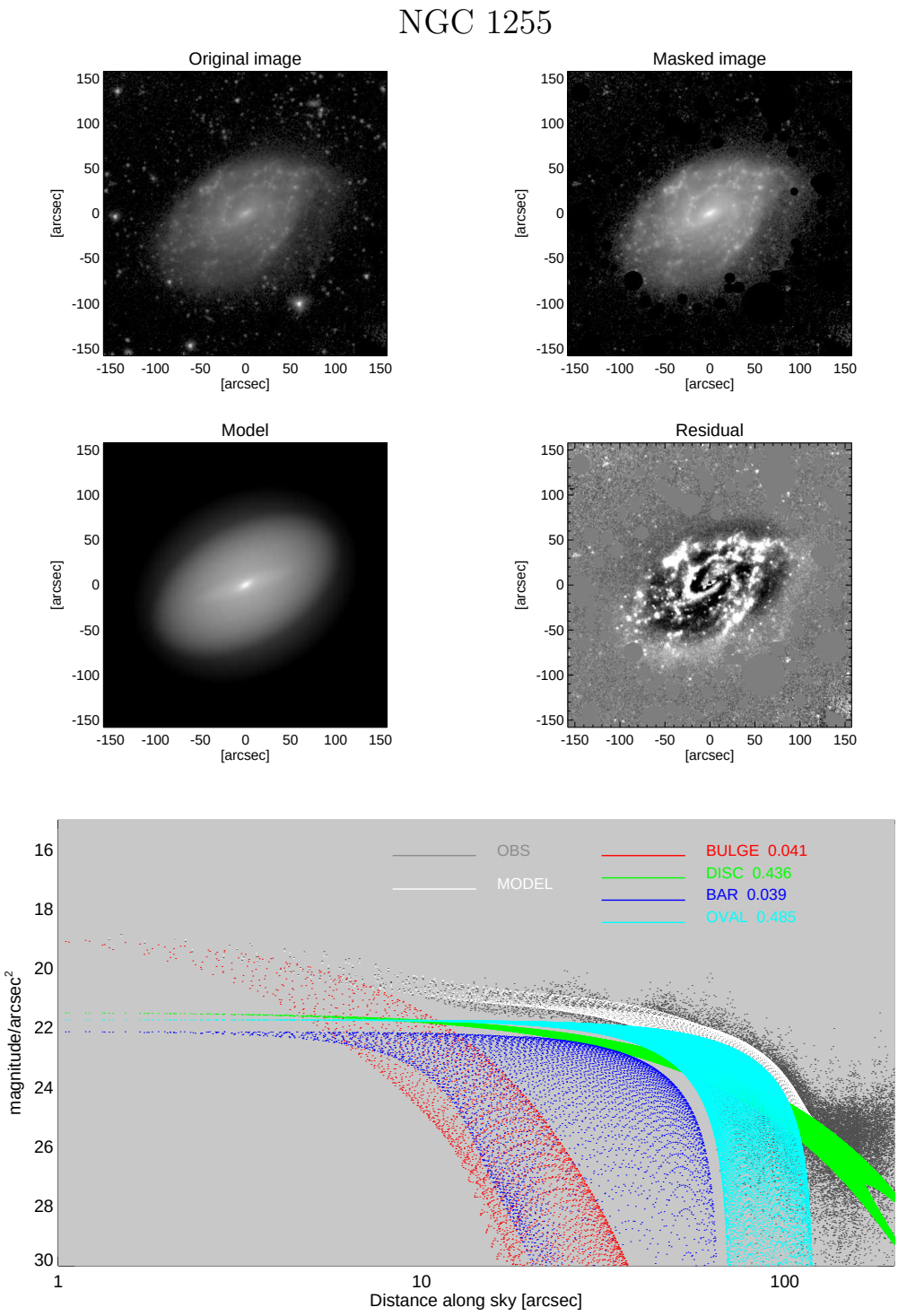

Figure C.2: (continued).

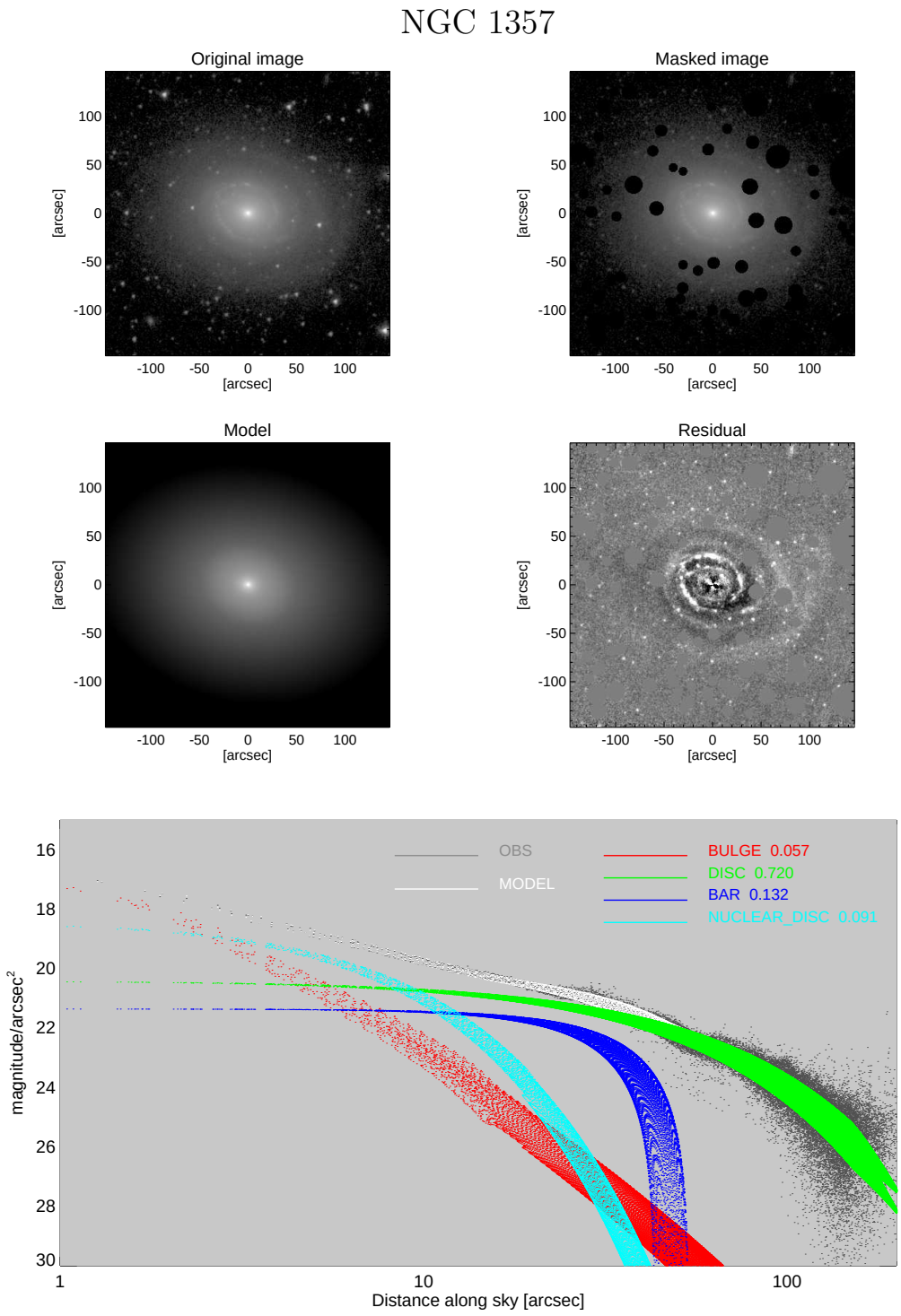

Figure C.2: (continued).

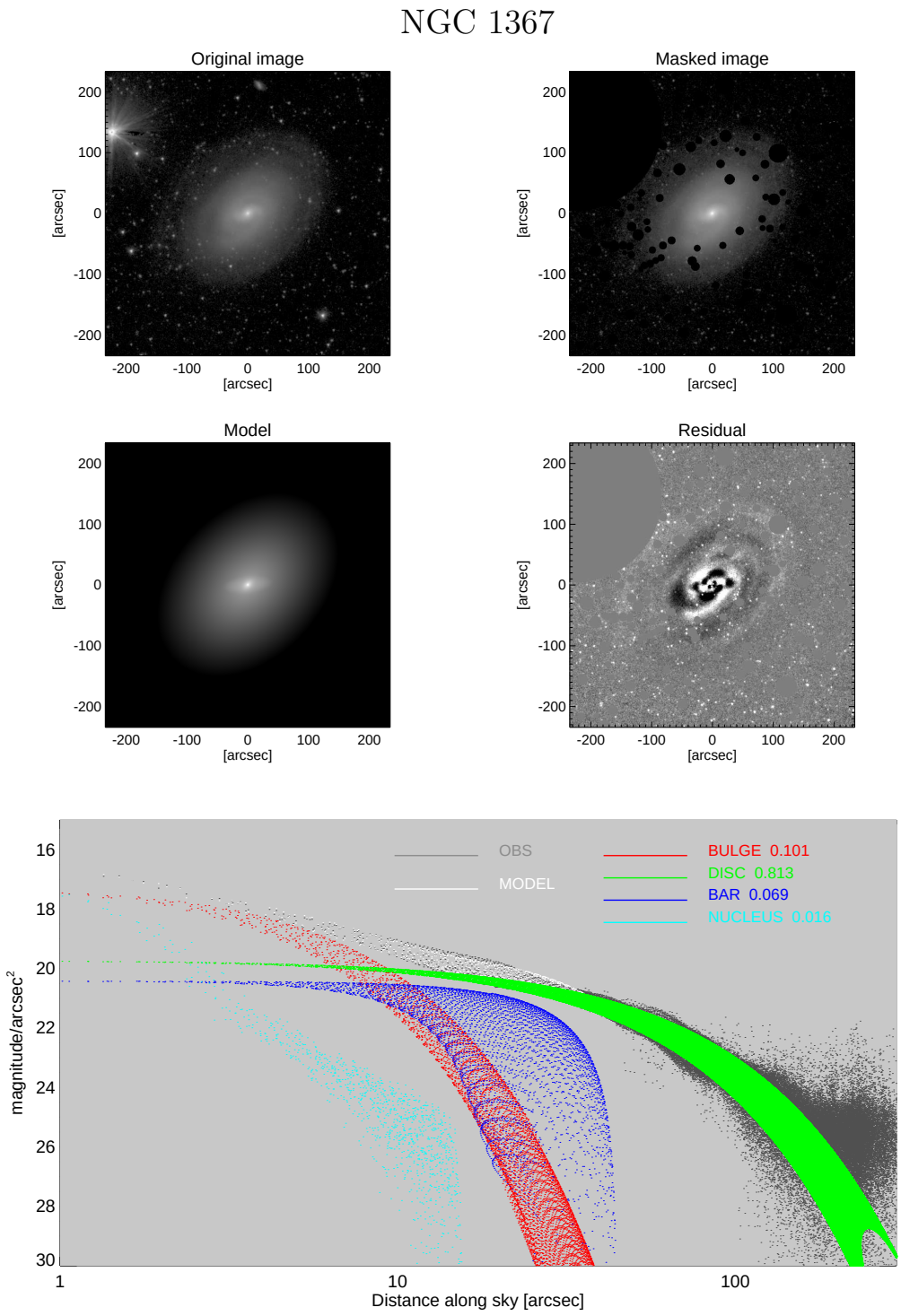

Figure C.2: (continued).

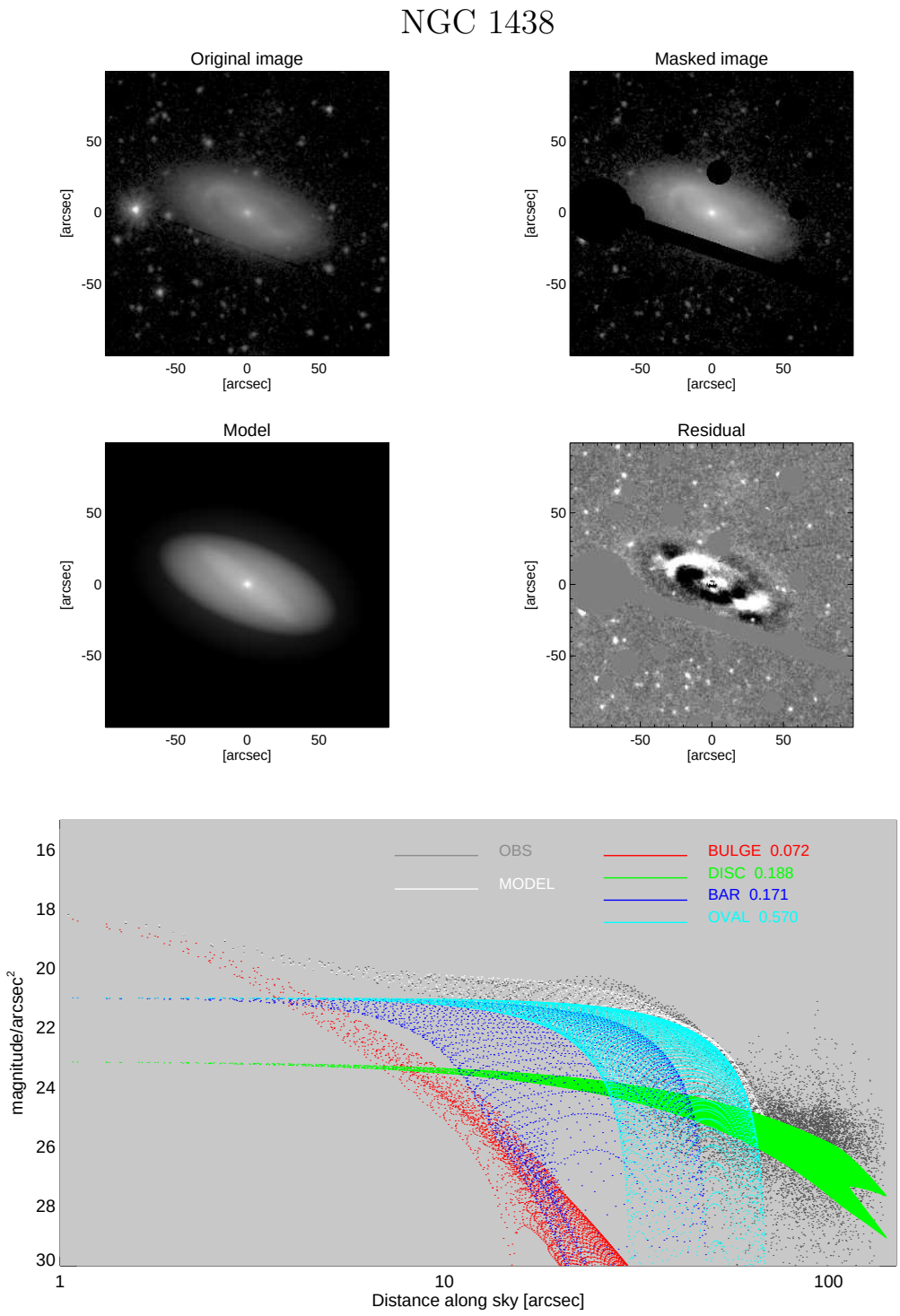

Figure C.2: (continued).

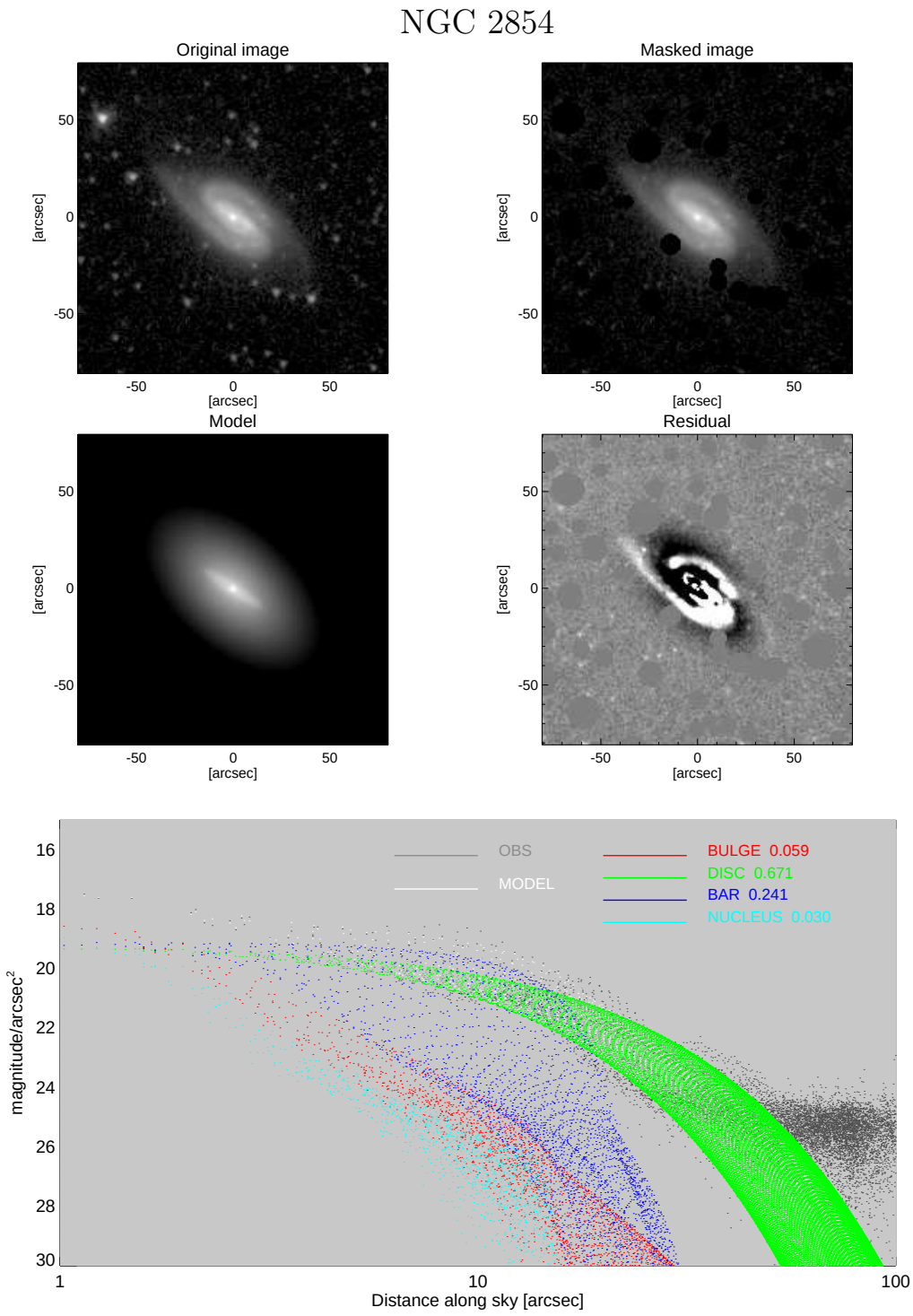

Figure C.2: (continued).

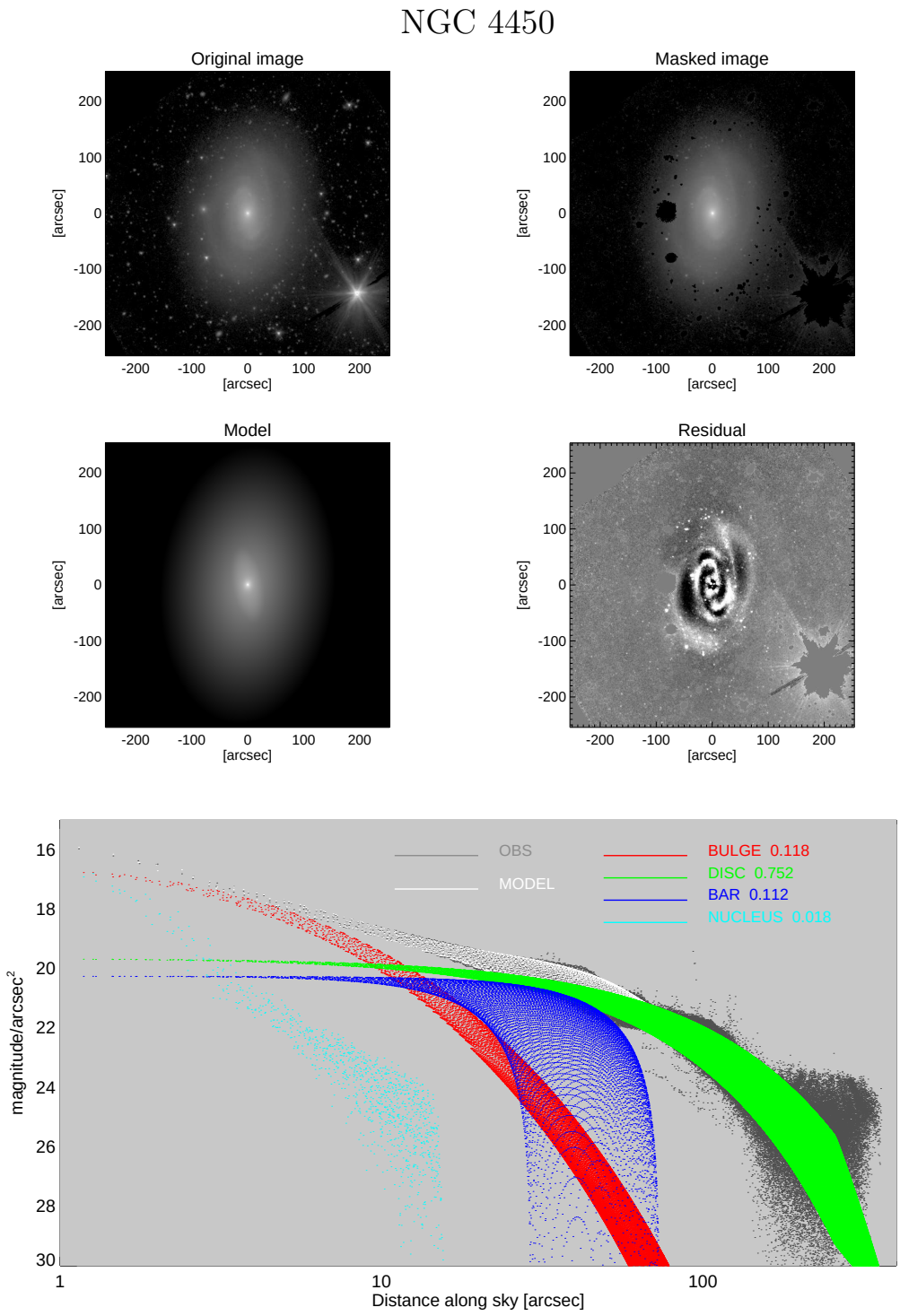

Figure C.2: (continued).

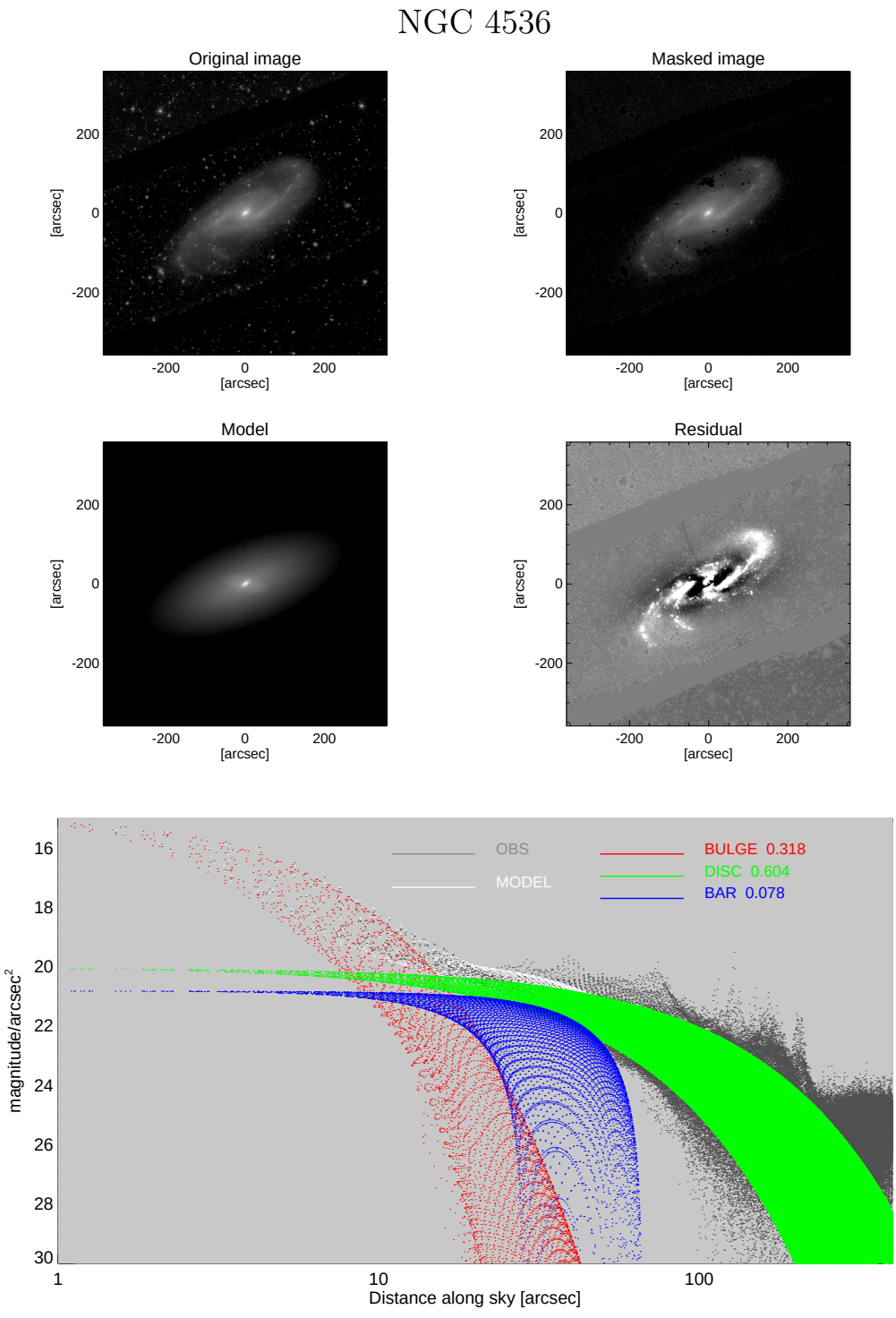

Figure C.2: (continued).

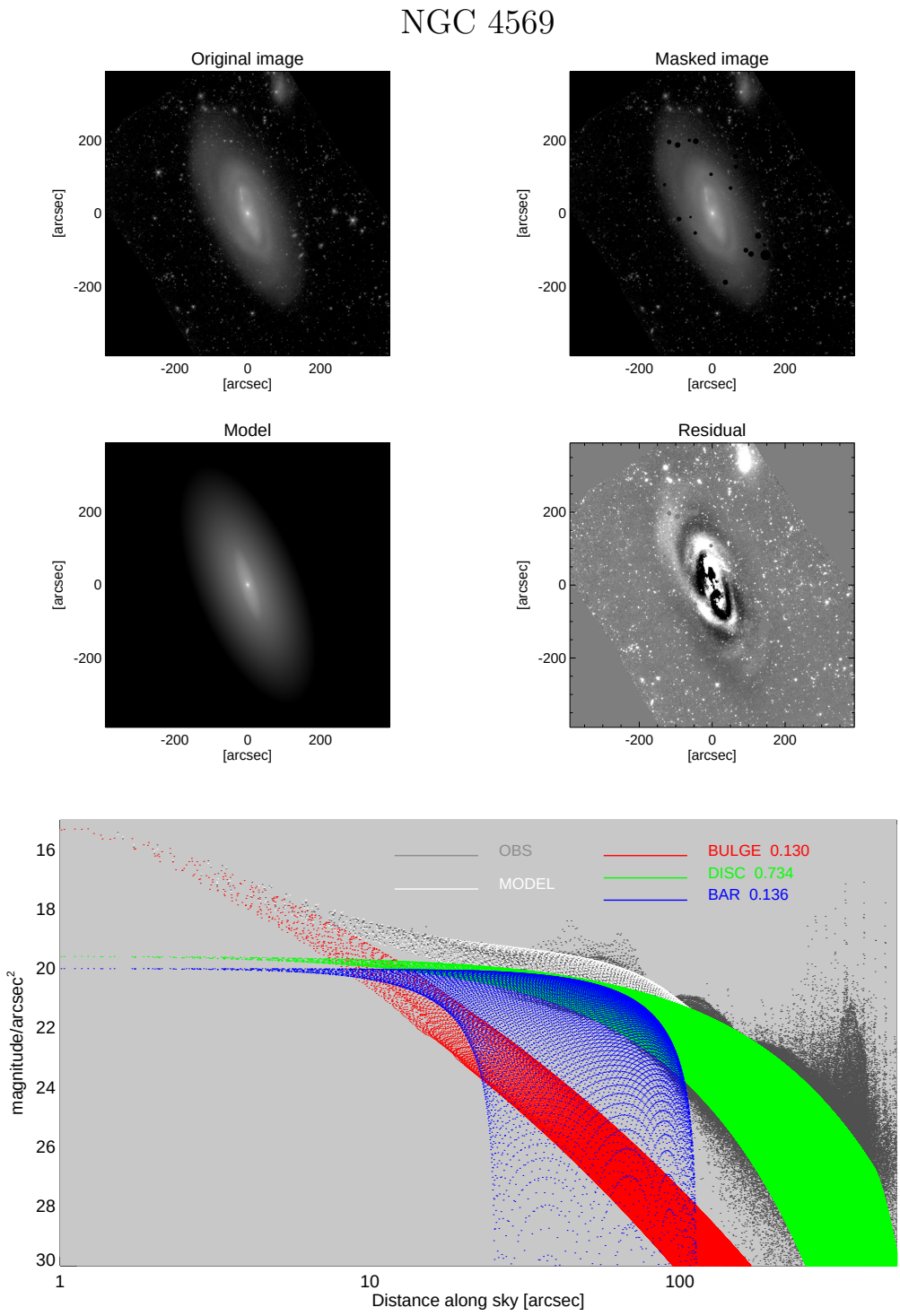

Figure C.2: (continued).

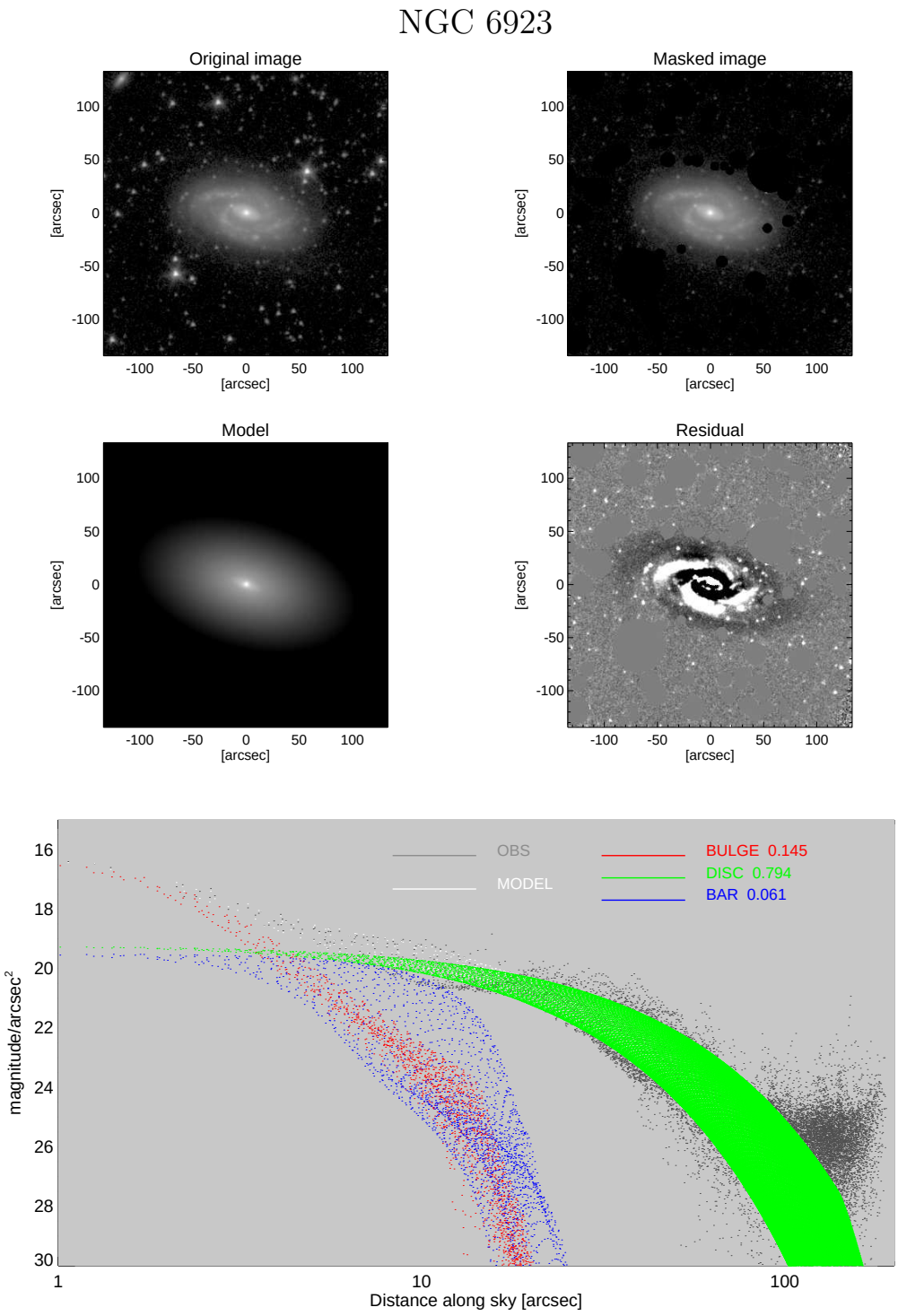

Figure C.2: (continued).

D

Glossary of acronyms

The list of aconyms used in the thesis is:

1D	One Dimensional
2D	Two Dimensional
2MASS	Two Micron All-Sky Survey
ACS	Advanced Camera for Surveys
AGB	Asymptotic Giant Branch
AGN	Active Galactic Nucleus
AINUR	Atlas of Images of NUclear Rings
CO	Carbon monoxyde
DSS	Digital Sky Survey
ESO	Identifier of the galaxies from the ESO/Uppsala Survey
FOC	Faint Object Camera
FWHM	Full Width at Half Maximum
GALFIT	A two-dimensional fitting algoritm (Peng et al. 2002; Peng et al. 2010)
HST	Hubble Space Telescope
Hα	First atomic transition in the Balmer series
H I	Atomic hydrogen
H II	Ionized hydrogen
HyperLEDA	Merger of LEDA and Hypercat (Paturel et al. 2003)
IC	Index Catalogue (Dreyer 1895)
ILR	Inner Lindblad Resonance
IPAC	Infrared Processing and Analysis Center
IR	Infrared
IRAF	Image Reduction and Analysis Facility
LEDA	Lyon-Meudon Extragalactic Database
LINER	Low-Ionization Nuclear Emission-Line Region
NASA	National Aeronautics and Space Administration

N II	One time ionized nitrogen
NICMOS	Near Infrared Camera and Multi-Object Spectrometer
NIRS0S	Near-IR S0 galaxy Survey (Laurikainen et al. 2005)
NED	NASA/IPAC Extragalactic Database
NGC	New General Catalogue (Dreyer 1888)
Paα	First atomic transition in the Paschen series
PA	Position Angle
PAH	Polycyclic Aromatic Hydrocarbon
PhD	Doctor of Philosophy
PSF	Point Spread Function
RC2	Reference Catalogue 2 (de Vaucouleurs et al. 1976)
RC3	Reference Catalogue 3 (de Vaucouleurs et al. 1991)
RGB	Red Giant Branch
RSA	Revised Shapley-Ames Catalogue of Bright galaxies (Sandage & Tammann 1981)
S^4G	Spitzer Survey of Stellar Structure in Galaxies (Sheth et al. 2010)
SDSS	Sloan Digital Sky Survey
SDSS DR5	Sloan Digital Sky Survey Data Release 5 (Adelman-McCarthy et al. 2007)
SDSS DR7	Sloan Digital Sky Survey Data Release 7 (Abazajian et al. 2009)
SMBH	Super Massive Black Hole
SF	Star Formation
SFR	Star Formation Rate
Sy	Seyfert galaxy
UCNR	Ultra-Compact Nuclear Ring
UGC	Uppsala General Catalog of Galaxies (Nilson 1973)
UV	Ultraviolet
WFPC2	Wide Field Planetary Camera 2
WHT	William Herschel Telescope

E

Scientific contributions

The list of scientific contributions on the topics presented in this work is given below:

E.1 Refereed publications

Comerón, S., et al., *Discovery of a faint thick disc in the galaxy NGC 4244 from S^{4}G imaging*, 2010, in preparation

Buta, R. J., et al. (including **Comerón, S.**), *Mid-Infrared Galaxy Morphology from the Spitzer Survey of Stellar Structure in Galaxies (S^{4}G): The Imprint of the de Vaucouleurs Revised Hubble-Sandage Classification System at 3.6 microns*, 2010, submitted to ApJS

Sheth, K., et al. (including **Comerón, S.**), *Introducing the Spitzer Survey of Stellar Structure (S^{4}G): A Warm Mission Legacy*, 2010, submitted to ApJ

Laurikainen, E., Salo, H., Buta, R., Knapen, J. H., and **Comerón S.**, *Photometric scaling relations for barred and non-barred early-type disk galaxies*, 2010, accepted for publication in MNRAS (http://arxiv.org/abs/1002.4370)

Comerón, S., Knapen, J. H., Beckman, J. E., Laurikainen, E., Salo, H., Martínez-Valpuesta, I., and Buta, R. J., *AINUR: Atlas of Images of NUclear Rings*, 2010, MNRAS, 402, 2462

Comerón, S., Martínez-Valpuesta, I., Knapen, J. H., Beckman, J. E., *On the curvature of dust lanes in galactic bars*, 2009, ApJ, 706, 256

Comerón, S., Knapen, J. H., Beckman, J. E., *On the morphology of sigma-drop galaxies*, 2008, A&A, 485, 695

Comerón, S., Knapen, J. H., Beckman, J. E., Shlosman, I., *Discovery of ultra-compact nuclear rings in three spiral galaxies*, 2008, A&A, 478, 403

E.2 Conference proceedings and abstracts

Comerón, S., Knapen, J. H., Beckman, J. E., *Estudio morfológico de galaxias con sigma-drops*, 2010, in J. Gorgas, L. J. Goicoechea, J. I. Gonzalez-Serrano, J. M. Diego, eds, Springer-Verlag, Highlights of Spanish Astrophysics V, Berlin Heidelberg, p. 271

Comerón, S., Knapen, J. H., Beckman, J. E., Laurikainen, E., Salo, H., Buta, R. J., and Martínez-Valpuesta, I., *AINUR: Atlas of Images of NUclear Rings*, 2010, 215$^{\rm th}$ AAS Meeting, Bulletin of the American Astronomical Society, Vol. 41, p. 592

Comerón, S., Knapen, J. H., Beckman, J. E., *On the classification of ultra-compact nuclear rings*, 2008, in R. Schoedel, A. Eckart, S. Pfalzner, E. Ros, eds, Journal of Physics: Conf. Ser. Vol. 131, The Universe Under the Microscope – Astrophysics at High Angular Resolution, p. 2046

Comerón, S., Knapen, J. H., Beckman, J. E., *A Statistical Study of Circumnuclear Morphology of Sigma-Drop Galaxies*, 2008, J. H. Knapen, T. J. Mahoney, A. VAzdekis, eds, ASP Conf. Ser. Vol. 390, Pathways through and eclectic Universe, Astron. Soc. Pac., San Francisco, p. 174

Comerón, S., Knapen, J. H., Beckman, J. E., *Discovery of Four New Ultra-compact Nuclear Rings in Three Spiral Galaxies*, 2008, J. H. Knapen, T. J. Mahoney, A. VAzdekis, eds, ASP Conf. Ser. Vol. 390, Pathways through and eclectic Universe, Astron. Soc. Pac., San Francisco, p. 172

Agradecimientos

- Porque está allí.

Esa fue la respuesta de George H. L. Mallory a los periodistas cuando le preguntaron por los motivos que lo impulsaban a escalar el Everest.

Si Mallory hubiera hecho un discurso de agradecimientos antes de empezar su tercer y trágico intento de ascensión al Everest, debería haber nombrado en primer lugar a Andrew S. Waugh y a su equipo por haber indicado a las generaciones futuras que el Monte Everest era el más elevado del globo.

Mi Andrew S. Waugh particular fue mi tío Fernando Comerón Tejero. Fue él quien me hizo conocer con su ejemplo la existencia de la astrofísica. Fue él quien me transmitió el interés por las ciencias y quien deslumbró a un receptivo niño mostrándole como se puede combinar trabajo y viajes a lugares exóticos.

Pero para culminar el ascenso el alpinista tiene que apoyarse en un complejo entramado logístico que incluye el establecimiento del campamentos base, la exploración de vías de ascensión y el abastecimiento de provisiones y material. Muchos son los que me han ayudado y enseñado antes de que pudiera iniciar esta tesis.

Los primeros formadores que quiero agradecer son Pere Bartrés Ametller y Vicenç Claveria Quintillà, maestros en el IES Argentona; el primero fue un profesor de física sinceramente preocupado por el aprendizaje y el bienestar de los alumnos y el segundo un profesor de matemáticas con una capacidad didáctica fuera de lo común. También recuerdo con afecto a los demás profesores del IES Argentona, quienes lograron darme una buena base de conocimiento general.

Tengo que agradecer también los profesores y becarios de prácticas de la Universidad de Barcelona; ellos hicieron que mi pensamiento se estructurara. Algunos, además de enseñarme, fueron tan amables como para escribir las cartas de recomendación que me permitieron trabajar en el IAC. También en la Universidad de Barcelona tuve mi primera experiencia profesional durante dos intensos veranos gracias a Guillem Anglada Escudé, Josep-Manel Carrasco Martínez, Salvador Ribas Rubio, Jordi Torra Roca, y Francesc Vilardell Salles.

También agradezco el esfuerzo de los profesores del master de astrofísica de la Universidad de la Laguna cuyas enseñanzas me ayudaron a tener una sólida base en computación.

I have very good remembrances from the time I spent in the city of Oulu, in Finland. I would like to acknowledge the warm reception from Eija Laurikainen and Heikki Salo who made my stay close to the Polar Circle very enjoyable. I also have good memories from Pertti Rautiainen and from Sami Airaksinen.

Recuerdo con mucho afecto la figura de Leonel Gutiérrez quién supo guiar mi vacilante camino por los vericuetos de IRAF y con el que compartí muchas horas de cafetería.

Agradezco la ayuda de Inma (García) Martínez Valpuesta, que tuvo la paciencia suficiente como para aguantarme en interminables reuniones de trabajo. Sin ella las partes de teoría de la tesis serían mucho más flojas y sin su ayuda las secciones de simulación serían inexistentes.

He de agradecer la inmensa ayuda de mis directores de tesis, Johan H. Knapen y John E. Beckman. Puedo decir que, sin lugar a dudas, no había mejor manera para orientarme que la que ellos han usado. También les agradezco su comprensión y ayuda en los mo-

mentos difíciles. Ellos han logrado que una relación jefes/estudiante (maestro/padawan) se transforme en una relación de igualdad entre colaboradores.

Pero no todo ha sido trabajo en estos años y ha habido multitud de personas a las que quiero agradecer su presencia en los momentos alegres y en los difíciles.

Vull recordar en aquestes pàgines els meus amics del Comitè d'Activitats Frikis de Mataró, Argentona i Dosrius (CAFMAD), Abel Torres Espín, Marçal Gallemí Rovira y Víctor Julià Jordan, que van venir a visitar-me alguna vegada, i a Cristian Pérez Verde que no en va tenir la ocasió. També vull recordar el difunt Tebi, mascota i President Etern del CAFMAD.

He pasado muy buenos momentos con mis compañeros de piso Fernando Buitrago Díaz y Alex Duralde Basterra. Nunca olvidaré las excursiones que hicimos (al monte Guajara, al barranco de Masca, a la Península de Anaga...), ni el fantástico Dragón Negro que me llegó de Nottingham. También he tenido muy buenos momentos con las compañeras 'guapetonas' Ángeles Piñero Cruz e Isabel Rodríguez Escribano.

Agradezco que Mirian Fernandéz Lorenzo y Pedro Rodríguez Folgueras me acompañaran en las horas frikis que he pasado en Tenerife. El Munchkin alcanza con vosotros las más altas cotas de entretenimiento y de refinamiento (quizás tendría que decir 'de retorcimiento') de las normas.

Agradezco los paseos y las partidas de Warhammer a Rafael San José Afonso y a Marta Gester Acosta y agradezco los buenos momentos pasados a todos los frikis de la tienda El Laberinto, especialmente a Yauci Fernández Inglés. ¡Lástima que no hubiera un torneo cada fin de semana! También agradezco a Ricardo Caamaño Brito que me pusiera en contacto con ellos.

Agradezco a Juan Bethancourt Rijo, Martín López Corredoira, Mn. Álex Marzo Guarinos, Fernando Moreno Isertis y Mn. Eduard de Ribot Martínez por las largas discusiones que tuvimos en las que mezclamos ciencia, filosofía y religión.

Las últimas amistades que quiero recordar son a Elena Sánchez Cabestrero y a Maritza Arlene Lara López; dos mujeres extraordinarias que no se han visto jamás pero que se parecen mucho. Ambas han sido de gran ayuda cuando he necesitado orientación y motivaciones para seguir trabajando. En cierta forma se han comportado como hermanas mayores que han guiado y protegido a un hermano menor. Les doy las gracias por su generosidad y por haber prestado siempre un oído atento a mis problemas.

Agradezco su ayuda a gente que siempre me ha acompañado pero que nunca conoceré en persona: Fernando Alonso Díaz, Neil Armstrong, Isaac Asimov, Charles Aznavour, los Bee Gees, Ludwig van Beethoven, Georges Bizet, Tim Burton, sir Arthur Conan Doyle, Joe Dassin, Alexandre Dumas, Harrisson Ford, Blind Guardian, Johnny Hallyday, Tracy Hickman, Steve Jackson, John Kovalic, Robert Kubica, H. P. Lovecraft, George Lucas, Manowar, Nightwish, Leonard Nimoy, Rhapsody of Fire, Robert Rodríguez, J. K. Rowling, Juan Rulfo, Dan Simmons, Steven Spielberg, Quentin Tarantino, J. R. R. Tolkien, Henri Vernes, Sebastian Vettel y Margaret Weis. Su imaginación y talento han sido objeto de grato pasatiempo.

Por último agradezco el apoyo incondicional de mi familia, en el seno de la cuál siempre he encontrado el plácido descanso vacacional. Quiero aquí nombrar a mis tíos Petia Andreeva, André Basso, Daniel Bouchon, María-José Castillo Ezquerra, Carmelo Comerón Tejero, Fernando Comerón Tejero, Bernadette Limbourg y Thérèse Limbourg.

Nombro también a primos y a sobrinos segundos con los que he pasado muy buenos momentos: Agnès Basso, François Basso, Pierre Basso, Inés Comerón Andreeva, Sara Comerón Andreeva, Alexandre Valero, David Valero, Mathias Valero y Sébastien Valero. Mención especial para David Comerón Castillo y Gabriel Comerón Castillo por haber compartido tantas horas frikis con su primo (Ovejitas, Munchkin, Warhammer, WoW y el juego de tablero de Galactica). ¡Os repito que el cylon no soy yo!

Gracias a mis abuelos Adolfo Comerón Martín, Jules Limbourg, Renée Poirier y Sara Tejero Luque; en sus casas he disfrutado del calor muy intenso de las reuniones familiares.

Un recuerdo para mis hermanitas, Irene Comerón Limbourg y Leticia Comerón Limbourg. Siempre han sido cariñosas y han recibido con alegría a su hermano mayor cuando regresaba a casa. Nunca olvidaron un cumpleaños u onomástica a pesar de mis numerosos, aunque no (siempre) intencionados, descuidos. ¡Y además me regalaron muchas cartas de Munchkin!

Gracias a mis padres por crearme y por pagarme unos estudios que, a la larga, me iban a permitir presentar esta tesis doctoral. Siempre me han apoyado en todo, siempre han estado atentos a mis caprichos y han propiciado una completa y muy útil formación, tanto intelectual como espiritual. Ellos han logrado que ningún lugar me parezca mejor para pasar unas vacaciones que el que fuera (y muchas veces considero que sigue siendo) mi hogar.

Y por último doy gracias a Dios por haber creado un Universo tan elegantemente matemático que permite rastrear el diseño cuidadoso y bello del Creador. Gracias por haber planteado a la Humanidad este estimulante desafío.